



Planet-disk interactions in the binary system Kepler-38 and contribution to the METIS/ELT instrument

von

Sabine Graf

aus Karlsruhe

Inaugural-Dissertation zur Erlangung des Doktorgrades der
Mathematisch-Naturwissenschaftlichen Fakultät der Universität zu Köln

Berichterstatter: Prof. Dr. Lucas Labadie
Prof. Dr. Andreas Eckart

Tag der letzten
mündlichen Prüfung: 22. August 2022
Veröffentlichung: November 2022

Abstract

The scope of this dissertation is two-fold. The first part studies the planet-disk interactions in the binary system Kepler 38. Close binary stars like Kepler 38 hosting a circumbinary planet are, with 23 systems known, not unusual. A number of those systems exhibit a non-zero mutual inclination between the planetary orbit and the orbital plane of the central binary. Such systems are excellent laboratories to test theories describing the dynamical interactions between the binary star, the primordial circumbinary disk and the planet during its formation process. In order to address the question of the physical mechanisms at the origin of the observed misalignment between any of the three different components of the system (binary star, CB planet, CB disk), three-dimensional hydrodynamic simulations are required.

In this thesis, in contrast to previous works, the orbital evolution of a circumbinary Saturn-Mass planet in a scenario of primordial co-alignment of the system (binary orbit, planet orbit, disk mid-plane) is studied. Based on the hypothesis that due to the tidal influence of the central binary turbulence across the disk develops, such turbulence could generate hydrodynamical forces onto an existing, migrating, planet, in a plane not co-planar with the binary orbit and the disk mid-plane. This could trigger an initial inclination of the planet orbit, which can be investigated with three-dimensional hydrodynamical codes (and only with 3D codes).

The second part of this dissertation describes the laboratory research work completed for the METIS project, one of the first-light instrument of the ELT with high relevance of high angular resolution studies of circumstellar disks and binary systems. The mid-infrared imager and spectrograph (METIS) will be equipped with a warm calibration unit (WCU), which is developed at the University of Cologne. Its task will be to deliver simulated sources for the test and calibration of the METIS instrument. In this thesis, general concepts of the WCU are presented together with the laboratory work to validate those concepts. This thesis aimed to produce the prototyping measurement to document and verify the temporal and spatial properties delivered by the integrating sphere. Furthermore, the calibration accuracy is determined, and the contribution to the development of the aperture mask and the pinhole wheels are presented.

Contents

1	Introduction	1
1.1	Motivation	1
1.2	Objectives	2
1.3	Procedure	4
2	Planets in binary systems an numerical methods	6
2.1	Physics of planets in binary systems	6
2.1.1	Protoplanetary disk structure and evolution	7
2.1.2	Influence of binary stars on disk structure	8
2.1.3	Planet evolution	10
2.1.4	Angular momentum in YSO systems	15
2.1.5	Resonance Processes	16
2.2	Numerical methods for simulations	17
2.2.1	Euler equations	18
2.2.2	Navier-Stokes Equations	20
2.2.3	State of the art in the field of the 3D simulations in planet formation	21
3	Setup of the Kepler 38 FARGO3D simulations	31
3.1	Kepler 38: observed parameters as input/output for simulation	31
3.2	FARGO3D – MHD Code	32
3.2.1	Main equations	32
3.2.2	Numerical and physical setup	36
3.2.3	Surface density	39
3.2.4	Disk mass	41
3.2.5	Boundary conditions	43
3.2.6	Transformation Code Units (CU) to CGS units	45
3.2.7	Transformation from Spherical to Cartesian coordinates	46
4	Results of the FARGO3D simulations	51
4.1	The case of the single star system (default case)	51
4.1.1	Velocity field	52

4.1.2	Boundary conditions with Stockholm vs. no Stockholm condition . . .	52
4.1.3	Angular momentum of the disk	55
4.1.4	Angular momentum of the planet	55
4.1.5	Force on a planet	57
4.2	The case of the single star system (no default case)	57
4.3	The case of binary systems	62
4.3.1	Convergence in resolution	64
4.3.2	Simulation with the Stockholm conditions - basic tests	64
4.3.3	Simulation with Stockholm conditions - final setup	67
4.3.4	Simulation without Stockholm conditions - basic tests	84
4.3.5	Simulation without Stockholm conditions - final setup	90
5	Contribution to the METIS instrument	117
5.1	METIS	117
5.1.1	Warm Calibration Unit	120
5.2	Laboratory tests and proof-of-concept	124
5.2.1	Description of the measurement devices	124
5.2.2	Laboratory tests of source stability	129
5.2.3	Characterization of the spatial uniformity	143
5.2.4	Aperture Mask experiment to measure the detector linearity	148
5.2.5	Pinhole tests	161
6	Discussion	166
6.1	Discussion	166
6.1.1	Kepler 38	166
6.1.2	METIS	172
6.2	Conclusion	175
	Appendix	179
	Bibliography	190
	List of Figures	198
	List of Tables	205

1 Introduction

1.1 Motivation

At least 217 of the already known exoplanets are in binary star systems (Schwarz et al., 2016)¹. Since multiplicity is a feature common to about half of the solar-type stars (Duquennoy & Mayor, 1991; Raghavan et al., 2010), binary stars represent an important aspect of our understanding of the formation and evolution of planetary systems. Twenty-three of the already found exoplanets in binary systems are p-type (circumbinary, CB) planets which means that the planet circles both central stars (Pilat-Lohinger et al., 2019, p. 118). The discovery of which has been largely achieved by the Kepler mission. A number of p-type planets in the Kepler systems exhibit a non-zero mutual inclination of their orbit relatively to the central binary orbital plane as, e.g., in Kepler 16, Kepler 34, Kepler 35, Kepler 38, and Kepler 413 (e.g. review by Welsh & Orosz (2018, pp. 9-13)). In these systems, the inner planets have been observed close to the stability limit (Orosz et al., 2012, p. 3; Kostov et al., 2014, p. 1; Welsh & Orosz, 2018, p. 15), which corresponds to the shortest separation before the planet becomes dynamically unstable, being then potentially ejected or accreted onto the star (Holman & Wiegert, 1999). The inclination values are small ($<0.5^\circ$, except for Kepler 413 with a 2.5° misalignment) but not negligible (Doyle et al., 2011, p. 4; Welsh et al., 2012, p. 476; Orosz et al., 2012, p. 22; Kostov et al., 2014, p. 1). The central stars are close binaries with orbital periods ranging from 10 to 41 days (Thun & Kley, 2018, p. 2). The orbital period of the planets varies from 66 to 289 days (Welsh et al., 2013, p. 7; Kostov et al., 2014, p. 1). Similarly, the mutual inclination between the binary star and the CB disk in which planets form is found to be statistically small ($\theta < 3^\circ$) for short-period binary stars similar to the Kepler targets (Czekala et al., 2019, p. 1).

Such systems are excellent laboratories to test theories describing the dynamical interactions between the binary stars, the primordial circumbinary disk and the planet during its formation process. For instance, Thun & Kley (2018) have studied the aforementioned Kepler systems in the context of planetary migration through two-dimensional hydrodynamical (HD) simulations to support the formation in the outer accretion-friendly regions of the disk

¹<https://www.univie.ac.at/adg/schwarz/multiple.html> (2022-06-01)

as opposed to in-situ formation, which appears unlikely (Pierens & Nelson, 2007, p. 993; Silsbee & Rafikov, 2015, p. 1) due to the expected destructive collisions of the planetesimals in close orbits. They could show that the planet migrates down to the edge of the disk's inner cavity that resulted from the dynamical interactions with the close binary star (Artymowicz & Lubow, 1994, p. 662), and that this cavity acts an inner barrier due to the sharp density drop.

Now, in order to address the question of the physical mechanisms at the origin of the observed misalignment between any of the three different components of the system (binary star, CB planet, CB disk), three-dimensional hydrodynamic simulations are required.

Already in the single star case harboring a planet, different teams exploited 3D simulation results to show how a primordial misalignment between the disk and an inclined planetary orbit can be damped over time following a damping law di/dt that is strongly depending on the initial inclination and eccentricity values (Cresswell et al., 2007, p. 329; Bitsch & Kley, 2011, p. 1). In the context of multiplicity, the perturbation effect of a close stellar companion on the disk inclination is evidenced by Smallwood et al. (2019, p. 2919). These authors investigated with the smoothed particle hydrodynamical (SPH) code PHANTOM tilted ($10^\circ - 60^\circ$) low-mass ($\sim 0.001 M_b$) circumbinary disks around eccentric binaries and found the latter to trigger tilt oscillations which amplitude correlates with the eccentricity of the binary star. Namely, the larger the eccentricity, the larger the amplitude of the tilt oscillations, and the smaller the damping of these oscillations. They further reveal that those disks may increase their inclination by a significant factor before they realign. Pierens & Nelson (2018, p. 2548) studied, in the specific case of the Kepler 413 planetary system, the impact of a primordial misalignment of circumbinary disk relative to the binary orbit onto the final orbital properties of a migrating planet embedded in the disk and initially co-aligned with it. The authors show that whether the planetary orbit realigns with the central binary stars or remains co-aligned with the disk depends on the disk's mass.

1.2 Objectives

In this thesis, in contrast to previous works, the orbital evolution of a circumbinary Saturn-Mass planet in a scenario of primordial co-alignment of the system (binary orbit, planet orbit, disk mid-plane) is studied. Indeed, earlier theoretical works by Kurbatov et al. (2014, 2017) have evidenced the development of turbulence across the disk due to the tidal influence of the central binary. Based on this hypothesis, such turbulence could generate hydrodynamical forces onto an existing, migrating, planet, in a plane not co-planar with the binary

orbit and the disk mid-plane. This could trigger an initial inclination of the planet orbit, which can be investigated with three-dimensional hydrodynamical codes (and only with 3D codes).

As such inclination effects are expected to be small, the system Kepler 38 is adopted as a test case, in which the circumbinary planet is tilted by less than 0.2° , and investigated how the disk properties (in particular its mass and viscosity) combined to the dynamical interaction with the central binary may result in inhomogeneities in the vertical disk's structure that may directly influence the inclination of the planetary orbit. For this purpose, the FARGO3D three-dimensional hydrodynamical (HD) code (Benítez-Llambay & Masset, 2016, p. 1) is used, which has been exploited to investigate the disk-response to inclined massive planets in single star systems or the processes of realignment of a planetary orbit in binary systems (Pierens & Nelson, 2018, p. 2547). In this thesis, it is referred to numerical experiments rather than numerical simulations for the following reason: The goal was not to develop a new code based on first principle equations which have already been done in the past, but to use existing code, to run different tests.

First, a test case to understand the limitation of the author's numerical experiment has to be examined, i.e., distinguish physical effects from numerical noise. Therefore, a single star has been implemented in the FARGO3D code instead of a binary star. Then the binary star of interest has been analyzed, Kepler 38, by studying the influence of different parameters on the planet's orbit. Consequently, different starting scenarios for the FARGO3D code have been implemented.

From the observations point of view, the questions addressed numerically are not simple to investigate. However, indirect effects on the planetary environment – namely the disk – could be investigated through observations. In the recent years, many infrared imaging campaigns have highlighted the complex spatial structure of disks (Garufi et al., 2017) resulting from the interaction with a possible (proto)planet. The type of disks relevant for the simulations in this thesis can be observed in the near- and mid-infrared. However, until recently, the current observational facilities lacked enough angular resolution. Through interferometry, there have been some attempts to reach the required angular resolution, but in the end, the results are models, not direct images. Nevertheless, the new telescope ELT with METIS will change this in the future, enabling direct imaging of these disks in the mid-IR and at high angular resolution.

Because of the high relevance of such instrumentation for the study of disks in single and binary systems, the opportunity arises with this thesis to contribute to the development of the METIS instrument. Concretely, this thesis will investigate and test parts of the warm calibration unit (WCU), a sub-system of the METIS instrument. The WCU is developed

by the working group of Prof. Dr. Labadie and belongs to the METIS instrument that will be part of the 39 m Telescope ELT. The first light of the ELT is planned for 2027² and will improve the observing quality of e.g. exoplanets and disks³.

METIS, the mid-infrared imager and spectrograph for the wavelength range 2.9-13.5 μm (astronomical L-, M- & N bands)⁴, will be equipped with a calibration unit, developed at the University of Cologne, which aims at delivering simulated sources for the test and calibration of the main imaging and spectral functionalities of METIS. The subsystem, as the entire METIS instrument, is currently in Phase C of the project, which leads to the Final Design Review expected by the end of November 2022.

This thesis aimed to produce the prototyping measurement to verify the flux properties coming from the integrating sphere. This helps to provide the calibration of the integrating sphere output. Furthermore, the calibration accuracy should be determined, and the contribution to developing the aperture mask and the pinholes are displayed. Thus this thesis will provide an estimate of the mask that should be used within the WCU. This work contributing to developing METIS will bring forward the understanding of the evolution of exoplanets in binary systems.

1.3 Procedure

This thesis is structured as follows, in chapter 2 the theoretical background of protoplanetary disks is given, with a focus on their structure, evolution, and the influence of binary stars on the disk structure. This is significant for choosing the initial parameter of the simulation and comparing it with the observational data. In addition, planet evolution is explained. Primarily type I migration is essential for evaluating the results of the Kepler 38 simulation. As the simulation is 3D, the angular momentum in those young stellar systems can be analyzed. A short introduction of resonance processes is given as well. Then, the numerical methods for simulations are displayed including two more theoretic sections on fluid motion and hydrodynamics to understand the science behind the FARGO3D code. The closing section of this chapter displays state of the art 3D simulations of planet formation. This overall view helps to place the analysis and results in the context of the findings in the scientific community.

In chapter 3 the setup of Kepler 38 FARGO3D simulations is presented. Firstly, observational

²<https://www.elt.eso.org/about/timeline/> (2021-07-06)

³<https://www.elt.eso.org/instrument/METIS/> (2021-06-17)

⁴<https://www.elt.eso.org/instrument/METIS/> (2021-06-17)

data is presented; secondly, the setup with all the parameters is described. The simulations of disks are addressed by focusing on the description of FARGO3D. In particular, the main equations are discussed, together with the numerical and physical setup, the surface density, disk mass, and boundary conditions, followed by the explanation of the transformation of the code units and the Coordinates. Those sections are crucial for understanding FARGO3D and choosing parameters consistent with the physics of these systems.

In chapter 4 the results of simulations of Kepler 38 are discussed. The first part focuses on the results of a single star system with a default star, followed by a single star system with no default star. Those preliminary setups were test cases to validate the setup and are the base for comparisons to the binary setup. The results of the binary setup were done with one significant difference; one time with the Stockholm condition and one time without it. This condition has a significant influence on the boundary condition and thus the disk mass. Those setups were also simulated, e.g., without a planet, to study the binary and disk interaction. The convergence of resolution was also tested because of the dependency of the results on the grid used in the code. Afterward, the Neptune-sized planet was inserted into the disk and studied in more detail.

In chapter 5 the basics about METIS and the WCU are presented. This is important for understanding the requirements, which will be tested in the following section. There the laboratory tests and the proof-of-concept experiments are discussed. As an introduction, the different measuring devices used in later experiments are displayed. The hub of delivering the calibration functionalities is the integrating sphere combined with the blackbody. Thus stability tests in the laboratory were performed on the blackbody. Another key concept for linear calibration is the aperture mask, as the tuning of the temperature of the blackbody changes the flux and the wavelength range. To keep those parameters constant is essential for linear calibration of the blackbody. The ideas to realize this setup are tested through experiments. Moreover, to generate artificial point sources, different pinholes were tested. Those components will enable the WCU to calibrate the METIS instrument to observe, for example, the inner parts of protoplanetary disks.

In chapter 6 a conclusion is given, and the results are discussed.

2 Planets in binary systems and numerical methods

This thesis focuses on the planet-disk interactions in the binary system Kepler 38. In the first section of this chapter, a closer look at the physics of planets in binary systems is taken. The protoplanetary disks, the influence of a stellar companion on the disk, the planet evolution, and the angular momentum in Young Stellar Objects (YSO) systems are detailed. The second section focuses on the numerical methods. Where the first two subsections are about the mathematical constructs within the disk. This includes the simplification of handling the gas as a fluid and the hydrodynamics within a disk. The closing subsection details the state of the art of three-dimensional (3D) simulations in planet formation to place this work in the current context of the scientific community.

2.1 Physics of planets in binary systems

It is observed that planets form in protoplanetary disks during the first few millions of years in the lifetime of a star. These protoplanetary disks consist of gas (99% by mass) and dust (1%) (Beckwith & Sargent, 1996, p. 141). Stars are born in prestellar cores with particle number densities of $n \sim 10^5 \text{ cm}^{-3}$. As the angular momentum is too large to collapse directly to stellar densities of $n \sim 10^{24} \text{ cm}^{-3}$, a disk is formed (Armitage, 2009b, p. 34). A dense core in such a scenario would have an angular momentum of $10^{21-22} \text{ cm}^2\text{s}^{-1}$ which evolves into pre-main-sequence binaries with an angular momentum of $10^{19-20} \text{ cm}^2\text{s}^{-1}$. Thus the angular momentum needs to be reduced by two orders of magnitude for a disk to form (Belloche, 2013, p. 2). For accretion to happen, angular momentum needs to be redistributed or lost within the gas disk. The specific angular momentum is approximately an increasing function of the radius ($l = r^2\Omega_k = \sqrt{GM}r$ with the Keplerian angular velocity $\Omega_k^2 = GM/r^3$) (Armitage, 2007, p. 17). This angular momentum loss happens at time scales which are a lot longer than the dynamical (orbital) time scale ($t_{\text{dyn}} = 1/\Omega_k$) (Armitage, 2009b, p. 34; Rosotti, 2014, p. 12; Klahr et al., 2018, p. 9).

2.1.1 Protoplanetary disk structure and evolution

It has been shown observationally that, as stars form in stellar clusters, most of these stars are part of binary or multiple systems (Duquennoy & Mayor, 1991, p. 520). Around half of the solar-type stars form in binary systems (Duquennoy & Mayor, 1991, p. 520; Raghavan et al., 2010, p. 28). The presence of binary systems will have an effect in the disk properties, such as initial mass, size, and chemical composition. Furthermore, the evolution of protoplanetary disks can be influenced by stellar radiation, stellar flybys, or ongoing gas accretion. Another dominant environmental effect can be external radiation from other stars within the cluster (Armitage, 2009b, pp. 34-35).

The early developing stages of stars are called Young Stellar Objects (YSO). YSOs are objects which have an evolving disk. They are often classified into four classes 0-III through the spectral energy distributions (SED) (Lada, 1987, pp. 6+10). The disk structure varies depending on the different classes (see Fig. 2.1). In this Ph.D. thesis, Class II YSOs are of interest. The infrared (IR) excess in those YSOs indicates the presence of a disk (Armitage, 2009b, pp. 37-38). In this stage, the envelope is gone, and the protoplanet has already formed. Class I objects also have a disk, but they are still embedded in an envelope. To simulate those objects is not the primary purpose of the FARGO3D code, other codes (e.g., FLASH) are more suited for it. In Class III objects, the disk has already dissipated. Disk masses of Class II objects range from approximately 0.001 to 0.5 solar masses (M_{\odot}) (Beckwith, 1990, p. 940) while the disk mass of the minimal-mass solar nebula (MMSN) lies between 0.01 and 0.1 M_{\odot} (Weidenschilling, 1977, p. 158).

Observations show that disks evolve. As a consequence, in-flowing gas needs to lose angular momentum to be accreted by the star. This is called angular momentum transport, as it allows local gas packages to reduce their angular momentum and spiral towards the star. It is generally considered that the loss of angular momentum can be caused by viscosity or loosely "friction" (Armitage, 2009c, p. 68). Out of different mechanisms to generate viscosity, the molecular viscosity of the gas is insufficient. For example, in a single star system with a sound speed of 0.5 km s^{-1} at 10 AU, the molecular viscosity is roughly $2.5 \cdot 10^7 \text{ cm}^2 \text{ s}^{-1}$. Therefore, the viscous time scale ($\tau_v \sim r^2/\nu = 3 \cdot 10^{13} \text{ yr}$) would be longer than the age of the universe ($\sim 14 \cdot 10^9 \text{ yr}$) (Armitage, 2009c, p. 79). This is in direct conflict with the observations. Thus there needs to be other causes for angular momentum loss. Those sources are still debated, with the magneto-rotational instability (MRI) being the most accepted theory (Birnstiel et al., 2010, p. 2). A parametrized description of the viscosity was introduced in the models of turbulent α viscosity by Shakura & Sunyaev (1973). These models can be tuned to make the disk viscous enough. The turbulent viscosity can be written as $\nu = \alpha c_s h$, where α is the turbulence parameter ($\alpha < 1$), c_s the sound speed and h the disk scale-height (Armitage,

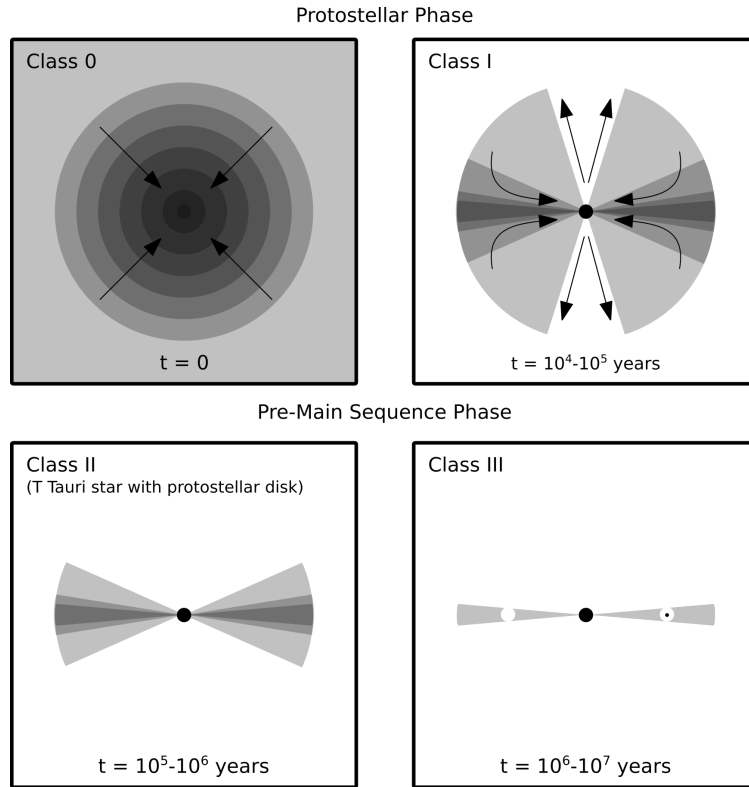


Fig. 2.1: The classification of YSOs. Showing, the evolution of the disk structure. A T Tauri Star is a young star with less than $2M_{\odot}$. The classification of YSOs Class I-III was done by Lada (1987, pp. 6+10). Class 0 was added later.

2009c, p. 79; Birnstiel et al., 2010, p. 2). In FARGO3D, which is used in this thesis, this turbulent viscosity drives the evolution of the disk and is represented by α . As mentioned before, the angular momentum is an increasing function of the radius. Thus because of viscosity, local gas packages reduce their angular momentum. Nevertheless, through the same viscosity, the disk gas must gain angular momentum and move outward because global angular momentum conservation is still valid (Armitage, 2009c, p. 68).

2.1.2 Influence of binary stars on disk structure

Compared to the single star system, the structure of protoplanetary disks in binary systems is strongly influenced by tidal forces from the binary system (Kley & Nelson, 2010, p. 136). The separation of the binary influences the strength of gravitational perturbations, which generate spiral waves in the disk (Pringle, 1991, p. 754; Thun et al., 2017, p. 2). These waves transport energy and angular momentum from the binary to the disk (Pringle, 1991, p. 754; Thun et al., 2017, p. 2). The effects mentioned above also lead to quicker disposal of the disk depending on the separation (Cieza et al., 2009, pp. L86-L87). Observational evidence for intermediate binaries shows that the circumstellar disks are 10 times smaller and are

disposed around 10 % quicker than in single star systems (Cieza et al., 2009, p. L87). Cieza et al. (2009, p. L86) found that this leads to lifetimes between 0.3-0.5 Myr for these disks.

Depending on the separation of the binary star, the disk forms as a circumbinary, circumprimary, or circumsecondary disk (Prato & Weinberger, 2010, p. 1) or combinations of it (see Tab. 2.1).

Tight binaries are defined as having a separation between 0.05 AU and 0.4 AU, models suggest a circumbinary disk is formed around those binaries (Quintana & Lissauer, 2006, p. 1). Observational evidence of circumbinary disks was found in the T Tauri binary systems DQ Tau (Mathieu et al., 1997, p. 1841) and UZ Tau E (Martín et al., 2005, p. 1). In these systems, the binary orbital period is between 15 and 18 days (Mathieu et al., 1997, p. 1841; Martín et al., 2005, p. 1). This indicates a separation of roughly 0.06 AU (Mathieu et al., 1997, p. 1844). Moreover, observations show, that those circumbinary accretion disks are turbulent. This nonmagnetic turbulence of the gas-dynamic is caused by instabilities produced by the tidal influence of the binary star (Kurbatov et al., 2014, p. 787). Kurbatov et al. (2014, p. 787) found through two-dimensional hydrodynamic simulations that the perturbations of the second binary component occur in the interior of the disk and produce turbulent gas. This turbulence propagates outwards through the disk (Kurbatov et al., 2017, p. 1036). Also, in already evolved tight binary systems, with main-sequence stars and fully developed planets, the remains of such a circumbinary disk are indicated through an existing circumbinary planet. In 2011, the first planet orbiting a tight main-sequence binary was discovered around Kepler 16 (Doyle et al., 2011, p. 1603). The binary of Kepler 16 consists of a K-type main-sequence star and an M-type red dwarf. The semi-major axis of the binary is 0.22 AU (41 days) and the semi-major axis of the discovered exoplanet is 0.7048 AU (228 days) (Doyle et al., 2011, p. 1605). Already one year later, Welsh et al. (2013, p. 7) listed the first six circumbinary exoplanets known, one of them being Kepler 38 (Orosz et al., 2012, p. 1).

A small binary is defined as a binary with a separation of the components between 0.4 AU and 40 AU. It hosts circumbinary and circumstellar disks (Augereau et al., 2015, p. 65). Observationally, the T Tauri WWCha binary has shown evidence that it hosts circumstellar and circumbinary disks. Its separation is 1.01 AU (207 days) (Eupen et al., 2021, p. 1). It is a unique system where the presence of circumstellar disks can be derived through the magnitude of excess (Eupen et al., 2021, p. 8). Binaries with separations between 40 AU and 100 AU are denoted as intermediate binaries, whereas binaries with separations larger than 100 AU are called wide binaries. Wide binaries and intermediate binaries host circumstellar disks (Augereau et al., 2015, p. 65). In the survey of T Tauri (Class II) stars, Akeson et al. (2019, p.20) found that the circumstellar disks around intermediate binaries are significantly less massive than those around wide binaries or single stars. A good example of

a T Tauri intermediate binary is DD Tau. Its separation is 79 AU and it has circumstellar disks (Duchêne, 2010, p. L117; Bouvier et al., 1992, p. 456). Recent examples of wide binaries are KK Oph and HD 144668 T Tauri binary systems (Panić et al., 2021, p. 4317). They have separations of 356 AU (KK Oph) and 235 AU (HD 144668) (Panić et al., 2021, pp. 4320-4321). Both systems host a circumstellar disk with no evidence of a circumbinary disk (Panić et al., 2021, p. 4318) but asymmetries are found in the primary disk in the outer regions, which are due to the secondary (Panić et al., 2021, p. 4317; Augereau et al., 2015, p. 61).

Tab. 2.1: Binary separations with disk types

typical binary separation [AU]	disk type
0.05-0.4	circumbinary
0.4-40	circumbinary and circumstellar
>40	circumstellar

Planet migration and terrestrial planet formation are more likely to be observed in the inner few AU of a circumstellar disk (Prato & Weinberger, 2010, p. 5). Thus this Ph.D. thesis focuses on this part of circumstellar disks.

2.1.3 Planet evolution

In the protoplanetary disks mentioned in the previous section, planets can evolve. Up until now, 217 exoplanets in 154 binary systems have been found (Schwarz, 2021). In this section, first, a closer look at planet evolution in single star systems is taken because later in the simulations conducted in this thesis, single star systems are used for comparison. This is followed by exploring planet evolution in binary star systems, which is the main focus of this thesis.

Planet evolution in single star systems

The core accretion model and the gravitational instability model are the two basic scenarios of planet formation today. Simplified, the accretion model is a multistage process starting with a collisional growth of submicron-sized dust grains, continuing with the formation of kilometer-sized planetesimals, and eventually leading to the growth of terrestrial planets in the inner region of the disk. Gas planets can form their massive cores in the outer region where they can accrete gas (Kley & Nelson, 2012, p. 212). In the second model, the gravitational instability model, the protoplanetary disk fragments into gaseous clumps. These

clumps have planetary masses. In this model, planet formation happens during the early stages when the disk mass is comparable to the central star's mass. Fragmentation is more likely to happen at large distances (>50 AU) in the disk where the cooling times are short (Kley & Nelson, 2012, p. 212).

In the disk of a single star system, a young planet disturbs the disk dynamically in two ways (see Fig. 2.2). First, through spiral waves, caused by the Keplerian differential rotation (Kley & Nelson, 2012, p. 213). Those spiral waves are radially propagating density waves (Kley & Nelson, 2012, p. 213) (see Fig. 2.2a). Second, the planet's disturbance separates the outer and inner disk by a co-orbital region (Kley & Nelson, 2012, p. 213) (see Fig. 2.2b). As the density structures are not symmetrical, gravitational torques are exerted on the planet. This causes changes in the orbital elements (Kley & Nelson, 2012, p. 213) which lead to migration of the planet. Thus, in viscous disks where these effects come to play, a planet always migrates (Kley & Nelson, 2012, p. 212).

The spiral arms are caused by the effect called Lindblad torques. The inner spiral which pulls the planet forward generates a positive torque. Through this effect, the planet gains angular momentum and migrates outwards. On the other hand, the outer spiral drives the migration inwards because of its pullback. The migration is the net effect of the residual between the two pulls. It depends on the physical details of the disk and is called type I migration (Kley & Nelson, 2012, p. 213).

Type I migration is characteristic for low-mass planets, which do not significantly alter the global disk, and no gaps are opened in the disk (Kley & Nelson, 2012, p. 216). For giant planet masses, 'the interaction becomes increasingly nonlinear' (Kley & Nelson, 2012, p. 223). Thus the density profile is modified, and a gap forms.

The gap opening criterion (P) is defined by Crida et al. (2006, p. 17) and transformed by Thun & Kley (2018, p. 8) to:

$$P = \frac{h}{q^{1/3}} + \frac{50\alpha h^2}{q} \leq 1 \quad (2.1)$$

where h corresponds to the disk's constant aspect ratio, α is the turbulent viscosity (α viscosity), and q is the mass-ratio of the planet and the star/binary.

Depending on the planet-to-star/binary mass-ratio and disc parameters, like alpha viscosity and aspect ratio, a Saturn-mass planet can undergo a type I migration.

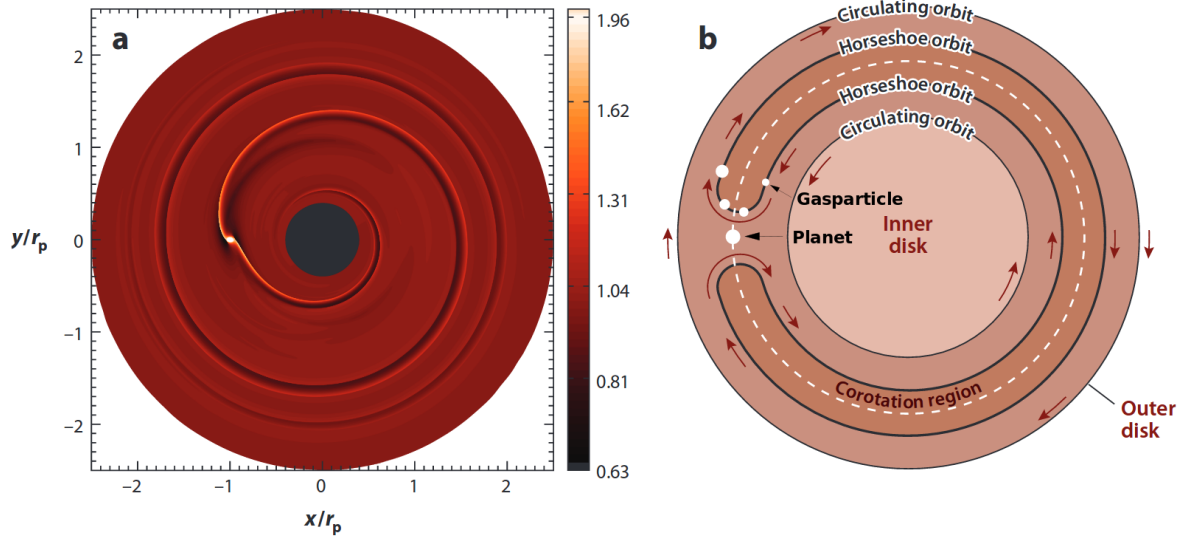


Fig. 2.2: A constant surface density disk which is normalized with an embedded planet with a mass-ratio $q = 9 \cdot 10^{-5}$ as a disk surface density and flow structure. This mass-ratio is comparable to a planet with $0.1 M_{\text{Jupiter}}$ around a solar-mass star. (a) Spiral arms and the inner leading and the outer trailing are visible. The planet was inserted five orbits before. The disk is in Keplerian rotation. Thus the gas-particle on smaller radii have larger velocities. (b) Topology of the flow field with the planet as the reference. The disk is split into an outer disk with clockwise moving material, a horseshoe-shaped co-rotation region (within the thick black lines), and an inner disk with counterclockwise movement. The clockwise moving of the material is because the planet acts as a reference frame. From its point of view, the slower outer particle seems to move backward and the quicker inner particles forward, but in the reference frame where the star is the reference, the particles still move in the same direction. The inner particle is faster than the outer one. This phenomenon can be seen on Earth with Mars when he has an apparent retrograde motion because Earth surpasses him. Of course, Mars still moves forward; that is why the reference frame is important. This figure is adopted from Kley & Nelson (2012, p. 214).

Planet evolution in binaries

In a single-star formation scenario, the giant gas planets need to form further outside in the disk, and migrate to the observed locations. In the binary case, the in situ formation scenario is even more unlikely than the accretion model because destructive collisions of the planetesimals in close orbits are expected (Pierens & Nelson, 2007, p. 1001; Silsbee & Rafikov, 2015, p. 1). Additional observations provide evidence for migration (Kley & Nelson, 2012, p. 212) and further evidence for this migration are the observations of giant planets in mean motion resonance (Kley & Nelson, 2012, p. 212). An example of a planet which underwent migration is the hot Saturn Kepler 38b (Orosz et al., 2012, p. 1).

A planet in a binary system can form in two ways. Firstly, the planet can form in a circumstellar disk around one of the two stars; then, it is called an s-type configuration. Secondly, the planet can form around both stars, then it is called p-type configuration (Kley & Nelson, 2010, p. 136).

The binary impacts the disk, leading to disadvantages for planet formation compared to single star systems (Marzari & Thebault, 2019, p. 1). The gravitational influence of the binary companion influences all stages of planet formation. The shorter lifetimes of disks in binary systems were mentioned before, but the proto-planetary disk formation and evolution are influenced as well. Also, the dust accumulation into planetesimals and the growth into planets is negatively influenced as the hindering accretion velocities are increased by the perturbations of the binary (Marzari & Thebault, 2019, p. 1). Another negative impact for the probability of planet formation in binary stars is the mean motion resonances which lead to unstable regions (Marzari & Thebault, 2019, p. 1). In those regions, planet formation is inhibited (Marzari & Thebault, 2019, p. 1). Furthermore, an already formed planet would be ejected out of the system if the planet migrates into this region (Marzari & Thebault, 2019, p. 1). Those effects exist in both s- and p-type systems (Marzari & Thebault, 2019, p. 1).

Planet migration in circumbinary disks (p-type) differs significantly from circumstellar disks around single stars. In circumbinary disks, spiral waves are generated due to the gravitational perturbation of the central binary star. These alter the evolution of the circumbinary disk and form an important dynamical feature, for instance, a central cavity in the circumbinary disk (Artymowicz & Lubow, 1994, p. 665; Thun et al., 2017, p. 4) (see Fig. 2.3).

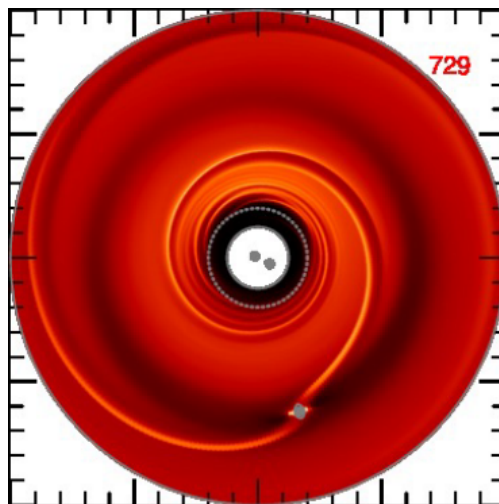


Fig. 2.3: The surface density of a 2 AU by 2 AU sized circumbinary disk around a binary is shown. The binary parameters are similar to Kepler 38. The red number indicates the time in Earth years. The two grey dots in the center are the locations of the binary stars, and the planet is the grey dot within the disk. This figure shows the spiral waves generated by the binary and the central cavity of the disk. This figure is taken from Kley & Haghighipour (2015, p. 8).

Dynamics of p-type planets

As mentioned above, at least twenty-three of the already found exoplanets in binary systems are in p-type systems (Pilat-Lohinger et al., 2019, p. 118; Schwarz, 2021). Primarily, the goal of the space-based Kepler Mission was to search for Earth-sized planets around solar-like stars (F to K dwarfs) (Koch et al., 2010, p. L79) analogue to our solar system. Searching in binary systems was not the focus. However, observing those stars, it was later found that 1.3% of them were actually binary systems (Kirk et al., 2016, p. 1). This corresponds to a total of 2878 objects out of roughly 200,000 observed objects (Kirk et al., 2016, p. 1). From the 217 exoplanets found in binary systems, 63 exoplanets were discovered in the original Kepler mission, and 12 exoplanets were discovered with the follow-up mission K2 (Schwarz, 2021; Johnson, 2017). For the 23 p-type exoplanets, nine were found in the original Kepler mission, and one was found in the following up mission (Schwarz, 2021).

Their orbits inclinations towards the binary plane are relatively low (mostly $< 0.5^\circ$ (Thun et al., 2017, p. 1; Doyle et al., 2011, p. 4; Welsh et al., 2012, p. 476; Orosz et al., 2012, p. 22; Kostov et al., 2014, p. 1)) because the probability of transits is higher if the planet's orbit is aligned with the binaries orbit. Thus coplanar systems are easier to detect with the transit method which the satellite Kepler (Johnson, 2017) uses.

Kepler 38, for example, has an inclination smaller than 0.2° (Kley & Haghighipour, 2014, p. 2). In contrast the maximal inclination in the solar system is Mercury which has an inclination of 7.0° toward the ecliptic (UCLA, UCLA).

A p-type planet has a stable orbit at the separation from the central binary given by the following equation (Haghighipour et al., 2010, p. 299), which shows the critical semi-major axis a_c corresponding to the closest stable orbit (Holman & Wiegert, 1999, p. 626).

$$\begin{aligned}
 a_c = & [(1.60 \pm 0.04) + (5.10 \pm 0.05)e_b + (4.12 \pm 0.09)\mu \\
 & + (-2.22 \pm 0.11)e_b^2 + (-4.27 \pm 0.017)\mu e_b + (-5.09 \pm 0.11)\mu^2 \\
 & + (4.61 \pm 0.36)\mu^2 e_b^2] a_b
 \end{aligned} \tag{2.2}$$

with e_b being the binary's eccentricity, a_b being the semi-major axis of the binary, and μ being the reduced mass ($m_1 m_2 / (m_1 + m_2)$). This is an empirical expression derived through a fit after studying test particles around eccentric binary systems by Holman & Wiegert (1999, pp. 621+626). Test particles that encounter one of the stars or escape are removed from the integration; only stable orbits were considered to find the critical semi-major axis (Holman & Wiegert, 1999, p. 622).

secular excursions (Wu & Lithwick, 2011, p. 1). But these effects are not enough to explain the population of misaligned hot Jupiters or hot Saturns (Batygin, 2012, p. 418). Although disk-driven migration theoretically should tend to maintain coplanar (Kley & Nelson, 2012, p. 243), studies of Batygin (2012, p. 420) suggest that disk-torque is the likely origin of the misalignment. Therefore, the missing link could be migration.

In the case of a slight misalignment with respect to the binary's orbit, the planet's orbit undergoes nodal precession circulating with a nearly constant tilt (Martin & Lubow, 2017, p. 1), resulting from a coupling between the binary's angular momentum and the planet's specific angular momentum. This coupling produces a torque on the planet which leads to the gyroscopic motion about the orbital rotation axis of the binary (Doolin & Blundell, 2011, p. 2657).

In a binary system each star, the planet and the disk has an angular momentum vector:

$$\mathbf{L} = m\mathbf{r} \times \mathbf{v} \quad (2.3)$$

with m being the mass, \mathbf{r} being the vector to the center of mass, and \mathbf{v} being the vector of the object's velocity. These vectors are important to calculate the mutual inclination:

$$i = \arccos \left(\frac{\mathbf{L}_1 \cdot \mathbf{L}_2}{|\mathbf{L}_1| |\mathbf{L}_2|} \right) \quad (2.4)$$

between two angular momentum vectors, e.g., the angular momentum vector of the secondary (\mathbf{L}_1) and the planet (\mathbf{L}_2).

2.1.5 Resonance Processes

Apart from the already mentioned resonances (Lindblad and Corotational resonances), more resonances like the mean-motion resonances (between the planet and the binary companion) are important. Those mean-motion resonances are frequent conjunctions at the same orbital location (Armitage, 2009a, p. 239). Thus a 2:1 resonance is when conjunction between the secondary and the planet occurs every period of the planet. Whereas in a 3:1 resonance, the conjunction happens every second orbit of the planet. During the migration process planets can be captured into a mean-motion resonance (Baruteau et al., 2013, p. 43). Nevertheless, a planetary system has more resonances, e.g., the Kozai-Lidov resonances (Armitage, 2009a, p. 244). Resonance processes can also create regions of instabilities.

2.2 Numerical methods for simulations

In the scientific community, there are typically two ways of treating hydrodynamical simulations (HD) of 3D protoplanetary disks. One is based on the grid method, which uses fluid dynamical equations to transfer information between adjacent cell boundaries (Agertz et al., 2007, p. 963). The other one is the smoothed particle hydrodynamical (SPH) method, where for each gas-particle, the properties are calculated through averaging neighboring particles (Agertz et al., 2007, p. 963). The advantage of grid codes, which are used in this thesis, is the capability to resolve and treat dynamical instabilities (Agertz et al., 2007, p. 963). An example of such a dynamical instability would be the Kelvin-Helmholtz instability which occurs when a velocity shear in a single continuous fluid is present (Agertz et al., 2007, p. 965). This instability should not be neglected as it is happening in the disk. However, with SPH codes, this process was poorly resolved until recently (Agertz et al., 2007, p. 963; Tricco, 2019, p. 1).

Fluid motions

One would think that as stars are gaseous, they should be dealt with kinetic theory and gas dynamics (Shore, 1992, p. 1). However, as the star creates its own gravitational field, it rather mimics the behavior of a fluid moving under gravity (Shore, 1992, p. 2). It is applicable to treat the collection of gas in disks as a continuum or fluid (Shu, 1992, p. 3), because the mean free path l is much smaller than the macroscopic length scale L , on which the properties of the fluid change measurably.

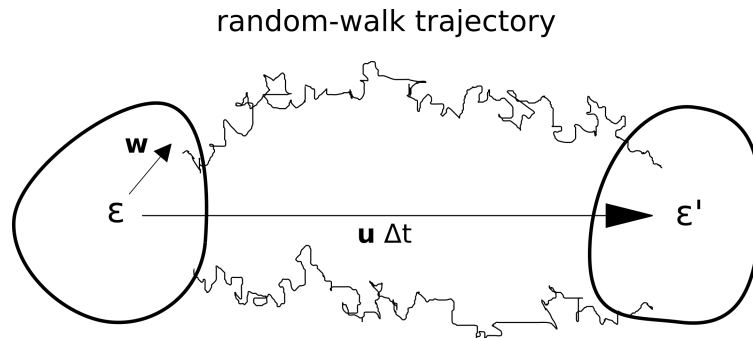


Fig. 2.5: As the mean free path l for particle collisions is small compared to the dimensions of the fluid element ϵ , the particle will be swept along by the fluid motions at bulk velocity \mathbf{u} .

Physically it makes sense to use the concept of a fluid element ϵ with volume V which is small in comparison to the separation of elements (L) but large in comparison to the mean free path (l) (Shu, 1992, p. 4) (see also Fig. 2.5). This allows to define a mean velocity \mathbf{u} for the collection, as the number of particles per fluid element is large. Adding a random component \mathbf{w} , the individual particle motions \mathbf{v} can be described (Shu, 1992, p. 3):

$$\mathbf{v} = \mathbf{u} + \mathbf{w} \quad . \quad (2.5)$$

In this thesis, the fluid hydrodynamical (HD) code FARGO3D (Benítez-Llambay & Masset, 2015a) is used. The important hydrodynamical equations used by FARGO3D are briefly described in this section.

There are two cases of hydrodynamical equations, for the perfect fluid, the Euler Equations, and for the non-ideal fluids, the Navier-Stokes Equations (Chorin & Marsden Jerrold E., 1993, p. 1). The continuity equations do not change for fluids with viscosity and heat transportation. Nevertheless, the formulas for momentum and energy conservation do change.

All formulas used in this thesis follow the Eulerian description. This means that the flow of the fluid, which is characterized by the density ρ , velocity \mathbf{u} , pressure P , temperature T , etc. are functions of the time t at different fixed locations \mathbf{x} (Shu, 1992, p. 44).

2.2.1 Euler equations

A continuum, consisting of perfect fluid or gas, is considered as described in Sect. 2.2. For the derivation of the Euler equations, three basic principles are used (Chorin & Marsden Jerrold E., 1993, p. 2):

- mass conservation (mass is neither created nor destroyed)
- momentum conservation (Newton's second law: the rate of change of momentum of a portion of the fluid equals the force applied to it)
- energy conservation (energy is neither created nor destroyed)

Mass conservation

With no volumetric sinks and sources of matter, the changing rate of the mass in volume V must be equal minus the changing rate of mass in flux $\rho\mathbf{u}$ 'past the element of area $\mathbf{n}dA$ integrated over the entire area A ' (Shu, 1992, p. 45):

$$\frac{d}{dt} \int_V \rho dV = - \oint_A \rho\mathbf{u} \cdot \mathbf{n}dA = - \int_V \nabla \cdot (\rho\mathbf{u})dV \quad (2.6)$$

The divergence theorem was used for the last expression.

$$\int_V \left[\frac{d}{dt} \rho + \nabla \cdot (\rho \mathbf{u}) \right] dV = 0 \quad (2.7)$$

It is valid for arbitrary volumes, thus the integrand vanishes (Shu, 1992, p. 45) which leads to the equation of continuity in differential form:

$$\frac{\partial \rho}{\partial t} + \nabla \cdot (\rho \mathbf{u}) = 0 \quad (2.8)$$

Momentum conservation

The force on the surface element dA is $-p(\mathbf{x}, t) \mathbf{n} dA$ because the pressure p acts vertically onto the surface. From the definition of the normal vector \mathbf{n} the force has a negative sign, as it should always be pointing away from the surface. For perfect fluids (Kley, 2013, p. 15):

$$-\oint_A P \mathbf{n} dA = -\int_V \nabla P dV \quad (2.9)$$

Again the divergence theorem was used to get the last expression of the force on a surface element. For the external forces the expression is (Kley, 2013, p. 15):

$$\int_V \rho \mathbf{k} dV \quad (2.10)$$

with the specific external forces \mathbf{k} . Those external forces include the Gravitation, Lorentz-, Coriolis- or Centripetal force. In combination with the pressure term, one has $-\nabla P + \rho \mathbf{k}$ (Kley, 2013, p. 15).

Equations 2.9 and 2.10 with the second Newtonian law in integral form then reads (Kley, 2013, p. 15):

$$\frac{d}{dt} \int_V \rho \mathbf{u} dV = -\int_V \nabla P dV + \int_V \rho \mathbf{k} dV \quad (2.11)$$

The left term describes the whole momentum change of one fluid element in the volume V . The differential form for arbitrary volumes can be derived from this integral form (Kley, 2013, pp. 15-16).

$$\rho \left(\frac{\partial \mathbf{u}}{\partial t} + (\mathbf{u} \cdot \nabla) \mathbf{u} \right) = -\nabla P + \rho \mathbf{k} \quad (2.12)$$

To get this equation it is necessary to write out the substantial derivative:

$$\begin{aligned} \frac{d}{dt} &= \frac{\partial}{\partial t} + \frac{dx}{dt} \cdot \frac{\partial}{\partial x} + \frac{dy}{dt} \cdot \frac{\partial}{\partial y} + \frac{dz}{dt} \cdot \frac{\partial}{\partial z} \\ &= \frac{\partial}{\partial t} + \mathbf{u} \cdot \nabla \end{aligned} \quad (2.13)$$

where $(\mathbf{u} \cdot \nabla) \mathbf{u}$ is the flow of momentum through the surface.

Energy conservation

The first law of thermodynamic can be reduced for adiabatic changes (See Eq. 2.14). Adiabatic changes have no energy sources and dissipative operations (Kley, 2013, p. 16).

$$dU = -PdV \quad (2.14)$$

$U = m\epsilon$ and ϵ is the specific inner energy, whereas $dV/dt = -V/\rho d\rho/dt$. This leads analogously to Eq. 2.12 to (Kley, 2013, p. 17):

$$\frac{\partial(\rho\epsilon)}{\partial t} + \nabla \cdot (\rho\epsilon \mathbf{u}) = -P \nabla \cdot \mathbf{u} \quad (2.15)$$

2.2.2 Navier-Stokes Equations

The Euler Equations describe the perfect fluid, whereas the Navier-Stokes Equations describe the non-ideal fluids. In non-ideal fluids, dissipative effects like viscosity and heat transportation take place. In those fluids the continuity equation (see Eq. 2.8) is still valid, but the momentum and energy equations need to be changed (Kley, 2013, p. 18).

Momentum equation

The momentum equation with viscosity becomes (Kley, 2013, p. 19):

$$\rho \frac{d\mathbf{u}}{dt} = -\nabla P + \rho \mathbf{k} + \nabla \cdot \underline{\underline{\sigma}} \quad (2.16)$$

with $\underline{\underline{\sigma}}$ as the friction tensor (see Eq. 2.17). Friction consists of kinetic viscosity ν and the bulk viscosity ζ as friction is the relative movement between two fluid elements. The components ν and ζ are functions of the thermal state of the fluid. Thus, they are material properties that depend strongly on local pressure and temperature (Kley, 2013, p. 19; Dellar, 2001, p. 2).

$$\sigma_{ij} = 2\nu \left[\frac{1}{2} \left(\frac{\partial u_i}{\partial x_j} + \frac{\partial u_j}{\partial x_i} \right) - \frac{1}{3} (\nabla \cdot \mathbf{u}) \delta_{ij} \right] + \zeta (\nabla \cdot \mathbf{u}) \delta_{ij} \quad (2.17)$$

Energy equation

The energy equation is (Kley, 2013, p. 21):

$$\frac{\partial(\rho\epsilon_{\text{tot}})}{\partial t} + \nabla \cdot (\rho\epsilon_{\text{tot}}\mathbf{u}) = -\nabla \cdot (P\mathbf{u}) + \nabla \cdot (\mathbf{u} \cdot \underline{\underline{\sigma}}) + \rho\mathbf{u} \cdot \mathbf{k} - \nabla \cdot \mathbf{F} \quad (2.18)$$

where \mathbf{F} is the energy flux [W/m²] and $\epsilon_{\text{tot}} = \epsilon_{\text{in}} + \frac{1}{2}\mathbf{u}^2$ is the specific total energy. The specific total energy consists of the specific inner energy and the kinetic energy. Energy sources are changing the total energy E_{tot} in a volume V . The total energy is defined (Kley, 2013, p. 20):

$$E_{\text{tot}} = \int_V \rho\epsilon_{\text{tot}} dV \quad (2.19)$$

Inner forces within the fluid, the work by external forces per time, and the energy supply through the surface (i.e., radiative transport and heat transportation) cause the energy production (Kley, 2013, p. 20).

2.2.3 State of the art in the field of the 3D simulations in planet formation

In the following subsection, the state of the art of 3D simulations is portrayed. The focus is on the founding work of simulation in different star system setups.

Previous 3D simulations in single star systems

The first setup explored for 3D HD simulation was undertaken for a single star embedded in a disk. Numerous teams have analyzed that setup and the migration of a planet embedded in the circumstellar disk, e.g., in Cresswell et al. (2007) and Bitsch & Kley (2011). The

author of the thesis takes the work of Cresswell et al. (2007) as founding work for the main focus of this thesis.

Cresswell et al. (2007) performed non-linear locally isothermal 3D HD-simulations with a planet embedded in a protoplanetary disk around a single star in order to study the migration of eccentric and inclined planets with respect to the disk's midplane. They also investigated the impact of those planet parameters on the disk structure (Cresswell et al., 2007, p. 329). To do so, they used the codes NIRVANA and RH2D (Cresswell et al., 2007, p. 331). Both codes are HD codes, but the NIRVANA code is a 3D magneto-hydrodynamical (MHD) code, and RH2D is a 2D HD code (Ziegler, 1998, p. 111; Günther & Kley, 2002, p. 552). Although NIRVANA is designed to include the effect of the disk's magnetic field, this component was neglected. Cresswell et al. (2007) used both codes to verify the robustness of the codes.

In their simulations the planet was light ($20 m_{\text{earth}}$) in a low-mass disk ($m_{\text{disk}} = 0.007 M_{\odot}$) with a computation domain from 2.08 AU to 13 AU. The planet's orbit was influenced by the torque exerted by the disk's gas (Cresswell et al., 2007, p. 331). Using a low mass disk and a low mass planet, the planet experienced a type I migration (see Eq. 2.1). In this regime they compared their results with known analytical studies (Tanaka et al., 2002; Tanaka & Ward, 2004, p. 388) of the inclination and the eccentricity damping rates (Tanaka & Ward, 2004, p. 388; Cresswell et al., 2007, pp. 334+340). For small values for the eccentricity and inclination ($e_p < 0.1$ and $i_p < 5^\circ$) Cresswell et al. (2007) results agreed with linear wave theory (Cresswell et al., 2007, pp. 338+340). With the linear wave theory the disk-planet interaction can be formulated, as the planet excites density waves in the disk. Those waves originate from Lindblad resonances and corotation resonances (see Sec. 2.1.3). In return the planet is influenced by that exerted torque of those density waves (Tanaka et al., 2002, p. 1257). The linear wave theory was derived by Tanaka & Ward (2004, p. 394) which found the exponential inclination damping ($di/dt \sim -i$).

Thus following the above theoretical model, the setup of Cresswell et al. (2007) led to the rapid damping of its inclination (Cresswell et al., 2007, p. 341).

Moreover Cresswell et al. (2007) compared their 3D simulations with 2D simulations. They reported that for coplanar planetary orbits (plane of the disk and the planet's orbit are aligned) and small eccentricities, the simulations are similar in terms of migration (Cresswell et al., 2007, p. 340).

In short, they confirmed through numerical simulations the analytically predicted effect of inclination damping depending on the initial inclination and eccentricity of the planet.

Bitsch & Kley (2011) also used local isothermal disks to explore the planet-disk interaction and the variation of the inclined and eccentric orbits of the migrating planet. They could

confirm, using NIRVANA and FARGO in a 3D context, exponential inclination damping for small inclinations ($di/dt \sim -i$ like Cresswell et al. (2007)) and inward migration for planets in single star systems (Bitsch & Kley, 2011, p. 1).

In addition to the dynamical effects of the planet, Kley & Nelson (2012) focused on the features of the disk. They investigated the disk-planet interaction and described that non-axisymmetric features (for instance, spiral waves and horseshoe region) create gravitational torques on the planets, which impact the orbital elements eccentricity, semi-major axis, and inclination (Kley & Nelson, 2012, pp. 4+37).

Kley & Nelson (2012) describe how those torques of the non-axisymmetric disk features influence the different orbital elements. For example, the semi-major axis is influenced through both disk features resulting in migration. On the one hand, the spiral waves create a net torque that leads to the migration of the planet (see Sec. 2.1.3). The sign of that net torque decides the direction of the migration (Kley & Nelson, 2012, p. 6). On the other hand, the horseshoe drag, which also leads to a non-zero net torque, is created by asymmetries between the two U-turns. It is called U-turns as the gas motion in the corotating planet frame performs U-turns and exchanges angular momentum between the disk and planet (Kley & Nelson, 2012, p. 9). This angular momentum exchange slows down the migration process (Kley & Nelson, 2012, p. 10).

For the effects on the eccentricity and inclination parameters, the forces on the planet need to be analyzed, taking the orbital plane into account. With no fixed vertical and radial position, the disk forces vary within an orbital period (Kley & Nelson, 2012, p. 20).

Thus Kley & Nelson (2012) is an excellent review paper on disk-planet interaction. In that paper, the authors do not run 3D simulations themselves but summarize and connect the findings of other authors.

Following these groundwork results, other authors explored several other aspects of single-star systems, e.g., Chametla et al. (2017) studied a gap opening inclined Jupiter mass planet in a singular system with FARGO3D and Kloster & Flock (2019) studied evolution with 2D/3D simulations of inclined and non-inclined planets which are low-mass and Jupiter size. As most stars form in multiple systems and half of the solar-type stars form in binary systems (Duquennoy & Mayor, 1991, p. 509; Raghavan et al., 2010, p. 38), it is not enough to understand planet formation in singular systems but also in binary systems.

Previous 3D simulations in s-type systems

As described in Subsec. 2.1.3, the planets in s-type systems are orbiting one star. The "first" s-type exoplanet was discovered by Campbell et al. (1988), but since they discovered

it before the first exoplanet around a sun-like star was discovered, they let themselves be convinced by the scientific community that this was not possible (Walker et al., 1992, p. L91; Haghighipour, 2008, p. 3). It was only re-announced by Hatzes et al. (2003, p. 1383) that γ Cephei has an s-type exoplanet after Queloz et al. (2000, p. 99) announced the first s-type exoplanet in Gliese 86.

In binary systems, the torque forced on the disk from the secondary can impact the planet formation differently than in a single star system (Batygin, 2012, p. 418; Foucart & Lai, 2014, p. 1740), this is because the disk is perturbed by a secondary star (Foucart & Lai, 2014, p. 1742) (see Fig. 2.6).

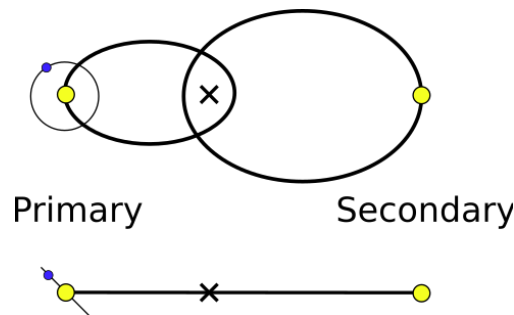


Fig. 2.6: Drawing of a s-type configuration with a misaligned disk/planet. Top: face-on view of the system. Bottom: edge-on view of the system.

Regarding 3D simulations in s-type systems, the first papers for planets in s-type systems were published relatively late as the simulations are more complex than single star simulations.

Batygin (2012) used Gauss's method, where an algorithm of algebraic equations solves the secular evolution of Keplerian rings which are gravitationally connected (Touma et al., 2009, p. 1087; Batygin, 2012, p. 418), to analyze the influence of a stellar companion in an s-type system taking inclination into account. This was an intermediate step before 3D hydrodynamic simulations were done.

The author showed that the initial aligned planetary orbits become misaligned with respect to the disk's midplane in s-type systems (Batygin, 2012, p. 418). This could be a consequence of the planet migration in the circumstellar disk and a distant massive body (Batygin, 2012, p. 418).

Picogna, G. & Marzari, F. (2015) analyzed planet inclination in s-type systems with the focus on migration and the influence of the secular star (Picogna, G. & Marzari, F., 2015, p. 1). Simulations were done with the 3D smoothed particle hydrodynamics (SPH) codes

VINE and PHANTOM (Picogna, G. & Marzari, F., 2015, p. 1).

The system which they analyzed is a circular, equal mass binary ($1 M_{\odot}$ each) with a Jupiter-mass planet circling the primary ($a_p = 5 \text{ AU}$) in a protoplanetary disk ($0.01 M_{\odot}$). The disk extends from 0.5 to 30 AU, and the distance to the secondary star is 100 AU. The disk's aspect ratio (h/r) is 0.037 and the α viscosity is 0.02 for the VINE code and 0.04 for the PHANTOM code (Picogna, G. & Marzari, F., 2015, p. 4).

The planet and the disk are initially coplanar and tilted by 45° or 60° towards the binary plane (Picogna, G. & Marzari, F., 2015, p. 4).

In both scenarios, the secular star led to a planet's inclination that differed from the inclination of the disk. Thus the planet was influenced by the second body evolving independently from the disk (Picogna, G. & Marzari, F., 2015, p. 1). The second focus of the paper was planet migration. Due to the inclination of the planet induced by the secondary, the planet leaves the disk. With every passing of the planet through the disk, it loses angular momentum through friction, which leads to a migration inward. But this migration is different from the type I/II migration described in an earlier section (Picogna, G. & Marzari, F., 2015, p. 1).

Martin et al. (2016) investigated via 3D simulations the evolution of a equal mass s-type system where the accreting planet is initially coplanar with the disk but misaligned (20° , 40° , 60°) towards the binary plane (Martin et al., 2016, p. 4346). The planet is massive ($0.001 M_b$) enough to open a gap in the disk (0.001 , 0.008 and $0.01 M_b$) (Martin et al., 2016, p. 4347) (see Eq. 2.1). The computational domain ranges from $0.025 a_b$ to $0.25 a_b$, the alpha viscosity is 0.05, the disk aspect ratio is set to 0.036 and the initial surface density is $\Sigma \sim R^{-3/2}$. The simulations were done with the SPH code PHANTOM (Price & Monaghan, 2004, p. 139), where only the parameter of the disk inclination and the disk mass was changed (Martin et al., 2016, p. 4347).

In their studies, they found that the planet undergoes two types of oscillation. Even at small inclination angles, the first type comes from the interaction with the stellar companion and the disk of the host star. Secular resonance amplifies this first oscillation (Martin et al., 2016, p. 4345). The second oscillation originates from the Kozai-Lidov oscillation at larger inclination angles (Martin et al., 2016, p. 4345). This oscillation influences the disk and the planet as it leads to an exchange of eccentricity and inclination of the planet. (Martin et al., 2016, p. 4345). That is why the Kozai-Lidov (KL) mechanism can lead to highly eccentric and inclined exoplanets as those planets are disturbed secular by the outer binary companion (Martin et al., 2016, p. 4347).

Thus, due to those mechanisms, an initial only low inclined planet in a massive disk can become highly inclined due to the KL oscillation ($20^\circ < i < 160^\circ$) (Martin et al., 2016, p. 4346).

Lubow & Martin (2016) is a work published before the latter and focused on accreting mildly inclined planets in s-type systems via SPH simulations (Lubow & Martin, 2016, p. 1). The 3D hydrodynamical setup is very similar (Lubow & Martin, 2016, p. 9).

Again the gap opening planet ($0.003 M_b$) is initially coplanar with the disk (0.0004 , 0.004 and $0.006 M_b$) but this time, less misaligned with the binary plane (10°). The computational domain, the aspect ratio, the initial surface density power-law, and the α viscosity is the same in both (Lubow & Martin, 2016, p. 9).

In this paper, the only variable is the disk mass. As the mass of the disk influences the gap opening, this leads to a different misalignment of the planet (Lubow & Martin, 2016, p. 12). Towards higher disk masses, the misalignment becomes more significant because of the secular resonance (Lubow & Martin, 2016, p. 13). They also found that the disk, on the other hand, re-aligns with the orbital plane because of disk dissipation (Lubow & Martin, 2016, p. 13). As those disks were only mildly inclined, they did not find KL and eccentricity oscillations.

Based on these works, other authors conducted further studies, e.g., Franchini et al. (2020) who studied a multiplanet-disk around one star of the binary. A general finding common in all works is that the planet's inclination increases due to the binary companion's presence.

Previous 3D simulations in p-type systems and their goals

Several authors guessed that additional perturbers, like a stellar companion, could excite the inclination of the planet/disk (Cresswell et al., 2007, p. 341; Batygin, 2012, p. 418; Smallwood et al., 2019, p. 2919). In contrast to the s-type system, the stellar companion is inside the planet's orbit.

Smallwood et al. (2019) investigated mildly tilted low-mass ($0.001 M_b$) circumbinary disks around eccentric binaries with the SPH code PHANTOM (Smallwood et al., 2019, p. 2921). In their simulation they vary the eccentricity of the binary (0.0, 0.3, 0.6 and 0.8) and the initial inclination of the disk (10° , 15° , 30° , 50° and 60°). The computational domain extends from $2 a_b$ to $5 a_b$. For one simulation the outer boundary is set to $40 a_b$. The initial surface density profile is $\Sigma \sim R^{-3/2}$, the α viscosity is 0.01 and the disk's aspect ratio is 0.1 (Smallwood et al., 2019, p. 2922).

They discovered that disks have tilt oscillations due to effects of the binary eccentricity (Smallwood et al., 2019, p. 2930). Furthermore, they found the relation between the binary eccentricity and the tilt oscillations. The larger the binary eccentricity, the larger the tilt oscillations and the smaller the damping of these oscillations. On top of it, they found that those disks increase their inclination by a significant factor before they align again (Small-

wood et al., 2019, p. 2919). For example, for a binary eccentricity of 0.8 and an initial inclination of 15° the disk's inclination increased to 50° (Smallwood et al., 2019, p. 2922). Another important aspect of that work was the analysis of the properties of the circumbinary disk around KH 15D. They used SPH simulations and linear theory and determined that that disk has a slight warping. Moreover, they found that small tilts are well in agreement with linear theory (Smallwood et al., 2019, p. 2930).

To do so, Smallwood et al. (2019) compared the 1D model with simulations assuming that the level of tilt is small. Moreover, they neglected the density evolution (Smallwood et al., 2019, p. 2926). This approach saves computational time in comparison to SPH simulations (Smallwood et al., 2019, p. 2926). To compare the simulations with linear theory, the secular torque equations (Farago & Laskar, 2010, p. 1190) due to the binary are implemented to calculate the maximum inclination (Smallwood et al., 2019, p. 2926):

$$i_{\max} = i_0 \sqrt{\frac{1 + 4e_b^2}{1 - e_b^2}} \quad (2.20)$$

where i_0 is the initial inclination and e_b is the eccentricity of the binary. The theoretical equation was compared with the results from the above-mentioned SPH simulations. They found that they are in good agreement for little tilts ($= 10^\circ$) (Smallwood et al., 2019, p. 2928).

The disk warping was introduced by Pierens & Nelson (2018) as a consequence of the finding of misaligned exoplanets in binary systems. They analyzed modestly inclined binary systems ($e_b = 0.12$) with 3D hydrodynamical simulations using FARGO3D and matching the observations of Kepler 413, 0.1 AU binary with a circumbinary planet detected (Kostov et al., 2014, p. 1). Using different disk parameters, for instance alpha viscosity α (0.0004, 0.0001 and 0.1), constant aspect ratio h_0 (0.05 and 0.01), flaring f (0 and 0.25) and binary inclination (0° , 2.5° , 5° and 8°) they could observe that the disks develop slowly varying warps (Pierens & Nelson, 2018, pp. 2547+2250). In those simulations a large outer boundary ($80 a_{\text{bin}}$) is used. Due to computational time, their results stop between 10^3 and 10^8 binary orbits (T_{bin}) (Pierens & Nelson, 2018, pp. 2551-2552). All simulations with tilted planets embedded suggest that the planet re-aligns with the binary orbit planet because of the disks age and mass loss, but the simulations were not long enough (Pierens & Nelson, 2018, p. 2547).

The authors put the mid-plane of the circumbinary disk at the equatorial plane of the computational disk but put the binary at an inclination. The disk does not have self-gravity, and it does not affect the binary orbit (Pierens & Nelson, 2018, p. 2549). Their approach had two goals, first to study the disk parameter over time and then, in later simulations, embed

a planet. The planet is inserted in the mid-plane of the disk and is not accreting material (Pierens & Nelson, 2018, p. 2552). Its mass-ratio is in some simulations small enough that it is undergoing a type I migration, but they also tested simulations where the planet can open a gap (type II migration). In the first case, it stops just outside the inner cavity. But for the latter migration type, the planet gets pushed by the outer disk into the cavity, and the fate of the system is uncertain, as simulations take too much time (Pierens & Nelson, 2018, pp. 2552-2553).

Pierens & Nelson (2018) found that for small disk masses, the planet re-aligns with the binary orbit plane, and thus the coplanarity with the circumbinary disk is not maintained. However, with higher disk masses (>2 MMSN), the disk gravity starts to change the evolution of the planet (Pierens & Nelson, 2018, p. 2558). Their main finding was that the disk has not to re-align with the orbital plane of the binary for the planet to re-align. The disk can be misaligned, but through mass loss, over time, the planet tends to re-align with the binary orbit nevertheless (Pierens & Nelson, 2018, p. 2559). This is in contrast to other studies where the disk aligns with the binary orbit, not only the planet (Lai & Foucart, 2012, p. 150; Foucart & Lai, 2014, p. 1743; Czekala et al., 2019, p. 19).

Several studies with non-eccentric binaries found that a previous misaligned disk aligns with the orbital plane of the binary (Nixon, 2012, p. 2597; Foucart & Lai, 2014, p. 1731). In circumbinary disks systems with a binary eccentricity, the angular momentum of the disk aligns with the angular momentum of the binary orbit or with the eccentricity vector of the binary (Aly et al., 2015, p. 1; Martin & Lubow, 2017, p. 3).

Chen et al. (2019) simulated, as well as Smallwood et al. (2019), misaligned planets around an eccentric orbit. To do so, they used the N-body simulation package REBOUND (Chen et al., 2019, p. 5635). They used three-body simulations where the planet and the binary interact gravitationally. Different values for the binary eccentricity (0.2, 0.5 and 0.8), the mass fraction (0.1 and 0.5) and the planet's initial inclination (10° - 180°) were used (Chen et al., 2019, pp. 5636, 5637+5644).

Their focus was on mapping possible orbits in these systems and determining stationary orbits. The authors identified the parameters that influence those possible orbits as being the binary eccentricity and the planet-to-binary angular momentum ratio (Chen et al., 2019, p. 5644).

Later studies by other authors focused on other objectives; they are only stated quickly to give an overview of the state of the art.

Monnier et al. (2019) studied the origin of disk features with FARGO3D. They wanted to know whether an unseen companion could be responsible for the disk structures in the HD

34700A system (Monnier et al., 2019, p. 15). They run different parameters for the companion and used the radiative transfer code RADMC3D (Dullemond et al., 2012) to compare the simulation results to the observations (Monnier et al., 2019, p. 16). Unfortunately, they could not find the same structures, as the stellar binary, the planetary orbit, and the disk could be misaligned instructing additional dynamics (Monnier et al., 2019, p. 16).

Pierens et al. (2020) simulated with FARGO3D, using a modified version which includes a particle module, three dimensional simulations with inviscid circumbinary disks (Pierens et al., 2020, pp. 2849-2850). This modification particle allows trajectories to be computed (Nelson & Gressel, 2010, p. 654; McNally et al., 2019, p. 6). They simulated circumbinary disks with binary parameters similar to Kepler 16 and focused on the eccentricity of the disk coming from the inner boundary and the formation of the inner cavity (Pierens et al., 2020, p. 2866).

They found that parametric instability is triggered through the interaction of the binary and the resulting disk eccentricity. Those instabilities generate turbulence and vertical velocity fluctuations which are small compared to the sound speed ($\sim 0.1\%$) (Pierens et al., 2020, p. 2866). Moreover, they looked at pebble accretion and found it is rather difficult for pebbles to grow close to the cavity edge. They suggest that the core is forming further away from the binary, as there is less turbulence, and then followed by migration towards the cavity (Pierens et al., 2020, p. 2866).

Chen et al. (2020) continued their studies with the REBOUND code to study the orbital stability of a close circumbinary planet around an eccentric binary. They varied the binary parameters: eccentricity (0.2, 0.5 and 0.8) and mass fraction (0.1 and 0.5). But they also varied the planet parameters: mass (0.001, 0.005 and $0.01 m_b$), semi-major axis ($1.5 a_{\text{bin}} - 6 a_{\text{bin}}$) and inclination ($0 - \pi$) (Chen et al., 2020, pp. 4645+4647). They found that the orbital alignment of the planet depends on the final alignment of the disk. Thus with a low-mass disc aligns either coplanar or polar (Chen et al., 2020, p. 4654). In their simulation the binary orbit is not fixed as the planet and disk interference (Chen et al., 2020, p. 4646).

Recent observations show that mostly short period binaries with periods (<20 d) have aligned coplanar within 3° . Binaries with larger periods have more significant inclinations and binary eccentricities (Czekala et al., 2019, p. 1). The binary eccentricity for binaries with periods smaller than 30 d seems limited due to effects of stellar tidal dissipation (Chen et al., 2020, p. 4654). Thus the coplanarity found in the Kepler systems may be caused by smaller orbital periods and low binary eccentricities (Chen et al., 2020, p. 4654).

There are other theories on how these misaligned exoplanets evolve, for example, through

turbulence in the forming gas clouds (Bate, 2012, p. 3121; Smallwood et al., 2019, p. 2920) or through the accretion process in a young binary where the material is likely to be misaligned (Bate et al., 2010, p. 3121; Smallwood et al., 2019, p. 2920).

3 Setup of the Kepler 38 FARGO3D simulations

This chapter introduces the observed parameters for the Kepler 38 system and the FARGO3D code used for the simulations in this thesis. The observed Kepler 38 system parameters provide information either used as input for the FARGO3D code or output. Of course, the simulation results come only close to the observed parameters, but this is discussed further when it occurs. Therefore, the FARGO3D code needs to be understood. Thus, the main equations, the numerical and physical setup, and the boundary conditions of the setup are explained. This includes the initial disk parameters. Moreover, if a parameter is not mentioned as being changed in the next chapter, this means that it is used as described in this chapter.

3.1 Kepler 38: observed parameters as input/output for simulation

The binary system Kepler 38 is roughly 1.22 kpc away and is located in the constellation of Lyra at 19^h07^m R.A. and 42.16° Dec in the sky (NASA, NASA). In October 2012, it was discovered that a circumbinary planet is circling both stars (Orosz et al., 2012, p. 1). The period of the binary is 18.8 days and the period of the planet is 105.6 days (Orosz et al., 2012, p. 1). The orbit of the binary is slightly eccentric (0.103), whereas the planet's orbit is almost circular ($e_p < 0.03$) (Orosz et al., 2012, p. 1). The binary's semi-major is 0.1469 AU and the planet's semi-major axis is 0.46 AU (Orosz et al., 2012, p. 1). The planet's orbit has an inclination of $< 0.02^\circ$ (Orosz et al., 2012, p. 1). The depth of eclipses of the binary are 3% for the primary and 0.1% for the secondary (Orosz et al., 2012, p. 2). The depth of eclipses for the planet is 0.05% (Welsh & Orosz, 2018, p. 11). The system is approximately 10 ± 3 billion years old (Orosz et al., 2012, p. 12) and consists of a primary main-sequence star with a mass of $M_1 = 0.95 M_\odot$. The primary is larger ($1.76 R_\odot$) than the sun, whereas the secondary is a red dwarf ($0.27 R_\odot$) (Orosz et al., 2012, p. 1). It roughly has a quarter of the mass of the sun ($M_2 = 0.249 M_\odot$) (Orosz et al., 2012, pp. 11-12). The semi-major axis of

the binary is 0.1469 AU (Orosz et al., 2012, p. 10). The planet in the system is Saturn-size (Orosz et al., 2012, p. 1). The planet and the binary parameters from observations are shown in Tab. 3.1.

mass ratio $q = M_2/M_1$	period [days]	a_b [AU]	e_b	
0.2626	18.8	0.1469	0.1032	
mass [M_{Jup}]	period [days]	a_p [AU]	e_p	i_p
0.34	105.6	0.46	< 0.03	< 0.2

Tab. 3.1: Top: Binary parameters of Kepler 38 from observations. Bottom: Planet parameters of Kepler 38 from observations (Orosz et al., 2012, p. 13)

3.2 FARGO3D – MHD Code

FARGO3D is a three-dimensional magneto-hydrodynamical (MHD) code. Protoplanetary disks and the interaction of the disks with embedded planets can be quickly simulated (Benítez-Llambay & Masset, 2016, p. 1). It achieves high speeds of processing by avoiding data transfer, as the whole simulation fits on the memory of GPU(s) (Benítez-Llambay & Masset, 2016, p. 1). On top of it, through automatic compilation to CUDA code, the code can be modified without knowledge of GPU programming.

FARGO3D can solve numerous problems, e.g., single star systems or binary star systems. One can create a specific setup subdirectory for the input parameters in order to structure each problem (see Fig. 3.1). The FARGO3D algorithm then builds the setup with the makefile using all the parameters given in the setup directory. The makefile was created by the developers of the code and did not need to be modified. The code can then be run by telling FARGO3D how many GPUs should be used with which parameters from the parameter file. Thus the code does not need to be rebuilt if only parameters in the parameter file are changed. One can use the output files created by FARGO3D to analyze, e.g., the disk structure and the planet’s migration.

3.2.1 Main equations

FARGO3D can solve three-dimensional MHD equations on an Eulerian mesh. This mesh can be cartesian, cylindrical, or spherical (Benítez-Llambay & Masset, 2016, p. 3). In this Ph.D. thesis, the code is used as an HD code (see Sect. 2.2). Thus all magnetic field terms can be neglected, and they become HD equations. The studies presented in Sec. 2.2.3, where

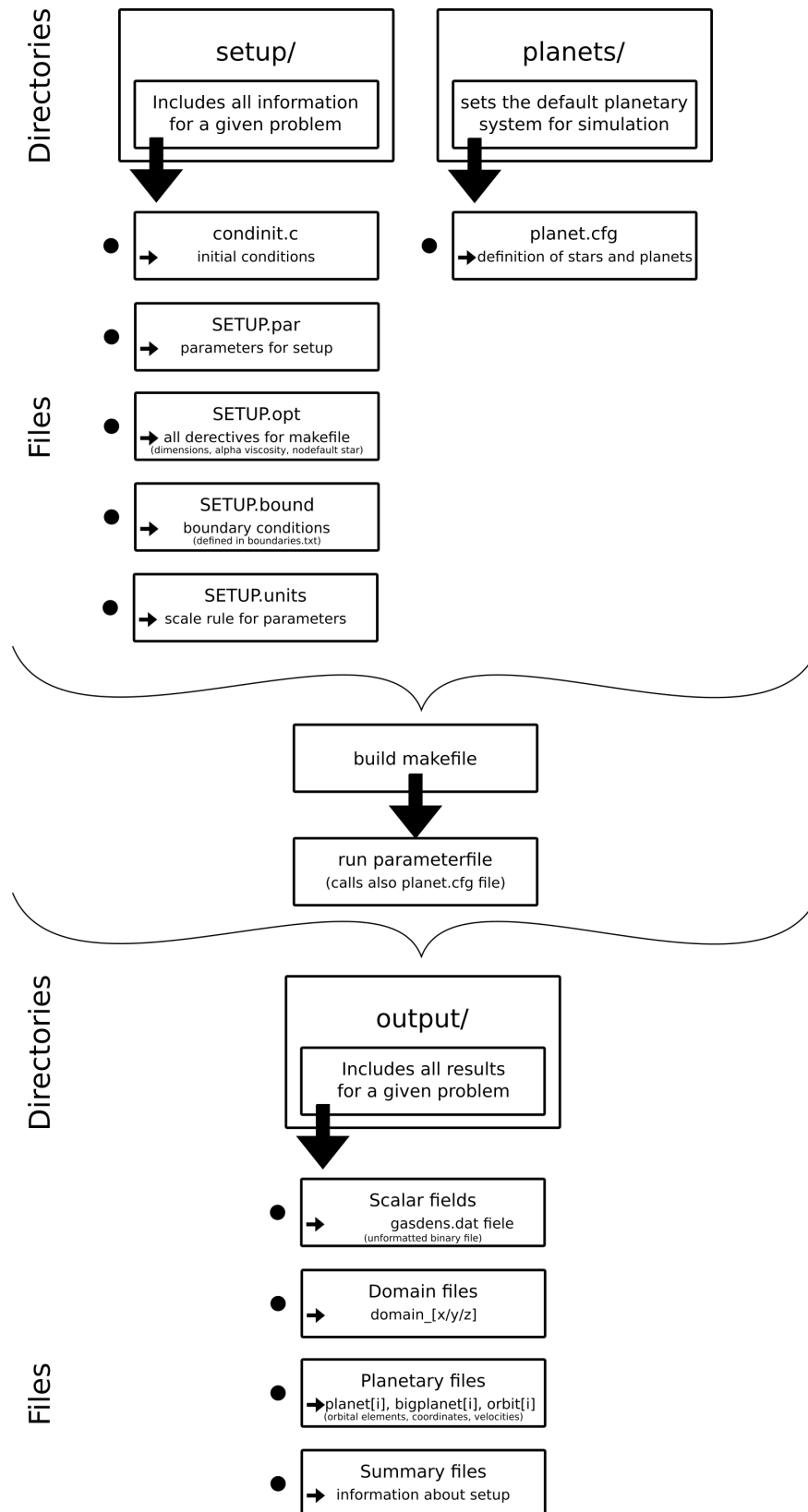


Fig. 3.1: Structure and flow chart for FARGO3D. Pictured are the input and output files. The focus is set for the usage in this thesis, thus the flow chart is reduced to the steps important for this work. Information taken from Benítez-Llambay & Masset (2015b, pp. 15-16, 65-68).

the state of the art of current 3D simulations is shown, have not included the magnetic field. Thus to make it comparable with those previous studies, the magnetic field is neglected in this thesis, too.

The gravity in the FARGO3D code is created by the objects in the planet file or the object in the center of mass. Furthermore, the code is designed to simulate a migrating planet in a non-self gravity disk. This means that the disk does not feel its own gravity, but the planets feel the disk's gravity (Benítez-Llambay et al., 2016, p. 5). This leads to the mutual interaction of the planet and the disk. It is reasonable to ignore self-gravity as described in Subsec. 2.2.3, since it is only important for disks larger than two times the MMSN (Pierens & Nelson, 2018, p. 2558), with MMSN having masses between 0.01 and 0.1 solar masses (Weidenschilling, 1977, p. 158) (see Subsec. 2.1.1).

In this thesis, the viscosity in the disk is modeled with the α -disk model by Shakura & Sunyaev (1973, p. 338). Therefore, the kinematic viscosity is $\nu = \alpha c_s H$ with the parameter $\alpha \leq 1$ (Shakura & Sunyaev, 1973, p. 338) (see Subsec. 2.1.1).

As a locally isothermal disk model is used, the (locally) isothermal equation of state is given by:

$$P = c_s^2 \rho \quad (3.1)$$

with the isothermal sound speed c_s and the volumic density ρ . The field $c_s(\mathbf{r}) = h\Omega_k$ is constant in time and it is set by the initial conditions (Benítez-Llambay & Masset, 2016, p. 3), exactly like the aspect ratio $h = H/r$ (see Fig. 3.2) and the Keplerian velocity of gas located at distance r ($\Omega_k = \sqrt{GM_{\text{bin}}/r}$) (Benítez-Llambay & Masset, 2015b, p. 36). Physically the aspect ratio h is the vertical thickness of the disk H at distance r .

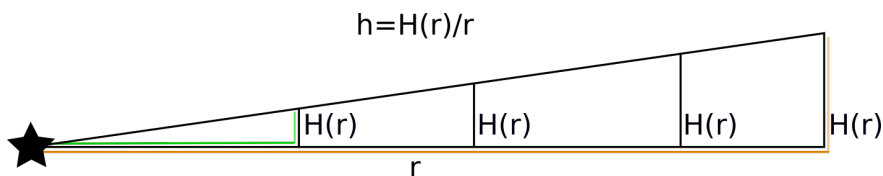


Fig. 3.2: Sketch of aspect ratio h and its dependence on vertical thickness $H(r)$ and r .

In the (local) isothermal case, the Eq. 2.15 is decoupled from the others and does not need to be solved (Benítez-Llambay & Masset, 2016, p. 3).

FARGO3D coordinates are named X, Y, and Z independently of Cartesian, spherical, or cylindrical coordinates. In this thesis, a spherical grid is used for the corresponding coordinates see Tab. 3.2.

Geometry	X	Y	Z
spherical	azimuth (ϕ)	radius (r)	colatitude (θ)

Tab. 3.2: Correspondence between X, Y, Z and the spherical coordinate system (Benítez-Llambay & Masset, 2016, p. 3).

For stability reasons, information like density, energy, and momenta cannot travel over more than one cell per time step (Benítez-Llambay & Masset, 2016, pp. 7-8). This is the Courant–Friedrichs–Lewy (CFL) condition or the Courant condition (Benítez-Llambay & Masset, 2016, p. 8), which is independent of substeps. It performs substeps; for example, first, it updates the velocity field, and then viscosity is added (Benítez-Llambay & Masset, 2016, p. 6), as the code cannot calculate every hydrodynamical equation at once. However, this means that the substeps performed per integration time step Δt (performs a complete cycle of hydrodynamic substeps) have to be limited (Benítez-Llambay & Masset, 2016, p. 8).

Heuristic methods are used to determine the maximum allowed time step in the FARGO3D code. The maximum time step is (Stone & Norman, 1992, p. 768; Benítez-Llambay & Masset, 2016, p. 8):

$$\Delta t = C \cdot \min \left[\left(\sum_i \Delta t_i^{-2} \right)^{-1/2} \right] \quad (3.2)$$

where $C \in [0, 1)$ is the Courant number and the different processes that individually limit the time step are represented with Δt_i like sound waves, fluid motion, viscosity, etc. (Benítez-Llambay & Masset, 2016, p. 8). The \min -function takes the minimum of the sum, which is calculated for each cell separately. The limitation most likely arises from the cells with the smallest radii, as the angular velocity is largest there (Crida et al., 2007, p. 1181). In FARGO3D this parameter is set to $C = 0.44$ which compromises between stability and speed for a wide range of problems (Benítez-Llambay & Masset, 2016, p. 8).

Whereas the time intervals are required to fulfill the CFL condition, the real parameter DT represents the time between two outputs (Benítez-Llambay & Masset, 2015b, p. 69). Thus, the time interval DT can be sliced in many Δt intervals to fulfill the CFL condition, allowing the last interval to be smaller than the CFL condition to exactly fit DT (Benítez-Llambay

& Masset, 2015b, p. 69). Therefore, DT can be smaller than the CFL condition and restrict the time step manually by setting DT in the parameter file (Benítez-Llambay & Masset, 2015b, p. 69). One should avoid this for the code to run (Benítez-Llambay & Masset, 2015b, p. 107). In this thesis, the time step DT is set to 1/10 of an orbit. Thus, the time step is larger than the CFL condition as the units of this simulation are set to:

- semi-major axis of the binary orbit: $a_{\text{bin}} = 1$
- mass of the binary: $M_{\text{bin}} = 1$
- gravitational constant: $G = 1$.

Thus, the unit of surface density is $M_0/R_0^2 = M_{\text{bin}}/a_{\text{bin}}^2 = 1$. The binary orbit (T_{bin}) can be calculated by the third Kepler's law:

$$T_{\text{bin}} = 2\pi \sqrt{\frac{a_b^3}{G \cdot M_b}} = 2\pi \quad (3.3)$$

DT which represents 1/10 of an binary orbit is:

$$\text{DT} = 2\pi/10 > C(= 0.44) \quad (3.4)$$

A fifth-order time-fixed Runge-Kutta method is used to simulate point-like masses which interact with the gas (Benítez-Llambay & Masset, 2016, p. 15).

3.2.2 Numerical and physical setup

For the simulations in this thesis, the parameters chosen are similar to the parameters of Kepler 38 to examine the evolution of the disk. For example, the simulations are done with and without a planet, the disk mass is varied, or the setup is simulated with just one star in the center. With those experiments, one can learn about the disk evolution and the planet parameters.

In simulations with the planet, the planet gets inserted with its final mass $M_{\text{Planet}} = 0.34 M_{\text{Jupiter}} = 1.14 M_{\text{Saturn}} = 6.34 M_{\text{Neptune}}$ (see Tab. 3.1) at 0.98 AU from the center of mass. The planet interacts with the disk and the binary but does not accrete material.

Surface density: The initial disk surface density is set to a $\Sigma(r) = \Sigma_{\text{ref}}(r/R_{\text{ref}})^{-3/2}$ profile for all models, where r is the distance from the binary’s center of mass, R_{ref} is $1 \text{ a}_{\text{abin}}$, and the surface density at $1 \text{ a}_{\text{abin}}$ is Σ_{ref} . The surface density depends on two parameters. Where in this thesis, only the reference surface density (Σ_{ref}) is varied, and the power-law (p) is kept constant at $-3/2$. In this thesis the power-law $p = -3/2$ is chosen as it is a good parameterization of the planet-forming regions ($< 40 \text{ AU}$) of the disk (Dullemond, 2013, p. 3). Nevertheless, one has to keep in mind that this is only a commonly used assumption (Dullemond, 2013, p. 3).

A test with $p = -1/2$ is done to verify the influence on the planet migration, at least in the same scenario (see Appendix. 6.2). Later in this thesis, the dependency on the reference surface density with a constant power-law of $p = -3/2$ is analyzed further.

Σ_{ref} reflects the mass of the disk because the FARGO3D code takes the surface density as an input and not the disk mass. The calculation of acquiring the surface density depending on the disk mass is described in Sec. 3.2.3 and the calculation of acquiring the disk mass is shown in Sec. 3.2.4. The disk mass is adapted from the minimum mass solar nebula, because the combined stellar mass of Kepler 38 is approximately $M_{\text{b}} = 1.2 M_{\odot}$ ($M_{\text{primary}} = 0.949 M_{\odot}$). Thus, it is a good approximation to assume the mass of the circumbinary disk to be the same as the protosun (Kley & Haghighipour, 2014, p. 3).

The migration speed is directly influenced by the disk mass (Thun & Kley, 2018, p. 3); thus, in this thesis, several different surface densities are simulated.

The initial surface density at $1 \text{ a}_{\text{abin}}$ is set to values between $\Sigma_{\text{ref}} = 6.2 \cdot 10^4 \text{ g/cm}^2$ (in code units (CU) $1.257 \cdot 10^{-4} \Sigma_0$ with $\Sigma_0 = M_0/R_0^2 = 1$) and $\Sigma_{\text{ref}} = 1.2 \cdot 10^6 \text{ g/cm}^2$ (in CU $2.514 \cdot 10^{-3} \Sigma_0$). This initial surface density is corresponding to a disk mass between $0.005 M_{\odot}$ and $0.1 M_{\odot}$ following the description of the disk mass (Dullemond & Dominik, 2004, p. 162):

$$M_{\text{disk}} = 2\pi \Sigma_{\text{ref}} R_{\text{ref}}^{-p} \frac{1}{p+2} \left[R_{\text{out}}^{p+2} - R_{\text{in}}^{p+2} \right] \quad (3.5)$$

with the initial slope $p = -3/2$, $\Sigma(r) = \Sigma_{\text{ref}}(r/R_{\text{ref}})^p$ is the surface density as a function of the radius and $R_{\text{out/in}}$ is the outer/inner radius of the disk.

Limitations of the disk mass: The disks analyzed in this thesis do not represent the majority of disks, as they are quite heavy. For example, the $0.01 M_{\odot}$ disk ranging from 0.1469 AU to 2.1 AU , corresponds according to Dullemond & Dominik (2004, p. 162), to a disk mass of $0.09 M_{\odot}$ for a classical disk size ranging from 0.1469 AU to 100 AU . This shows that rather heavy disks are simulated in this thesis, but there are a few heavy disks, according to Beckwith (1990, p. 936).

When analyzing the even smaller $0.01 M_{\odot}$ disk between 0.19 AU to 2.1 AU , it is clear that it is over-dimensional and unrealistic. Nevertheless, it is crucial to understand what happens in

such an unrealistic case with fast evolution timescales. This is needed because long low-mass simulations consume much computational time and are not feasible for this Ph.D. thesis. Nevertheless, a search for trends is possible with these different disk masses. With knowing those limitations, the results of the simulations are discussed later on.

Parameters: The viscosity parameter in the simulations is set to $\alpha = 0.01$ leading to an evolution fast enough to be numerically simulated (Kley & Haghighipour, 2014, p. 3). It is varied to analyze the influence (see Sec. 4.3.4). Another disk parameter is $H/r = 0.05$ and represents the aspect ratio of the disk. It is kept constant in all the simulations. The smoothing parameter $\epsilon = 0.6$ accounts for the finite thickness of the disk (Kley & Haghighipour, 2014, p. 3; Thun et al., 2017, p. 3). It is represented in the smoothed potential function $\Phi \propto -1/(r^2 + \epsilon^2)^{1/2}$ with r being the distance to the gravitating object. In 3D simulations, this parameter assures stability as with point-like masses in the disk, singularities through diverging distances in the potential could arise (Masset, 2002, p. 608; Müller et al., 2012, p. 1; Kley & Haghighipour, 2014, p. 3). For the shift of positions between the binary’s center of mass and the origin of the coordinate system, indirect terms are used. They compensate the fictitious force arising from frame acceleration (Masset, 2002, p. 608).

As an inner cavity develops, a density floor $\Sigma_{\text{floor}} = 10^{-13}$ (in code units) is used to avoid numerical overflow, as the surface density drops significantly (Thun et al., 2017, p. 4). All the simulations start at the periastron of the binary (Kley & Haghighipour, 2014, p. 3).

Computational domain: It ranges in the radial direction from $R_{\text{min}} = 1/1.3 a_b = 0.15/0.19 \text{ AU}$ to $R_{\text{max}} = 14.28 a_b = 2.1 \text{ AU}$, in the azimuthal direction from $-\pi$ to π and from $\pi/2 - 3H/R_0$ to $3H/R_0 + \pi/2$ in the colatitude. The parameter a_{bin} is the semi-major axis of the binary star and H/R_0 is the disks aspect ratio at $r = R_0$. As it is a scale free unit system, R_0 is 1.

The outer boundary $a_{\text{bin}} = 2.1 \text{ AU}$ is close to the parameter used by Kley & Haghighipour (2014, p. 3) and a good trade-off between computational time and size. Tests with a larger outer boundary were performed, too. The results are quite similar; thus, for time efficiency, the smaller setup is used (see Appendix 6.2).

The binary orbit is not included in the computational domain, which means the gas flow from the disk onto the stars is not shown. This is an acceptable limitation as it is assumed that there will be no circumstellar disks in tight binaries (Quintana & Lissauer, 2006, p. 1) like Kepler 38. This setup leads to a time-efficient simulation. Nevertheless, the different potentials and orbits of the stars are included in the simulations. As a rule of thumb, the inner computational radius should be close to $R_{\text{min}} \approx a_b$ in a circumbinary disk model to

have a realistic model (Thun et al., 2017, p. 8).

The resolution was tested through a convergence tests and is set in the main simulations to $216 \times 512 \times 39$ grid cells (see Appendix 6.2). Thus the number of azimuthal cells (N_x) are 216, the number of radial cells (N_y) are 512 and the number of colatitude cells (N_z) are 39. The grid is logarithmically spaced.

3.2.3 Surface density

The surface density is in direct relation with the disk mass ($\Sigma \sim M_{\text{disk}}$) and the size of the disk ($\Sigma \sim (R_{\text{in}}, R_{\text{out}})$) (Dullemond & Dominik, 2004, p. 162). Thus, the density increases by taking the same mass in a small disk instead of a large disk. Therefore, when simulating a small disk with ~ 2 AU, while keeping the results comparable to an observed disk, one needs to decrease the mass in the central region.

To calculate Σ_{ref} in g/cm^2 for the classical case presented in Dullemond & Dominik (2004, p. 162) with a total mass of the disk of $0.012 M_{\odot}$ and a $R_{\text{in}} = 0.15$ AU and $R_{\text{out}} = 200$ AU at $R_{\text{ref}} = 200$ AU, one needs Eq. 3.5 to calculate:

$$\begin{aligned} \Sigma(200 \text{ AU}) &= \frac{M_{\text{disk}}}{2\pi(200^{1.5})^{-\frac{1}{-1.5+2}} [200^{0.5} - 0.15^{0.5}]} \\ &= 2.18040 \text{ kg}/\text{m}^2 \\ &= 0.21804 \text{ g}/\text{cm}^2 \end{aligned} \tag{3.6}$$

This leads to a surface density at the inner radius:

$$\begin{aligned} \Sigma(0.15 \text{ AU}) &= \Sigma(200 \text{ AU}) \left(\frac{0.15}{200}\right)^{-1.5} \\ &= 10615 \text{ g}/\text{cm}^2 \end{aligned} \tag{3.7}$$

This scheme can be used to calculate the surface density of any disk size and mass. Exemplary, the values from Thun & Kley (2018) ($R_{\text{in/out}} = 0.15/6$ AU with a total mass of $0.012 M_{\odot}$) and from this thesis ($R_{\text{in/out}} = 0.15/2$ AU with a total mass of $0.012 M_{\odot}$) are implemented (see Tab. 3.3).

In some of the literature, like in Thun et al. (2017, p. 4) and Thun & Kley (2018, p. 3), an f_{gap} (Günther & Kley, 2002, p. 555) as a dampening function is included:

$$f_{\text{gab}} = \left(1 + \exp\left(-\frac{r - r_{\text{gap}}}{0.1r_{\text{gap}}}\right)\right)^{-1} \tag{3.8}$$

where r_{gap} is an approximate gap radius ($\sim 2.5 a_{\text{bin}}$) estimated by Artymowicz & Lubow (1994, p. 651).

It already represents the gap that will be created by the binary (Thun & Kley, 2018, p. 3). Neglecting this dampening function does not influence the outcome of the simulation, as the cavity is a physical result of the binary interacting with the disk (Artymowicz & Lubow, 1994, p. 665; Thun et al., 2017, p. 4). Thus, this cavity is formed without the dampening factor f_{gap} , too. This will be shown later in this thesis when the results of binary simulations are discussed (i.e., see Fig. 4.45). The dampening function only starts the simulation with a starting curve closer to the observed one, saving computational time. To show the slope of different surface densities over the disk radius, Fig. 3.3 was added. As expected, the surface density is higher for smaller disks when the disk mass is kept constant.

The comparisons with surface densities that are used for 2D simulations are possible as the vertical direction can be analytically modeled (Taha et al., 2018, p. 12). Thus in the 3D case, a factor, which FARGO3D automatically implements, is scaling the density depending on the distance to the mid-plane (Taha et al., 2018, p. 12):

$$h(r) = \frac{H(r)}{r} = \left(H \left(\frac{r}{R_0} \right)^{1+\beta} \right) \cdot \frac{1}{r} = h \left(\frac{r}{R_0} \right)^\beta \quad (3.9)$$

with h being the aspect ratio (H/R_0) and β the flaring index. In this thesis, the flaring index is always zero; this is a common assumption for models (Pierens & Nelson, 2018, p. 2549). Furthermore, Thun et al. (2017, p. 3), Thun & Kley (2018, p. 2) and Kley & Haghighipour (2014, p. 3) made the same assumption of a constant aspect ratio, and with their results, the results in this thesis are mainly compared.

The reference surface density, the aspect ratio, and the flaring index are all input parameters needed from the FARGO3D code; the code can calculate all required and dependent values.

Tab. 3.3: Surface density of different disk sizes and masses at the inner boundary of 0.15 AU. The calculations were done analogue to Eq. 3.6 and 3.7. Except of the last line, this was calculated from the values presented by Thun & Kley (2018, p. 3) with $\Sigma_{\text{ref}} = 1.67535 \cdot 10^{-4} \cdot 1.2 \cdot M_\odot / (0.15 \text{ AU})^2$ multiplied by the f_{gap} function.

$R_{\text{in/out}}$ and disk mass	$\Sigma(0.15 \text{ AU})$
0.15/200 AU and $0.012 M_\odot$	10615 g/cm ²
0.15/6 AU and $0.012 M_\odot$	70842 g/cm ²
0.15/2 AU and $0.012 M_\odot$	142261 g/cm ²
<i>0.15/6 AU and $0.012 M_\odot$ with f_{gap}</i>	<i>196 g/cm²</i>

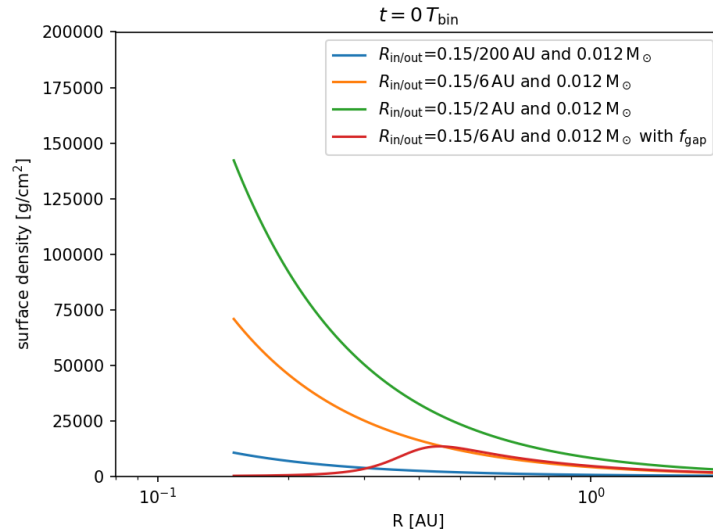


Fig. 3.3: Slopes of the surface density of different disk sizes and masses. The same disks as in Tab. 3.3 are displayed. In the outer part of the disk, the densities are similar, but the surface density strongly differs in the inner region. The blue curve shows the surface density of a classical disk described in Dullemond & Dominik (2004, p. 162) adapted to a total mass of $0.012 M_{\odot}$. Thus if one wants to simulate a similar but smaller disk, one needs to decrease the mass. The orange curve displaces the surface density for a similar mass but a smaller disk. This disk is similar to the disk implemented by Thun & Kley (2018, p. 3). The green curve shows the surface density very similar of one of the setups used in this thesis. The red curve shows the case of Thun & Kley (2018, p. 3), but with the damping factor f_{gap} .

3.2.4 Disk mass

The disk mass is not given as output directly but can be calculated from the gas densities. In case of the spherical output generated by FARGO3D one needs to calculate the volume of each cell:

$$dV = dx dy dz = dr r d\theta r \sin \theta d\phi = r^2 \sin \theta dr d\theta d\phi \quad (3.10)$$

and then multiply it by the density of that volume. This has to be done for the entire disk, and the sum results in the total disk mass.

One could also do a transformation to linearly spaced Cartesian Coordinates (see Sec. 3.2.7). Then it is possible to calculate the size of a cell. Therefore, in the transformed output file with the gas densities all the values of the cell need to be summed and then multiplied with the factor m_{trans} (see Eq. 3.11).

$$m_{\text{trans}} = \frac{M_0}{R_0^3} \cdot (\text{size_of_cell_CU} \cdot R_0^3) \quad (3.11)$$

where M_0 is the combined mass of the central stars which is 1 in CU, R_0 is the reference distance to the center of mass which is also 1 in CU and size_of_cell_CU is the size of

one cell. The calculation how to get `size_of_cell_CU` is explained in the Sec. 3.2.7. To transform the CU in CGS units the equivalents for those values need to be inserted.

To calculate the starting disk mass from the simulation results, one needs to use the gas densities at $t = 0$. The starting disk mass at $t = 0$ can be analytically calculated for the setup, too. Therefore, the density taken from Taha et al. (2018, p. 6) is integrated over cylindrical coordinates.

$$\begin{aligned} M &= \int \int \int \rho(r, z) r dr d\phi dz \\ &= 2\pi \int \int \frac{\Sigma(r)}{H(r)\sqrt{2\pi}} r \exp\left(-\frac{1}{2}\left(\frac{z}{H(r)}\right)^2\right) dr dz \end{aligned} \quad (3.12)$$

with Eq. 3.9 and the surface density as function of the radius:

$$\Sigma(r) = \Sigma_{\text{ref}} \left(\frac{r}{R_{\text{ref}}}\right)^p \quad (3.13)$$

the function of the mass can be written as:

$$M = \frac{2\pi}{\sqrt{2\pi}} \frac{\Sigma_{\text{ref}}}{H} R_{\text{ref}}^{\beta+1-p} \int \int r^{p-\beta} \exp\left(-\frac{1}{2} \frac{z^2}{H^2} \frac{r^{-2-2\beta}}{R_{\text{ref}}}\right) dr dz \quad (3.14)$$

The term in the exponent can be rewritten:

$$\left(-\frac{1}{2} \frac{z^2}{H^2} \frac{r^{-2-2\beta}}{R_{\text{ref}}}\right) = -\left(\frac{z^2}{\sqrt{2}H^2} \frac{r^{-1-1\beta}}{R_{\text{ref}}}\right)^2 \quad (3.15)$$

so that the term inside the brackets can be substituted by Z leading to $dz = \sqrt{2}H(r/R_0)^{(1+\beta)}dZ$. Multiplying and dividing the mass function by $2/\sqrt{\pi}$ leads to:

$$M = \sqrt{2\pi} \frac{\sqrt{\pi}}{2} \frac{\Sigma_{\text{ref}}}{H} R_{\text{ref}}^{\beta+1-p} \int r^{p-\beta} \int \frac{2}{\sqrt{\pi}} \exp(-Z)^2 \sqrt{2}H \frac{r^{(1+\beta)}}{R_{\text{ref}}} dZ dr \quad (3.16)$$

with $\int \frac{2}{\sqrt{\pi}} \exp(-Z)^2 dZ$ being the Gaussian error function. If this function is integrated from minus infinity to plus infinity the result is two (Andrews, 1997, p. 110). This leads to:

$$\begin{aligned} M &= 2\pi \Sigma_{\text{ref}} R_{\text{ref}}^{-p} \int r^{p-\beta} \int_{R_{\text{in}}}^{R_{\text{out}}} r^{1+p} dr \\ &= 2\pi \Sigma_{\text{ref}} R_{\text{ref}}^{-p} \frac{1}{p+2} [R_{\text{out}}^{p+2} - R_{\text{in}}^{p+2}] \end{aligned} \quad (3.17)$$

which is the same function as in Dullemond & Dominik (2004, p. 162) (see Eq. 3.5). Even so Dullemond & Dominik (2004, p. 162) uses the 2D case and Eq. 3.17 is the 3D case where the scale height is parametrised. Now with that value one has the z information and thus a

3D description of the disk.

With $\beta = 0$ and $p = -1.5$ Eq. 3.17 simplifies to

$$M = 4\pi\Sigma_{\text{ref}}R_{\text{ref}}^{1.5} [R_{\text{out}}^{0.5} - R_{\text{in}}^{0.5}]. \quad (3.18)$$

This last Eq. 3.18, with the values for the setup, results in the total disk mass.

For calculating the total disk mass, the Cartesian transformed approach is possible. However, for calculating only the mass of the inner disk, this approach becomes less accurate (see Tab. 3.4). The transformation to linearly spaced Cartesian Coordinates loses information, especially towards the inner parts (see Sec. 3.2.7).

Tab. 3.4: Disk mass calculated with the different methods. As an example, the results of a binary setup with $R_{\text{in/out}} = 0.19/2.09$ AU and $\Sigma_{\text{ref}} = 2.51390456 \cdot 10^{-4}$ is used. This setup will be discussed further in Sec. 4.3.5. First column: analytically (see Eq. 3.18). Second column: directly from the spherical coordinates FARGO3D output file. Third column: from the transformed FARGO3D output file to a linearly spaced Cartesian grid. In brackets the derivation to the analytically calculated mass is displayed.

disk size	mass _{calc} [M_{\odot}]	mass _{sph} [M_{\odot}]	mass _{eCart} [M_{\odot}]
0.19 - 2.09 AU	0.010305	0.0099543 (-3.40 %)	0.0099852 (-3.10 %)
0.19 - 0.3 AU	0.001141	0.0010961 (-3.94 %)	0.0014257 (24.95 %)
0.19 - 0.5 AU	0.002768	0.0026645 (-3.74 %)	0.0031147 (12.53 %)
0.19 - 0.6 AU	0.003457	0.0033302 (-3.67 %)	0.0038052 (10.07 %)

3.2.5 Boundary conditions

In a polar-coordinate and spherical-coordinate grid, R_{min} cannot be zero; therefore, all simulations using this kind of grid will have a computational hole in the domain (Thun et al., 2017, p. 5). Thus, in every simulation there is an inner boundary. The inner boundary condition can have a significant influence on the outcome of the simulations (Thun et al., 2017, p. 5), e.g., the inner cavity is highly influenced by the location of the inner boundary (Thun et al., 2017, p. 5). Previous studies by Thun et al. (2017, p. 7) analyzed this problem and found approaches to minimize the effect of the inner boundary condition.

In the simulations done in this thesis, the outer boundary condition is closed, which does not allow a mass flow. The inner boundary is open. This means the gas can leave the computational domain, but it is not accreted onto the stars. The mass of the stars stays constant over all simulations. For the open inner boundary, the Keplerian extrapolation is used; as the simulation is in 3D, the extrapolation is on ρ (volumic density). At the mid-plane, it

follows a power-law with the exponent $\text{SIGMASLOPE}+1$. Due to strong binary-disk interaction, there is no well-defined Keplerian velocity at the inner boundary. This is why a Keplerian extrapolation boundary condition is also used for the angular velocity $\Omega_\phi = u_\phi/R$ with u_ϕ being the azimuthal velocity, which is periodic in the ϕ direction (Thun et al., 2017, p. 4). Also, in the colatitude, a Keplerian extrapolation is used, which means, e.g., the volumic density ρ at the mid-plane is extrapolated with a power-law slope to the ghost cells (Kimmig, C. N. et al., 2020, p. 3). Outside of the mid-plane, the extrapolation is no longer a simple power-law. An open inner boundary is needed because of numerical and physical reasons. Previous studies by other authors showed that closed inner boundary conditions could lead to unstable numerical results (Thun et al., 2017, p. 7). In the case of a closed boundary, there would be no mass flow through the inner gap (Thun et al., 2017, p. 7).

In the FARGO3D code, a damping criterion for the boundary conditions is included. This means that this criterion takes cells from the active mesh and adds a damping region between the ghost cells and active cells (Benítez-Llambay et al., 2016, p. 3). The ghost and buffer cells (each three cells wide) are the cells where the boundary conditions are applied (Benítez-Llambay & Masset, 2019). The buffer cells should not be confused with the damping region. Those buffer cells are defined as the three outermost cells of the active mesh. The active mesh is defined by N_x , N_y , and N_z (Benítez-Llambay & Masset, 2019). The damping criterion is called STOCKHOLM, and it activates the wave-killing recipe of De Val-Borro et al. (2006, p. 533):

$$\frac{dx}{dt} = -\frac{x - x_0}{\tau}R(r) \quad (3.19)$$

where $R(r)$ is a parabolic function (0 inside the wave-killing zone inside the domain and 1 at the domain boundary), τ is the orbital period of the boundary, and x is either the surface density or the velocity components. This damping criterion does not conserve mass, but the loss is very small (De Val-Borro et al., 2006, p. 533). This criteria only becomes necessary when there is a solid inner boundary (De Val-Borro et al., 2006, p. 533). As this is not the case in this thesis, using the condition is optional. Thus, it needs to be tested how the results are influenced. It is designed to damp disturbances near the boundary of the mesh and is set in the FARGO3D code to 10% of the radius of the mesh (Benítez-Llambay & Masset, 2019). The size of the dampening zone depends on the size of the of the mesh in the radial direction (Benítez-Llambay & Masset, 2019). The decision of the usage of the damping of the boundary condition depends on each setup and the science goal (Benítez-Llambay & Masset, 2019). In the following, simulations with and without this condition are made. Because of the small computational area, this criterium has a significant impact on the results. Using

the Stockholm condition in this setup, it damps the set boundary conditions so much that the set boundary parameters do not influence the simulation anymore. Thus the results are all the same, no matter which set boundary condition is used. If the Stockholm condition is not used, the boundary conditions of the setup are dominant. In the simulations, the boundary conditions are set to lead to a decreasing disk mass over time.

Thun et al. (2017, p. 7) investigated the optimal location of R_{\min} with 2D FARGO3D simulations. In their study, they focused on computational efficiency and reliable results. Concluding, all major mean-motion resonances should be inside of the computational domain to obtain physical solutions. Especially the 3 : 1 Lindblad resonance needs to be inside this domain, as it is important for the disk eccentricity (Thun et al., 2017, p. 7; Pierens, A. & Nelson, R. P., 2013, p. 16).

Another finding was that there is an increase of surface density at the inner radius with a smaller inner radius (Thun et al., 2017, p. 7). Thus, the material can leave the computational domain through a smaller area. Consequently, a too large R_{\min} allows too much mass to leave the computational domain. Thus it has to be chosen small to show all the dynamics. This will be discussed in more detail in the next section. Nevertheless, the surface density profile did not depend on the location of the inner boundary in their studies (Thun et al., 2017, p. 8).

Regarding the outer radius R_{\max} , it should have a value large enough to not interfere with the dynamical behaviour of the inner disk (Thun et al., 2017, p. 8). Thun et al. (2017, p. 8) adopted $R_{\max} = 4.0$ AU. In this thesis $R_{\max} = 2.1$ AU is used which is similar to Kley & Haghighipour (2014, p. 7) but smaller than Thun et al. (2017, p. 8). Tests with a larger outer boundary were performed, too. The results were quite similar; thus, for time efficiency, the smaller setup is used (see Appendix 6.2).

3.2.6 Transformation Code Units (CU) to CGS units

Very crucial for analyzing the results is the correct transformation from CU to CGS units. Test simulations with the standard single star setup were done to understand the transformation. Depending, if one wants to have results in CU or CGS units, one has to select for compiling "make UNITS = 0 RESCALE = 0" in the first case and "make UNITS = CGS RESCALE = 1" in the second case. The keyword "RESCALE = 1" enables FARGO3D to produce the result already in physical units. This allows one to test the correctness of the transformation of units. As a test, values at the same location for the different unit systems and different evolution times of the binary (T_{bin}) were picked, and the following transforma-

tion formulas were tested. In all simulations, the results at the same location need to be the same no matter which unit system was used. This was confirmed with this very fast and basic test.

In this thesis, the transformation of the binary setup is of interest, but testing the transformation of units only works in the single star setup with a default star. In this case, the FARGO3D code places a star with a defined mass in the center of mesh of the simulation. The transformation has to be performed manually as soon as the stars are inserted in the planetary file because FARGO3D uses the mass of the default star as a mass reference for the transformation. The input needs to be in CGS units to get CGS units directly from FARGO3D in the binary case. This was not done, as the input parameters in CU are simplified.

To transform the gas density from CU to CGS units one has to multiply each cell by a multiplication factor ρ_{trans} defined by:

$$\rho_{\text{trans}} = \frac{M_0}{R_0^3} = \frac{M_{\text{bin}} \cdot 1 M_{\text{sun}}}{(a_{\text{bin}} \cdot 1 \text{ AU})^3} \quad (3.20)$$

It already includes the variables for the binary transformation, but for the single setup these values for a_{bin} and M_{bin} are assumed 1. The units for M_{sun} and Astronomical Unit (AU) were CGS in Units. The same holds for the following multiplication factor.

To transform the velocities from CU to CGS units one has to multiply each cell by a multiplication factor v_{trans} defined by:

$$v_{\text{trans}} = \Omega \cdot (R_0) = \sqrt{\frac{GM_0}{R_0^3}} \cdot (R_0) = \sqrt{\frac{GM_{\text{bin}}M_{\text{sun}}}{(a_{\text{bin}}\text{AU})^3}} \cdot (a_{\text{bin}}\text{AU}) \quad (3.21)$$

It could be confirmed that the transformation was done correctly (see Fig. 3.4 and Fig. 3.5). With this knowledge, the simulations can be analyzed.

3.2.7 Transformation from Spherical to Cartesian coordinates

This subsection tests whether the calculation of the size of a cell in code units in a linearly spaced and Cartesian grid simplifies the calculating and plotting of the results. Therefore, the spherical logarithmic spaced output file coming from FARGO3D needs to be transformed. To do this transformation, Pablo Benitez-Llambay (Co-Developer of the FARGO3D code) developed a script that can be publicly accessed (<https://bitbucket.org/pbllambay/f3d2x3d/src/master/> Accessed: 2021-03-10). With this transformation, the cells become linearly spaced on a 600x600x40 grid (see Fig. 3.6). Knowing the grid size of this linearly spaced

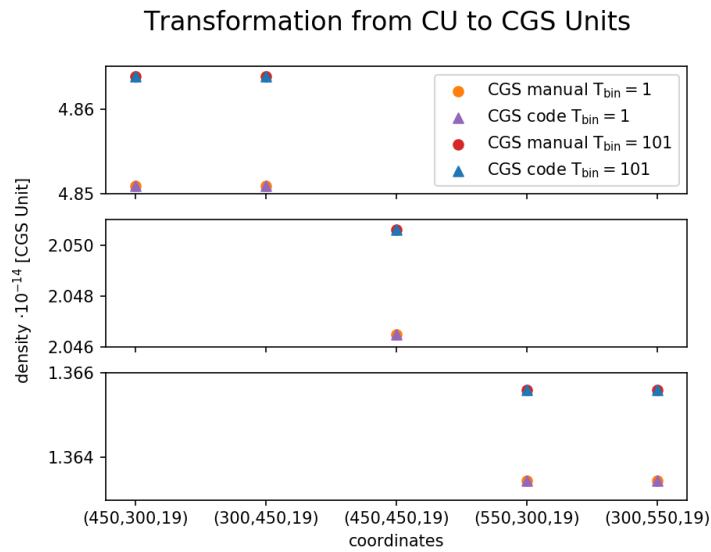


Fig. 3.4: Density transformation CU to CGS units at different coordinates inside the disk. The difference between the transformation done by the FARGO3D code automatically with "make UNITS = CGS RESCALE = 1" (triangles) is the same as the transformation done manually in this thesis (dots) with "make UNITS = 0 RESCALE = 0" and then manually transformed with Eq. 3.20. It was tested for five different coordinates in the disk at the mid-plane at two different times ($T_{\text{bin}} = 1$ and $T_{\text{bin}} = 101$).

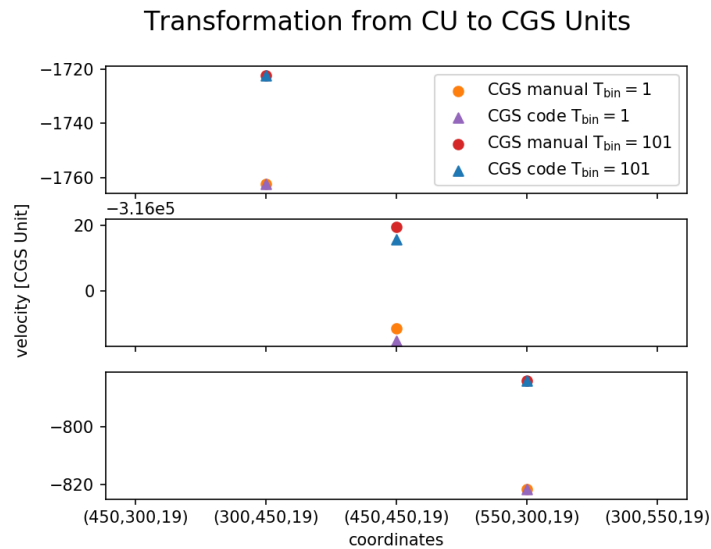


Fig. 3.5: Velocity transformation CU to CGS units at different coordinates inside the disk. The difference between the transformation done by the FARGO3D code automatically with "make UNITS = CGS RESCALE = 1" (triangles) is the same as the transformation done manually in this thesis (dots) with "make UNITS = 0 RESCALE = 0" and then manually transformed with Eq. 3.20. It was tested for five different coordinates in the disk at the mid-plane at two different times ($T_{\text{bin}} = 1$ and $T_{\text{bin}} = 101$).

grid and the size of the mesh used to compile the code, one can calculate the size of a cell.

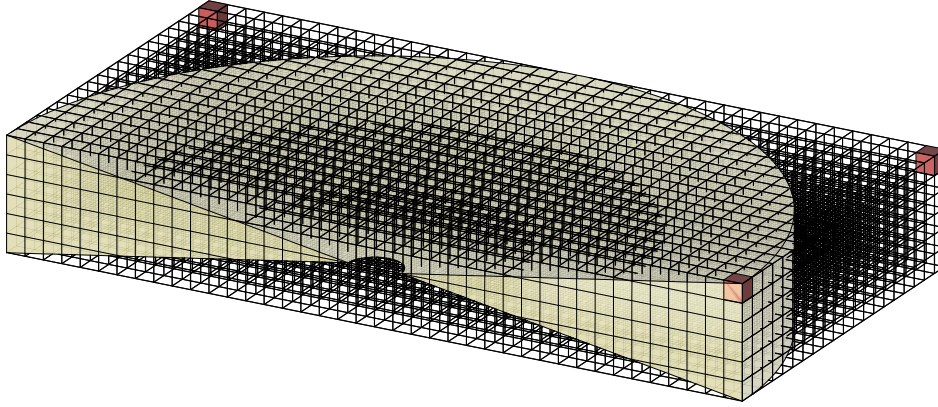


Fig. 3.6: Sketch of linearly spaced grid cells after the transformation. The size of each cell can be calculated by knowing the dimensions of the disk and the number of cells in each direction. The yellow disk displays the simulated area. Thus, the grid is equally spaced within the computational area and outside. The red cubes visualize the three dimensions of the grid.

After that transformation, one can calculate the cell size in xy direction with:

$$(14.28 \cdot 2)/600 = 0.0476 \text{ CU} \quad (3.22)$$

14.28 is the radius of the disk in CU, which was the input in the FARGO3D setup file (see Appendix 6.2). In the transformed Cartesian grid, one can calculate the size of each cell in xy direction by dividing the diameter of the disk through the numbers of cells which are linearly spaced within that disks diameter.

One has to use the mesh's borders in the code to calculate the size of the cell in z direction, which is $3 H/r$. To get the max height of the disk, one has to multiply $3 H/r$ ($3 \cdot 0.05$) by the radius of that disk. As the disk extent is symmetrical to the mid-plane in z direction, one needs to multiply everything by two before dividing it by the number of cells in the z direction.

$$(0.15 \cdot 14.28 \cdot 2)/40 = 0.107 \text{ CU} \quad (3.23)$$

By comparing the transformed results with the results without using the transformation code

to space each cell linearly, one can see the results are visually the same; just at the edge of the disk, the transformed file is less accurate (see Fig. 3.7). At first glimpse, for displaying the results, this limitation is acceptable. However, this transformation becomes inaccurate for calculating the disk mass and later the force on the planet. As shown in Sec. 3.2.4, the transformation in the inner region of the disk deviates more the closer one comes to the inner edge. This is because the resolution is lost at the inner edge (see Fig. 3.8). The 39 cells of the disk in the FARGO3D simulation get linearly spread over 40 cells. Now at the inner edge, the disk only fills the inner cells of the linearly spaced Cartesian grid. Thus the resolution is drastically reduced. This is also visible when performing a subtraction of the mid-plane and plotting the results at point unequal zero (see Fig. 3.9). Thus, using the transformation code for a linearly spaced Cartesian grid needs to be handled with care as the resolution is influenced and thus the result. If one wants to use this code in the future, one needs to test whether an increase of resolution solves that problem.

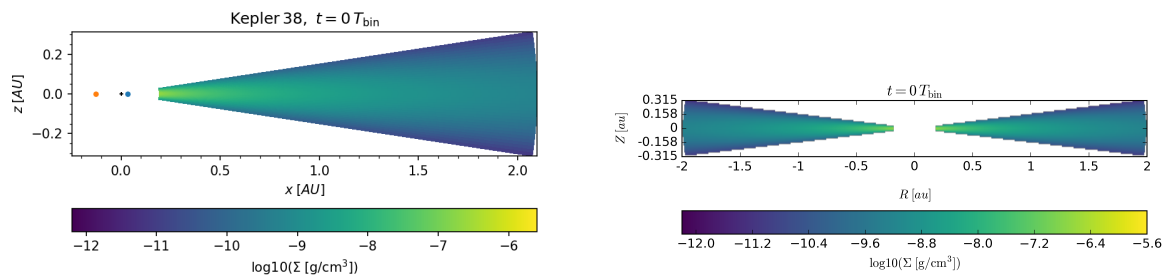


Fig. 3.7: The volume density distribution of the z plane of a binary setup at $T_{\text{bin}} = 0$. (left) Plotted directly from the density output file from FARGO3D and then transformed into Cartesian coordinates. (right) Plotted from the transformed density file with the Code by Benitez-Llambay, all cells are equal size.

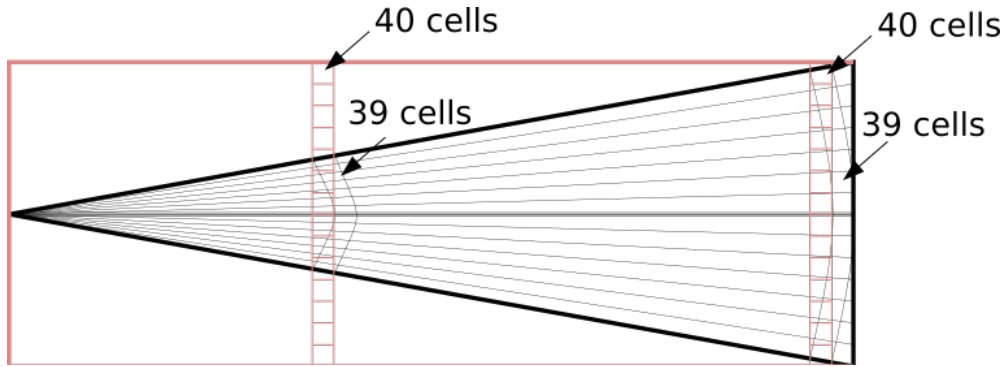


Fig. 3.8: Disk with Cartesian Grid vs. polar grid of the z plane. For simplicity reasons, the drawing is in 2D. (red) Cartesian coordinates. (grey) polar coordinates. One can see that the size of each cell varies for the polar coordinates. This is also true for the spherical coordinates. More importantly, one can see that the resolution of the grid is much less in the inner region with the transformed linearly spaced Cartesian grid.

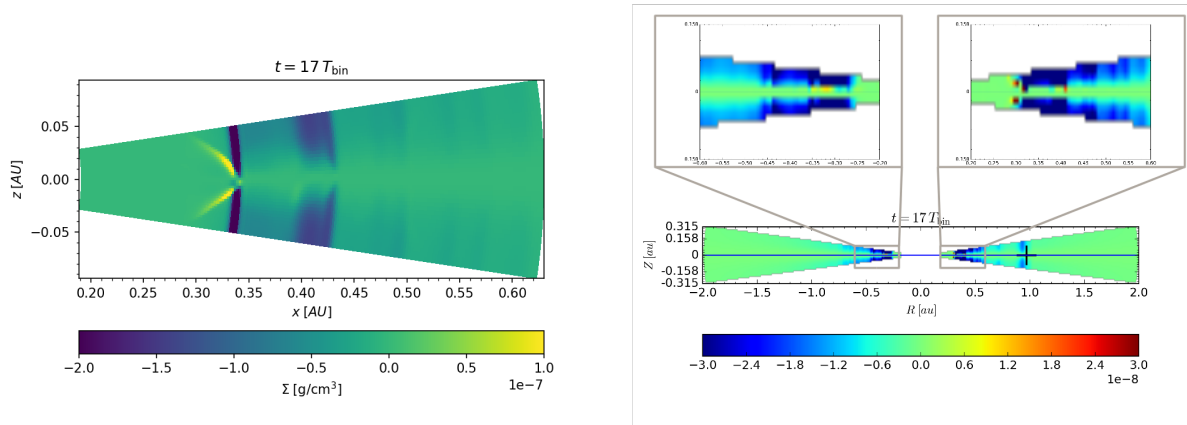


Fig. 3.9: The volume density distribution of the z plane of a binary setup plotted at $T_{\text{bin}} = 17$, where the mid-plane is subtracted. (left) Directly plotted from the volume density output file from FARGO3D and then transformed into Cartesian coordinates. (right) Plotted from the transformed volume density file with the code by Benitez-Llambay, all cells are equal in size. Even so, the color-code and the unit ranges are different; one can see the significant differences.

4 Results of the FARGO3D simulations

The Kepler 38 system is analyzed with 3D simulations in this section. Different simulations with varied parameters were run to understand how the system evolved towards today's observed status.

As mentioned before, the Kepler 38 system hosts a planet with an inclination smaller than 0.2° (Kley & Haghighipour, 2014, p. 2). Previous studies by Kley & Haghighipour (2014) and Thun & Kley (2018) were assuming that 0.2° (Orosz et al., 2012, p. 10) is small enough to simulate the system in 2D as they were focusing mainly on the planet migration. Here the focus is on very small effects using the 3D code. Usually, those effects are neglected, for instance, in the papers mentioned earlier. However, with a 3D code, it is possible to investigate those effects. In this thesis, the focus is on understanding the origin of those small characteristics, i.e., the gas distribution in z direction and movement of the planet in the z direction. Furthermore, the hydrodynamic and gravitational interactions between the planet, the host disk, and the stars are investigated.

At the beginning ($t = 0 T_{\text{bin}}$), in all the simulations, the binary orbit and the disk's mid-plane are always aligned. Moreover, the planet's orbit is also initially aligned with the binary orbit and the mid-plane of the disk ($z = 0$). In this thesis, two types of inclination are considered: the mutual inclination of the angular momentum vectors (see Fig. 4.1 i_1) and the angle coming from the displacement of the planet in the z direction towards the mid-plane (i_2). Thus, if the planet is no longer in the mid-plane, the angle between the angular momentum vectors of the binary and the planet is considered as inclination as well as the angular offset towards the binary orbital plane (mid-plane).

4.1 The case of the single star system (default case)

The single star setup with a default case enables testing the simulation results and the self-written codes for this Ph.D. thesis. Moreover, it validates the transformation of units and the stringency of the analyzing codes written during this thesis (see Chapter 3).

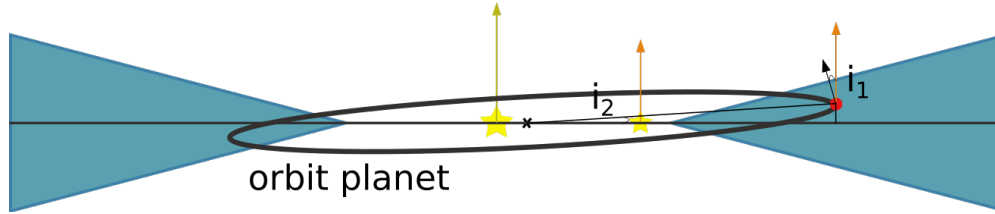


Fig. 4.1: Sketch of setup. Initially, the binary and planet (red dot), as well as the disk, are aligned. Later, the planet becomes misaligned; therefore, two different kinds of inclination are discussed. First, the inclination between the angular momentum vector of the binary (which is also the normal vector to the computational mid-plane as the binary components are kept aligned in this plane, orange arrows) and the angular momentum vector of the planet (black arrow) is indicated through i_1 . Second, the inclination angle displays the offset of the planet towards the mid-plane is indicated through i_2 .

In the FARGO3D CU single star setup, which is used in this thesis, the term $T_{\text{bin}} = 2\pi$ is an absolute reference time and is therefore also valid in the single star setup.

4.1.1 Velocity field

The velocity vectors of the setup with just a central star and a disk were analyzed. The transformation to CGS units was performed with Eq. 3.21. The vector field was plotted after the time unit $1 T_{\text{bin}}$ (see Fig. 4.2). The shape is expected; one can see a higher velocity at the inner region and a slower at the out regions as expected of a disk in Keplerian rotation. This is quantitative analysed by plotting the azimuthally-averaged radial velocity as a function of the radius. This is then compared with the analytical solution of the Keplerian velocity ($\Omega_{\text{k}}^2 = GM/r$) (Armitage, 2007, p. 17)) (see Fig. 4.2). No further analysis of the vector field is intended. It will be later used, e.g., to calculate the angular momentum vector of the disk and the total force derivated from the first Newtonian law. Therefore, it is important to check whether the data is extracted correctly, and this is the case here.

4.1.2 Boundary conditions with Stockholm vs. no Stockholm condition

Calculating the disk mass over time (Sec. 3.2.4) showed that the boundary conditions are too much damped with the Stockholm condition (see Sec. 3.2.5). Especially in the binary case, this has a significant impact on the results. This is discussed further in Sec. 4.3.

For the single star case, the simulation was run one time with Stockholm and one time without Stockholm (Sec. 3.2.5) with an initial disk mass of $0.01 M_{\odot}$. In those simulations the mass develops differently over time (see Fig. 4.3).

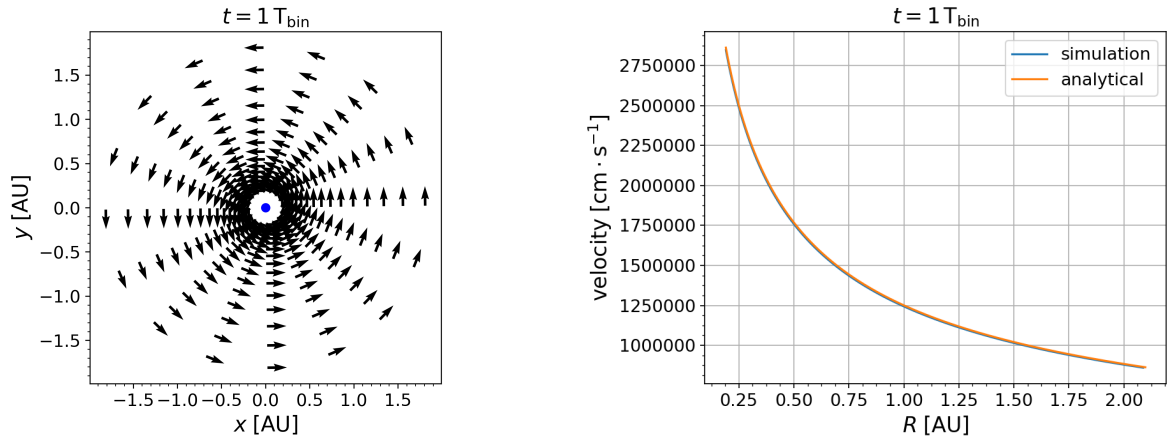


Fig. 4.2: (right) The growing vector size towards the center of the plot is expected, as the disk is in Keplerian rotation. The vectors shown are normalized. (left) The velocity from the simulation is plotted against the radius, and the velocity is analytically calculated. The figures displace the disk at $1 T_{\text{bin}}$.

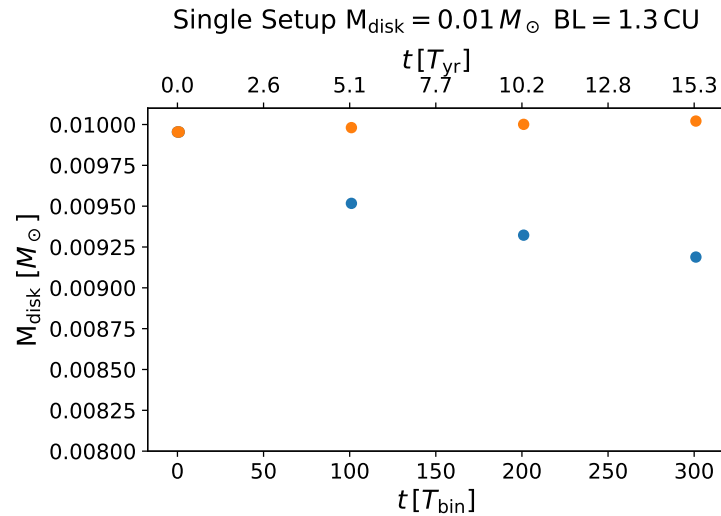


Fig. 4.3: The plot shows the development of the disk mass over time. In the case of Stockholm conditions turned on (orange plot), the disk's mass is slowly rising, as the open inner boundary condition and the closed outer boundary condition are damped and thus have no influence on the result. This leads to an increase of mass of 0.7% over 15.3 years. With the Stockholm conditions turned off (blue plot), the set boundary condition can function properly, and the disk mass drops over time. The mass reduction is 7.7% over 15.3 years. The single star setup is used with the default star in the center of the grid, and the inner boundary location is at 1.3 code units. On the top axis time is indicated in earth years, on the lower in binary revolutions.

This dampening of the boundary conditions through the Stockholm condition also influences the planet parameter (see Fig. 4.4). Nevertheless, the planet migrates towards the central star with a low eccentricity and almost no inclination in both cases. This is expected for the singular case. In the following paragraphs, the singular case is only discussed without the Stockholm condition, as the Stockholm criterion only becomes necessary for a closed inner boundary (De Val-Borro et al., 2006, p. 533). As this is not the case here, the dampening condition is unnecessary. Nevertheless, in this thesis it will be analyzed to see correlations depending on mass.

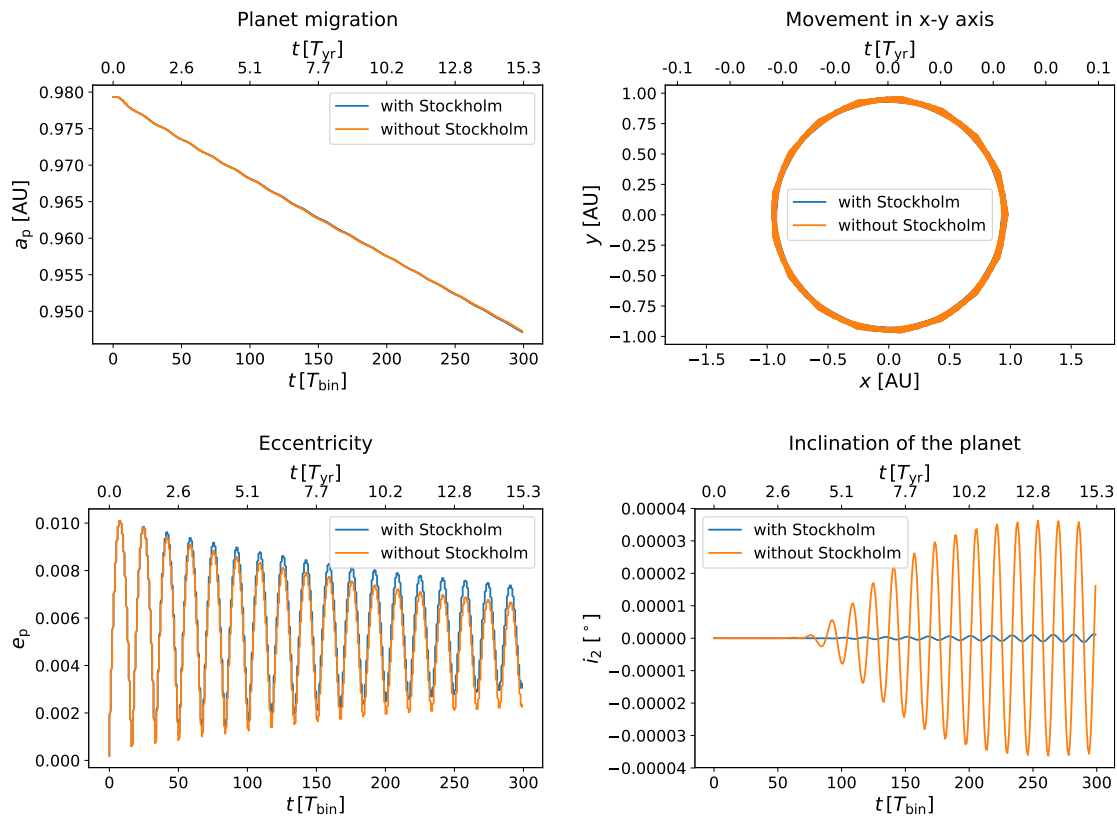


Fig. 4.4: In these plots the different planet parameters are displayed. In the top left plot one can see that the migration of the planet is similar with and without the Stockholm condition. The same holds for the movement in the mid-plane in the top right plot. The planet eccentricity in the bottom left plot is slightly different between the two setups, whereas the inclination from the mid-plane in in degree overtime is influenced by the boundary condition significantly more (see the bottom right plot). It is calculated as the angular offset from the binary orbital plane through $i_2 = \tan(z/R)$, where R and z are the radial and vertical positions of the planet in the grid. Compared to later simulations with a binary, those inclination regimes are negligibly small. The cause of the inclination is discussed later. In all plots the same setup as in Fig. 4.3 (without Stockholm condition) is used. Thus the single star setup with default star in the center of the grid, the disk mass is $0.01 M_{\odot}$ and the inner boundary location is at 1.3 code units. On the top axis time is indicated in earth years, on the lower in binary revolutions.

4.1.3 Angular momentum of the disk

The results of the single star setup are used to analyze the disk's angular momentum and validate the self-written python analyzing code. The star in the center of mass is not rotating. Nevertheless, it is assumed that the star's angular momentum corresponds to the normal vector, which is perpendicular to the mid-plane of the disk. In a single star system that was initialized co-planar with the mid-plane of the disk and the planet, one would expect that the vectors of the star's angular momentum (in this thesis: \mathbf{N} which equals the normal vector) are aligned with the angular momentum of the disk. The angular momentum of every disk cell is calculated with the following formula:

$$\mathbf{L} = m\mathbf{r} \times \mathbf{v} \quad (4.1)$$

with the knowledge of the gas density distribution and the velocity field. The resulting vector and the normal vector can be used to calculate the mutual inclination (i_1) between those vectors:

$$i_1 = \arccos \left(\frac{\mathbf{N} \cdot \mathbf{L}_{\text{disk}}}{|\mathbf{N}| |\mathbf{L}_{\text{disk}}|} \right) \quad (4.2)$$

All results from the simulations were first transformed into CGS units. For the mid-plane, the results can be shown graphically (see Fig. 4.5). Therefore, the vectors for each cell in every plane are calculated and then summed up, resulting in an angle of $\sim 0.0000444^\circ$ after 17 binary revolutions, which is numerical noise and negligibly small. More evolved cases are tested for the single star setups without the default star.

4.1.4 Angular momentum of the planet

The angular momentum of the planet and star can also be calculated. Again the results of the simulations with a single star system with default star and an inner boundary location of 1.3 code units are used. The mutual inclination between the angular momentum vector of the planet and the normal vector (0,0,1) is shown in Fig. 4.6. Again the angle is negligibly small and results out of numerical noise. The degree of inclination calculated with the formula for the angular momentum results in the same regime, as calculating the degree of inclination from the angular offset from the binary orbital plane (see Fig 4.4 (bottom right plot, without Stockholm condition)). This is expected as those are two different methods to display the same physical effect, i.e., the displacement of the planet from the mid-plane.

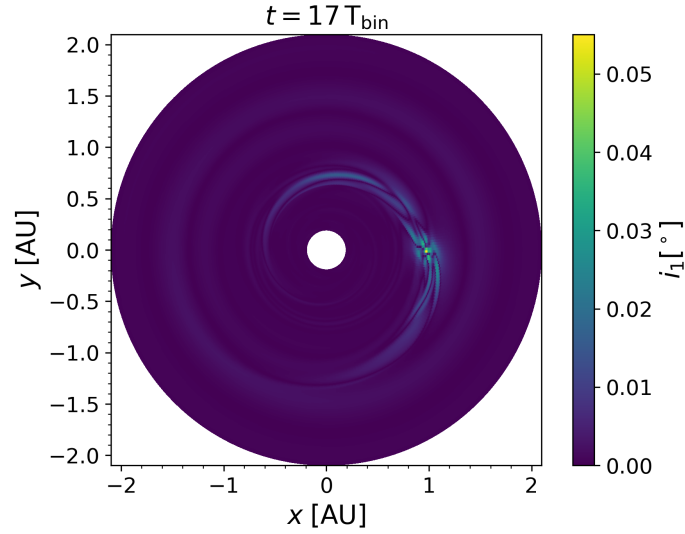


Fig. 4.5: Mutual inclination in degree between the angular momentum of each cell of the disk and the normal vector in the mid-plane. The initial disk mass is $0.01 M_{\odot}$. For the single star setup with planet the inner boundary is set to $1.3 a_{\text{bin}}$ and no Stockholm condition is used. As expected the disk's angular momentum vector is parallel with the normal vector in the disk's mid-plane. Only close to the planet and along the spiral arms it is slightly not zero. The time is indicated on the top of the figure.

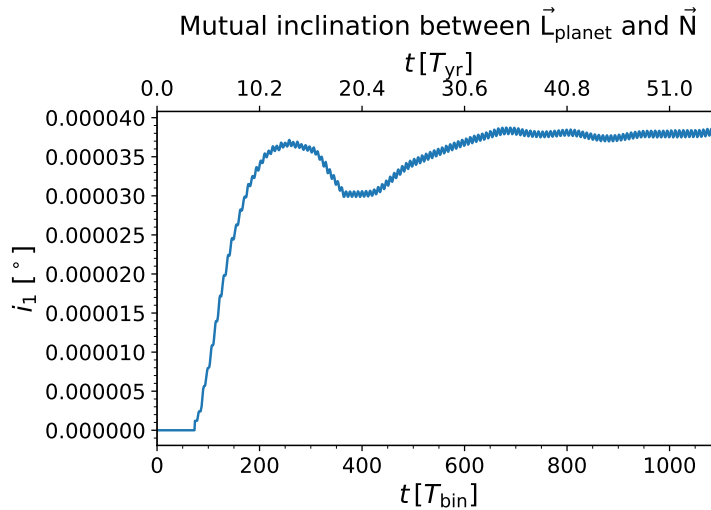


Fig. 4.6: Mutual inclination in degree between the angular momentum vector of the planet and the angular momentum vector star (normal vector) for a $0.01 M_{\odot}$. It is the same simulation as in Fig. 4.5. On the top axis time is indicated in earth years, on the lower in binary revolutions.

4.1.5 Force on a planet

A code was written to calculate the force on the planet coming from the disk and the star (later in the binary case from the stars). This code uses the simulation results and the following equations:

$$\mathbf{F}_{\text{star}} = G \frac{M_{\text{star}} m_{\text{planet}}}{d_{\text{star_planet}}^3} \mathbf{d}_{\text{star_planet}} \quad (4.3)$$

$$\mathbf{F}_{\text{disk}} = \sum_{ijk} G \frac{M_{\text{cell}} m_{\text{planet}}}{d_{\text{cell}_{ijk_planet}}^3} \mathbf{d}_{\text{cell}_{ijk_planet}} \quad (4.4)$$

with $M_{\text{star/cell}}$ being the mass of the star/each cell, m_{planet} being the mass of the planet and $d_{\text{star_planet/cell_planet}}$ being the distance between the location of the star/each cell and the location of the planet.

The results of the combined forces in the single star setup for two different disk masses are shown in Tab. 4.1. The force from the default star on the planet at $T_{\text{bin}} = 0$ is mainly in x direction. For example, for the setups with $0.01 M_{\odot}$ and $0.1 M_{\odot}$, the force from the central star in x direction is $-4.42 \cdot 10^{29} \text{ g cm/s}^2$ (CGS units). This number is reasonable, as the star and the planet are aligned on the x axis, and the star is at the center of mass. If one calculates the force with the analytical formula, one gets $-4.25 \cdot 10^{29}$ CGS units which is in the same regime. The direction of the force acting on the planet is along the negative x axis. Focusing on the disk at $T_{\text{bin}} = 0$, the disk should be homogeneous, and thus the force in z direction from the disk should be zero. As a result of the numerical experiment, the gas distribution in the disk is not completely homogeneous. Thus those small differences add up and for a simulation with a starting disk mass of $0.01 M_{\odot}$ the force vector is at the beginning of the simulation $(-3.57 \cdot 10^{18}, 2.97 \cdot 10^{16}, -3.57 \cdot 10^{17})$ CGS units. The forces along the y and z axis are orders of magnitude below the force along the x axis. The force of the $0.01 M_{\odot}$ disk in z direction is $-3.57 \cdot 10^{17}$ which is 10x smaller than the force coming from the 10x heavier $0.1 M_{\odot}$ disk in z direction $(-3.57 \cdot 10^{18})$.

The analyzing codes written for this thesis work can now be transformed for a setup with no default star. The single star setup with no default star is later transformed to a binary setup.

4.2 The case of the single star system (no default case)

The previous section looked at the results of a default single star system, which is good for testing the code and the transformation from CU to CGS units. In a second step, the feature of FARGO3D to remove the default star is used. All simulations in this section were

Tab. 4.1: Force in CGS units in x,y,z direction on planet at different T_{bin} for different disk masses.

	$0.01M_{\odot}$	$0.1M_{\odot}$
$T_{\text{bin}} = 0$ x	$-4.42 \cdot 10^{29}$	$-4.42 \cdot 10^{29}$
y	$2.97 \cdot 10^{16}$	$2.97 \cdot 10^{17}$
z	$-3.57 \cdot 10^{17}$	$-3.57 \cdot 10^{18}$
$T_{\text{bin}} = 17$ x	$-4.45 \cdot 10^{29}$	$-3.83 \cdot 10^{29}$
y	$1.89 \cdot 10^{27}$	$-3.37 \cdot 10^{29}$
z	$-4.51 \cdot 10^{19}$	$-1.65 \cdot 10^{20}$
$T_{\text{bin}} = 910$ x	$-4.36 \cdot 10^{29}$	$3.66 \cdot 10^{29}$
y	$-2.09 \cdot 10^{29}$	$-4.54 \cdot 10^{30}$
z	$-9.83 \cdot 10^{22}$	$1.01 \cdot 10^{24}$

performed with the Stockholm condition turned off. With FARGO3D, one can define planets and stars in the planet file in the code. The code detects through the mass of the object, when a star or a planet is added. For this purpose, the code checks whether the object is bigger or smaller than an arbitrary threshold (e.g. $0.05 \cdot \text{MSTAR}$) (Benítez-Llambay & Masset, 2015b, p. 50). In this setup, MSTAR is set to 1. Thus it is, for example, possible to add one star with planets or multiple stars with planets. In this thesis, the focus is on adding one star with and without a planet and adding two stars as a tight binary system with or without a planet.

The scenario in this section with a single star is the benchmark scenario, as the setup results of the single star system can be compared with the results of the binary setup later. This enables one to confirm the physical nature of the observed objects. One has to be careful only to compare the single case without the Stockholm condition with the binary case without the Stockholm condition. Nevertheless, comparing two simulations needs to be handled carefully, as the planet is at different locations in the single and binary case with respect to the central star object(s). Of course, the simulations were also run for the setup with the Stockholm condition. Those results are discussed later, directly comparing it to the binary setup.

For the single star setup, the star is put with a distance of zero to the center of the grid in the planet file. As the center of mass is the center of the mesh, the star needs to move around that center, as the center of the mass of the system considers the mass of the planet and the mass of the star. This leads to a tiny movement of the star on the mesh (see Fig. 4.7). Everything else is kept the same towards the previous setup.

In the single star system, one can see spiral arms and the migration of the planet towards the star-like expected (see Fig. 4.8 and Fig. 4.9). This has been discussed lengthily in the past by publications of other authors, e.g., Cresswell et al. (2007) and Kley & Nelson (2012)

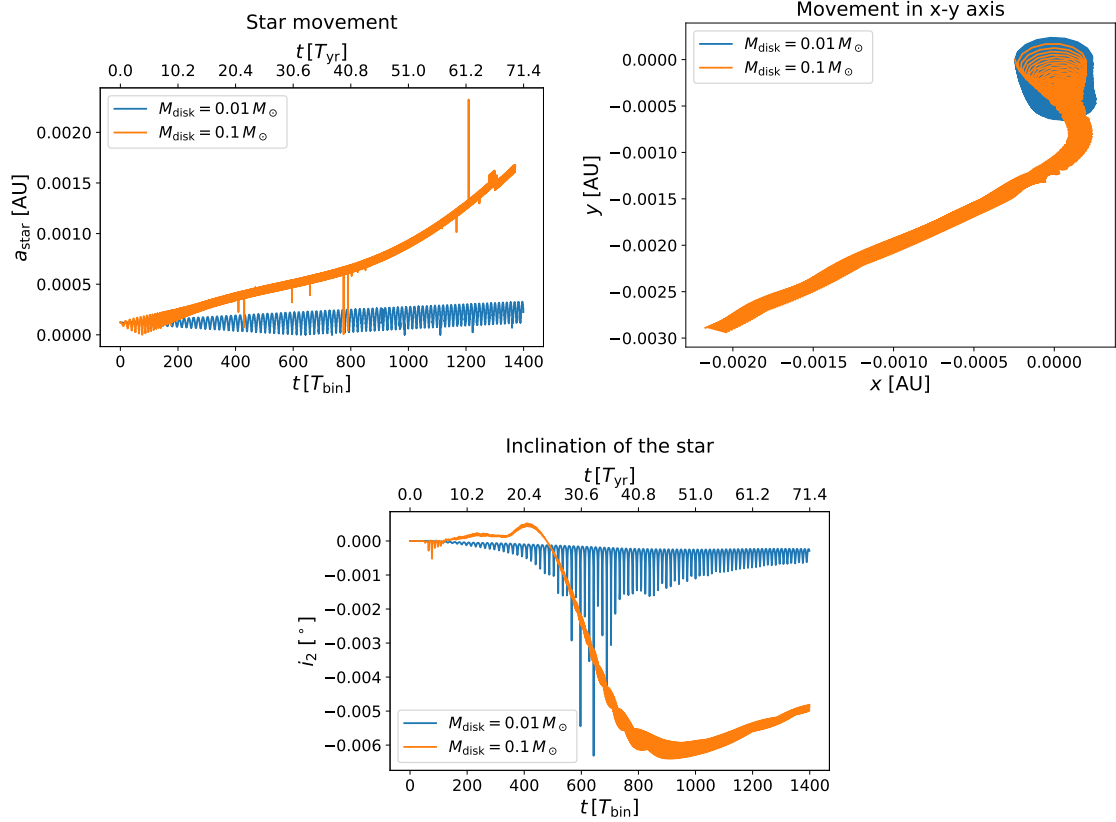


Fig. 4.7: Plots of stellar parameter for a star in a $0.01 M_{\odot}$ disk and $0.1 M_{\odot}$ disk. The top plots show the stellar movement in the xy plane (a_{star} and movement in xy axis), and the bottom plot shows the stellar movement in the z plane (inclination of the star with respect to the mid-plane). For the lighter disk, the star moves closely around the center of mass. In contrast, the star with the heavier disk has a larger semi-major axis and thus larger movement in the xy axis. Nevertheless, it is still close to the center of mass. This movement of the stars seems large compared to the lighter disk, but if one looks at the axis displacement of the star, one can see that it is still very close to the center of mass and very far away from the inner boundary location. This simulation of a single star system is without a default star, the boundary location is $1.3 a_{\text{bin}}$ and the Stockholm condition is turned off. On the top axis time is indicated in earth years, on the lower in binary revolutions.

and in Sec. 2.1.3.

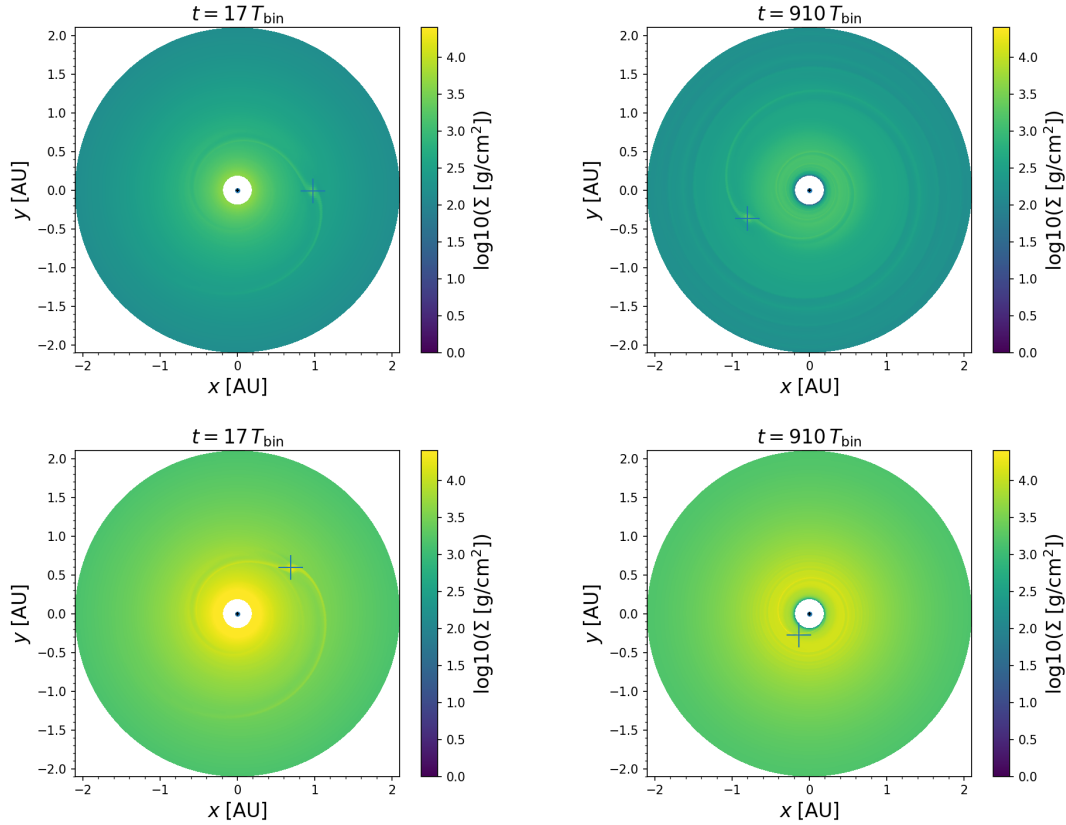


Fig. 4.8: Evolution of the $0.01 M_{\odot}$ disk (top) and a $0.1 M_{\odot}$ disk (bottom) single star disk shown in a two-dimensional surface density plot at the mid-plane with an isothermal simulation and a planet (indicated through the cross). The perturbations of the surface density at different times are shown. It is color-coded with the logarithm of the gas surface density at the mid-plane. The white areas are outside of the computational domain. The plots are 4.2×4.2 AU in size. On top of each figure, time is indicated as a multiple of the orbital period. One can see the spiral arms and the migration of the planet. The setup is used like in Fig. 4.7

The angular momentum of the whole $0.01 M_{\odot}$ disk at $T_{\text{bin}} = 910$ is $2.21 \cdot 10^{51} \text{ g cm}^2/\text{s}$. The angular momentum of a disk ten times heavier is $2.21 \cdot 10^{52} \text{ g cm}^2/\text{s}$. This is expected as a 10x heavier disk leads to a 10x larger angular momentum (see Eq. 4.1).

The mutual inclination of the disk's angular momentum vector and the normal vector in the single star case is quite small (see Tab. 4.2). The mutual inclination of the planet's angular momentum vector and the star's angular momentum vector in a $0.01 M_{\odot}$ and $0.1 M_{\odot}$ disk is displayed in Tab. 4.3 for $17 T_{\text{bin}}$ and $910 T_{\text{bin}}$. Those tables display a negligible small inclination compared with the results later in the binary case. This can be further analysed by looking at the mutual inclination over time in a $0.1 M_{\odot}$ disk (see Fig. 4.10). One can see how small the mutual inclination between the normal vector and the angular momentum vector of the planet is. This also holds for the force on the planet resolving from the star

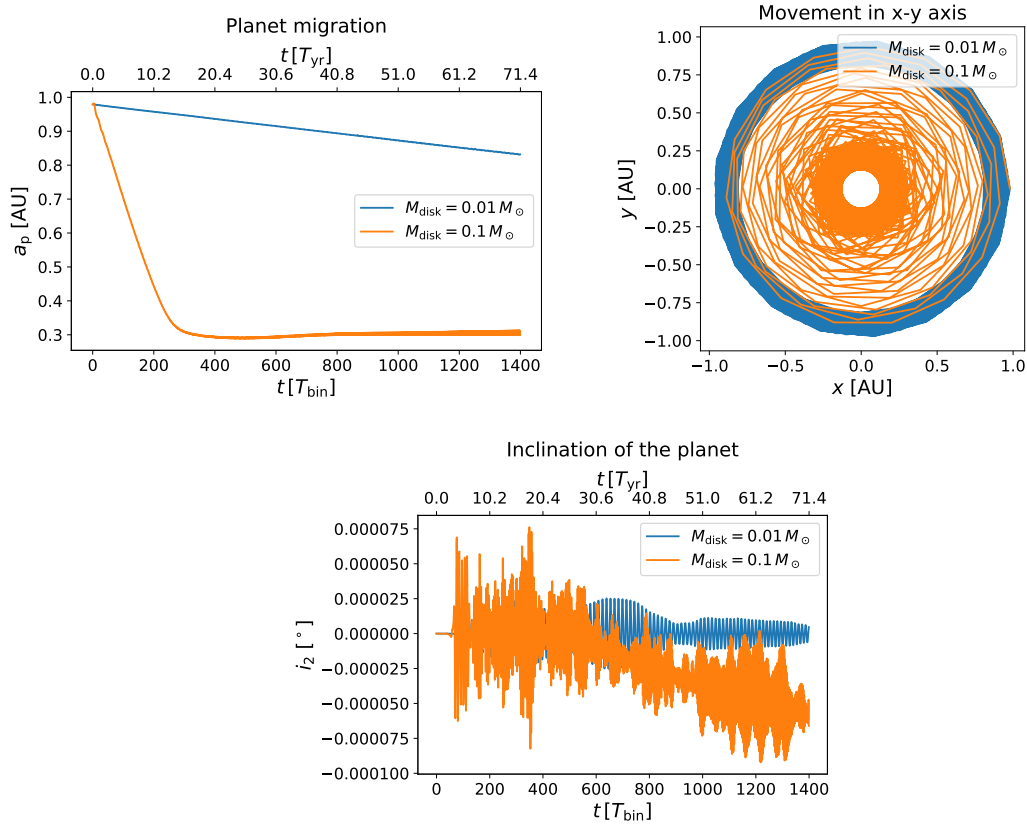


Fig. 4.9: Plots of planet parameter for a planet in a $0.01 M_{\odot}$ disk and $0.1 M_{\odot}$ disk. The top plots show the planet movement in the xy plane (a_p and movement in xy axis), and the bottom plot shows the planet movement in the z plane (inclination of the star with respect to the mid-plane). This simulation of a single star system is without a default star, the boundary location is $1.3 a_{\text{bin}}$ and the Stockholm condition is turned off, like in Fig. 4.7. On the top axis time is indicated in earth years, on the lower in binary revolutions.

and the disk (see Tab. 4.4). Again in this setup, the force in z direction coming from the disk is for the 10x lighter disk roughly 10x smaller than for the 10x heavier disk.

Tab. 4.2: Mutual inclination in degree of the normal vector and the disk’s angular momentum vector at different T_{bin} for different disk masses. The normal vector is used as the star has only a inclination of 0.001° later in the simulation with the lighter disk ($0.01 M_\odot$) at $910 T_{\text{bin}}$. At $910 T_{\text{bin}}$ in the heavier disk ($0.1 M_\odot$) the star has a inclination of 179.993° . Which comes from angular momentum which points in the opposite direction of the star.

	$0.01M_\odot$	$0.1M_\odot$
$T_{\text{bin}} = 17$	0.0000703	0.0000636
$T_{\text{bin}} = 910$	0.000119	0.000358

Tab. 4.3: Mutual inclination in degree of the normal vector and the planet’s angular momentum vector at different T_{bin} for different disk masses.

	$0.01M_\odot$	$0.1M_\odot$
$T_{\text{bin}} = 17$	0.0	0.0
$T_{\text{bin}} = 910$	$7.24 \cdot 10^{-6}$	$2.59 \cdot 10^{-5}$

Tab. 4.4: Force in CGS units in x , y , z direction on planet at different T_{bin} for different disk masses. The values for y and z direction at $0 T_{\text{bin}}$ is due to numerical noise.

	$0.01M_\odot$	$0.1M_\odot$
$T_{\text{bin}} = 0$ x	$-4.42 \cdot 10^{29}$	$-4.42 \cdot 10^{29}$
y	$2.97 \cdot 10^{16}$	$2.97 \cdot 10^{17}$
z	$-3.57 \cdot 10^{17}$	$-3.57 \cdot 10^{18}$
$T_{\text{bin}} = 17$ x	$-4.44 \cdot 10^{29}$	$-3.86 \cdot 10^{29}$
y	$6.09 \cdot 10^{27}$	$3.32 \cdot 10^{29}$
z	$-2.98 \cdot 10^{19}$	$-1.02 \cdot 10^{20}$
$T_{\text{bin}} = 910$ x	$4.98 \cdot 10^{29}$	$2.00 \cdot 10^{30}$
y	$2.28 \cdot 10^{29}$	$4.07 \cdot 10^{30}$
z	$2.28 \cdot 10^{22}$	$-4.80 \cdot 10^{23}$

The boundary conditions in the singular setup lead to a mass reduction of the disk (see Fig. 4.11). This mass reduction is in the same order as in the single star setup with a default star (see Fig. 4.3).

4.3 The case of binary systems

As a proper and physical singular setup with no default star is established, adding another star in the planet file is the next step. As stated earlier, one needs to define the star parameters in this planet file, e.g., star eccentricity and mass. To analyze and understand the

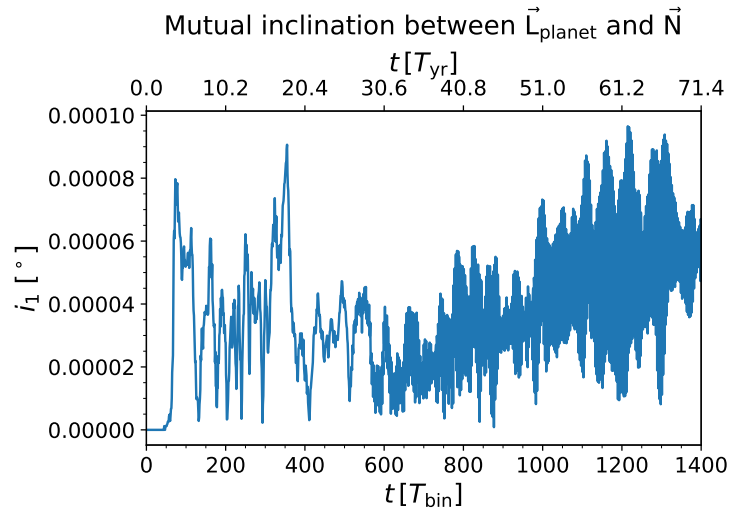


Fig. 4.10: Mutual inclination of the planet's angular momentum vector and the star's angular momentum vector (normal vector) for the single star setup with no default star and a $0.1 M_{\odot}$ disk.

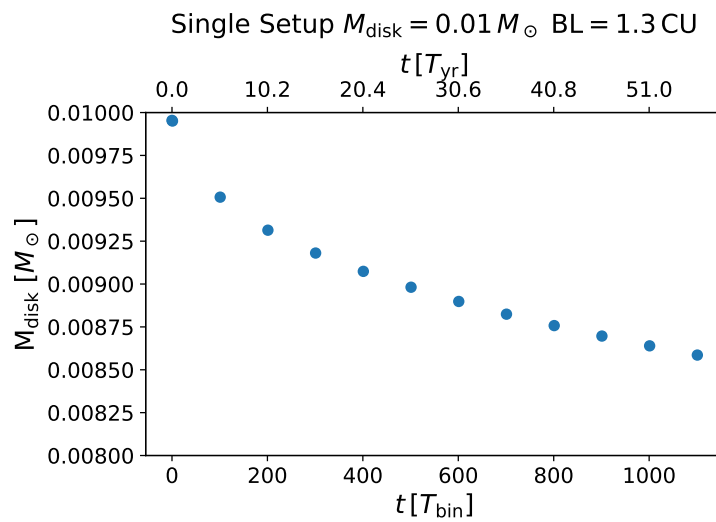


Fig. 4.11: Evolution of the disk mass of the single case with $M_{\text{disk}} = 0.01 M_{\odot}$, no default star and without the Stockholm condition. The mass decreases over time, i.e. it decreases 7.8% over 15.3 years and 13.2% over 51 years.

binary system, Kepler 38 is the primary goal of this thesis.

Different parameters were tested to reach this goal, and the results are displayed in this section. In the following, the section is split by the main parameter. The simulation was run with different parameters with and without the Stockholm condition. As shown in the previous section, this has a significant impact on the disk mass; the results are shown after each other to discuss the impact of the disk mass on all other parameters more closely. Nevertheless, it is clear that the Stockholm condition needs to be turned off for a physical result. This is also advised by the literature, as the inner boundary condition is open (De Val-Borro et al., 2006, p. 533). This is done similarly to the single star setup.

4.3.1 Convergence in resolution

The numerical schemes of the grid code can influence the results because of the dependency of the disk structure on numerical parameters (Thun et al., 2017, p. 17). Thus the grid resolution needs to be tested.

Therefore, the system of Kepler 38 is tested with different resolutions. The results are shown in the Appendix 6.2. As the results of the different resolutions are similar, the resolution with the shortest simulation time is chosen which is $N_x = 256$, $N_y = 512$ and $N_z = 39$.

4.3.2 Simulation with the Stockholm conditions - basic tests

The following simulations were done with an inner boundary location of $1 a_{\text{bin}}$ and an initial disk mass of $0.007 M_{\odot}$ ($\Sigma_{\text{ref}} = 82466 \text{ g/cm}^2$ at $1 a_{\text{bin}}$ or $\Sigma_p = 4791 \text{ g/cm}^2$ at 0.98 AU).

Planet does not feel disk

In the following test simulation, the planet does not feel the influence of the disk. The planet file needs to be changed to simulate this. In all the simulations, the stars are not influenced by the gas gravity. Expectedly, this reduces the simulation to a simple three-body problem in which, after several hundreds of binary revolutions, no variations in the orbital properties of the planet can be observed, i.e., there is no movement in the z direction, planet migration, or change in the planet's eccentricity (see Fig. 4.12).

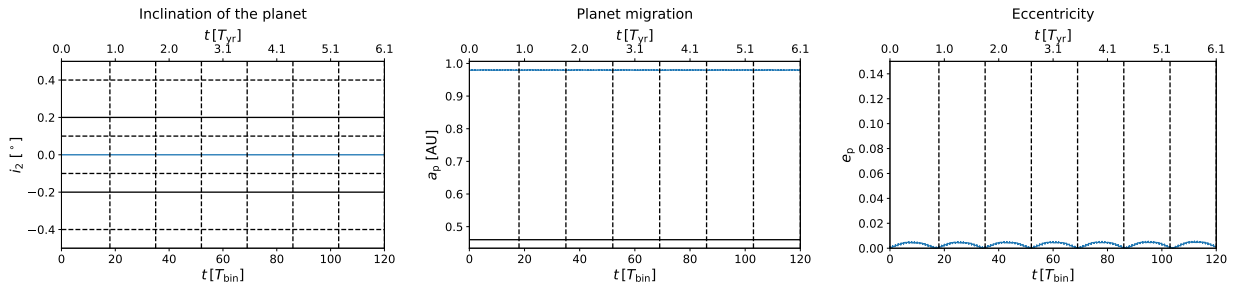


Fig. 4.12: Simulation of a binary system with the Stockholm condition, but the planet does not feel the disk. The figure shows the first $120 T_{\text{bin}}$. The vertical dashed lines show the revolutions of the planet. Left: planet inclination towards the mid-plane. The horizontal lines indicate the inclinations with the disk in later simulations. Middle: planet semi-major axis. Where the horizontal line shows the observed location of the planet. Right: planet eccentricity. On the top axis, time is indicated in Earth years on the lower in binary revolutions.

Pure disk-binary interaction

The planet is removed from the simulation, and it is just run with the binary and the disk to analyze the influence of the binary on the disk in more detail. For analyzing the results, the mid-planes gas surface density was subtracted from each gas surface density value at the same radial distance to highlight the disk's asymmetry. Even without a planet, one can see that the binary is influencing the gas surface density distribution (see Fig. 4.13). This contrasts with the single star system, where there is no asymmetry in the disk (see Appendix. 6.2).

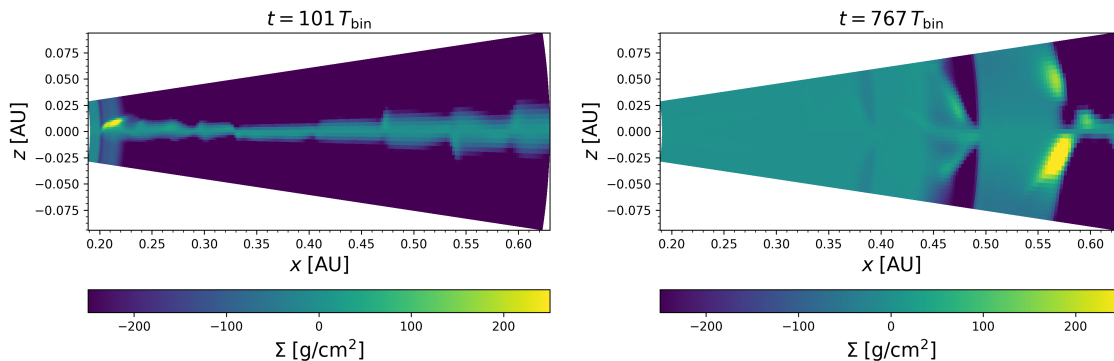


Fig. 4.13: Evolution of the Kepler 38 $0.007 M_{\odot}$ disk without a planet and with the Stockholm condition shown in a two-dimensional surface density plot of the xz plane at (left) 101 and (right) 767 binary revolutions, where the mid-plane is subtracted from each plane in the disk. The figure displays a zoom on the gas on the right side of the disk. The asymmetry in the gas density in the disk is shown even without a planet. The difference in the gas density is linear color-coded. The plot is 0.4×0.1626 AU in size.

Analyzing the gas surface distribution of the disk leads to the conclusion that there is an asymmetry in the disk. Especially interesting is the asymmetry in the xz plane.

Furthermore, the mutual inclination of the angular momentum vector of each disk cell towards the normal vector in the mid-plane is displayed (see Fig. 4.14). This figure shows a turbulent inner region that comes from the influence of the binary onto the disk, which is in contrast to the single star case where there is no turbulence in the disk even though a planet is present (see Fig. 4.5).

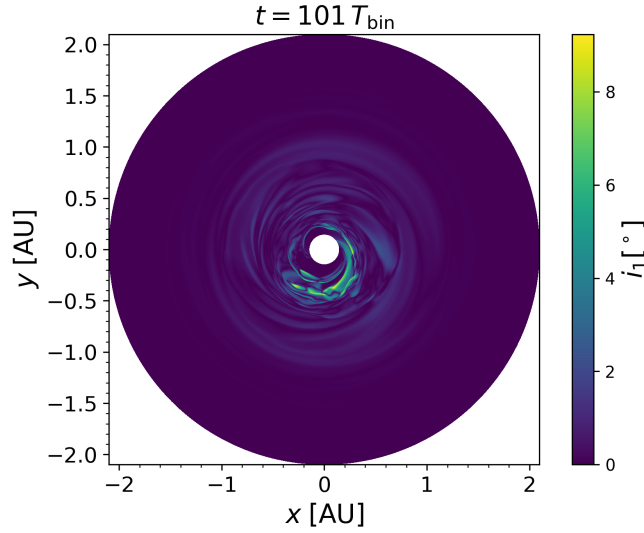


Fig. 4.14: Mutual inclination in degree between the angular momentum of each cell of the disk and the normal vector in the mid-plane. The initial disk mass is $0.007 M_{\odot}$. For this binary star setup without planet the inner boundary is set to $1.0 a_{\text{bin}}$ and the Stockholm condition is used. One can see that the inner region is turbulent.

The mutual inclination between the angular momentum vector of the disk and the angular momentum vector of the binary is calculated for a few T_{bin} and displayed in Tab. 4.5 and Fig 4.15. These show that the mutual inclination of the disk varied over time and was influenced highly by the binary.

Tab. 4.5: Mutual inclination in degree between the normal vector and the angular momentum of the disk at different T_{bin} for $0.007 M_{\odot}$ disk mass. The normal vector is used as the binary has no inclination.

	$0.007 M_{\odot}$
$T_{\text{bin}} = 17$	0.00863
$T_{\text{bin}} = 101$	0.102
$T_{\text{bin}} = 767$	0.0112
$T_{\text{bin}} = 910$	0.00556

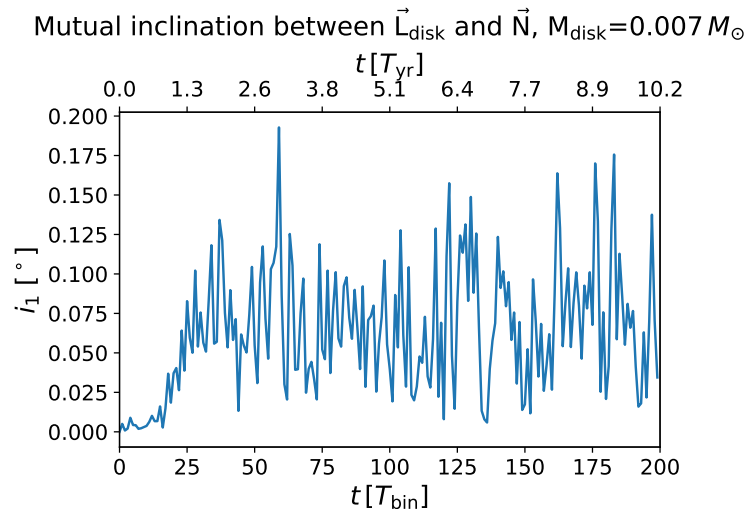


Fig. 4.15: Evolution of the mutual inclination in degree between the angular momentum of the disk and the normal vector in the mid-plane. The initial disk mass is $0.007 M_{\odot}$. For this binary star setup without planet the inner boundary is set to $1.0 a_{\text{bin}}$ and the Stockholm condition is used.

Disk mass

Again, one can calculate the disk mass of the previous simulation over time (see Fig. 4.16). This rising disk mass is due to the dampening of the boundary conditions through the Stockholm condition. In all setups with the Stockholm condition, the dampening leads to no influence of the set boundary conditions; instead, the code runs as if no special boundary conditions were set. This is because the computational domain is too small for that criteria to fulfill its purpose.

The disk with the Stockholm condition is like a slowly accreting star with a vast mass reservoir outside of the computational domain which supplies the inner region.

4.3.3 Simulation with Stockholm conditions - final setup

The same simulations as in the previous section were performed but with a planet to analyze the influence of the disk with its asymmetries on the planet to simulate a system close to the Kepler 38 system.

Structure of disk and disk mass

The Kepler 38 system has been studied through observations and simulations. Kley & Haghighipour (2014) and Thun & Kley (2018) have studied it through two-dimensional hy-

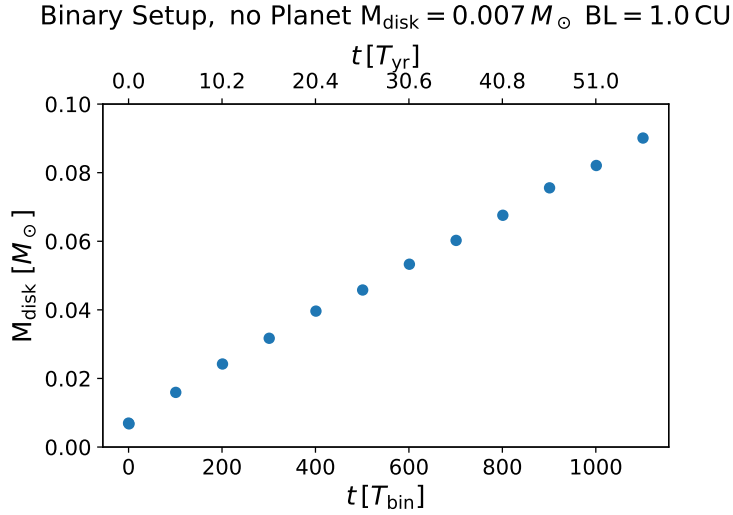


Fig. 4.16: Disk mass over time increases linearly by a factor of up to 10. The Stockholm condition is turned on, the inner boundary is at $1 a_{\text{bin}}$ and no planet is inserted. Thus the setup is the same as in Fig. 4.13

hydrodynamical (HD) simulations. They analyzed the circumbinary exoplanets' properties, focusing on the exoplanet's migration, neglecting 3D constraints.

To compare the 3D simulations with the 2D simulations, not only the surface density of the disk's mid-plane is analyzed (see Fig. 4.17), but also its overall surface density (see Fig. 4.18). Therefore, all surface densities of the xy planes of the 3D simulation were integrated to derive the 2D surface density.

As reported in the previous figures (see Fig. 4.17 and Fig. 4.18), the central binary star rapidly opens a cavity within the first ~ 30 orbital periods. This is in agreement with Artymowicz & Lubow (1994, p. 662). The cavity grows in radius to reach $\sim 2.5 a_{\text{bin}}$ after a few hundred orbital periods. As described in the previous chapter, the f_{gap} function by Pierens & Nelson (2018, p. 2549) to produce an analytically cavity is not implemented, as the cavity forms due to the binary truncations even with the steep surface density profile at the edge of the computational domain. In agreement with Kley & Haghighipour (2014), the precession of the cavity is observed.

The disk mass development over time is not influenced by the planet and keeps rising over time (see Fig. 4.19). This increase is in agreement with the evolution of the surface density (see Fig. 4.20). At $2018 T_{\text{bin}}$ the peak is roughly at 1200000 g/cm^2 . The planet forms no clear dip, which the large surface gas density values with respect to the planet's mass explain. Nevertheless, one can see a clear density drop at the inner edge. Previous studies (Masset &

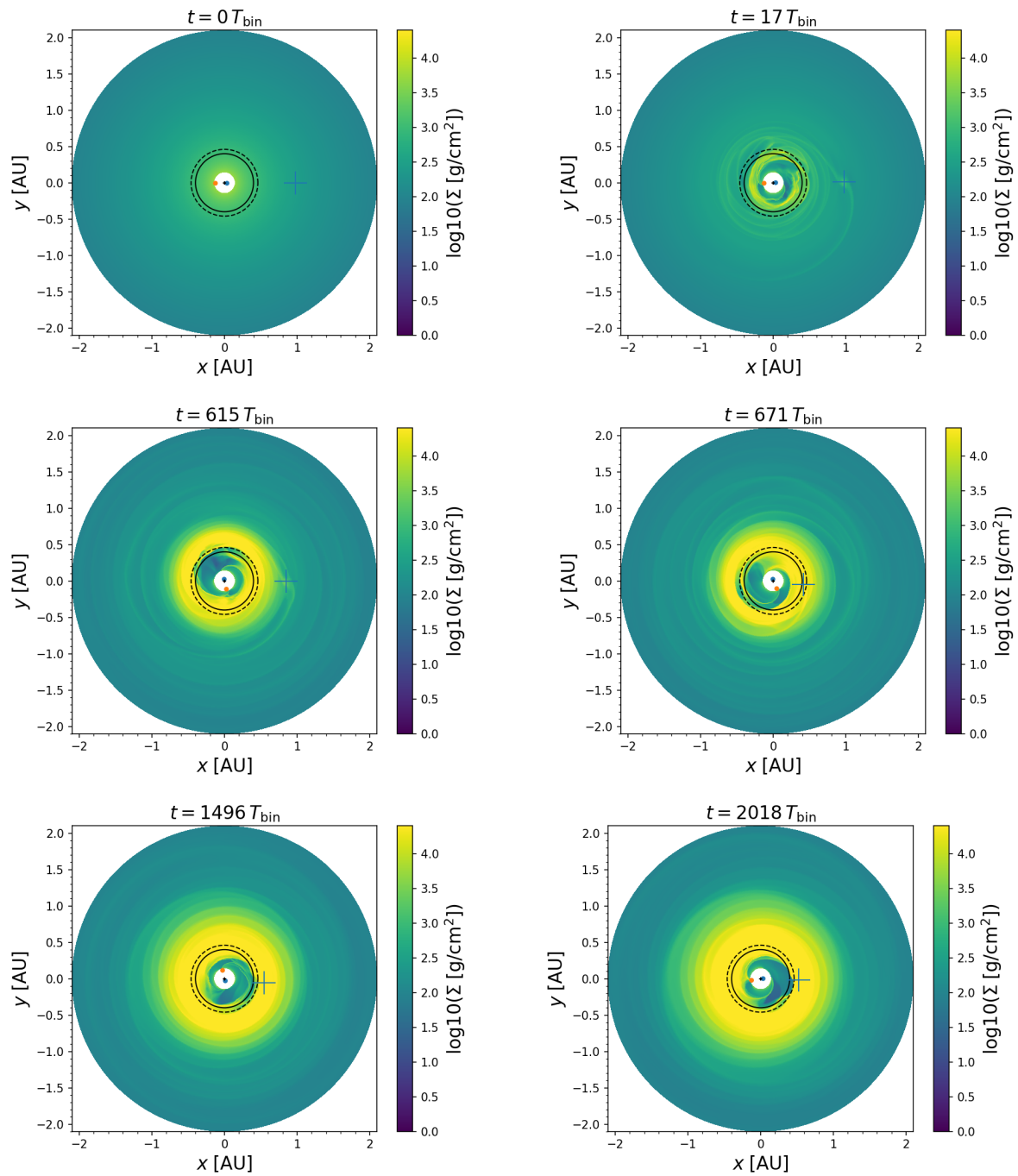


Fig. 4.17: Evolution of the Kepler 38 disk shown in a two-dimensional surface density plot at the mid-plane with an isothermal simulation and a planet (indicated through the cross) migrating from ~ 1 AU to 0.51 AU. The perturbations of the surface density at different times are shown. It is color-coded with the logarithm of the gas surface density at the mid-plane. The white areas are outside of the computational domain. Thus, the binary revolutions are not included in the simulation. The black circle at 0.4 AU is the stability radius for Kepler 38. The dotted line is the observed orbit of Kepler 38 at 0.46 AU. The plots are 4.2×4.2 AU in size. On top of each figure, time is indicated as a multiple of the orbital period ($0 T_{\text{bin}}$, $17 T_{\text{bin}}$, $615 T_{\text{bin}}$, $671 T_{\text{bin}}$, $1496 T_{\text{bin}}$ and $2018 T_{\text{bin}}$).

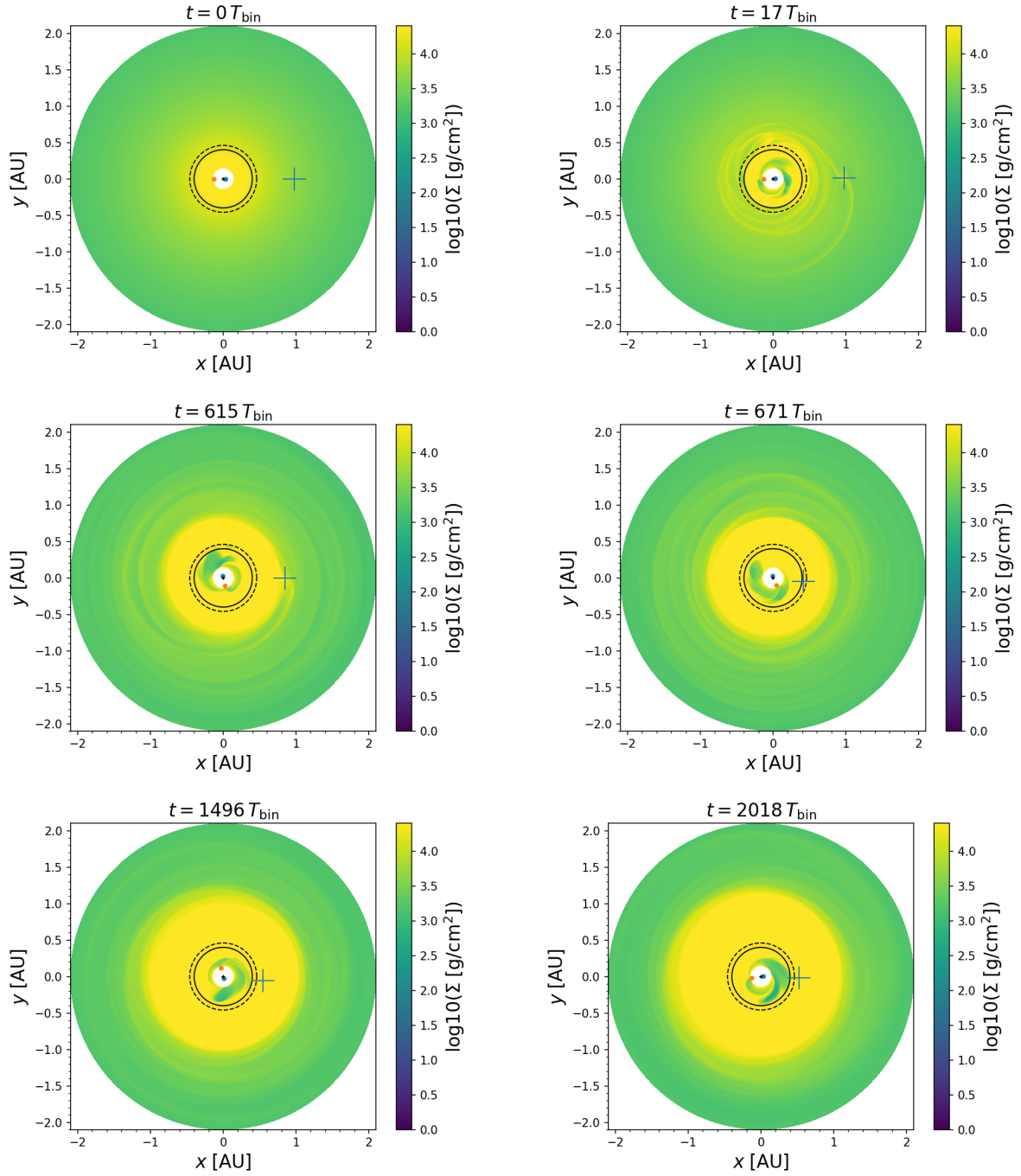


Fig. 4.18: Evolution of the Kepler 38 disk shown in a two-dimensional xy plane plot of the surface density with an isothermal simulation and a planet (indicated through cross) migrating from ~ 1 AU to 0.51 AU. It is the same setup as Fig. 4.17 but now showing the surface density of each plane integrated over the disk height. However, the perturbations of the surface density at different times are shown. It is color-coded with the logarithm of the gas surface density. The white areas are outside of the computational domain. Thus, the binary revolutions are not included in the simulation. The plots are 4.2×4.2 AU in size. On top of each figure, time is indicated as a multiple of the orbital period ($0 T_{\text{bin}}$, $17 T_{\text{bin}}$, $615 T_{\text{bin}}$, $671 T_{\text{bin}}$, $1496 T_{\text{bin}}$ and $2018 T_{\text{bin}}$).

Benítez-Llambay, 2016, p. 485; Thun et al., 2017, p. 15; Pierens & Nelson, 2018, pp. 2552-2553; Pierens et al., 2020, pp. 2866) showed that this prevents the migration of the planet further in. Another factor that influences the migration process is the mass of the disk. As the disk mass is analytically derived from the surface density of the disk, the density of the disk or mass of the disk is highly influencing the migration process (see Fig. 4.21) because the migration speed is proportional to the disk mass (Thun & Kley, 2018, p. 11). However, the stopping location is the same. The planet stops outside of the cavity. The migration is further discussed in the last paragraph of Sec. 4.3.3.

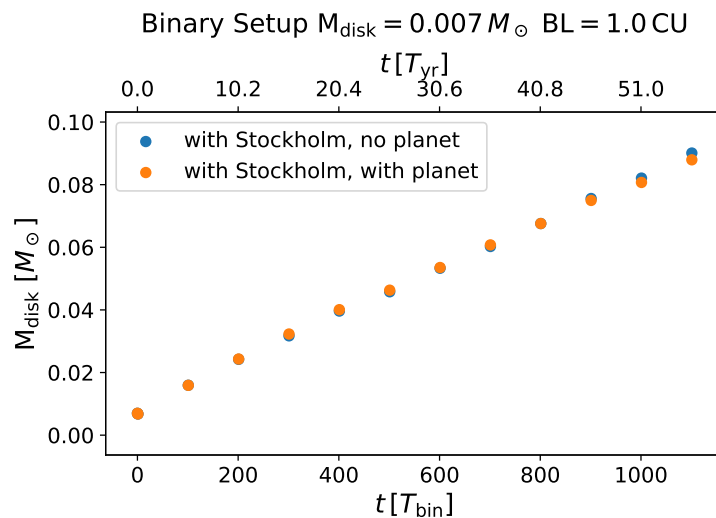


Fig. 4.19: Disk mass over time. The Stockholm condition is turned on; the inner boundary is at $1 a_{\text{bin}}$. The blue dots show the simulation with no planet (comparable with Fig. 4.16), and the orange dots show the simulation with a planet inserted. The difference in increase is 0.6% between the simulation with the planet and without planet after 40.8 years. This is the turning point where the disk in the simulation with no planet becomes more massive than the disk in the simulation without the planet.

Inclination of the planets orbit

The disk/planet/binary system is initially co-planar. Thus, angular momentum transfer has to occur to change the planet’s orbital properties. Turbulence in the disk is expected to play a role and is investigated further. FARGO3D enables to explore the evolution of the vertical gas density.

In this simulation (see Fig. 4.22), the planet, which is initially co-planar with the binary star orbit, shows a non-zero inclination starting at $\sim 50 T_{\text{bin}}$ that steadily increases over the first $120 T_{\text{bin}}$ to $i_2 = 0.08^\circ$ (middle plot). The inclination i_2 is simply calculated with the arctangent of the z coordinate divided by the distance to the center of mass ($\sqrt{x^2 + y^2}$).

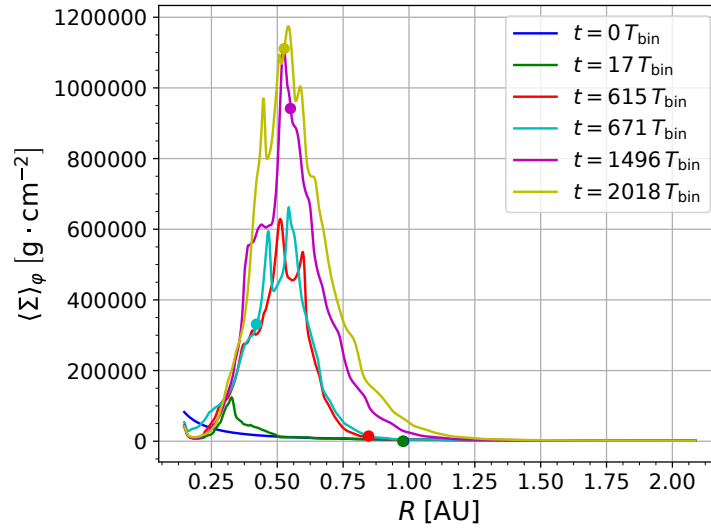


Fig. 4.20: Evolution of Kepler 38 disk shown in an azimuthally-averaged plot of the surface density and a planet migrating from ~ 1 AU to 0.51 AU. It is the same setup as Fig. 4.17. The points indicate the location of the planet on the x-axis, not on the y-axis as they are manually placed on the density curve. In the legend, time is indicated as a multiple of the orbital period ($0 T_{bin}$, $17 T_{bin}$, $615 T_{bin}$, $671 T_{bin}$, $1496 T_{bin}$ and $2018 T_{bin}$).

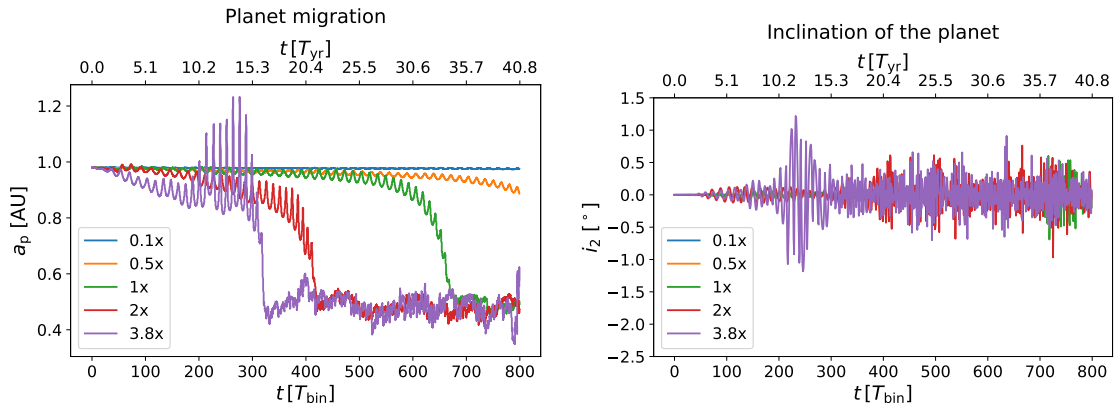


Fig. 4.21: Evolution of the Kepler 38 with different densities of the disk indicated as multiples of the standard surface density used in the setup. The mass of the planet and all the other parameters are kept the same. Left: the semi-major axis of the planet at different densities as a multiple of the original setting. The stopping location of the planet is independent of the density of the disk, but the speed is. Right: the inclination of the planet in in degree for the different densities.

The plots visually analyzed show that a large amount of inclinations stay between 0.2° and $\sim 0.4^\circ$ over $5500 T_{\text{bin}}$ and are synchronized with the planet’s revolutions. The alterations of the planet’s inclination are in the range of the observed inclination of the planet in the Kepler 38 system (see Tab. 3.1). A comparison with the inclination of the single star system with the Stockholm condition shows the inclination towards the mid-plane is zero over $1400 T_{\text{bin}}$ (see Appendix 6.2). This result already points at the critical influence of the binarity on the induced planet misalignment, even for the case of initial co-planarity. In this thesis the notion of “plane-symmetry” is used to describe the level of symmetry/asymmetry of the gas distribution with respect to the mid-plane of the disk at $z = 0$.

In Fig. 4.23 one can observe, on top of an overall plane-symmetric distribution, clear asymmetries in the disk gas density within 0.25 AU of the migration planet, due to the binary, planet, and spiral arms. This figure shows the xz plane at the location of the planet of the surface density. They are at the same points in time as in Fig. 4.17, where the xy plane is shown. To highlight the non-axisymmetric gas surface distribution with respect to the mid-plane, Fig. 4.24 is displayed. The value of the mid-plane’s surface density ($\Phi = 0$) was subtracted from the value of the gas surface density at each plane. In the figure the most pronounced asymmetry is well visible for $17 T_{\text{bin}}$ at ~ 0.5 AU, for $615 T_{\text{bin}}$ at ~ 0.6 AU, for $671 T_{\text{bin}}$ at ~ 0.25 AU, for $1496 T_{\text{bin}}$ at ~ 0.35 AU and for $2018 T_{\text{bin}}$ at ~ 0.4 AU. Such overdensities are a factor of more than 250 in excess of the mid-plane density. If one compares the axis symmetries with the simulation without the planet in Fig. 4.13, one can see that the planet has a significant impact on the density clusters. In the numerical experiments with the planet those clusters are larger compared to the simulations without the planet. To analyze the influence of these disk asymmetries, the gravitational forces exerted on the planet are calculated, as the planet feels the gravitation of the disk (Kley & Haghighipour, 2014, p. 3).

That gravitational pull can be calculated by the force in the z direction for different points in time. Similar to the single star setup case (see Eq. 4.3), but with the binary force included.

The final equation for the force of the binaries is:

$$\begin{aligned} \mathbf{F}_{\text{bin}} = & G \frac{M_{\text{primary}} m_{\text{planet}}}{d_{\text{primary_planet}}^3} \mathbf{d}_{\text{primary_planet}} \\ & + G \frac{M_{\text{secondary}} m_{\text{planet}}}{d_{\text{secondary_planet}}^3} \mathbf{d}_{\text{secondary_planet}} \end{aligned} \quad (4.5)$$

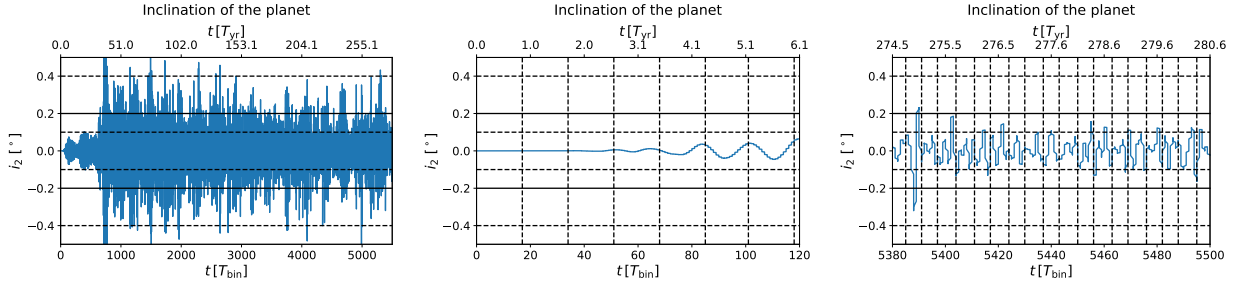


Fig. 4.22: The plot shows the inclination of the planet with respect to the mid-plane. The stars are not shown, as they do not incline. The left plot shows the evolution of the inclination over 5500 binary revolutions (280.6 Earth years). The solid lines show the observed inclination of 0.2° and -0.2° (axis-symmetric) in the Kepler 38 system. The area between the dashed horizontal lines shows where most of the inclinations lie (the lower area shows the axis-symmetry area). Those areas expand from 0.05 to 0.4 and from -0.05 to -0.4. The dashed black lines in the middle and right figure show the time the planet needs for a revolution. The middle plot shows the first 120 orbits, and the right plot shows the last 120 orbits until the end of the simulation.

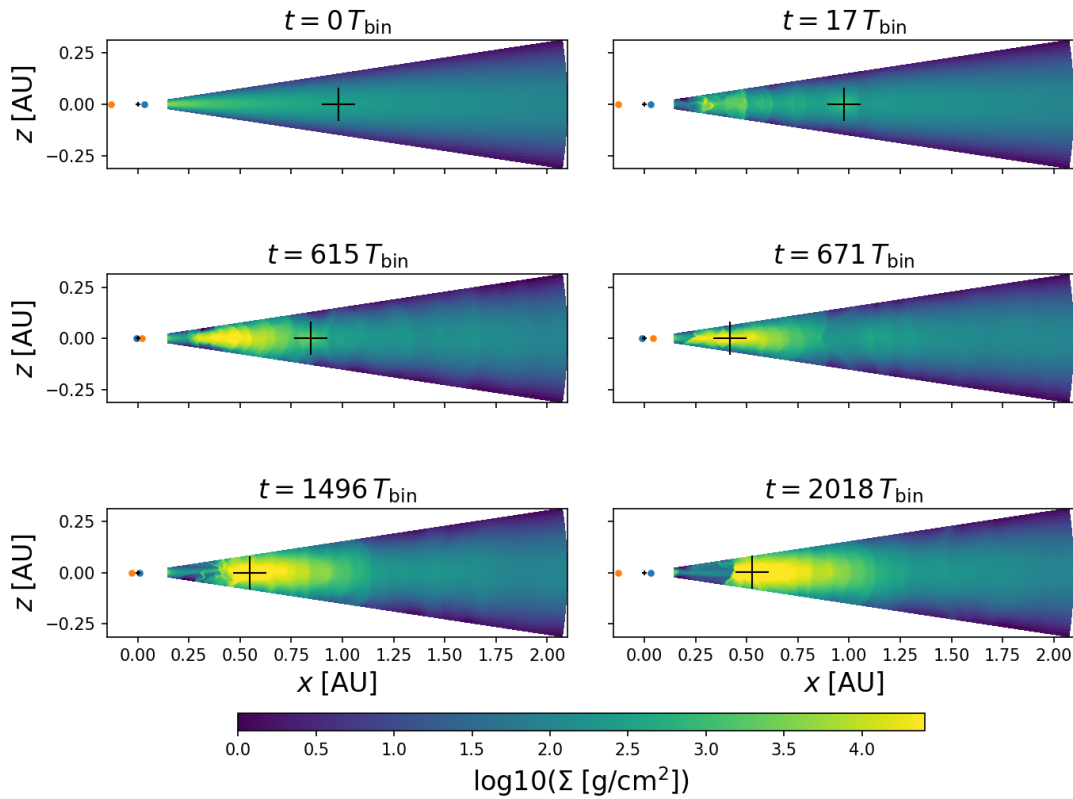


Fig. 4.23: Evolution of the Kepler 38 disk shown in a two-dimensional surface density plot of the xz plane with an isothermal simulation at the same points in time as Fig. 4.17. The black marker shows the location of the planet. The white area is outside of the computational domain. The plots are 2.25×0.63 AU in size and in CGS units. The logarithm of the gas surface density is color-coded, and the time is indicated on top of each figure.

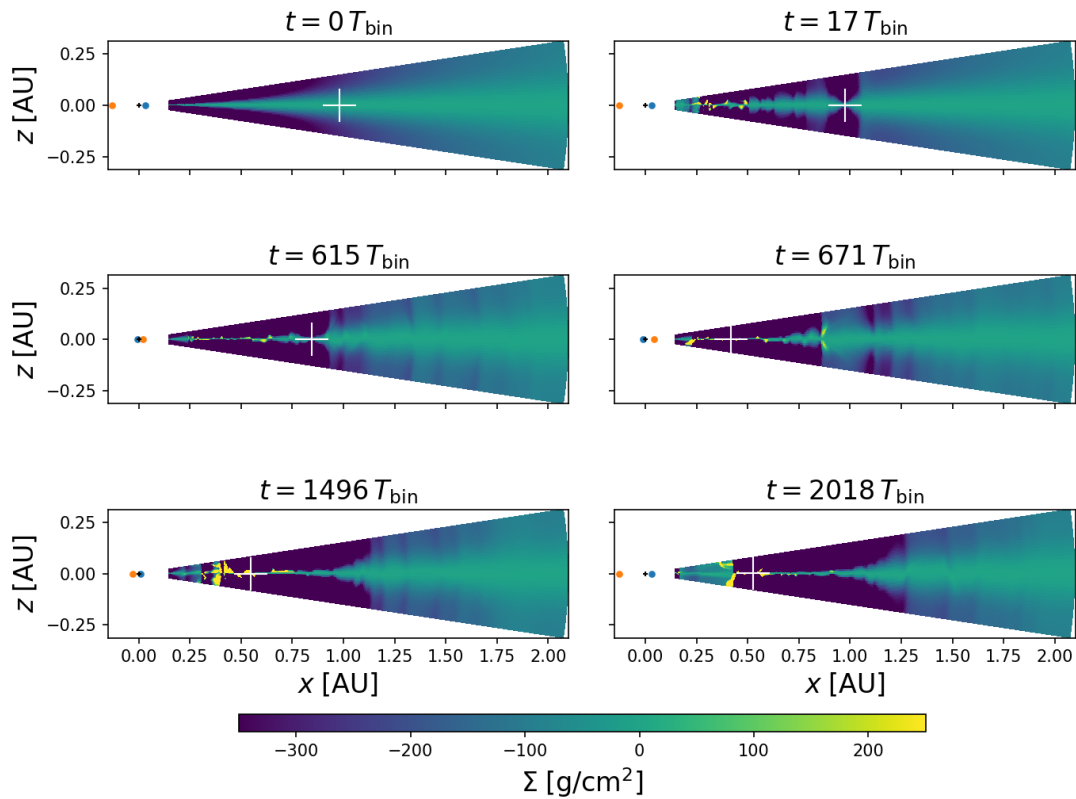


Fig. 4.24: Evolution of the Kepler 38 density shown in a two-dimensional plot of the xz plane, where the surface density of the mid-plane is subtracted from the surface density of each plane in the disk. It is the same setup as in Fig. 4.23. The asymmetry in the gas surface density in the disk shows the gravitational influence on the planet. The planet is marked with a white cross. The gas density is linear color-coded. The plots are 2.25×0.63 AU in size. On top of each figure, time is indicated as a multiple of the binary's orbital period.

The way of how the force of every cell acting on the planet (\mathbf{F}_{disk}) is calculated stays the same as in the single star system. Thus Eq. 4.4 stays the same.

The evolution of the force in z direction is displayed in Fig. 4.26. This is hard to compare with the singular case as the mass rises differently over time (see Fig. 4.25). At $T_{\text{bin}} = 0$, when one analyzes further and compares the force on the planet from the disk for the single case $(-2.64 \cdot 10^{18}, 2.20 \cdot 10^{16}, -2.64 \cdot 10^{17})$ in CGS units and for the binary case $(-2.64 \cdot 10^{18}, 2.20 \cdot 10^{26}, -2.64 \cdot 10^{17})$ in CGS units in the x and y direction, then one sees they are the same. This is the starting disk which should be as homogeneous as possible. Hence, the numerical noise in z direction is in the order of a few times 10^{17} in CGS units. However, as the force on the planet is higher in later parts of the simulation, a mass-force relation can be seen. Moreover, one can see that the force coming from the binary dominates the force in z direction. In order to induce a tilt of the planet's orbit with respect to the binary orbit, a force component in the vertical z direction needs to act on the planet. Beside the gravitational forces from the disk and the binary, the planet is subject to the hydrodynamic forces due to the viscous disk.

From the computed velocity of the constant mass planet companion and the resulting linear momentum \mathbf{p} , the total resulting force on the planet is calculated through:

$$\mathbf{F}_{\text{tot}} = d\mathbf{p}/dt \quad (4.6)$$

using a temporal resolution $\Delta T = 1 T_{\text{bin}}$.

The hydrodynamic force action on the plane is obtained as

$$\mathbf{F}_{\text{hd}} = \mathbf{F}_{\text{tot}} - \mathbf{F}_{\text{bin}} - \mathbf{F}_{\text{disk}} \quad (4.7)$$

These same equations are used accordingly for the single star setup. In the following the vertical component F_z of these forces is treated.

In this simulation with the Stockholm condition and an initial disk mass of $0.007 M_{\odot}$, the comparison between the single star and binary star setup in Fig. 4.27 (right plot) indicates that the planet becomes rapidly (at $\sim 10 T_{\text{bin}}$) subject to the pull of $F_{\text{tot},z}$, which amplitude starts oscillating from $\sim 50 T_{\text{bin}}$ with the planetary period of $\sim 17 T_{\text{bin}}$. This results from the planet with its increasingly inclined orbital plane periodically crossing the binary star orbital plane. Comparatively, the pull in F_z in the single star case remains negligibly. The gravitational force contribution of the binary star $F_{\text{bin},z}$ and the total force magnitude change

the domination of the vertical component F_z , as this is visible in Fig. 4.27 (left plot). Thus, in the early phases, i.e., within the first $10 T_{\text{bin}}$ of the system evolution, it is visible that the hydrodynamic force causes the original misalignment of the planet with respect to the binary.

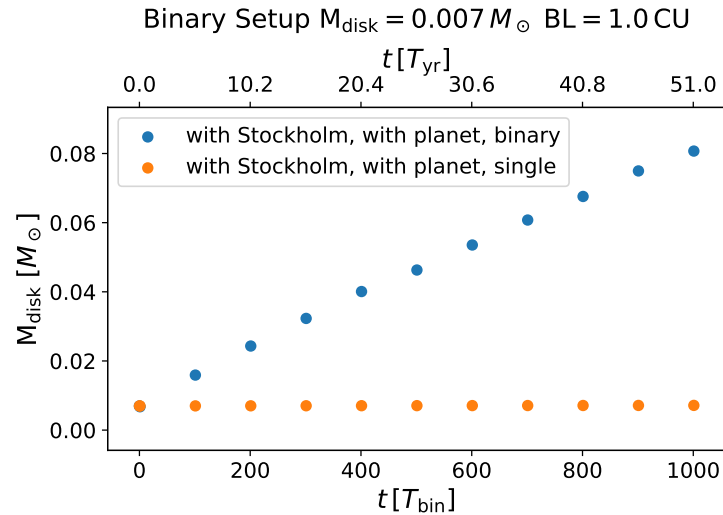


Fig. 4.25: The mass of the binary disk rises much more rapidly as the mass in the singular disk. In the singular case the mass increase is 1.98% over 40.8 years and in the binary case the mass increase is 868%.

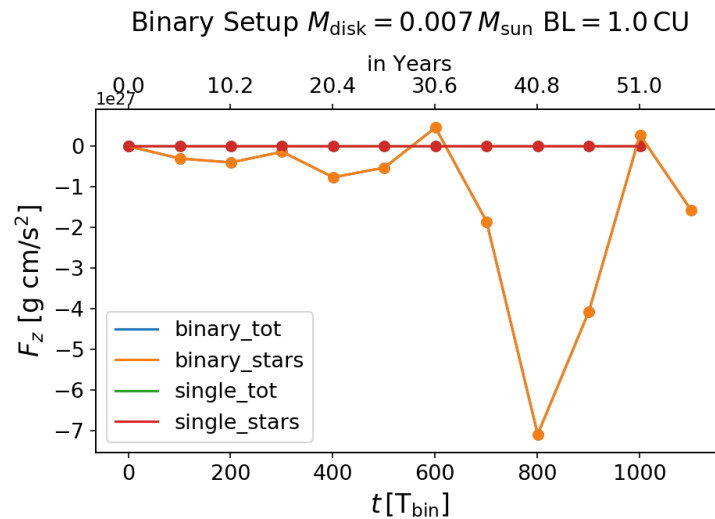


Fig. 4.26: Evolution of the force on the planet in a $0.007 M_{\odot}$ system in z direction. Thus the sign shows the direction of the force. The blue and orange dots/lines signal the binary simulation running up to $1300 T_{\text{bin}}$ and the green/red dots signal the single case simulation up to $1000 T_{\text{bin}}$. One can see, later in the simulation of the binary case the force on the planet is much higher compared to the single case. Moreover, one can see that the stars dominate of the force in z direction.

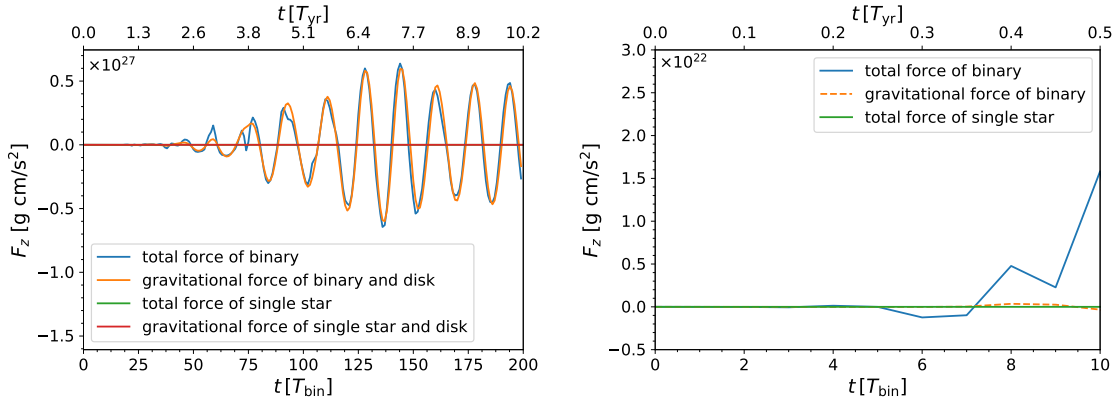


Fig. 4.27: Evolution of the force on the planet in a $0.007 M_{\odot}$ disk mass system in z-direction. Thus the negative sign shows the direction of the force. The gravitational force of the stars and disk in the z-direction starts later than the force calculated from the impulse of the planet.

Angular momentum of the disk and planet

To analyse the angular momentum transfer the angular momentum of the disk and the planet are investigated and compared to the angular offset from the binary orbital plane analysed earlier in this section.

To be able to compare the single star setup with the binary setup and the different binary setup with each other, the mutual inclination of angular momentum vector of each cell of the mid-plane of the disk and the normal vector is displayed (see Fig. 4.28). The inner region is similarly disturbed as in the setup without a planet (see Fig. 4.14). The mutual inclination between the angular momentum vector of the disk and the angular momentum vector of the binary is written in Tab. 4.6 (left table). If one compares those values to the values of the single star setup (right table), one can see that the values in the binary setup are significantly higher.

Tab. 4.6: Mutual inclination in degree between the normal vector and the angular momentum of the disk at different T_{bin} for $0.007 M_{\odot}$ disk mass. The normal vector is used as the binary has no inclination. The left table shows the results for the binary case and the right table for the single case.

binary	$0.007 M_{\odot}$	single	$0.007 M_{\odot}$
$T_{\text{bin}} = 17$	0.00118	$T_{\text{bin}} = 17$	0.0000622
$T_{\text{bin}} = 101$	0.0916	$T_{\text{bin}} = 101$	0.0000368
$T_{\text{bin}} = 767$	0.0630	$T_{\text{bin}} = 767$	0.0000715
$T_{\text{bin}} = 910$	0.0493	$T_{\text{bin}} = 910$	0.0000708

In a second step, the angular momentum of the planet is analyzed. At $1 T_{\text{bin}}$ the planet's angular momentum vector has a mutual inclination of 0° towards the normal vector (which

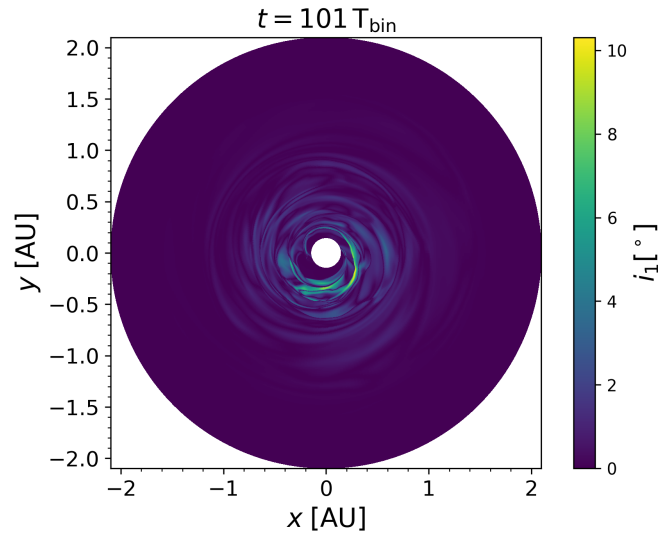


Fig. 4.28: Mutual inclination in degree between the angular momentum of each cell of the disk and the normal vector in the mid-plane. The initial disk mass $0.007 M_{\odot}$. For this binary star setup with the planet, the inner boundary is set to $1.0 a_{\text{bin}}$, and the Stockholm condition is used. One can see that the inner region is turbulent. At the location of the planet at ca. 0.98 AU , the disk is not inclined. The disk looks very similar to the Fig. 4.14.

is the same as $\mathbf{L}_{\text{second}}$ and $\mathbf{L}_{\text{primary}}$) in z direction, whereas the planet's angular momentum vector has a mutual inclination of 0.04° towards the normal vector at $101 T_{\text{bin}}$, for more results see Tab. 4.7 and Fig. 4.29. The binary values are compared with the single star values in the table, in the single star setup all values show a mutual inclination of 0° . Thus in the single star simulation, where the second star is removed, and everything else is kept the same, the planet is aligned with the star in the mid-plane of the simulation grid. This is expected as the results are comparable to the results shown earlier when analysing the angular offset towards the mid-plane. Again, this result points at the critical influence of the binarity on the induced planet misalignment even for the case of initial coplanarity. Thus the inclination of the planets' orbit is induced by the binary. Towards the end of the single star simulation, a small angle is 0.0000012° seen, which is so small that it is in the noise regime. The mutual inclination in the binary setup derived from the angular momentum vector of the planet and the normal vector can be compared with the inclination towards the mid-plane derived from the planets' orbit parameter in Fig. 4.22

Noise of simulation

The same setup was run 3x with precisely the same setup. This simulation shows that the simulations are quite similar (see Fig. 4.30). Thus the numerical noise, which is in z direction roughly 0.1° is smaller than the inclination of the planet.

Tab. 4.7: Mutual inclination in degree between the normal vector (binary angular momentum) and the angular momentum of the planet at different T_{bin} for $0.007 M_{\odot}$ disk mass. The left table shows the results for the binary case and the right table for the single case.

binary	$0.007 M_{\odot}$	single	$0.007 M_{\odot}$
$T_{\text{bin}} = 17$	0.000075	$T_{\text{bin}} = 17$	0.0
$T_{\text{bin}} = 101$	0.041	$T_{\text{bin}} = 101$	0.0
$T_{\text{bin}} = 767$	0.81	$T_{\text{bin}} = 767$	0.0
$T_{\text{bin}} = 910$	0.35	$T_{\text{bin}} = 910$	0.0

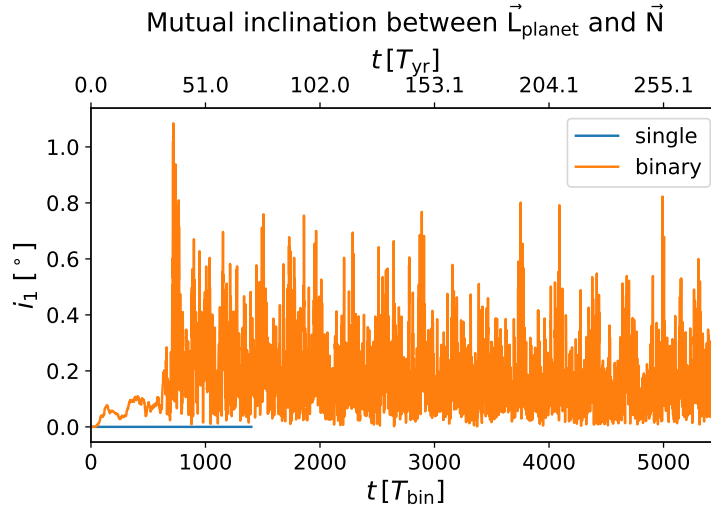


Fig. 4.29: Mutual inclination in degree of the angular momentum vector of the planet towards the normal vector in z direction/ $\mathbf{L}_{\text{binary}}$. The initial mass of the disk is $0.007 M_{\odot}$ and the star eccentricity is 0.1. The single star setup (blue) is compared to the binary case setup (orange)

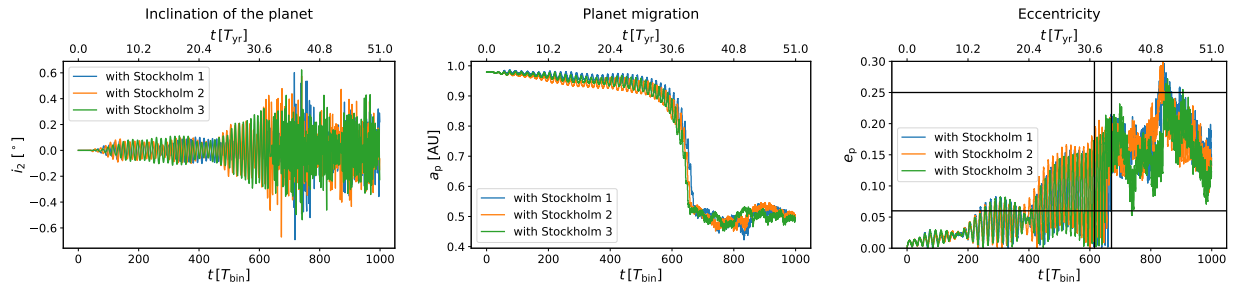


Fig. 4.30: Simulation of setup run several times nothing on the setup was changed. Left: planet inclination. Middle: planet semi-major axis. Right: planet eccentricity.

Migration

The evolution of the planet through the disk is shown in Fig. 4.31. The left plot shows the planet's evolution over 5500 binary revolutions, which are ~ 279 Earth years. The middle and right plots show a zoom on the first 120 binary revolutions and the last 120 binary revolutions. These one-dimensional plots show a slight periodic change of the planet's distance to the center of mass. This movement corresponds to the planet's evolution around the binary star, which the plots with its periodicities show. At the beginning in the simulation the migration is relatively low. In 6.1 Earth years, the migration is just ~ 0.02 AU. The simulation shows that the planet has a period of 17 binary revolutions in the beginning and six binary revolutions towards the end of the simulation that equals 111.6 Earth days, thus $T_p/T_{\text{bin}} \approx 6.0$. During observations, the planet period was determined to be five binary revolutions which equal 105.6 Earth days, thus $T_p/T_{\text{bin}} \approx 5.0$.

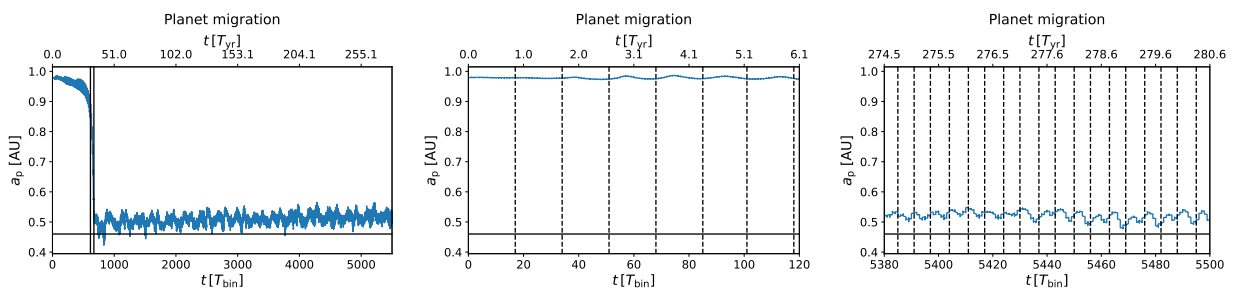


Fig. 4.31: The planets' evolution of the semi-major axis. The left figure shows the evolution of over 5500 binary revolutions (On the top axis, the transformation to Earth years is shown). The horizontal line is the observed planet's location (0.46 AU). The migration happens mostly between 615 and 671 binary revolutions (solid vertical lines). The quasi-equilibrium state is reached roughly after 1500 binary revolutions. Then the planet periodically changes around its final position. The dashed black lines in the middle and right two plot show the time the planet needs for a revolution. The duration of the planet orbits was reduced from 18 binary revolutions (middle plot) to six binary revolutions (right plot) at the end of the simulation. The middle figure shows the evolution in the first 120 binary revolutions (6.1 Earth years), and the right figure shows the last 120 orbits (274.5 to 280.6 Earth years).

To check whether the evolution of the planet in the simulation compares with the third Kepler Law the following equation was solved:

$$\frac{a^3}{T^2} = \frac{G(M + m)}{4\pi^2} \quad (4.8)$$

This lead to an evolution time of

$$\begin{aligned} T &= 2\pi \sqrt{\frac{a^3}{G(M + m)}} = 2\pi \sqrt{\frac{6.6667^3}{1(1 + 0.00025)}} \\ &= 108.14 \text{ CU} \quad | : 2\pi \\ &= 17.21 T_{\text{bin}} \end{aligned} \quad (4.9)$$

Thus the simulation is an excellent fit for the third Kepler Law. The influence of the disk is not visible after the first few revolution.

The migration of the planet stops shortly outside of the inner cavity (see Fig. 4.17). The planet migrates from having a semi-major axis of 0.98 AU to 0.51 AU (min. 0.44 AU) and stop's shortly outside the inner cavity. Moreover, the stopping location is larger than the stability limit (a_c) which is in case of Kepler 38 around 0.4 AU (Kley & Haghighipour, 2014, p. 5; Holman & Wiegert, 1999, p. 626). The inner cavity acts as an inner barrier because of the sudden drop of density as shown in previous studies (Masset et al., 2006, p. 485). That drop is also visible in this simulation (see Fig. 4.20). No clear gap is opened in the disk because the gap opening criterion is not met (Eq. 2.1), which indicates type I migration.

Kley & Haghighipour (2014, p. 7) found in their simulation that the planet migrates to an average value of $a_p = 0.436$ AU. This difference to the value $a_p = 0.51$ AU found in this simulation could be due to the larger inner radius of the computational domain in their simulation. Whereas Thun & Kley (2018, p. 8) found that with the similar inner boundary condition the slightly heavier planet ($0.384 M_{\text{Jup}}$) migrates to 0.597 AU in two-dimensional simulations. So the results found here are well in between the values found in those papers. Thun & Kley (2018, p. 8) showed that the planet's final position is independent of its initial position. They conclude that this is because of the type I migration of the planet. Thus the slightly different starting distance does not influence the outcome. The same is observed in this thesis; the final position does not depend on the starting distance (see Fig. 4.32). Moreover, the stopping location of the migration process is not influenced by the disk mass (see Fig. 4.21 (left plot)), just the migration timescale is influenced. This is addressed further in the next section without the Stockholm condition.

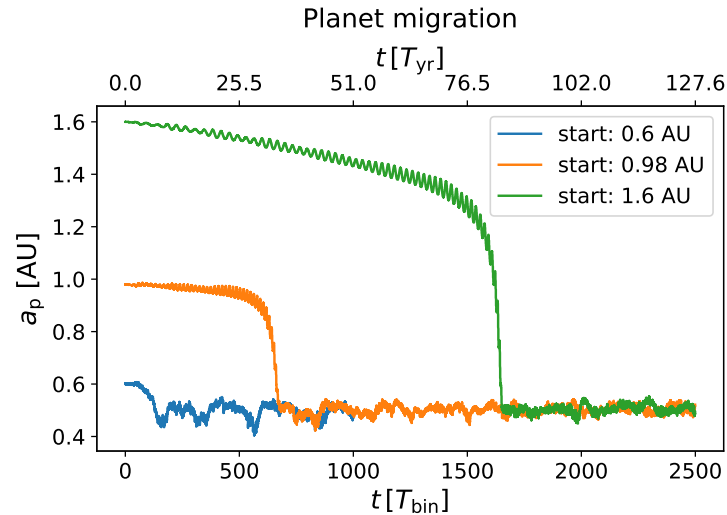


Fig. 4.32: The planet’s evolution of the semi-major axis with different starting positions of the planet (0.6 AU, 0.98 AU and 1.6 AU). It shows that the migration process is independent of the starting point it will reach the same final position.

Fig. 4.33 shows the evolution of the planet’s eccentricity. One can see that the eccentricity of the planet rises with the migration towards the binary. In this simulation, an oscillation of the planet’s eccentricity between ~ 0.06 and 0.25 is found, which is very similar to the findings of Kley & Haghighipour (2014, p. 7). They found a planet oscillation of 0.15 and 0.2. Thun & Kley (2018, p. 9) showed that the eccentricity is dependant on the mass of the planet. With a $0.384 M_{\text{Jup}}$ planet, he gets an eccentricity oscillation of ~ 0.03 . Whereas with a $0.3 M_{\text{Jup}}$ planet he gets an eccentricity oscillating around 0.2.

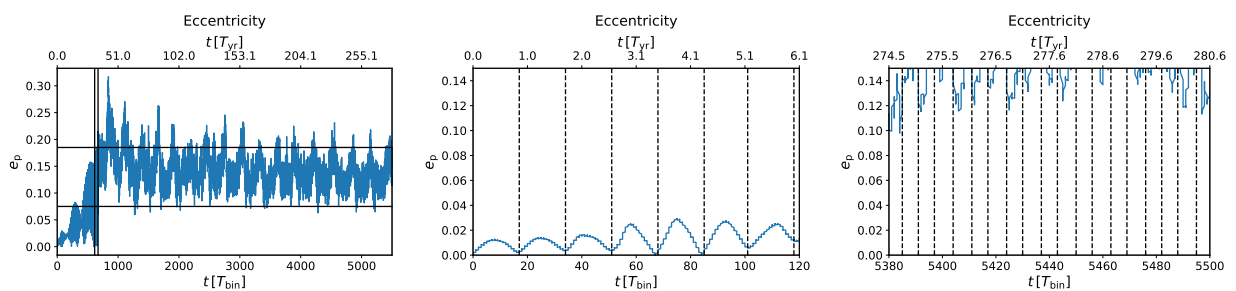


Fig. 4.33: The eccentricity of the planet is plotted against the number of binary revolutions (lower axis)/ Earth years (top axis). The left figure shows the evolution of over 5500 binary revolutions (280.6 Earth years). Between 615 and 671 orbits, there is a big periodic change of eccentricity (vertical solid lines). The horizontal lines display the area of the oscillation (between 0.07 and 0.18). The middle figure shows the evolution in the first 120 binary revolutions, and the right figure the last 120 orbits are shown. The dashed black lines in the middle and right plot show the time the planet needs for a revolution.

4.3.4 Simulation without Stockholm conditions - basic tests

The previous section tested and analyzed the simulation with the Stockholm condition. In this section, the focus is on simulation without Stockholm conditions. This means a mass transfer from the disk onto the star, and no material from the outer disk enters the simulation. Thus, this scenario compares to other studies by other authors.

Thus the disk mass is reduced over time (see Fig. 4.34) where the calculated disk total mass vs. time is plotted. This was already visible in the single star case with the default star (see Fig 4.3). In the case of the binary setup, a rapid exponential decay up to $4000 T_{\text{bin}}$ is observed. Followed by a linear decay with a slope of $\dot{M}_{\text{disk}} = 1.26 \times 10^{-6} M_{\odot}/\text{yr}$. The linear decay results from the choice of a closed outer boundary condition which prevents a replenishing inflow from outside to compensate the outflow at the open inner boundary. The theoretical accretion rate for a steady-state disk is obtained with $\dot{M}_{\text{th}} \equiv 3\pi\Sigma\nu$, which translates into $\dot{M}_{\text{th}} = 5.9 \times 10^{-7} M_{\odot}/\text{yr}$ for an isothermal disk at $T = 300 \text{ K}$.

The decrease over 51 years in the binary (13.17%) and single (13.2%) cases are in the same regime (see Fig. 4.11 and Fig. 4.34). In roughly 500 years the mass decreases by $\sim 25\%$. In comparison the mass in Kley & Haghighipour (2014, p. 4) the mass decreases by $\sim 13\%$ over 500 years. They lose less mass even so their inner boundary ($0.25 a_{\text{bin}}$) is larger than in this thesis ($1.3 a_{\text{bin}}$). However, they simulate the disk in 2D, and here it is done in 3D, which adds vertical space to the inner boundary condition where mass can be accreted.

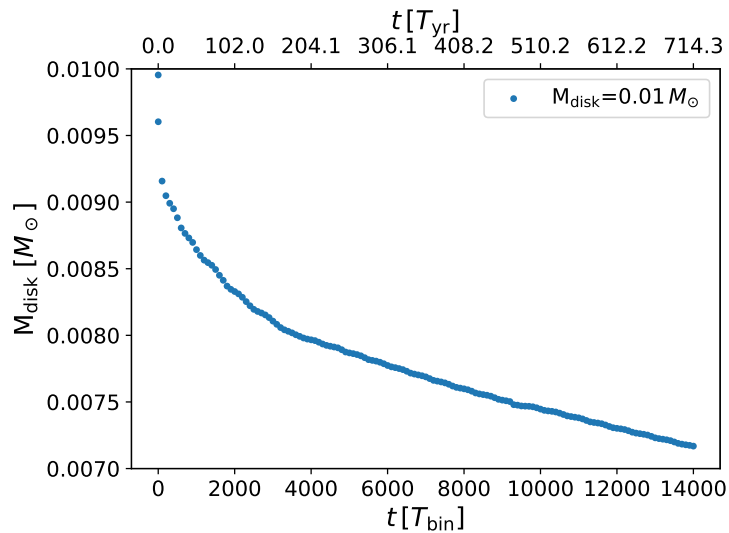


Fig. 4.34: Evolution of the disk mass for the case $M_{\text{disk}} = 0.01 M_{\odot}$, the boundary location is $1.3 a_{\text{bin}}$ and a binary orbit eccentricity of 0.1. The mass decreases over time as the Stockholm condition is turned off, i.e., it decreases 12.29% over 40.8 years, 13.17% over 51 years and about 24.52% over 459 years.

No Planet, just disk, and binary

A closer look is taken on just the disk for the setup without the Stockholm condition. If one compares the disk with the previous setup, one can see that the asymmetry in this setup is smaller, see Fig. 4.35. This is expectable, as the disk mass is significantly smaller than in the previous setup.

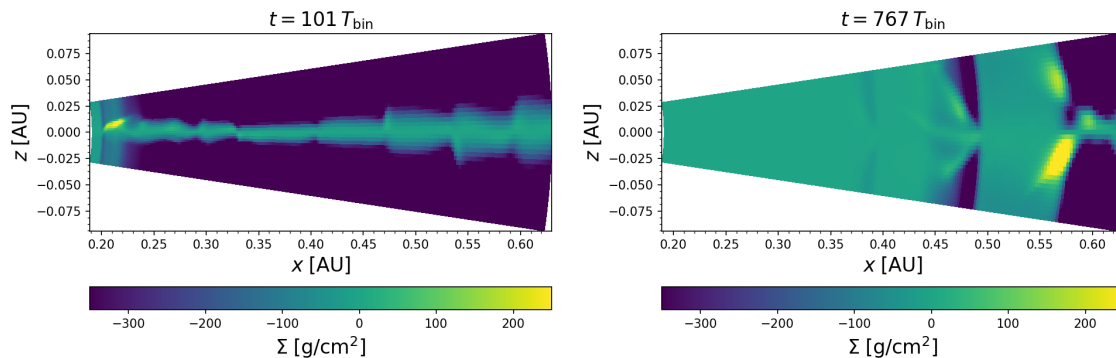


Fig. 4.35: Simulation with no planet and without the Stockholm condition with a zoom on the inner disk. The evolution of the surface density is shown in a two-dimensional plot of the xz -plane, where the mid-plane is subtracted from each plane in the disk. The asymmetry in the disk is smaller than in the setup with the Stockholm condition (see Fig. 4.13). In the beginning, the disk mass is $0.01 M_{\odot}$, the binary has an eccentricity of 0.1, and the boundary location is $1.3 a_{\text{bin}}$.

Influence of different inner boundary location

In these simulations, the influence of the binary parameter on the planet's parameter is a focus. Thus different binary orbit eccentricities are simulated. For this purpose, a bigger inner boundary is needed as the secondary is entering the mesh with the 0.5 binary eccentricity when the inner boundary stays at $1 a_{\text{bin}}$. This induces an acceleration on the fluid and the time step goes to zero and the simulation is not possible.

Thus the inner boundary is moved from $1 a_{\text{bin}}$ to $1.3 a_{\text{bin}}$ for the planet parameter evolution (see Fig. 4.36). The movement of the planet is similar in both simulations. However, a wider inner boundary location reduces the inclination of the planet. Thun et al. (2017, p. 7-8) found that the inner boundary condition does not influence the results of the simulation significantly as long the 3:1 Lindblad resonance ($R_{3:1} \approx 0.28 \text{ AU}$) is inside the computational domain. Nevertheless, he states that the surface density profile is influenced as less material can leave the domain with a smaller inner boundary. This can be shown, here as well, through the evolution of the disk mass over time (see Fig. 4.37). Nevertheless, he concludes that it is enough to be in the order of a_{bin} , but for compromises, in long-term simulations,

he also uses a $1.3 a_{\text{bin}}$ inner boundary location as a smaller inner radius is more time-intensive.

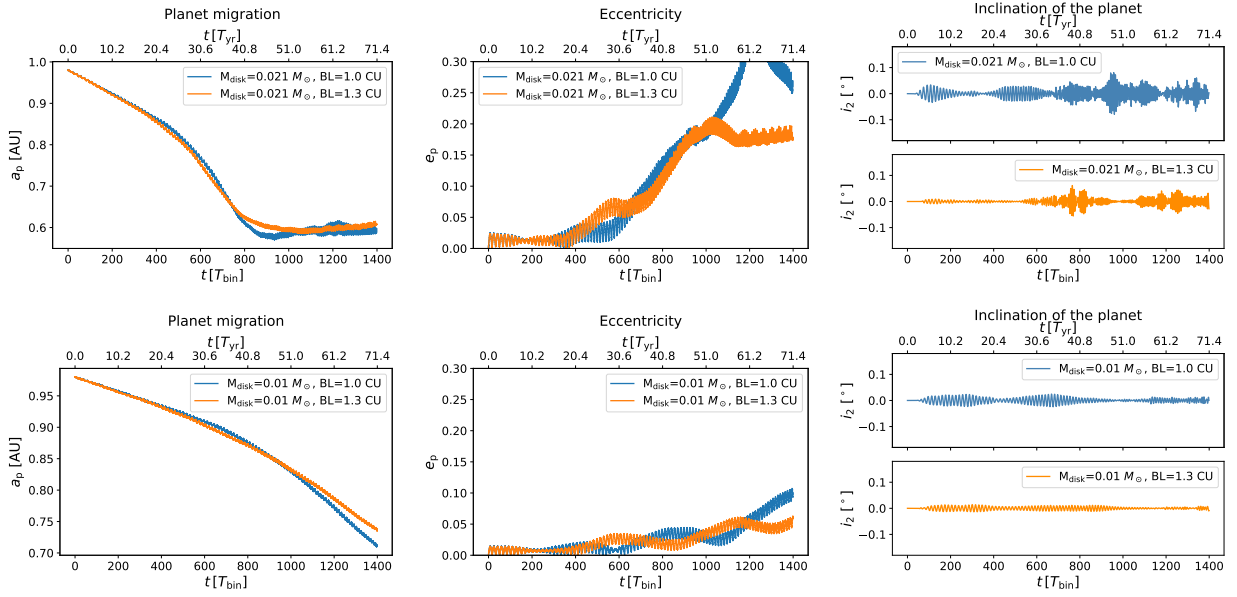


Fig. 4.36: Movement of the planet with different boundary locations. (top) The starting disk mass was $0.021 M_{\odot}$. (bottom) The starting disk mass was $0.01 M_{\odot}$.

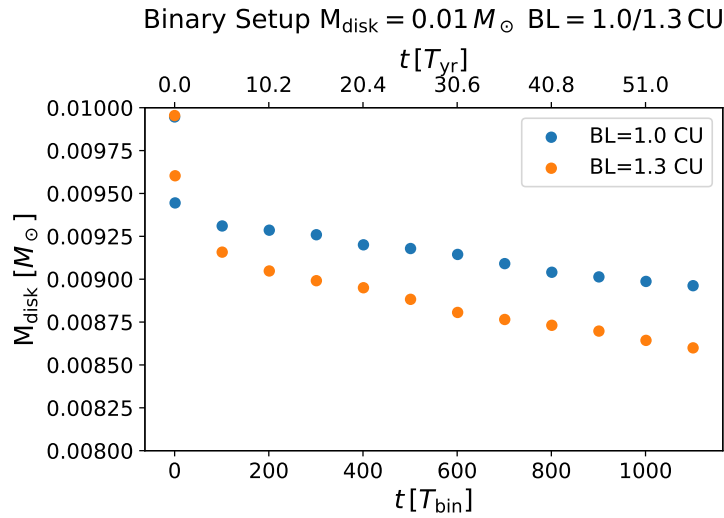


Fig. 4.37: Evolution of the disk mass. The starting disk mass was $0.01 M_{\odot}$. One can see that the simulation with the greater inner boundary loses more mass (13.17% over 51 years) than the simulation with a closer inner boundary location (9.64% over 51 years).

Nevertheless, it is important to keep in mind that the larger inner boundary influences the size of the cavity (see Fig. 4.38). One can see that the cavity of the larger inner boundary ($1.3 a_{\text{bin}}$) is slightly larger than the other simulation ($1.0 a_{\text{bin}}$).

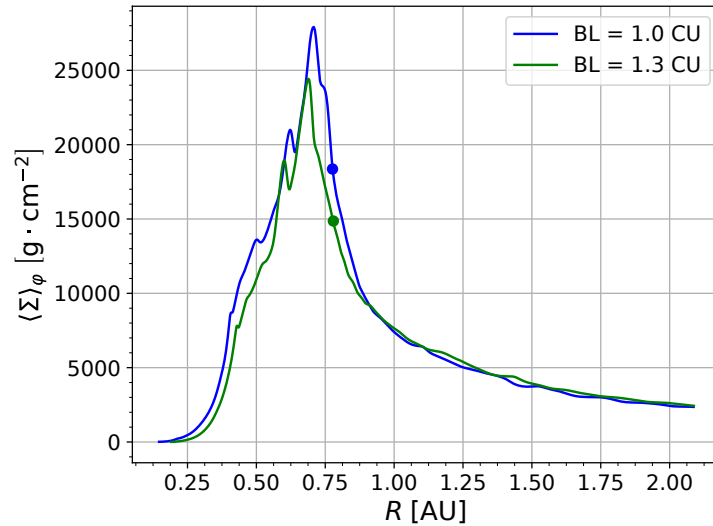


Fig. 4.38: The Kepler 38 $0.01 M_\odot$ disk shown in an azimuthally-averaged plot of the surface density without the Stockholm condition. One time, the simulation with the boundary location at 1.0 CU is displayed, and the other time the boundary location is at 1.3 CU. The blue/green point indicates the planet’s location on the x-axis, not on the y-axis. The time is $1200 T_{\text{bin}}$ in both simulations.

Influence of viscosity

The viscosity of the simulation also influences the simulations. Thun et al. (2017, p. 14) showed that with higher viscosities, the cavity size is reduced. This influences the stopping location of the planet. He explains that a larger viscosity leads to an increase of the disk’s viscous spreading, which counteracts the gravitational torques of the binary. Those torques are responsible for the cavity creation.

To verify his finding is not part of this thesis. Nevertheless, though a quick check at $t = 1200 T_{\text{bin}}$ it could be confirmed that a higher viscosity leads to a smaller cavity (see Fig. 4.39). However, one can see that with the lower viscosity, the inclination of the planet increases (see Fig. 4.40) as the torques of the binary play an important role.

This is further analysed by computing simulations with $M_{\text{disk}} = 0.01 M_\odot$ and $M_{\text{disk}} = 0.1 M_\odot$ with three different α viscosities, namely 0.01, 0.001 and 0.0001. The focus is on the first $10 T_{\text{bin}}$ (see Fig. 4.41). Thus, the simulation output is set to every 1/10th of the binary orbit. The time resolution of the simulation in this thesis is the same for all simulations (1/10th of the binary orbit), but for data storage reasons, the output in the long term evolutions of the planet and disk is saved only every T_{bin} . In this figure, as it only displays the first $10 T_{\text{bin}}$, it is important to show the full time resolution of the hydrodynamic force acting on the planet. One can detect that the force rises with a decrease of the α viscosity, in both cases independent of the disk mass. Nevertheless, one can also detect that the forces are higher

on the planet in the disk with the higher mass. A higher hydrodynamic force in z direction leads to a higher inclination that is already displayed in Fig. 4.40.

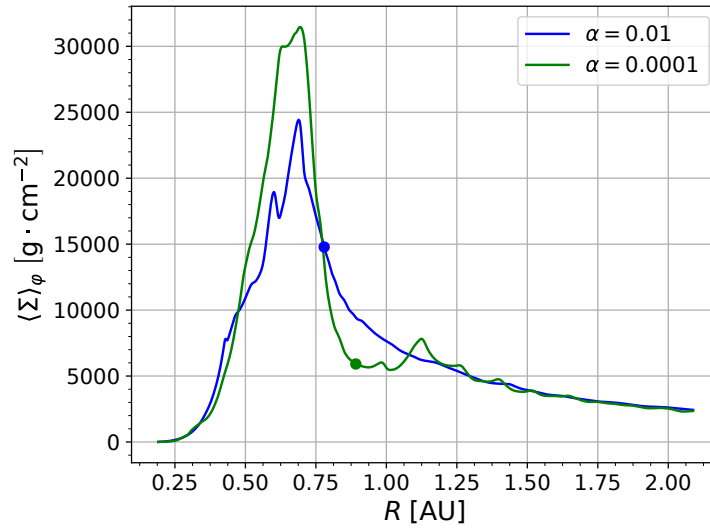


Fig. 4.39: The Kepler 38 disk is shown in an azimuthally-averaged plot of the surface density without the Stockholm condition. One time, the simulation with the α viscosity 0.01 is displayed, and the other time the α viscosity 0.0001. The blue/green point indicates the planet's location on the x-axis, not on the y-axis. The time is $1200 T_{\text{bin}}$ in both simulations.

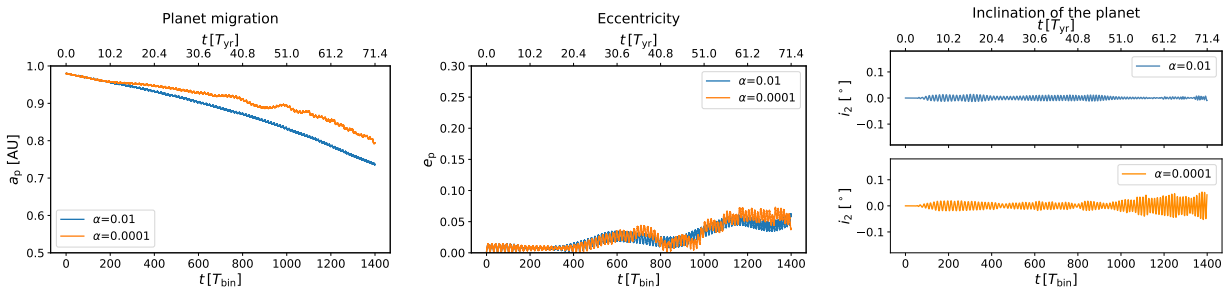


Fig. 4.40: Movement of the planet with different alpha viscosity's. The starting disk mass was $0.01 M_{\odot}$. Right: The migration is slower with the lower alpha viscosity of 0.0001. Middle: the eccentricity of the planet is similar in both simulations. Left: the inclination of the planet towards the mid-plane is larger with the lower alpha viscosity.

Noise

The same noise test as with the Stockholm condition was done again. This time the simulation was run 4x precisely with the same setup. Resulting in quite similar simulations (see Fig. 4.42). Thus the numerical noise, which is in z direction roughly 0.001° smaller than the inclination of the planets' orbit towards the mid-plane.

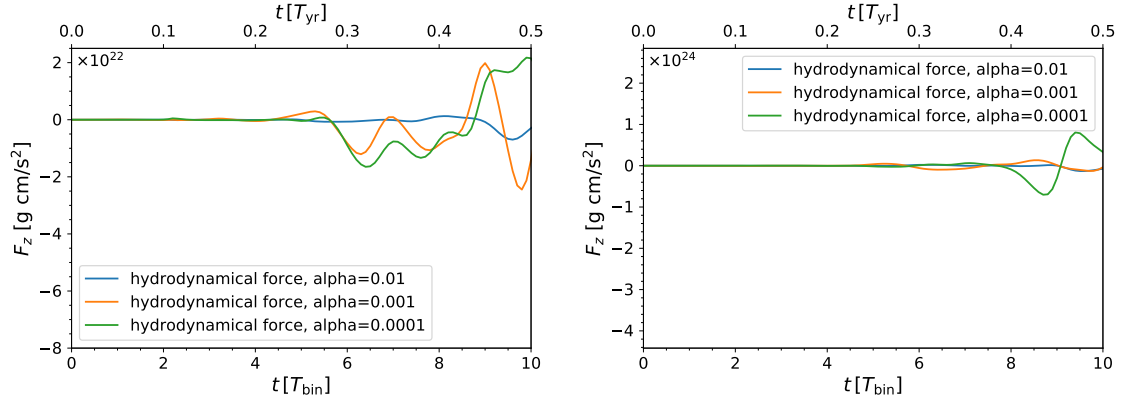


Fig. 4.41: Hydrodynamic force in z direction on the planet with different α viscosities and disk masses. The starting disk mass was (left) $0.01 M_{\odot}$ and (right) $0.1 M_{\odot}$.

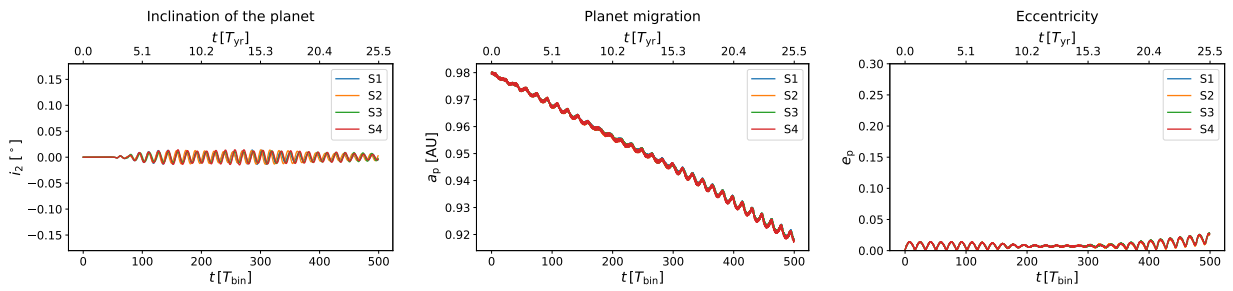


Fig. 4.42: Simulation of the no Stockholm binary setup run several times where nothing on the setup was changed. Left: planet's orbit inclination. Middle: planet's orbit semi-major axis. Right: planet's orbit eccentricity.

4.3.5 Simulation without Stockholm conditions - final setup

Simulations with the same setting as in the section with the Stockholm condition were performed but without this particular condition to analyze the influence of the disk with its asymmetries on the planet. A closer look at other aspects was also taken for further investigations of the results. For example, the disk mass is varied between $0.005 M_{\odot}$ and $0.1 M_{\odot}$, the binary eccentricity is also varied between 0.1 and 0.5, and the boundary location is set to $1.3 a_{\text{bin}} = 0.19 \text{ AU}$.

All other parameters are kept the same. The alpha viscosity is 0.01, and the outer boundary is still 2.1 AU. The planets' mass is also kept constant.

Structure of disk and disk mass

The gas surface density files of the mid-plane are displayed to compare the 3D simulation without the Stockholm condition to the simulations done with the Stockholm condition (see Fig. 4.43). Again, one can report that the central binary star rapidly opens a cavity in the $0.01 M_{\odot}$ within the first ~ 30 orbital periods in agreement with the previous simulations and Artymowicz & Lubow (1994, p. 662). The gap grows in radius to reach $\sim 2.5 a_{\text{bin}}$ after a few hundreds of orbital periods. Furthermore, enabling the comparison with previous studies by Kley & Haghighipour (2014) and Thun & Kley (2018) the integral over all planes was done to calculate the surface density (see Fig. 4.44).

Similar to the previous section, those figures show the spiral arms, inner cavity, and precession. The difference is in the slightly larger inner boundary location, which does not influence the simulation (see previous paragraphs), and in the smaller gas surface density as the disk mass decreases. Again the sudden drop of density is shown in the azimuthally-averaged surface density profiles (see Fig. 4.45). In this figure, one can not observe a clear gap opening in the disk, suggesting type I migration. The gap opening criterion $P \lesssim 1$ (Eq. 2.1) stays the same, comparing it to the previous section with the Stockholm condition, as this criterion depends on the viscosity and aspect ratio disk parameters ($\alpha = 0.01$, $h = 0.05$) which are the same in both setups. Thus the value of $P \sim 5.4$ is independent of the Stockholm condition. Thus this confirms that the condition for a type II migration is not met in this thesis. Moreover, it is noteworthy that the planet does not form a clear dip in the radial profile of the gas density values, which are larger by a factor of ~ 4.5 to Kley & Haghighipour (2014, p.). $\Sigma_{\text{disk}}/M_{\text{p}}$ (in g/cm^2 and M_{jup} , respectively) for the different cases of Thun & Kley (2018, Fig. 7), a dip is observed for $t = 12000 T_{\text{bin}}$ for ratios below 2×10^4 . The higher ratio of 2.6×10^4 observed in this simulation for $t = 9000 T_{\text{bin}}$ could explain the absence of a clear

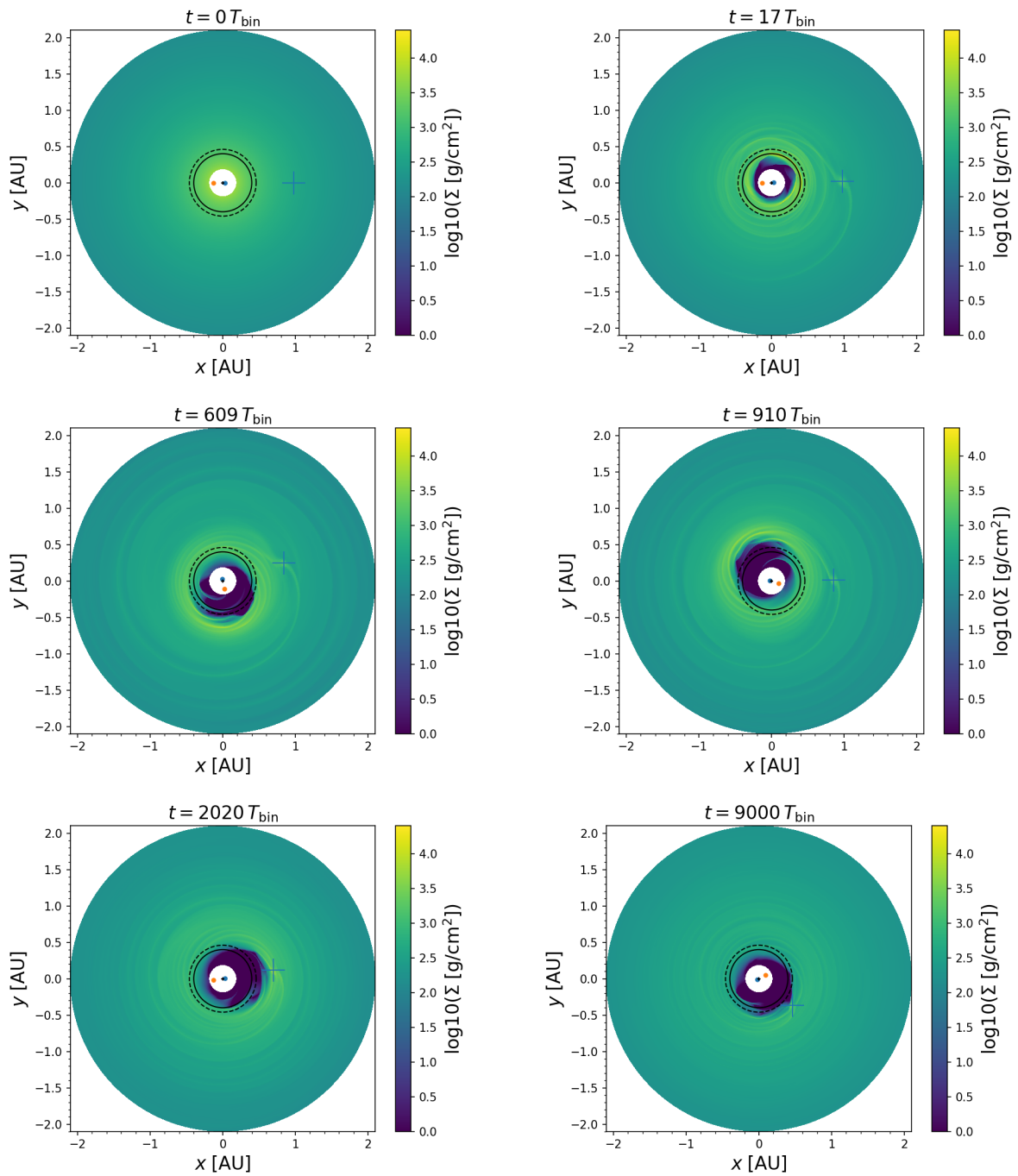


Fig. 4.43: Evolution of the Kepler 38 $0.01 M_{\odot}$ disk is shown in a two-dimensional surface density plot of the mid-plane with an isothermal simulation without the Stockholm condition and a planet migrating from ~ 1 AU to 0.54 AU. The perturbations of the surface density at different times are shown. It is color-coded with the logarithm of the gas surface density at the mid-plane. The white areas are outside of the computational domain. Thus the binary revolutions are not included in the simulation. The black circle at 0.4 AU is the stability radius for Kepler 38. The dotted line is the observed orbit of Kepler 38 at 0.46 AU. The plots are 4.2×4.2 AU in size. On top of each figure, time is indicated as a multiple of the orbital period ($0 T_{\text{bin}}$, $17 T_{\text{bin}}$, $609 T_{\text{bin}}$, $910 T_{\text{bin}}$, $2020 T_{\text{bin}}$ and $9000 T_{\text{bin}}$).

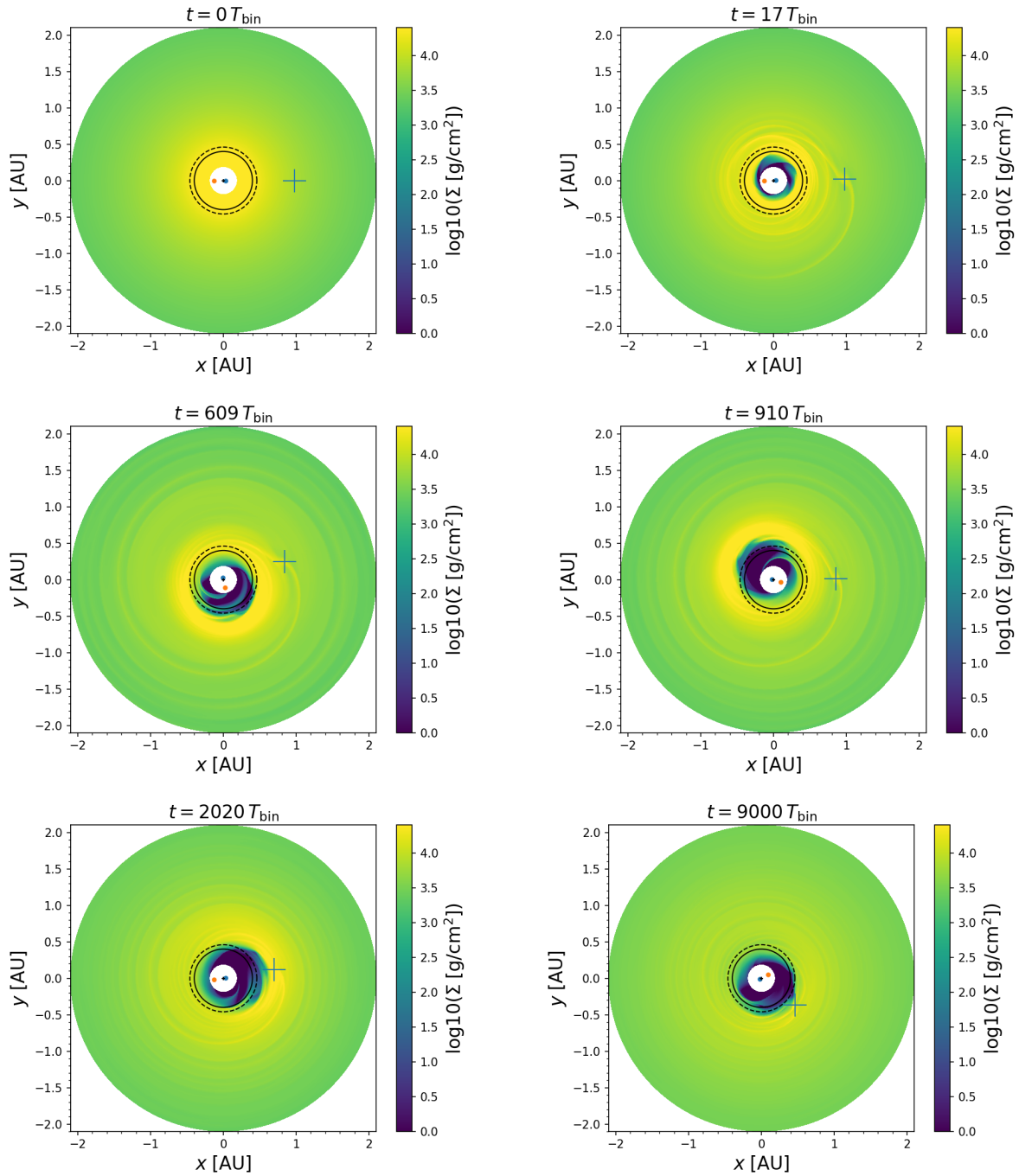


Fig. 4.44: Evolution of the Kepler 38 $0.01 M_{\odot}$ disk is shown in a two-dimensional plot of the surface density with an isothermal simulation without the Stockholm condition and a planet migrating from ~ 1 AU to 0.54 AU. It is the same setup as Fig. 4.17. However, the perturbations of the surface density (ρ) at different times are shown. It is color-coded with the logarithm of the gas density. The planet is visible through a density accumulation. The white areas are outside of the computational domain. Thus, the binary revolutions are not included in the simulation. The plots are 4.2×4.2 AU in size. On top of each figure, time is indicated as a multiple of the orbital period ($0 T_{\text{bin}}$, $17 T_{\text{bin}}$, $609 T_{\text{bin}}$, $910 T_{\text{bin}}$, $2020 T_{\text{bin}}$ and $9000 T_{\text{bin}}$).

dip in the surface density.

The evolution of the surface density profile of the disk over $14000 T_{\text{bin}}$ is also displayed in the previous mentioned figure. This evolution is in agreement with a decreasing disk mass mainly in the inner region, with a surface density peaking at about 8500 g/cm^2 after $14000 T_{\text{bin}}$.

In this simulation, the initial planet migration speed is rapid within $t = 4000 T_{\text{bin}}$ then slows down before reaching its final separation after ~ 400 years for an initial disk mass of $0.01 M_{\odot}$. Nevertheless, the migration of the planet takes much longer in this simulation than in the previous ones with the Stockholm condition (see Fig. 4.46), where it reaches a stable separation $\sim 0.54 \text{ AU}$ beyond the stability limit of $\sim 0.4 \text{ AU}$ for Kepler 38 (Holman & Wiegert, 1999, p. 626). The planet migration stops outside of the inner disk's cavity, which is opened by the central binary star, where its relative period verifies $T_p/T_{\text{bin}} \approx 7.0$. As shown in the previous setup and by Masset et al. (2006, p. 481), the cavity acts as a barrier to a further migration resulting from a sudden drop of density. The final stopping location of the planet (0.54 AU) is slightly further out in the simulation without the Stockholm condition compared with the planet's stopping location with the Stockholm condition (0.51 AU) due to the slightly larger cavity resulting from the marginally larger inner boundary location. As shown in the paragraph comparing the different inner boundary locations, the stopping location is further out for the 1.3 CU boundary condition as for the 1.0 CU. This explains the difference in the stopping location with and without Stockholm condition setups. In this simulation, as before in the section with the Stockholm condition, one can see that the sudden drop of density prevents the migration of the planet further in.

Another factor that influences the migration process is the disk mass. Thus, the migration timescale is influenced by the surface density at the planet's location and, therefore, by the total disk mass for a given disk size. This dependency was already shown with the Stockholm condition but is now confirmed for the case without the Stockholm condition (see Fig. 4.47). In the left figure, the migration for the higher disk masses is very similar to the migration with the Stockholm condition turned on (see Fig. 4.21). Thus, those figures evidence the evolution of the migration timescale, which shortens with increasing surface densities at the location of the planet following Tanaka et al. (2002, p. 1271). The migration process starts quicker than in the simulation without the Stockholm condition, as the maximum disk mass is already reached. In the simulation with the Stockholm condition, the starting disk mass is lower and rises over time. With rising mass, the migration process accelerates. The fast migration process is happening in the setup with the Stockholm condition at a disk mass between 0.05 and $0.06 M_{\odot}$.

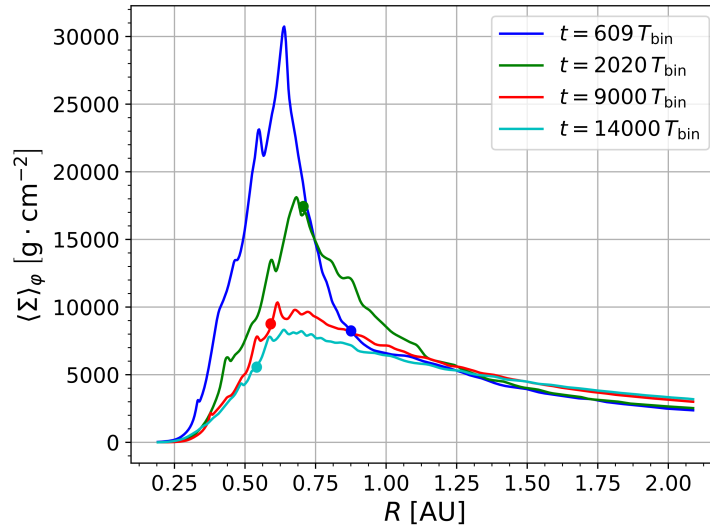


Fig. 4.45: Evolution of the Kepler 38 disk is shown in an azimuthally-averaged plot of the surface density without Stockholm condition and a planet migrating from ~ 1 AU to 0.54 au. It is the same setup as Fig. 4.43. The colored points indicate the location in the x-axis of the planet. Time is indicated as a multiple of the orbital period ($609 T_{bin}$, $2020 T_{bin}$, $9000 T_{bin}$ and $14000 T_{bin}$).

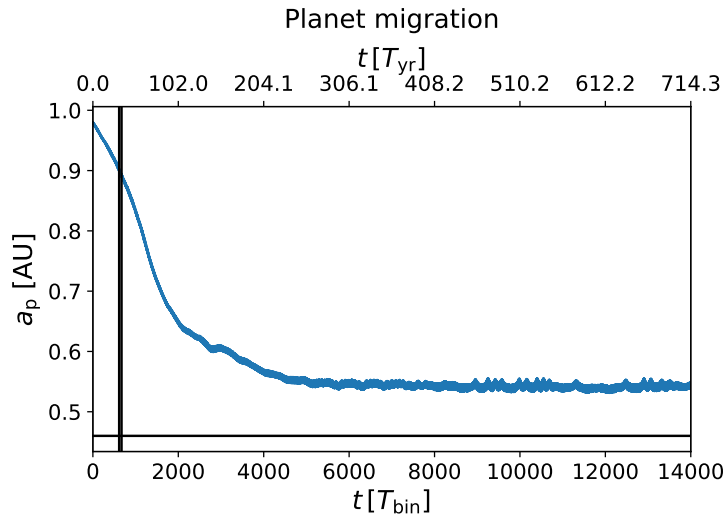


Fig. 4.46: Evolution of the disk mass for the case $M_{disk} = 0.01 M_\odot$ over 14000 binary revolutions (On the top axis, the transformation to Earth years is shown). The horizontal line is the observed planet's location (0.46 AU). The solid vertical lines indicate the migration in the setup with the Stockholm condition turned on.

Tab. 4.8: Computed migration time t_{mig} following Baruteau et al. (2013) (B13) and Tanaka et al. (2002) (T02) for the 2D and 3D simulation case, respectively, and applied to the system parameters of Kley & Haghighipour (2014) (KH14), Thun & Kley (2018) (TK18) and this work. In the last column is reported the estimated migration time scale $t_{\text{mig,exp}}$ from the numerical experiments of the three different works.

Reference	M_p [M_{jup}] (r_p)	M_{disk} [M_{\odot}]	Σ_p [g/cm^2]	p	t_{mig} [yr]		$t_{\text{mig,exp}}$ [yr]
					(B13)	(T02)	
KH14	0.34 (1 AU)	0.0038	3000	0.5	2387	1098	3000-5000
TK18	0.384 (0.88 AU)	0.012	5582	1.5	1210	557	900-1400
This work	0.34 (0.98 AU)	0.01	7210	1.5	1004	461	306-406

This thesis can confirm the finding of Thun & Kley (2018, p. 11) that the disk mass and the migration speed are proportional, and the stopping location is independent of them. This is also analytically shown by Tanaka et al. (2002, p. 1271), where he treats theoretically the three-dimensional evolution for disks. He found for the case of an isothermal disk and type I migration, the migration timescale of:

$$t_{\text{mig}} = (2.7 + 1.1 p)^{-1} \frac{h^2}{M_p} \frac{M_*^2}{\Sigma_p r_p^2} \Omega_p^{-1} \quad (4.10)$$

where Σ_p is the disk surface density at the planet's starting radius r_p , Ω_p the angular velocity of the disk perturber and p is the exponent of the surface density. This formulation shows in the prefactor a dependence of the migration timescale with p , which is taken constant to 1/2 in Eq. 3 of Baruteau et al. (2013, p. 3). This implies that for a disk setup with negative radial gradient of the surface density ($p > 0$), the migration timescale t_{mig} will be shorter by a factor ~ 2 following Tanaka et al. (2002, p. 1271). In Table 4.8 a comparison of t_{mig} for different simulations of the Kepler 38 system is reported. Without tackling here the important problem of the far too efficient migration type I migration, the results are consistent with the expectations of the three-dimensional approach and with the trend showing that, for typical disk surface density profiles (i.e. $p \sim 0.5-1.5$), the migration timescale diminishes when the effect of the steeper density profile is included.

In this simulation, it is confirmed again that the inner cavity is the main factor for the stopping location of the planet. Further tests to prove this statement are performed later in this section by varying the inner cavity size with different star eccentricities or star mass ratios.

The disk mass over time is decreasing (see Fig. 4.37), which is a significant difference from the simulation with the Stockholm condition (see Fig. 4.19). This means that the open inner boundary condition allows mass transfer on the star and the outer boundary condition

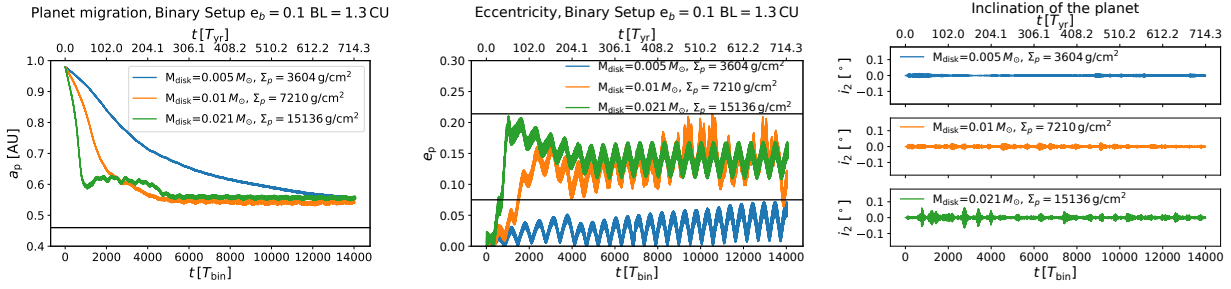


Fig. 4.47: Evolution of the Kepler 38 without Stockholm condition and different densities of the disk, with the surface density at the location of the planet (Σ_p) is displayed. The timescale is given in number of binary periods T_{bin} (bottom) and in years (top). Left: observed migration via change in the semi-major axis. The continuous black horizontal line defines the observed planet separation of ~ 0.46 AU. Middle: eccentricity of the planet. The horizontal lines display the extent of the oscillations beyond $t = 3000 T_{\text{bin}}$. Right: inclination of planet towards the mid-plane. The mass of the planet and all the other parameters are kept the same. Those initial disk masses M_{disk} of 0.005, 0.01 and 0.021 M_{\odot} are in agreement with the observed masses of disks in low-mass pre-main sequence stars (Beckwith, 1990, p. 936).

prevents inflow from the outer disk.

Influence of central binary's parameters

In this paragraph, a closer look is taken at the binary's parameter. Those parameters, namely the eccentricity e_b and mass ratio μ , influence the critical semi-major axis, which is the smallest stable orbit for a p-type planet (see Eq. 2.2) (Holman & Wiegert, 1999, p. 626). These authors treat however the case of a system governed by celestial mechanics in which the interaction with the circumbinary disk is not included. Nevertheless, this equation shows, the binary's parameters influence the migration process.

Here, a disk with a larger initial disk mass $M_{\text{disk}} = 0.021 M_{\odot}$ is simulated with three different eccentricity values of the central binary star, namely $e_b = 0.1, 0.3,$ and 0.5 . This enables testing the influence of the binary eccentricities, which led to new stability limits for the planet (see Tab. 4.9). Moreover, the larger the binary eccentricity, the larger is the inner cavity (see Fig. 4.48). For example, in the left plot with $e_b = 0.5$, one needs to remember that the planet has an elliptic orbit with its semi-major axis around 0.8 AU with an eccentricity of the orbit $e_p = 0.26$ after the migration process at $1200 T_{\text{bin}}$. Thus in the figure, the current location is not the semi-major axis, but the planet's position within the disk, and this position can be smaller than the semi-major axis. The larger cavity leads to different stopping locations of the planet (see Fig. 4.49). This figure shows a significant impact of the binary eccentricity on the stopping location of the migrating planet. One can conclude that binaries with higher eccentricities have a stopping location of the planet's migration

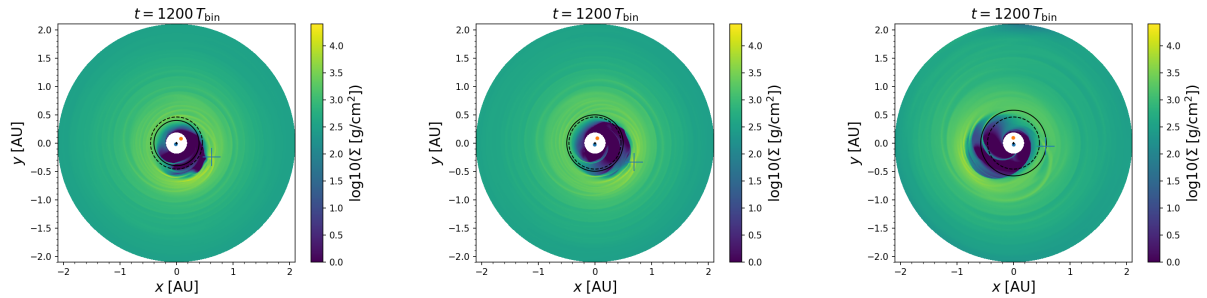


Fig. 4.48: Formation of the disk inner cavity as a function of the eccentricity of the central binary star after $1200 T_{\text{bin}}$ for an initial disk mass of $0.021 M_{\text{disk}}$. From left to right, the binary eccentricity e_b is 0.1, 0.3 and 0.5 respectively. The computational hole is marked as a white disk, and the blue and orange dots show the location of the stars. The dashed-line circle indicates the reported location of Kepler 38 at 0.46 AU. The continuous-line circle indicates the critical radius a_c derived from Holman & Wiegert (1999), which from top to bottom is calculated at ~ 0.4 , 0.5 and 0.6, respectively. See text for details.

process further out if all parameters are kept the same. This confirms Thun et al. (2017, p. 15) finding with 2D simulations.

Tab. 4.9: Stability limits for p-type planets semi-major axis (see Eq. 2.2), for different binary eccentricities.

e_b	a_c [AU]
0.1	0.394
0.3	0.498
0.5	0.580

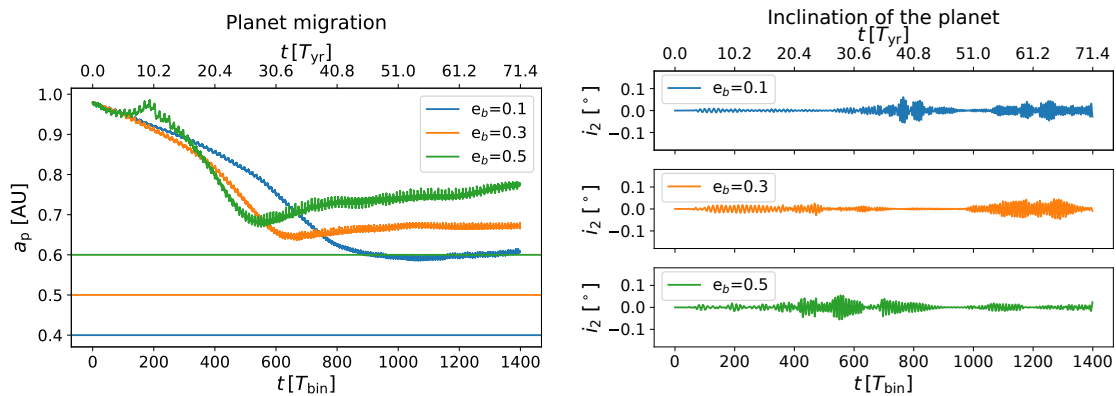


Fig. 4.49: Evolution of the Kepler 38 $0.021 M_{\odot}$ disk without the Stockholm condition and different e_b . Left: Time evolution of the planet semi-major axis a_p . For each value of e_b , the colored horizontal lines give the estimated critical semi-major axis a_c . Right: Inclination of planet towards the mid-plane. The mass of the planet and all the other parameters are kept the same.

The disk mass does not influence the location of the stability limit of the semi-major axis, but the disk mass still influences the migration process. In this case, the relatively massive

disk results in a rapid migration with an eccentricity-dependent ending location that is proportional to the critical semi-major axis by an empirical factor of $\sim 1.5^{(1-e_b)}$. Nevertheless, for a simulation with a heavy disk mass and a large binary eccentricity, the planet may get ejected out of the system (see Fig. 4.50).

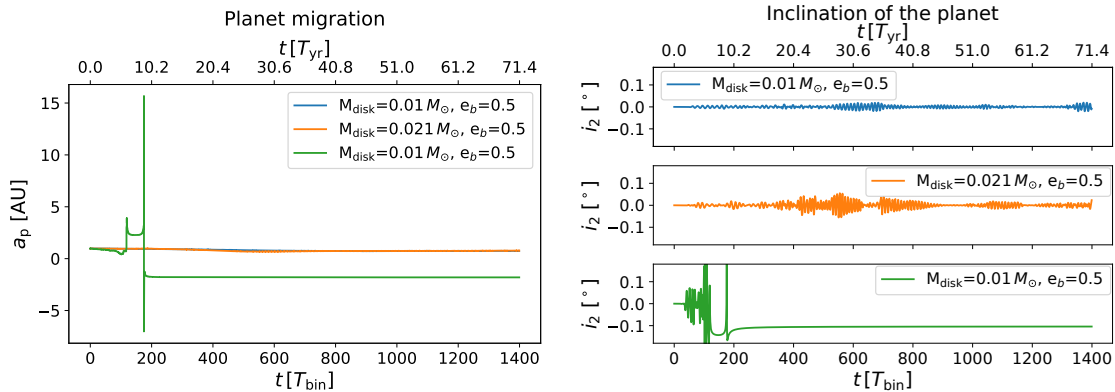


Fig. 4.50: Evolution of the Kepler 38 without Stockholm condition, $e_b = 0.5$ and different disk masses. Left: Time evolution of the planet semi-major axis a_p . Right: Inclination of planet towards the mid-plane. The mass of the planet and all the other parameters are kept the same.

A closer look at the influence of a different mass ratio is taken. The different mass ratio μ (ranging from 0.25-1) of the binary also leads to a different stability limit for the planet (see Tab. 4.10). Compared to the influence of the binary eccentricity, the influence of the mass ratio is moderate. This explains the finding of very similar stopping locations for the planet (see Fig. 4.51). Only for the smallest value of μ a noticeable difference is seen in the stopping location of the planet following a rapid migration. This corresponds to findings of Thun et al. (2017, p. 15) who only found a weak impact through variation of the mass ratio.

Tab. 4.10: Stability limits for p-type planets semi-major axis (see Eq. 2.2) for different binary mass ratios and $e_b = 0.1$.

binary ratio	a_c [AU]
0.8/0.2	0.394
0.7/0.3	0.408
0.6/0.4	0.414
0.5/0.5	0.415

If one looks at the inclination of the planet towards the mid-plane in the simulation with different binary eccentricities (see Fig. 4.49), one can see that the location of the stars primarily affects the inclination. Thus, the eccentricity of the stars seems to disturb the disk faster, and the planet's inclination happens earlier.

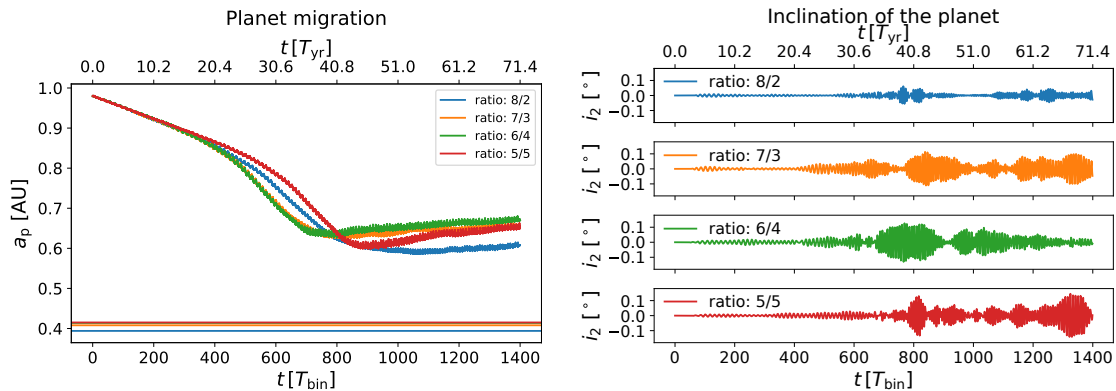


Fig. 4.51: Evolution of the planet in a circumbinary disk. The simulation is done without the Stockholm condition, $e_b = 0.1$ and different mass ratios. Left: semi-major axis. Right: inclination of planet towards the mid-plane. The mass of the planet and all the other parameters are kept the same.

The star mass ratio seems to have a negligible influence on the amplitude of inclination towards the mid-plane of the planet (see Fig. 4.51). The times of the episodes with inclinations vary, but that is explainable, as it is influenced by the location of the planet towards the binary stars and the planet is at different locations at the same T_{bin} .

Inclination of planet

In the previous section and paragraphs, the validity of the three-dimensional simulation approach was established by reproducing results on the planet migration process and disk evolution that are coherent with previous studies and with the parameters assumed, in particular regarding the higher disk surface density. Also, here, in the simulation without the Stockholm condition, an inclination of the planet is visible. As shown before, it is highly dependent on the disk mass; thus, it is hard to compare this simulation to the simulation with the Stockholm condition. In the simulation with the Stockholm condition, the mass raises over time from $0.007 M_{\odot}$ to over $0.1 M_{\odot}$ (see Fig. 4.19). Thus for the simulation without the Stockholm condition the disk mass of $0.01 M_{\odot}$ and $0.1 M_{\odot}$ are compared (see Fig 4.52). Focusing on the inclination one can detect, that for the case of $M_{\text{disk}} = 0.01 M_{\odot}$, the planet, which is initially co-planar with the binary star orbit, shows a non-zero inclination starting at $t \sim 60 T_{\text{bin}}$ that steadily increases over the first $120 T_{\text{bin}}$ timescale to $\sim 0.01^{\circ}$. The same can also be detected while analyzing the mutual inclination of the binary/planet (see Fig. 4.53). There the inclination rises to 0.015° in the first $120 T_{\text{bin}}$. Beyond that point in time, the inclination towards the mid-plane and the mutual inclination varies but never exceeds $i_{1/2} \sim 0.025^{\circ}$ over a timescale of $9000 T_{\text{bin}}$. A direct comparison with the case of the single star scenario is shown in Fig. 4.53, and the planet's inclination with respect to

Tab. 4.11: Mutual inclination in degree between the normal vector and the angular momentum vector of the disk at different T_{bin} for different disk masses and star eccentricities. Left: the planet gets ejected out of the system at the simulation $0.1M_{\odot}$ & $0.5 e_{\odot}$. At $910 T_{\text{bin}}$ the planet is already 200 AU away. Right: single star case.

binary	$0.01M_{\odot}$	$0.1M_{\odot}$	single	$0.01M_{\odot}$	$0.1M_{\odot}$
$0.1 e_{\odot} T_{\text{bin}} = 17$	0.00116	0.00111	$T_{\text{bin}} = 17$	0.0000703	0.0000636
$T_{\text{bin}} = 910$	0.00588	0.00667	$T_{\text{bin}} = 910$	0.000119	0.000358
$0.5 e_{\odot} T_{\text{bin}} = 17$	0.00292	0.00228			
$T_{\text{bin}} = 910$	0.00684	0.00789			

the mid-plane in a single star case for different disk masses is shown in Fig. 4.9 (bottom plot). Those plots show that in the single star case, both types of inclinations are almost zero over $1400 T_{\text{bin}}$. This results again points out the critical influence of the binarity on the introduced planet misalignment, even for the case of initial co-planarity.

The more extreme case is also explored (see Fig. 4.52 (bottom plots) and Fig. 4.53 (right plot)). This case with $M_{\text{disk}} = 0.1 M_{\odot}$ is unlike a real T Tauri system. It has an inner disk ten times more massive than the previously discussed system. In this case, the evolution timescale was limited to $1/6^{\text{th}}$ of the lower disk's mass case. In those figures, one can observe a behavior comparable to the lower disk's mass case in terms of increase of mutual inclination, but with an amplitude up to 0.2° , i.e., about ten times larger than the case $M_{\text{disk}} = 0.01 M_{\odot}$ and close to the observed inclination of Kepler 38.

An important aspect concerns the disk dynamics under the gravitational potential of the central binary star. The author computed the binary/disk mutual inclination i_1 up to $200 T_{\text{bin}}$ due to the high computation cost. One can observe in Fig. 4.54 the rapid development of the mutual inclination with a modest amplitude $\lesssim 0.02^{\circ}$. For more comparisons of the mutual inclination of the disk at a later point in time (see Tab. 4.11). The Tab. 4.12 is added to show the direct comparison of the mutual inclination of the planet at the same points in time. Nevertheless, one needs to be careful because of the high fluctuations not to compare a large angle at $0.01 M_{\odot}$ with a low angle at $0.1 M_{\odot}$. As one can not read a trend from a single data point, one needs to be careful before drawing conclusions from it. However, one can compare the two later tables with each other as one displays the planet's mutual inclination and the other the disk's mutual inclination. For the general trend of the planets evolution (see Fig. 4.52 and Fig. 4.53).

In both simulation asymmetries in the xz plane are visible (see Fig. 4.55). Fig. 4.56 shows the z plane at the same points in time as Fig. 4.44. Those are similar points in time as used with the Stockholm condition, where the planet just finished a revolution, to make it comparable. Again the focus is on the asymmetries in the z plane. Thus Fig. 4.57 are

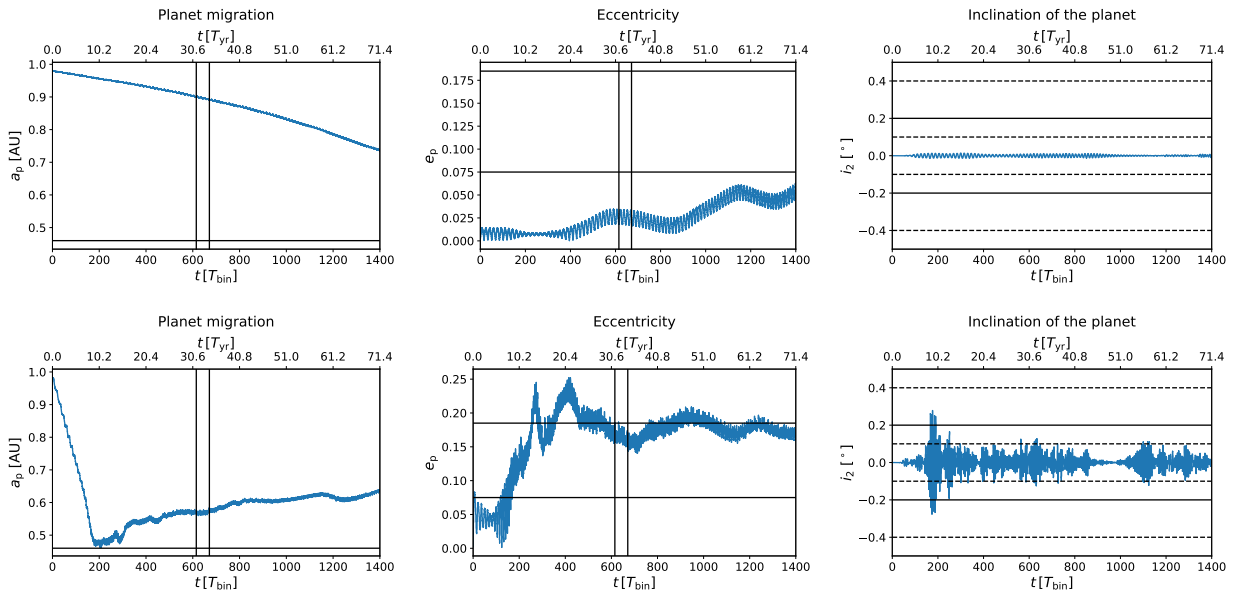


Fig. 4.52: The planets' evolution of the semi-major axis. The left figure shows the evolution over 1400 binary revolutions (on the top axis, the transformation to Earth years is shown). The horizontal line is the observed planet's location (0.46 AU). The migration in the setup with Stockholm condition happened mostly between 615 and 671 binary revolutions (solid vertical lines). In the top simulation the migration process takes much longer and in the bottom process it happens in the first 200 T_{bin} . The middle figure shows the evolution of the eccentricity of the planet and the right figure the planet's inclination towards the mid-plane is shown. In the later figures the black lines are the same as in the with Stockholm setup. This helps with the comparison. The top row shows the evolution for a disk with the mass of $0.01 M_{\odot}$ and the bottom row shows the disk with the mass of $0.1 M_{\odot}$. One can see, the inclination towards the mid-plane is smaller in this setup compared to the setup with the Stockholm condition.

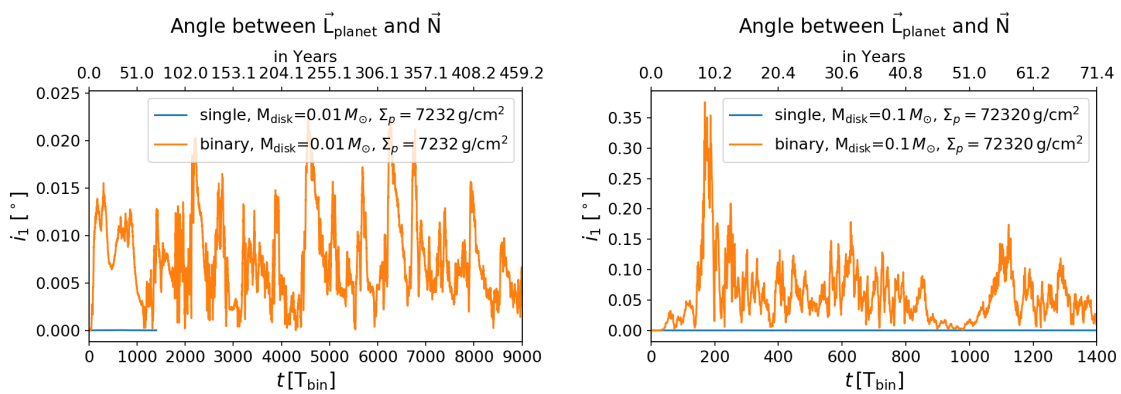


Fig. 4.53: Mutual inclination of the angular momentum vector of the planet towards the normal vector in z direction/ L_{binary} . The mass of the disk is (left) $0.01 M_{\odot}$ and (right) $0.1 M_{\odot}$. The star eccentricity is 0.1.

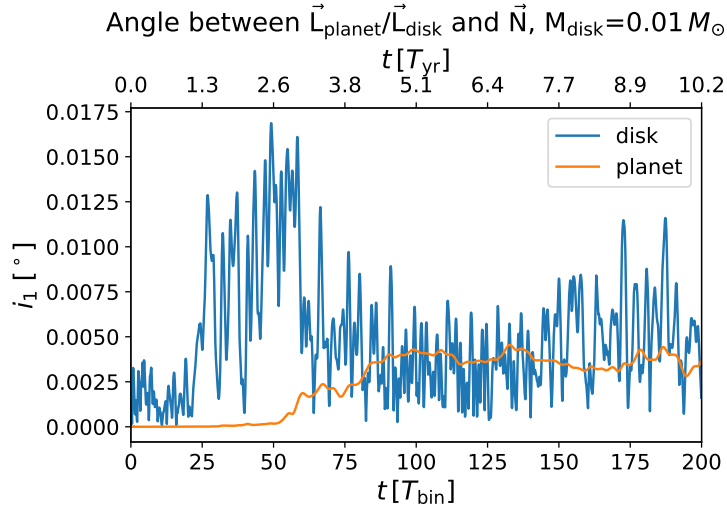


Fig. 4.54: Mutual inclination of the angular momentum vector of the disk and the angular momentum vector of the normal vector, as well as, the mutual inclination of the angular momentum vector of the planet and the angular momentum vector of the normal vector in a $0.01 M_{\odot}$ disk mass system.

Tab. 4.12: Mutual inclination in degree between the normal vector and the angular momentum vector of the planet at different T_{bin} for different disk masses and star eccentricities. Left: the planet gets ejected out of the system at the simulation $0.1 M_{\odot}$ & $0.5 e_{\odot}$. At $910 T_{\text{bin}}$ the planet is already 200 AU away. Right: single star case.

	$0.01 M_{\odot}$	$0.1 M_{\odot}$		$0.01 M_{\odot}$	$0.1 M_{\odot}$
$0.1 e_{\odot}$ $T_{\text{bin}} = 17$	0.0	0.0000225	single	0.0	0.0
$T_{\text{bin}} = 910$	0.010	0.013	$T_{\text{bin}} = 17$	0.0	0.0
$0.5 e_{\odot}$ $T_{\text{bin}} = 17$	0.00000121	0.000467	$T_{\text{bin}} = 910$	0.000007	0.00003
$T_{\text{bin}} = 910$	0.0080	0.193			

done the same way as Fig. 4.24 in the previous section. In contrast to the simulations with the Stockholm condition, the asymmetries are towards the beginning of the simulation and become less towards the end (see Fig. 4.57 and Fig. 4.58). This is explainable as the mass of the disk decreases over time. The time points vary in both simulations a bit, as the planet's evolution depends on the disk mass. The times were chosen that the planet had just finished a revolution.

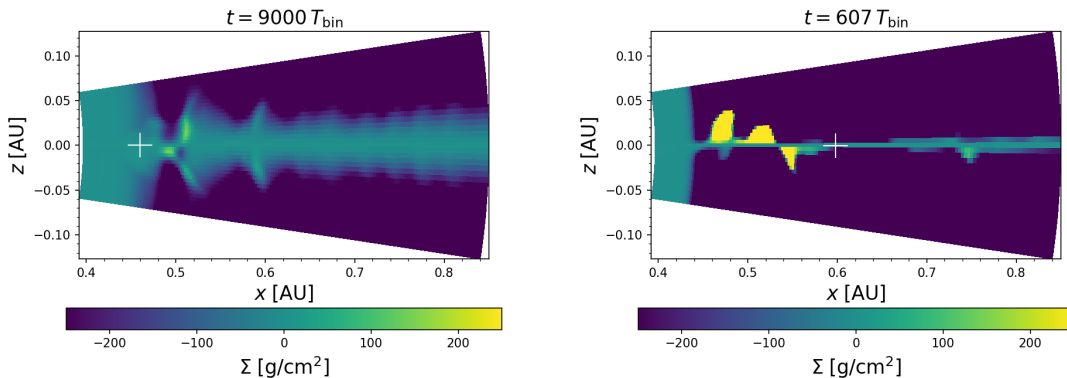


Fig. 4.55: Evolution of the Kepler 38 disk is shown in a two-dimensional surface density plot of the z plane after the migration process at (left) 9000 binary revolutions and $0.01 M_{\odot}$ disk mass (right) 607 binary revolutions and $0.1 M_{\odot}$ disk mass, where the mid-plane is subtracted from each plane in the disk. A zoom on the inner gas around the planet is shown. The asymmetry in the gas density in the disk shows the gravitational influence on the planet. The the gas density is linear color-coded. The plot is 0.43×0.26 AU in size.

Comparing the axis symmetries with the simulation without the planet in Fig. 4.35, one can see that again; the planet has a significant impact on the density clusters. Thus not only the binary and the spiral arms influence the disk structure but also the planet itself.

Moreover, comparing the results with the single-star case and the planet at ~ 1 AU. The simulation was evolved until $t \sim 9000 T_{\text{bin}}$. Figure 4.59 shows a visually plane-symmetric gas density distribution in the vertical plane at the planet azimuth at $t = 8008 T_{\text{bin}}$ for the single-star case.

When comparing the central binary case corresponding to Kepler 38 by similarly tracing the vertical gas density distribution for the same time duration, up to $t \sim 9000 T_{\text{bin}}$. On top of an overall plane-symmetric distribution, once can observe clear asymmetries in the disk gas density within 0.1 AU of the migrating planet. Note that the Hill radius of the planet is typically less than 0.03 AU. In Fig. 4.57, the plane-asymmetry is well visible for $t = 2020 T_{\text{bin}}$ at ~ 0.6 AU as well as for $t = 9000 T_{\text{bin}}$ at ~ 0.5 AU, although with lower contrast between the upper and lower overdensities in the latter case. Such overdensities are found to be of

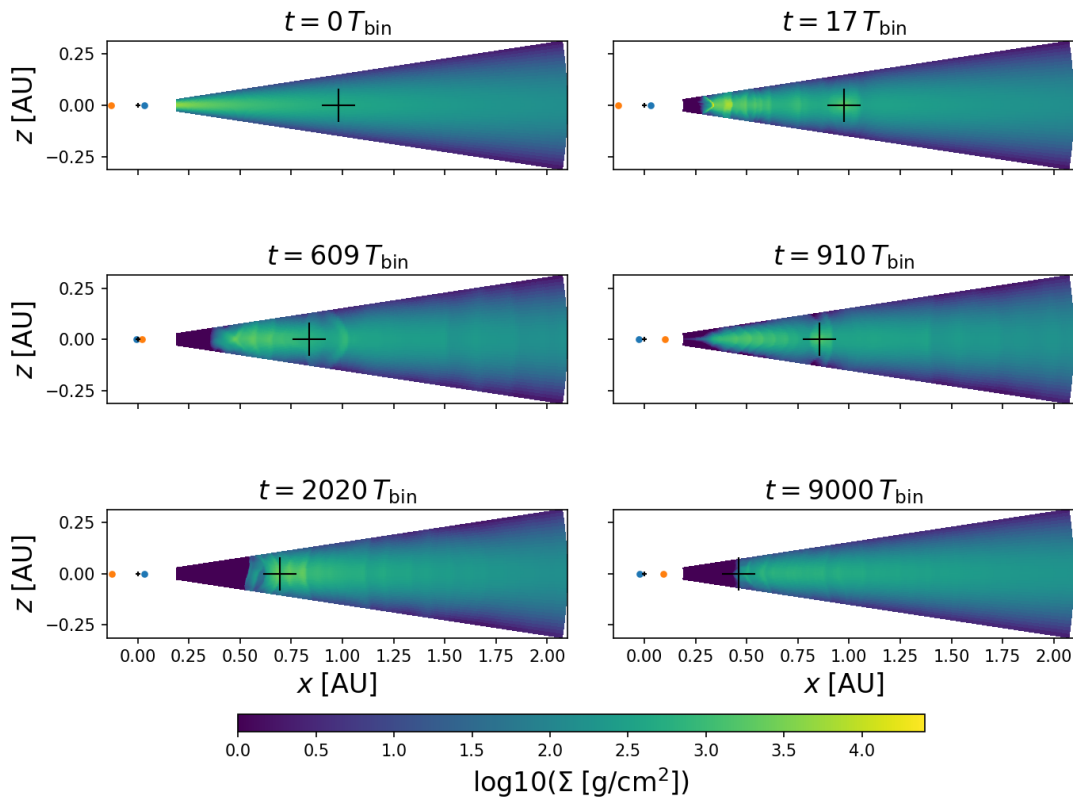


Fig. 4.56: Evolution of Kepler 38 $0.01 M_{\odot}$ disk shown in a two-dimensional surface density plot of the xz plane with an isothermal simulation without the Stockholm condition at the same points in time as Fig. 4.43. The black marker shows the location of the planet. The white area is also outside of the computational domain as it is the same setup. The plots are 2.25×0.63 AU in size and in CGS units. The logarithm of the gas density is color-coded, and the time is indicated on top of each figure.

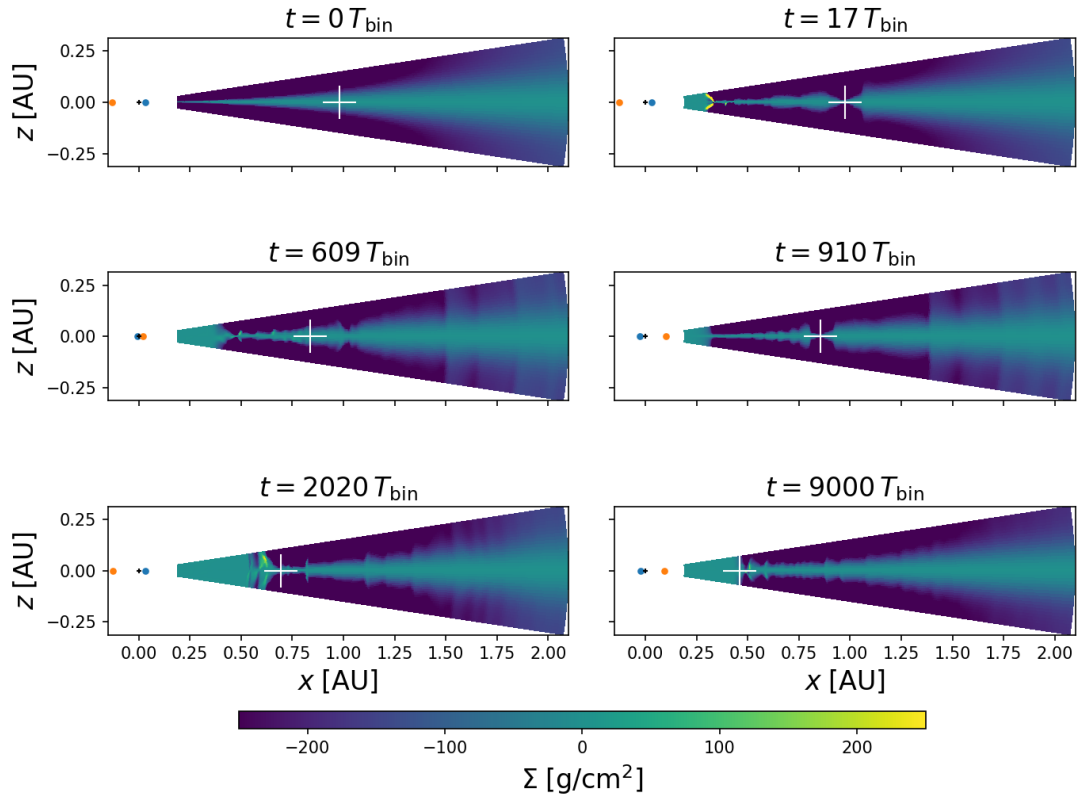


Fig. 4.57: Evolution of the Kepler 38 $0.01 M_{\odot}$ disk surface density is shown in a two-dimensional plot of the xz plane, where the mid-plane is subtracted from each plane in the disk. It is the same setup as in Fig. 4.56. The asymmetry in the gas surface density in the disk shows the gravitational influence on the planet. The planet is marked in the right zoomed area with a white cross. The gas surface density is linear color-coded. The plots are 2.25×0.63 AU in size. On top of each figure, time is indicated as a multiple of the binary's orbital period.

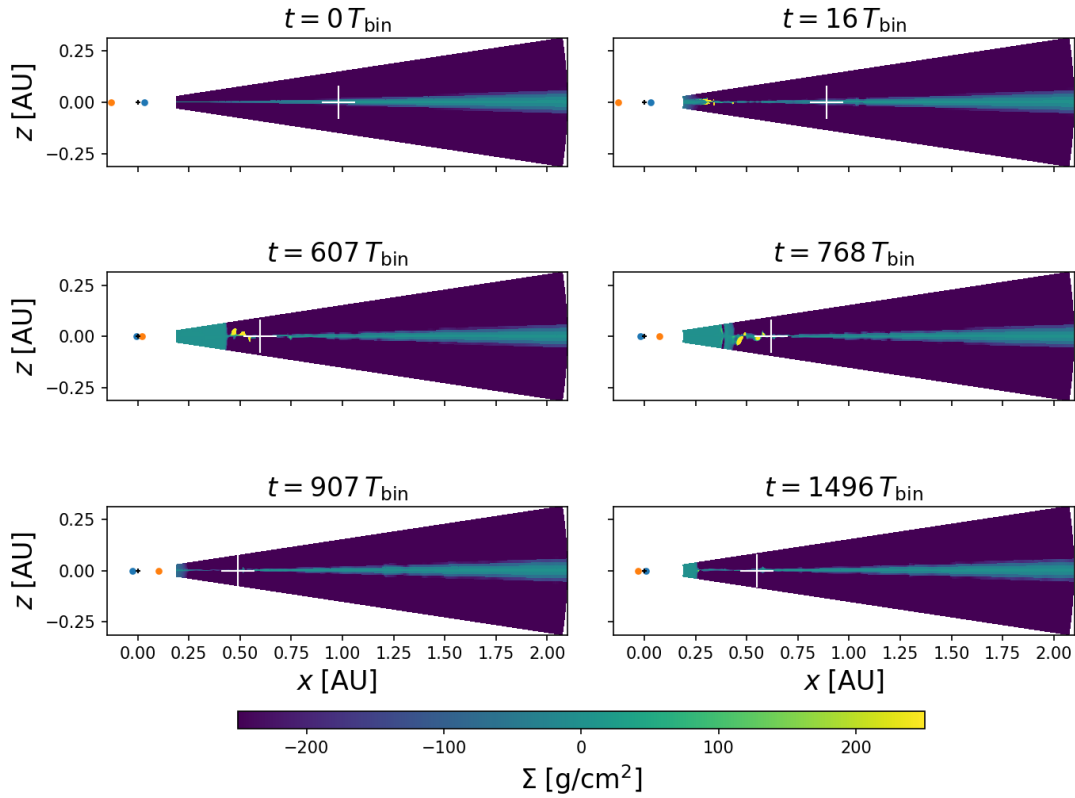


Fig. 4.58: Evolution of the Kepler 38 density is shown in a two-dimensional surface density plot of the xz plane, where the mid-plane is subtracted from each plane in the disk. The disk mass is $0.1 M_{\odot}$. The asymmetry in the gas surface density in the disk shows the gravitational influence on the planet. The planet is marked in the right zoomed area with a white cross. The gas surface density is linear color-coded. The plots are 2.25×0.63 AU in size. On top of each figure, time is indicated as a multiple of the binary's orbital period.

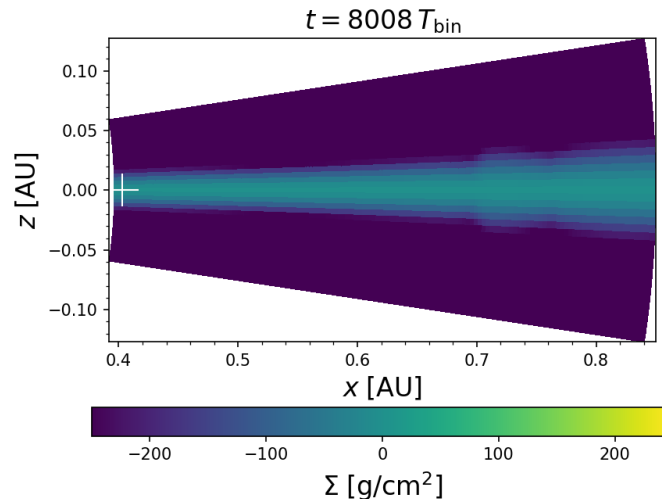


Fig. 4.59: The evolution of the single star case surface density of the $0.01 M_{\odot}$ disk is shown in a two-dimensional plot of the xz plane, where the mid-plane is subtracted from each plane in the disk. The asymmetry in the gas density in the disk shows the gravitational influence on the planet (white marker). The author zooms on the inner region of the disk. The gas density is linear color-coded. The planet is in the migration process. The time T_{bin} is a fixed time frame and corresponds to 19.6 years. Thus, $8008 T_{\text{bin}}$ equals ~ 409 Earth years.

~ 100 - 200 in excess to the mid-plane density.

The comparison between the single-star and binary-star cases points at the gravitational influence of the central binary star with $m = 0.26$ mass ration in the formation and evolution of plane-asymmetric gas density structures. The strength and contrast of the plane-asymmetric structure appears to depend on the disk mass. In the extreme case of $M_{\text{d}} = 0.1 M_{\odot}$, one can observe in Fig. 4.58 the rapid formation ($t = 768 T_{\text{bin}}$) of vertical asymmetries with a density of $\sim 3000 \text{ g/cm}^2$ in excess to the mid-plane.

Then, as a possible quantitative metric of the vertical disk symmetry/asymmetry, one can compute the ratio $\rho_{\phi}(r) = \Sigma_{\text{up}}/\Sigma_{\text{low}}$ where Σ_{up} and Σ_{low} is the integrated surface density in the upper and lower disk hemisphere, respectively, at the radial and azimuthal positions r and ϕ (see Fig. 4.61). Deviations from $\rho_{\phi} = 1$ indicate the strength of the asymmetry relative to the mid-plane.

Furthermore the influence of the disk asymmetries by calculating the gravitational and hydrodynamic forces exerted on the planet are analyzed. In this setup the total force is calculated using a temporal resolution $\Delta T = 0.1 T_{\text{bin}}$. The comparison between the single star and binary star setups in Fig. 4.62 indicate that the planet becomes rapidly (at $\sim 25 T_{\text{bin}}$) subject to the pull of $F_{\text{tot},z}$, which amplitude starts oscillating from $\sim 55 T_{\text{bin}}$ with the planetary

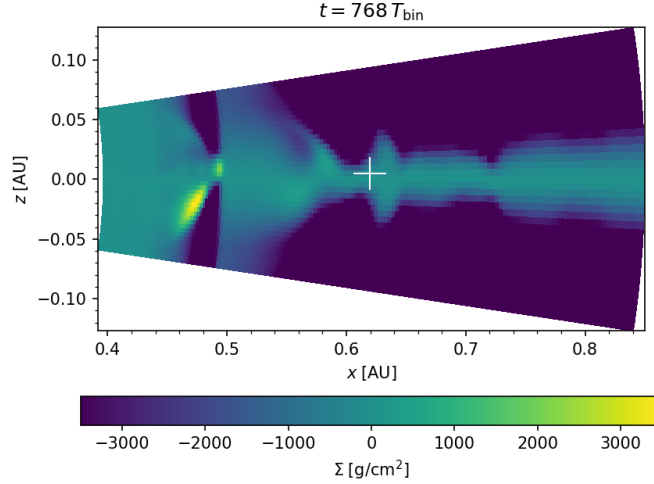


Fig. 4.60: The evolution of the Kepler 38 $0.1 M_{\odot}$ disk is shown in a two-dimensional surface density plot of the xz -plane at 17 binary revolutions, where the mid-plane is subtracted from each plane in the disk. The author zooms on the gas around the inner disk at the planet's side. The asymmetry in the gas density in the disk shows the gravitational influence on the planet. The gas density is linear color-coded. The migration process is already finished.

period of $\sim 17 T_{\text{bin}}$. This results from the planet with its increasingly inclined orbital plane periodically crossing the binary star orbital plane. Comparatively, the pull of $F_{\text{tot},z}$ in the single star case remains negligible by a factor $\gtrsim 100$. Beyond $\sim 70 T_{\text{bin}}$, the gravitational force contribution of the binary star $F_{\text{bs},z}$ dominates the total force in magnitude, as this is visible in Fig. 4.62. In the early phases, i.e. within the first $10 T_{\text{bin}}$ of the system evolution, it is visible that the hydrodynamic force $F_{\text{hd},z}$ is the dominant contribution to the total net force, which causes the original misalignment of the planet with respect to the binary orbit.

As the planet feels the gravitation of the disk, the pull in z direction first increases and then decreases over time (see Fig. 4.63). The force was calculated using the Eq. 4.5 and Eq. 4.4. This time the mass-force relation is less visible as the mass decrease is much smaller (see Fig. 4.64), compared to the mass increase in the simulation with the Stockholm condition. In the simulation with the Stockholm condition the mass increases over time and the force increases as well. Furthermore, to compare the results with the corresponding single star setups where the secondary were removed from the simulations, the results were added to the figure. Then, when comparing the single star setup with the binary setup, one can see that the force in z direction is significantly lower in the single case than in the binary case. This is in line with the observed z movement of the planetary orbit in the binary case. By only looking at the force of the disk on the planet at $400 T_{\text{bin}}$ (20.4 years) for the binary setup $0.01 M_{\odot}$ $(-2.22 \cdot 10^{19}, 1.45 \cdot 10^{18}, -5.87 \cdot 10^{18})$ and the binary setup $0.1 M_{\odot}$

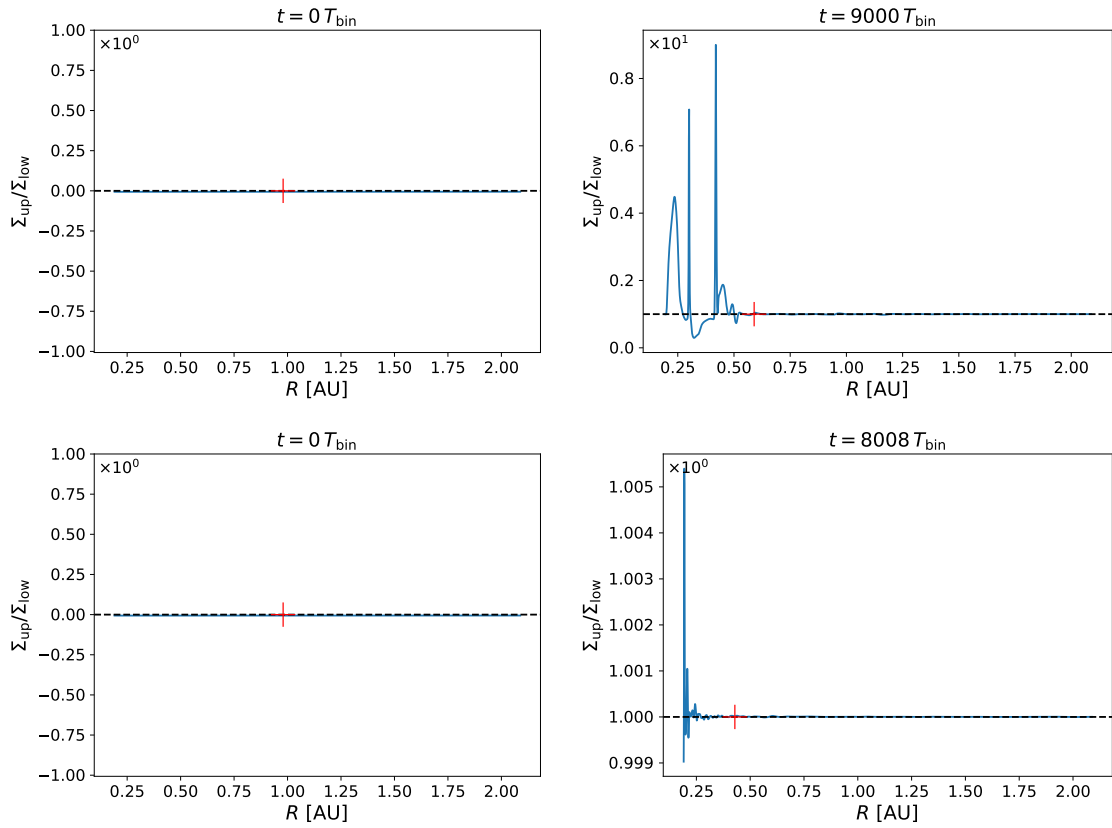


Fig. 4.61: The evolution of $0.01 M_{\odot}$ disk is computed by the ratio $\rho_{\phi}(r) = \Sigma_{\text{up}}/\Sigma_{\text{low}}$ (top) binary case and (bottom) single case. (left top) binary simulation at the start of the simulation $0 T_{\text{bin}}$. (right top) binary simulation after the migration process $9000 T_{\text{bin}}$. (left bottom) single simulation at the start of the simulation $0 T_{\text{bin}}$. (right bottom) single simulation during the migration process $8008 T_{\text{bin}}$. The red marker indicates the location of the planet.

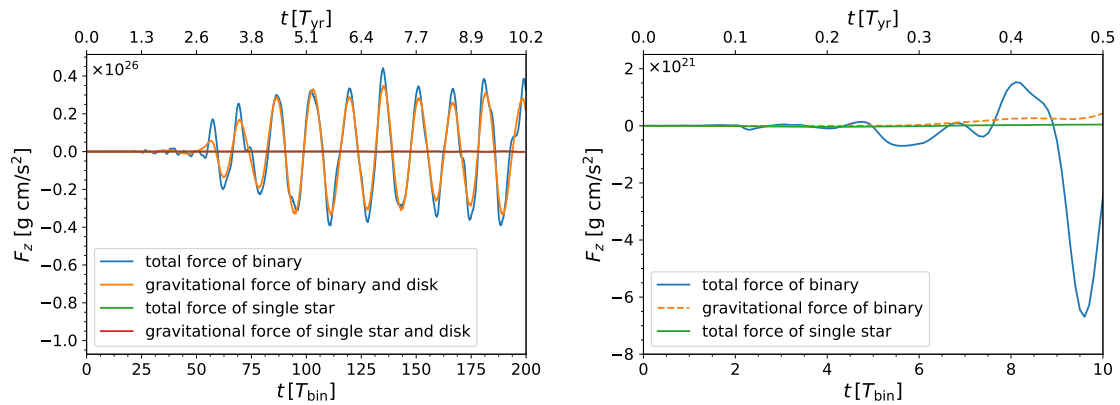


Fig. 4.62: Evolution of the force on the planet in a $0.01 M_{\odot}$ disk mass system in z-direction. Thus the negative sign shows the direction of the force. The gravitational force of the stars and disk in the z-direction starts later than the force calculated from the impulse of the planet.

$(-8.64 \cdot 10^{19}, -2.02 \cdot 10^{19}, -1.26 \cdot 10^{19})$, one can see that again the higher disk mass influences the force by a factor of ten which was also the case for the single star setup. Nevertheless, the force on the planet is dominated by the gravitational force of the binary stars.

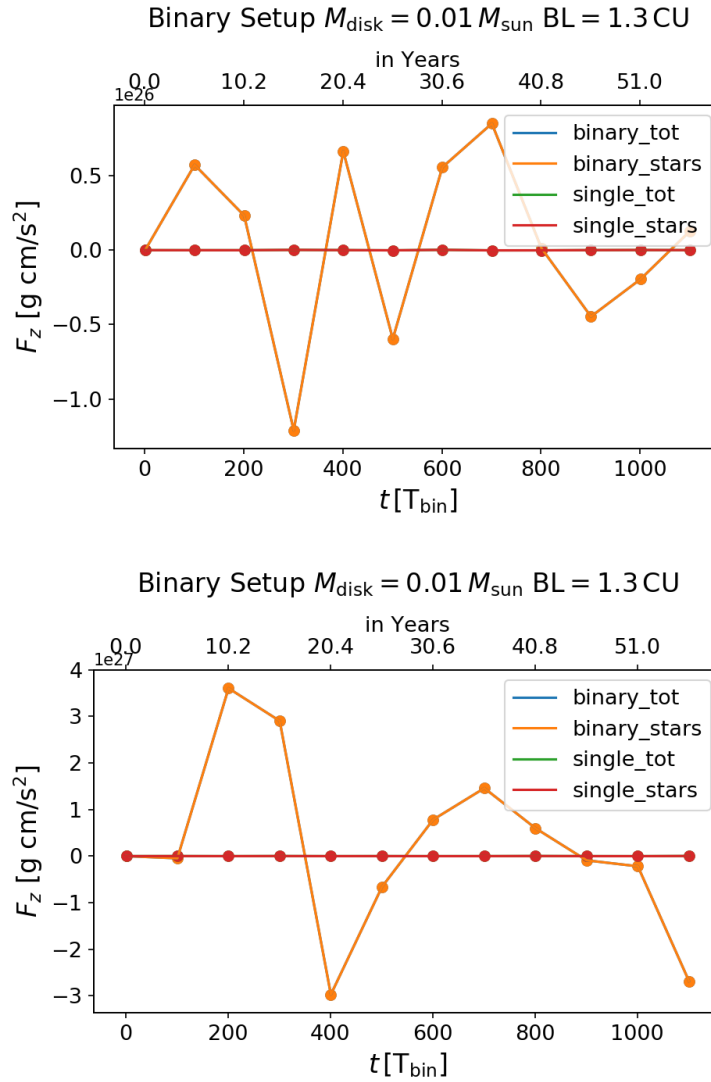


Fig. 4.63: Evolution of the force on the planet in a $0.01 M_{\odot}$ (top) and $0.1 M_{\odot}$ (bottom) system in z direction. Thus the negative sign shows the direction of the force. One can see in the binary case the force on the planet is higher. The force in z direction of the stars and the total force are roughly the same. Thus the main force is exerted from the stars. Furthermore, the force is depending on the location of the planet.

The mass-force relation can be seen if one compares different binary eccentricities and disk masses (see Tab. 4.13). The binary orbits' eccentricities do not lead to an increase in force, but for $17 T_{\text{bin}}$, the force is higher at a higher eccentricity. This is not contradicting the findings in the previous paragraph. There it was shown that a higher binary eccentricity leads to an earlier inclination.

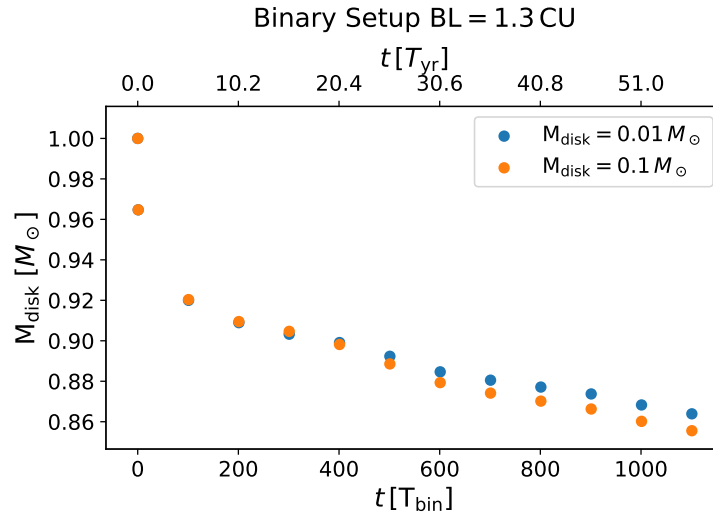


Fig. 4.64: Normalized disk mass over time for a disk with initial $0.01 M_{\odot}$ (decrease 13.17% over 51 years) and $0.1 M_{\odot}$ (13.98% over 51 years) disk mass. The Stockholm condition is turned off and the inner boundary is at $1.3 a_{\text{bin}}$.

The comparison of the different mass ratios and the influence on the force is difficult. As the planet is at different locations at the same point in time and the force of the planet is highly dependent on the location within the disk plus the binary.

Physical effect vs. numerical noise The author tested a different boundary condition to verify that the above effects are physical and not originating from numerical noise. Therefore, the author changed the open inner OUTFLOW boundary condition to the ANTISYMMETRIC closed boundary condition. This new boundary condition prevents mass flow onto the stars, and the mass of the disk stays constant during the simulation (see Fig. 4.65). Those simulations show that the inclination is independent of the choice of the boundary condition. Therefore, the inclination has a physical origin. If it would depend on the boundary condition, than the chance is high that it is numerical noise. With the ANTISYMMETRIC setup, a higher mutual inclination between the angular momentum of the planet and the normal vector (see Fig. 4.66) than with the open boundary condition can be detected. The higher disk mass leads to a higher force onto the planet (see Fig. 4.67).

In the last three months, a new version of the code was released due to the findings in this thesis. To understand the effects of this thesis, Frédéric Masset needed to investigate the viscosity tensor in spherical coordinates. He found a change was needed to ensure the physical correctness of the code. The author tested the simulations with the new code (see Fig. 4.68). Despite the new version of the code, the physical effect found by the author

Tab. 4.13: Force in CGS units in z direction on planet of the Kepler 38 system at different T_{bin} for different disk masses and star eccentricities. The planet gets ejected out of the system at the simulation $0.1M_{\odot}$ & $0.5 e_{\odot}$. At $910 T_{\text{bin}}$ the planet is already 200 AU away.

		$0.01M_{\odot}$	$0.021M_{\odot}$	$0.05M_{\odot}$	$0.1M_{\odot}$
0.1	$e_{\odot} T_{\text{bin}} = 17x$	$-4.50 \cdot 10^{29}$	$-4.51 \cdot 10^{29}$	$-4.45 \cdot 10^{29}$	$-3.90 \cdot 10^{29}$
	y	$-8.06 \cdot 10^{27}$	$-4.26 \cdot 10^{28}$	$-1.38 \cdot 10^{29}$	$-3.19 \cdot 10^{29}$
	z	$1.15 \cdot 10^{21}$	$-1.67 \cdot 10^{22}$	$3.61 \cdot 10^{22}$	$-2.22 \cdot 10^{22}$
	$e_{\odot} T_{\text{bin}} = 910x$	$-5.85 \cdot 10^{29}$	$4.84 \cdot 10^{29}$	$-1.37 \cdot 10^{30}$	$6.33 \cdot 10^{29}$
	y	$-1.09 \cdot 10^{28}$	$1.39 \cdot 10^{30}$	$1.21 \cdot 10^{30}$	$-5.59 \cdot 10^{29}$
	z	$-7.30 \cdot 10^{25}$	$-3.09 \cdot 10^{26}$	$-4.33 \cdot 10^{26}$	$-1.46 \cdot 10^{26}$
0.5	$e_{\odot} T_{\text{bin}} = 17x$	$-4.53 \cdot 10^{29}$	$-4.52 \cdot 10^{29}$	$-4.52 \cdot 10^{29}$	$-3.74 \cdot 10^{29}$
	y	$-2.49 \cdot 10^{28}$	$-5.72 \cdot 10^{28}$	$-1.72 \cdot 10^{29}$	$-3.45 \cdot 10^{29}$
	z	$-3.53 \cdot 10^{21}$	$2.44 \cdot 10^{22}$	$-6.00 \cdot 10^{25}$	$-1.45 \cdot 10^{24}$
	$e_{\odot} T_{\text{bin}} = 910x$	$4.81 \cdot 10^{29}$	$1.23 \cdot 10^{28}$	$-1.05 \cdot 10^{30}$	$1.11 \cdot 10^{16}$
	y	$-3.02 \cdot 10^{29}$	$-5.42 \cdot 10^{29}$	$-3.94 \cdot 10^{29}$	$1.14 \cdot 10^{15}$
	z	$5.72 \cdot 10^{25}$	$-6.87 \cdot 10^{23}$	$-3.44 \cdot 10^{26}$	$3.47 \cdot 10^{12}$

before is kept. This gives even more confidence in the physicality of the effect. One can see that the effect develops slightly later. Nevertheless, the effects described previously are visible, and the results reinforce the previous findings of this physical effect. Significantly, the early development of the hydrodynamical force shows the same physical behavior, and just the starting time is delayed (see Fig. 4.69). Another symmetry test is performed to ensure the physical effect. Therefore, the velocity field of the disk is analyzed with the following equation:

$$v_z(r, \phi, \pi + \theta) + v_z(r, \phi, \pi - \theta) = v_{zc} \quad (4.11)$$

where v_z is the Cartesian velocity in the z direction with an offset (positive and negative) towards the mid-plane of θ . For mirror symmetry towards the mid-plane in the disk v_{zc} from the Eq. 4.11 should be zero.

The author applies this formula to the velocity field of the new simulation, and the results lead to a comparable result to the density distribution. Namely, zero at the beginning of the simulation ($0 T_{\text{bin}}$) and non-zero at a later point in time of the simulation ($150 T_{\text{bin}}$). Similarly, the asymmetries are located in the inner part of the simulated disk. The results of the binary and single star setup are displayed in Fig. 4.70. It visualizes that the turbulence displayed through the velocity is neglectable small in the single star system and significantly large in the binary system. This underlines the findings of the significant role of the binary in this thesis. Letting the binary system further evolve, one can observe a broader region

with $v_z c$ velocities $\neq 0$ (see Fig. 4.71). The asymmetry level is 18 times smaller in the outer region than in the inner region. Nevertheless, in the more involved case, the turbulent inner region expands to 1.5 AU (small turbulence is seen over the complete disk) where the turbulent inner region expands to 1 AU at an early stage. This is in line with the findings of Kurbatov et al. (2014, p. 787) and Kurbatov et al. (2017, p. 1036) where he found that the turbulence is induced by the binary and propagates through the disk.

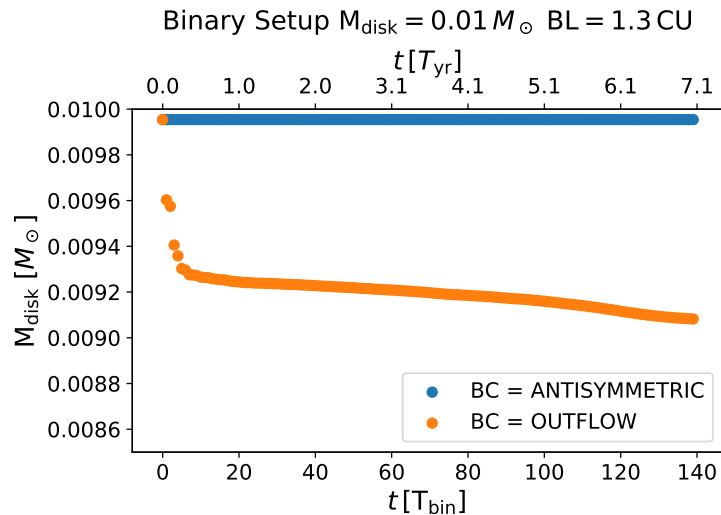


Fig. 4.65: Disk mass over time for a disk with $0.01 M_{\odot}$. The blue dots show the ANTISYMMETRIC boundary condition, where the disk mass stays constant over the simulation. The orange dots show the previous open boundary condition which is called in the code OUTFLOW. The Stockholm condition is turned off and the inner boundary is at $1.3 a_{\text{bin}}$.

Therefore, the author found a correlation between the turbulence and the vertical displacement of the planet. The turbulence is the initiator of the vertical displacement, and then the influence of the binary takes over.

Future studies need to analyze how to maintain this inclination, e.g., a larger computational domain could be of interest. In this chapter, it was found that the planet's inclination depends on the disk mass, and on the perturbation induced by the binary, mainly via its eccentricity. The mass ratio of the binary as well as the starting position of the planet play a secondary role. The viscosity parameter influences the inclination of the planet significantly. This thesis did not analyze the influence of the planet's mass itself, but this would be an exciting additional point for future work. Another interesting numerical experiment could be to test the influence of the binary semi-major axis on the inclination of the planet.

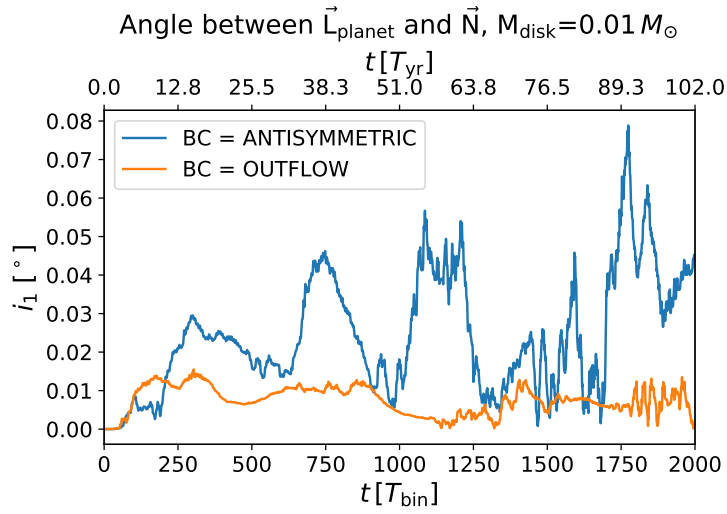


Fig. 4.66: Mutual inclination of the planet’s angular momentum and the normal vector for a disk with $0.01 M_{\odot}$ with the ANTISYMMETRIC closed boundary condition and the OUTFLOW open boundary condition. The blue curve shows the ANTISYMMETRIC boundary condition, where the inclination is higher. The orange curve shows the previous open boundary condition which is called in the code OUTFLOW. The Stockholm condition is turned off, and the inner boundary is at $1.3 a_{\text{bin}}$.

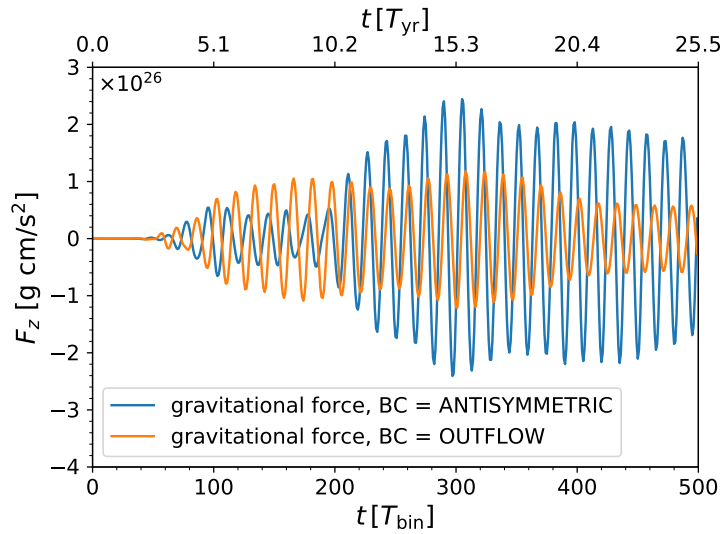


Fig. 4.67: Evolution of the force on the planet in a $0.01 M_{\odot}$ disk mass system in z-direction with the ANTISYMMETRIC closed boundary condition and the OUTFLOW open boundary condition. Thus the negative sign shows the direction of the force. The blue curve shows the ANTISYMMETRIC boundary condition, where the force grows and stays at a higher level. The orange curve shows the previous open boundary condition, which is called in the code OUTFLOW. There the force is initially higher but decreases over time. The force of the ANTISYMMETRIC condition stays higher. This compares with the inclination development in Fig. 4.66, where the inclination raises first equally. Then, the inclination of the OUTFLOW condition elevates higher, but after roughly $200 T_{\text{bin}}$ the inclination of the ANTISYMMETRIC boundary condition becomes higher and stays higher. The Stockholm condition is turned off, and the inner boundary is at $1.3 a_{\text{bin}}$.

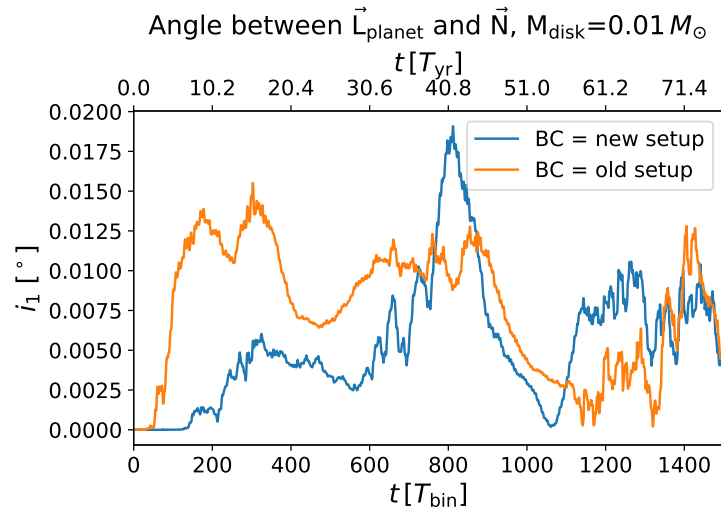


Fig. 4.68: Mutual inclination of the planet’s angular momentum and the normal vector for a disk with $0.01 M_{\odot}$ with the old and the new version of the code. The blue curve shows the new code, where the inclination starts later. The orange curve shows the previous setup of the code. The Stockholm condition is turned off, and the inner boundary is at $1.3 a_{\text{bin}}$.

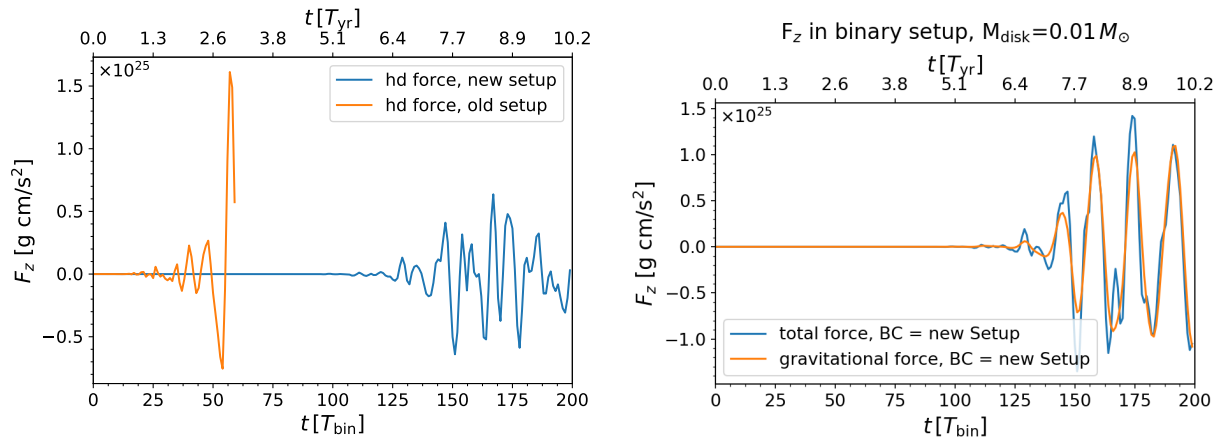


Fig. 4.69: (left) Hydrodynamical force for a disk with $0.01 M_{\odot}$ with the old and the new version of the code. The blue curve shows the resulting hydrodynamical force of the new code, where the inclination starts later. The orange curve shows the previous setup of the code. The Stockholm condition is turned off and the inner boundary is at $1.3 a_{\text{bin}}$. Comparing the results to the mutual inclinations in Fig. 4.68, one can see that the inclination rises earlier and higher with the old setup, thus the hydrodynamical force also rises earlier and higher. (right) Evolution of the total force and gravitational force in z-direction for a disk with $0.01 M_{\odot}$ and for the new version of the code. One can see that the inclination behaves similar to the old version of the code.

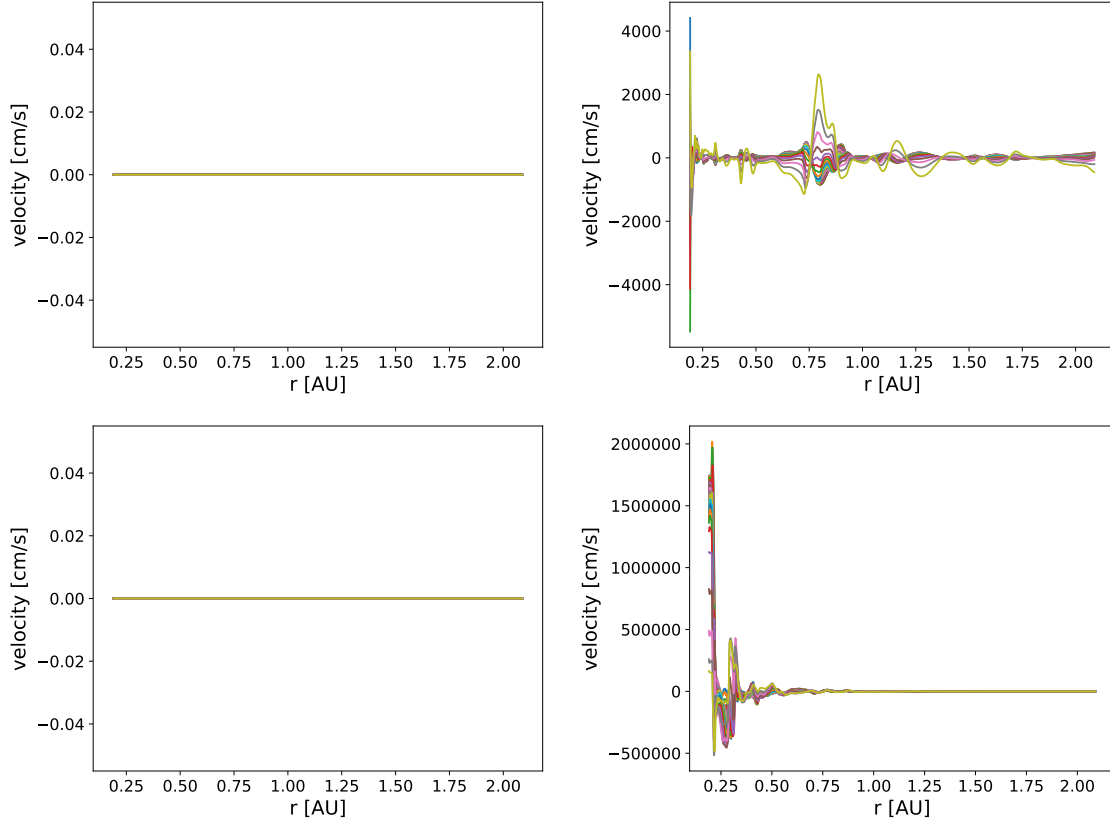


Fig. 4.70: 19 combined ($\pi + \theta$ and $\pi - \theta$) velocities in z direction in the disk in the single star setup (top) and new binary setup for a disk (bottom) with $0.01 M_{\odot}$ plotted against the radial distance to the center of mass. The Stockholm condition is turned off and the inner boundary is at $1.3 a_{\text{bin}}$. (left) $0 T_{\text{bin}}$ (right) $150 T_{\text{bin}}$. As expected, the mirror symmetry is at the beginning of the simulation (v_{zc} is zero over the whole disk) and it becomes asymmetric over time. If one compared the evolved single star setup with the binary setup, one can see the difference of magnitude between those cases.

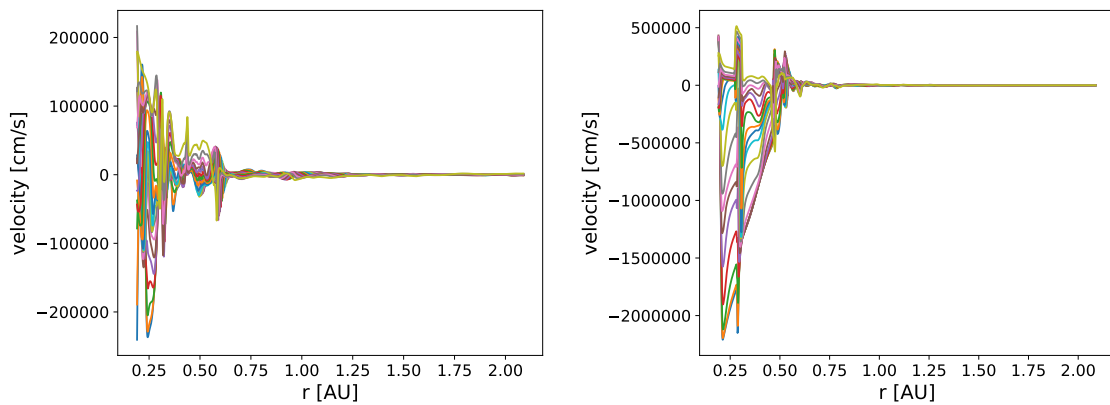


Fig. 4.71: 19 combined ($\pi + \theta$ and $\pi - \theta$) velocities in z direction in the disk in the new binary setup for a disk with $0.01 M_{\odot}$ plotted against the radial distance to the center of mass. The Stockholm condition is turned off and the inner boundary is at $1.3 a_{\text{bin}}$. (left) $3004 T_{\text{bin}}$ (right) $3907 T_{\text{bin}}$. The velocity is displayed in the xz plane where the planet is located. As expected, the turbulence is distributing through the disk.

5 Contribution to the METIS instrument

In parallel to the work presented in Chapter 4 in the field of numerical experiments and comparison to observations, the author of this thesis contributed to the instrument development of the Mid-infrared ELT Imager and Spectrograph (METIS). The scientific objective of METIS is, among other goals, to serve the science of protoplanetary disks (Brandl et al., 2016, p. 2), which the author has discussed in the context of Kepler 38 in the first part of this thesis.

The current instruments on the Very Large Telescope (VLT)¹, an 8.2 m telescope, have a limited angular resolution (λ/D) by the VLT's diameter and focus mainly on the UV, visible and near-infrared spectrum of the light. Only two instruments, the CRyogenic high-resolution InfraRed Echelle Spectrograph (CRIRES) and the VLT Imager and Spectrometer for mid-InfraRed (VISIR), focus on the mid-infrared. The METIS instrument is the successor of those two infrared instruments at the VLT² and will provide a roughly five times higher angular resolution considering the 40-meter diameter of the Extremely Large Telescope (ELT)³. In this chapter, the author will highlight the results she contributed. Therefore, a general overview of the instrument METIS is given, followed by the laboratory tests and proof-of-concept for the METIS instrument.

5.1 METIS

To improve the sensitivity and (spatial) resolution of telescopes observing, e.g., protoplanetary disks, the European Southern Observatory is developing the largest mirror telescope for optical and infrared observations in the world, the ELT. The ELT is a 40 m class telescope which is currently under construction in Chile and should start operations in 2027⁴.

It will be a next-generation telescope which is enabled through technological improvements,

¹<https://www.eso.org/public/germany/teles-instr/paranal-observatory/vlt/> (2021-07-06)

²<https://www.eso.org/public/announcements/ann15073/> (2022-03-16)

³<https://www.eso.org/sci/facilities/eelt/> (2018-04-09)

⁴<https://www.elt.eso.org/about/timeline/> (2021-07-06)

e.g., in the area of adaptive optics (AO) and large segmented mirrors, combined with learnings from past ground-breaking developments like the ground-based VLT (pioneering adaptive optics⁵) and the Keck telescopes (pioneering segmented telescope technology⁶). The ELT has a primary mirror which is 16 times larger than the primary mirror of the widely known Hubble Space Telescope (HST)⁷. However, the HST observes in the wavelength range of 0.1 - 2.5 μm (UV, visible, and near-infrared), whereas the wavelength range of METIS/ELT covers the wavelength regime 3 - 13.5 μm (mid-infrared) (Brandl et al., 2016, p. 1). Therefore the instrumentation of Hubble and METIS are not directly comparable. METIS on the ELT is more directly comparable with the successor of the Hubble telescope, namely the James Webb Space Telescope (JWST)⁸ and its 6.5 m primary mirror, which was recently launched and designed for observing primarily in the infrared. The JWST instrumentation covers a wavelength range from 0.6 to 28 μm . The ELT will have a much-increased collecting power as this is proportional to D^2 , where D is the telescope diameter. Thus, in theory the sensitivity of the ELT is much increased. However, the ELT remains a ground-based telescope and therefore faces the problem of the strong contribution from thermal background, which is of course not the case for the space telescope JWST. This means that even though the ELT benefits from a larger diameter than the JWST, it will be less sensitive because of the presence of the huge infrared thermal background on Earth.

One of the first light instruments of the European ELT is METIS⁹, which will be installed on the Nasmyth platform (Brandl et al., 2016, p. 1). The other two first-light instruments, MICADO and HARMONI, focus diffraction-limited imaging and integral field spectroscopy in the optical and near-infrared ranges (0.47 - 2.45 μm). A fourth instrument, MAORY, will not perform observations by itself, but will rather implement multi-conjugated adaptive optics to compensate for the atmospheric turbulence¹⁰ and mainly serve the MICADO instrument. The role of MAORY is to provide MICADO with stable and sharp images across a large field of view through state of the art adaptive optics. MICARDO and MAORY together will provide a 50.5" \times 50.5" field of view with a pixelscale of 4 milli-arc seconds (mas), and a higher resolution option with 1.5 mas over a 19" \times 19" field of view¹¹.

The METIS instrument will enable the study of high redshift infrared galaxies, active galactic nuclei, Solar System bodies, protoplanetary disks, and exoplanets (Brandl et al., 2016,

⁵<https://www.eso.org/public/announcements/ann18066/> (2022-03-16)

⁶<https://www.keckobservatory.org/about/telescopes-instrumentation/> (2022-03-16)

⁷<https://www.hubblesite.org/mission-and-telescope/the-telescope> (2021-09-06)

⁸<https://www.webb.nasa.gov/content/about/comparisonWebbVsHubble.html> (2022-03-16)

⁹<https://www.elt.eso.org/instrument/METIS/> (2021-06-17)

¹⁰<https://www.elt.eso.org/instrument/> (2021-06-17)

¹¹<https://www.elt.eso.org/instrument/MICADO/#science> (2022-03-16)

p. 2). In particular, since one of the key science cases of METIS concerns the study of protoplanetary disks and exoplanets, it is especially interesting for the author of this thesis to participate to the development of this instrument.

On the topic of circumstellar/circumbinary disks and planet formation, METIS will be able to study the dynamics of the molecular gas in the planet-forming region. Moreover, gaps and cavities in disks will be observed (Brandl et al., 2018, p. 2). Even though METIS cannot directly image the Kepler 38 system due to the small separation of 0.37 mas in comparison to the ~ 20 mas resolution of the instrument in the L band, comparable low-mass young binary stars hosting disks such as the famous GG Tau system could be observed in order to obtain a direct insight into the structure and the planet-induced asymmetries of the host disk(s). Therefore, the work of the author of this thesis in helping developing the METIS instrument is an indirect contribution to these future studies.

The instrument is built by a consortium consisting of the University of Cologne (Germany), NOVA (The Netherlands), MPA Heidelberg (Germany), CEA-Saclay (France), UK-ATC (United Kingdom), KU Leuven (Belgium), ETH Zürich (Switzerland), University of Michigan (US), ASIAA (Taiwan) and the A Consortium (Austria). The instrument will be fully assembled and tested in Leiden before being shipped to Chile (Rutowska et al., 2020, p. 1). It consists of two separate units. Those units are the imager and the spectrograph, both located inside a cryostat, which reduces the instrumental thermal background radiation (Brandl et al., 2016, p. 12). This is especially important for an instrument operating from the ground in the mid-infrared since the thermal background from the night sky and in particular from the telescope itself are already orders of magnitudes larger than the scientific signal. By putting the instrument in a cryostat, the thermal background from the instrument itself is much reduced, while the detector is separately cooled down to its operational temperature of a few tens of Kelvins. A schematic overview of the METIS instrument is shown in Fig. 5.1.

5.1.1 Warm Calibration Unit

The METIS instrument is divided into different sub-systems to be developed by different consortium partners. One of the sub-systems is the Warm Calibration Unit (WCU) developed at the University of Cologne, Germany. As the name suggests it, the WCU is located outside of the cryogenic part of METIS and delivers calibration during on-sky operations ensuring long-term measurement repeatability. The foreseen WCU calibration functionalities are summarized in Fig. 5.2.

Conceptual design of the WCU

In this paragraph, the general design chosen for the WCU and developed by the team in Cologne is introduced (see Fig. 5.3). The WCU is built on an optical bench that holds the relay optics and the focal plane sources. It is supported by an hexapod, which is interfaced with the METIS cryostat in order to maintain the WCU on top of the instrument (see Fig. 5.1). A folded mirror placed on a translation stage in the periscopic arm can be moved into the beam in order to inject the light from the calibration sources into METIS. When scientific operations are carried out during the night, the folded mirror is translated out from the beam in order to let the ELT beam through.

In the WCU, there are two focal-plane stations: one for the infrared wavelength range (named WCU-FP2.1) and one for the visible wavelength range (named WCU-FP2.2). Both focal planes of WCU-FP2.1 and WCU-FP2.2 can be re-imaged at a particular location in the periscopic arm named WCU-FP1, which is the replication of the ELT focal plane. This is illustrated in Fig. 5.3.

The visible station WCU-FP2.2 contains a CCD camera, which is used for the visualization and inspection of the focal plane inside the METIS cryostat, in particular during the AIV phase.

The infrared station WCU FP2.1 is the main calibration station and is the focus of this part of the thesis. It generates the majority of spectral and spatial sources (Baccichet et al., 2018, p. 4), in the form of extended sources, or a series of point sources (i.e., pinholes which are back-illuminated). These artificial sources can emit over the L ($3.8 \mu\text{m}$), M ($4.7 \mu\text{m}$), and N ($10 \mu\text{m}$) bands (Baccichet et al., 2018, p. 1). The main role of the artificial sources at FP2.1 is to provide calibration sources for the monitoring of the image quality and the field distortion of the METIS imager, the linearity and flat-field of the detector, as well as the spectral response of the METIS high-resolution spectrograph. The hardware components generating those artificial sources are, in particular, the blackbody source (BB), the aperture mask wheel, and the integrating sphere (IS). The inputs of the integrating sphere are one port for interfacing the blackbody source and three fiber ports for the monochromatic calibration

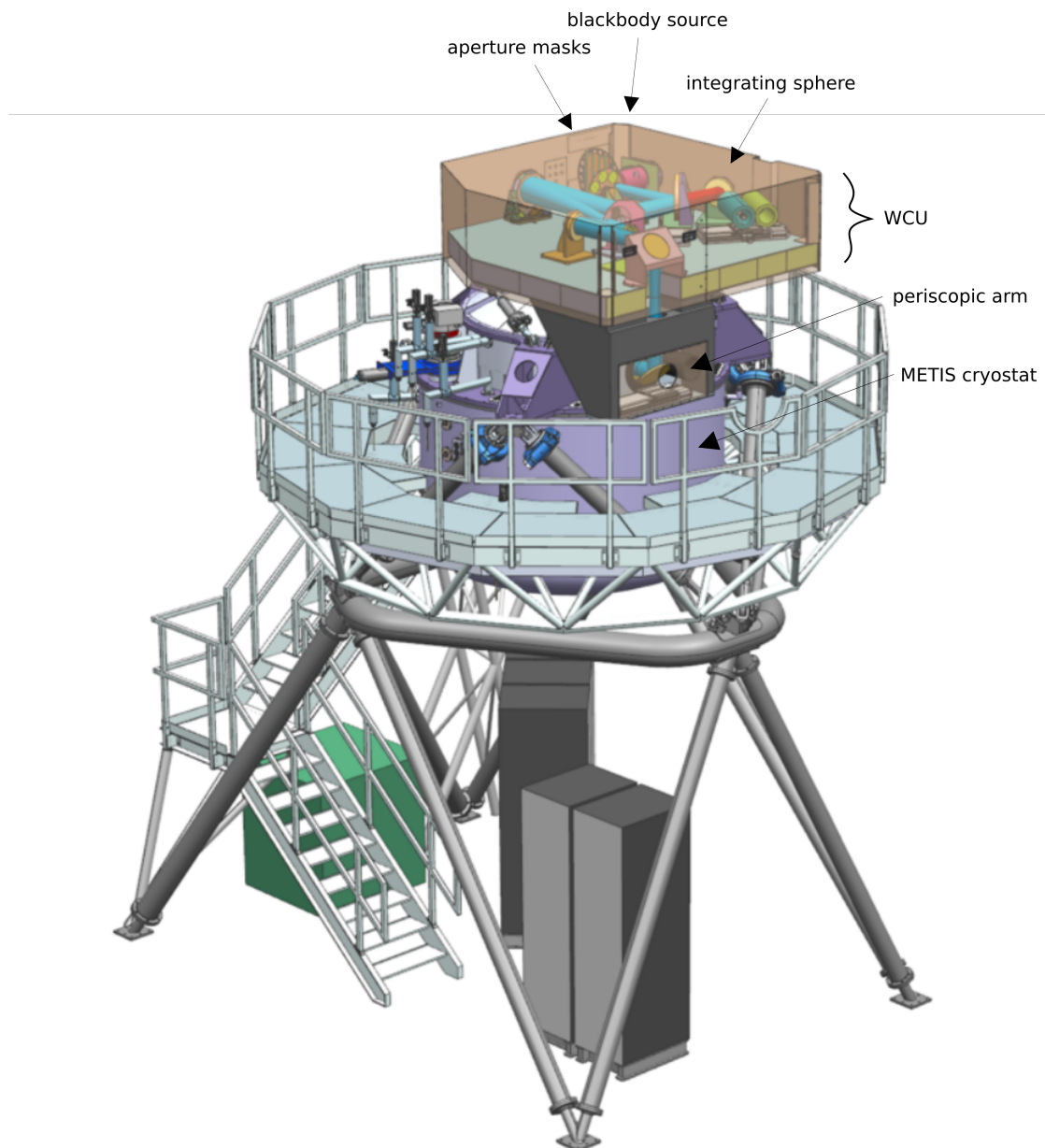


Fig. 5.1: Schematic view of the METIS instrument. On the top is the Warm Calibration Unit (WCU). The three essential measurement devices (aperture mask, blackbody source, and integrating sphere) for this thesis are indicated within the WCU. The periscopic arm consists of mirrors that root the light from the artificial sources of the WCU into METIS. When the calibration unit is no longer operated, the mirror in the periscopic arm can be translated out to let the ELT beam through. The Warm Support Structure (WSS) forms the hexapod structure supporting the METIS cryostat. This figure is adapted from Rutowska et al. (2020, p. 2).

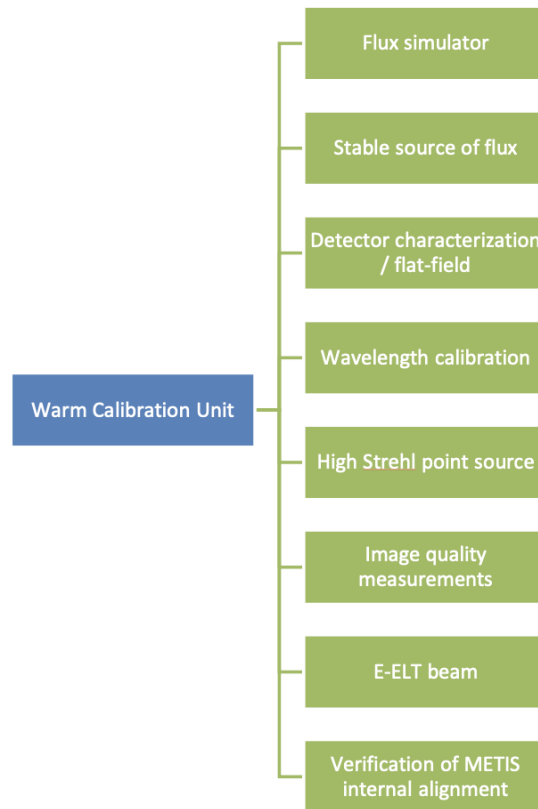


Fig. 5.2: Structure of the WCU calibration functionalities adapted from the WCU Preliminary Design Review documentation.

sources. These are three laser sources used to calibrate the response of the spectrograph using the precise knowledge of laser lines. In between the blackbody source, which temperature is roughly tunable in temperature between 290 and 1300 K, and the integrating sphere, an aperture mask is placed, which role is to rapidly vary the flux entering the integrating sphere for the purpose of detector linearity tests.

Contributed tests

In the following the experiments and tests which were led by the author of this thesis on the METIS part are listed. They are essentially presented in a chronological order.

- Measurements on the influence of the external and laboratory-specific air-conditioning system onto the overall temporal stability: the goal is to identify potential biases on the measured quantities.
- Measurements on the blackbody response time scale: for calibration purpose, the blackbody source is expected to emit a highly stable flux over several hours. The author

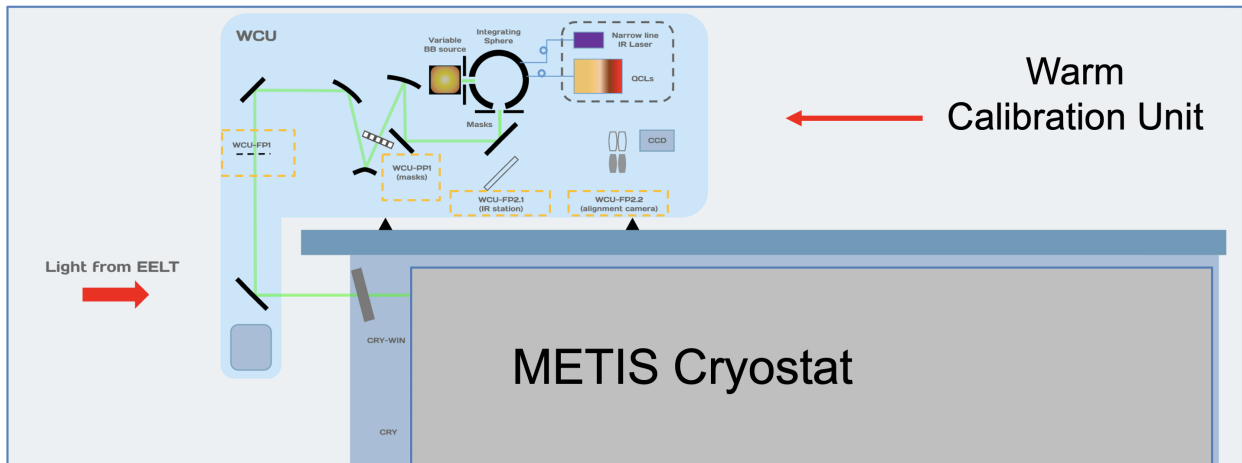


Fig. 5.3: Schematic of the WCU. The dashed orange squares indicate the two focal-plane stations (FP2.1 and FP2.2), the focal plane in the periscopic arm (FP1), as well as the position of the pupil-plane WCU-PP1. The light path is indicated as a green light in the configuration where FP2.1 is active. By inserting a beam-splitter (not visualized here) the station FP2.2 can become active for alignment monitoring.

investigated this parameter and estimated the intrinsic source stability.

- Measurements on the flux passing through the integrating sphere as a function of the blackbody temperature: these measurements enable the comparison with the analytically calculated flux to ensure the correctness of the assumed theory. In particular, this permits to benefit from a model of the flux emitted by the blackbody + integrating sphere assembly for the purpose of signal-to-noise ratio.
- Measurements on the thermal characteristics of the assembly blackbody source coupled to integrating sphere: the influence of the self-radiation through heating of the integrating sphere was investigated by the author. In an experiment, one must ensure to measure real signals and not the thermal background.
- Measurement of the flux temporal stability of the assembly blackbody source coupled to the integrating sphere.
- Measurement of the spatial uniformity of the integrating sphere output: the METIS requirement on the spatial uniformity is on the order of better than 1%. The author therefore investigated the level of uniformity reachable using a similar laboratory setup.
- Proof-of-concept of the aperture mask assembly for the measurement of the METIS detector linearity. The goal is to control the flux input but without varying the flux spectrum that would result from a change in the temperature of the blackbody. This characterization should be achievable in a short amount of time (typically less than ~ 1 hour).

- Measurements of suitable material to serve as pinhole sources: the METIS instrument relies on the usage of the integrating sphere, which output port is masked by different pinhole geometries.

5.2 Laboratory tests and proof-of-concept

In this section, the details of the laboratory work pursued by the author are presented. Thanks to this work, most of the concepts presented at the Preliminary Design Review and in the subsequent period could be validated.

5.2.1 Description of the measurement devices

For the experiments, different measuring devices are used, with their properties described hereafter.

Blackbody source

The blackbody source used in the WCU is the IR-563/301 blackbody system by Infrared Systems Development Corporation. It is an industry-standard ideal source for near-, mid-, and far-infrared. In Tab. 5.2.1 the important specifications of the device are presented.

Parameter	Value
BB source operating temperatures [° C]	50 - 1050
Emissivity of the internal coating	> 0.99
Diameter of the cavity aperture [mm]	25.4

Tab. 5.1: Parameters of the blackbody source¹²

Powermeter

The powermeter is the S302C Thermal Power Head by Thorlabs, which was made for broadband measurements¹³. Specifications of the powermeter are shown in Tab. 5.2. An important information is that the powermeter presents a relatively flat response across the operational bandwidth.

¹²<https://www.infraredsystems.com/Products/blackbody563.html> (2018-04-09)

¹³<https://www.infraredsystems.com/Products/blackbody563.html> (2018-04-09)

¹⁴<https://www.thorlabs.de/drawings/d132d3a99d47351d-13910445-96EE-2E09-184EEB7D98BE0866/S302C-SpecSheet.pdf> (2018-04-09)

Parameter	Value
Optical power range	100 μ W - 2 W
Wavelength range of operation	190 nm - 25 μ m
Power resolution	1 μ W

Tab. 5.2: Parameters of the powermeter¹⁴.

Testo 174-2010 Mini-Datalogger for temperature

The Testo 174-2010 is a temperature sensor that is made for long-term temperature monitoring. It can measure up to 16000 values which can be read out via a USB-connection¹⁵. The key parameters of the Testo Mini-Datalogger are displayed in Tab. 5.3.

Parameter	Value
Range	-30 to + 70° C
Resolution	\pm 0.5° C

Tab. 5.3: Parameters of the Testo 174-2010 Mini-Datalogger¹⁶.

Integrating sphere

The integrating sphere planned for the final WCU will have an internal diameter of 30 cm, while the output port will be 10 cm in diameter (see Fig. 5.4). It will host one input port to feed in the radiation from the blackbody source, as well as three ports to find in monochromatic radiation through fibers. A CAD¹⁷ model of the sphere is shown in Fig. 5.4.

¹⁵<https://www.testo.com/de-DE/testo-174-t-set/p/0572-0561> (2018-04-27)

¹⁶<https://www.thorlabs.de/drawings/d132d3a99d47351d-13910445-96EE-2E09-184EEB7D98BE0866/S302C-SpecSheet.pdf> (2018-04-09)

¹⁷Computer Aided Design

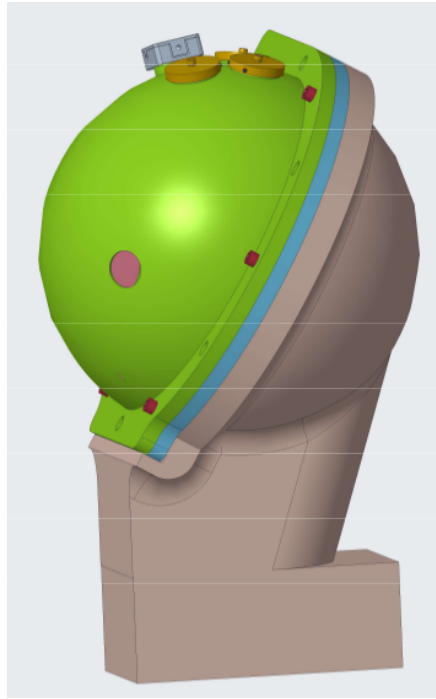


Fig. 5.4: Computer Aided Design model of the Integrating Sphere which will be placed in the WCU. It has three fiber ports for laser sources and one port for interfacing the blackbody source.

For the tests made in this thesis, a smaller commercial integrating sphere with a diameter of 15.24 cm was used instead¹⁸, namely the integrating sphere 819D by Newport. The integrating sphere used for the tests has a diameter of 15.24 cm and three output ports (two of them with a diameter of 2.54 cm and one of them with a diameter of 6.35 cm)¹⁹.

The basic principle of the integrating sphere is to allow multiple inner reflections of the ray entering the sphere to produce a spatially smooth and uniform output radiance profile through multiple reflections (Hanssen & Snail, 2006, p. 3). The inner area of an integrating sphere is typically coated with a highly reflective diffusive material to enable as many multiple reflections as possible. Since the IS needs to operate over a large wavelength range, the material gold is chosen to cover that large wavelength range (see Fig 5.5). In this case, the IS is made out of infragold (Baccichet, 2017, p. 15). Thus, the IS allows a detector to receive, independently of its location, flux proportional to the light entering the sphere (Hanssen & Snail, 2006, p. 3).

¹⁸https://www.newport.com/medias/sys_master/images/images/hc3/h13/8797116858398/Integrating-Spheres-Datasheet.pdf (2021-06-17)

¹⁹https://www.newport.com/medias/sys_master/images/images/hc3/h13/8797116858398/Integrating-Spheres-Datasheet.pdf (2021-06-17)

²⁰<https://host.web-print-design.com/labsphere/products/images/graphs/infragold.gif> (2022-03-17)

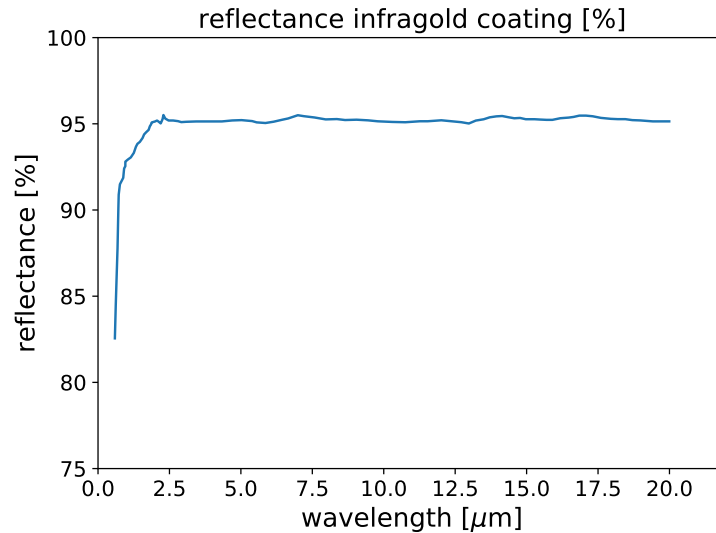


Fig. 5.5: The reflectance of infragold is displayed against the wavelength. The reflectance of infragold is stable at 95% over a large wavelength range in the mid-infrared. This figure has been plotted from data provided by labsphere²⁰.

The radiance at the output port of the integrating sphere can be calculated as

$$L_S = \frac{\Phi_i}{\pi A_S} M + L_{is} \quad [\text{W}/\text{m}^2/\text{sr}] \quad (5.1)$$

Φ_i is the incoming flux crossing the input port. A_S is the internal surface area of the sphere, L_{is} is the self-emission generated by the sphere, which can be understood as background contribution, and M is the sphere multiplier factor. Physically, this factor represents the increase in the radiance due to the numerous reflections inside the integrating sphere. This factor is calculated as

$$M = \frac{\rho}{1 - \rho(1 - f)} \quad (5.2)$$

with ρ being the average internal coating's reflectivity ($\sim 95\%$) and f being the port fraction given by

$$f = \frac{A_i + A_e}{A_S} \quad (5.3)$$

where A_i is the area of the input port, whereas A_e is the area of the output port. In case the sphere presents more than two ports, f is computed from the sum of all the ports.

From those formulas, one can deduce that an efficient integrating sphere needs to have a small total area of the ports compared to the total internal area in order to keep the parameter f as small as possible. In most real integrating sphere, a typical value is $0.02 < f < 0.05$ (see Fig. 5.6). Later in this chapter, those formulas are applied in a test case.

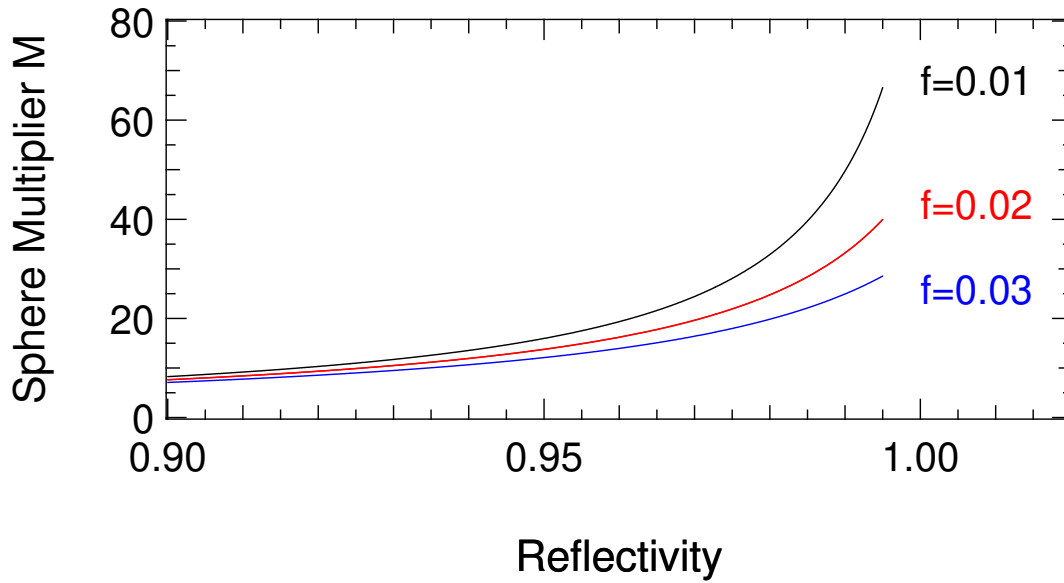


Fig. 5.6: Dependence of the sphere multiplier M as a function of the reflectivity of the coating ρ and the port fraction f (top). The input reflectivity is varied from 90% to 99.5%. With the port parameters of the sphere used in the author's experiment, one obtains a port fraction of $f = 0.014$, hence a sphere multiplier of ~ 15 .

Uncooled IR camera - Gobi640 GigE

The uncooled IR camera - Gobi640 GigE hosts an uncooled microbolometer detector with a resolution of 640 x 480 pixels²¹. A microbolometer detector is made of amorphous silicon and is used for detecting infrared radiation. The radiation heats a thermally insulated membrane which has its electrical resistance changed. This change is measured and converted into an electrical signal²². Some parameters of the Gobi640 GigE are displayed in Tab. 5.4.

Parameter	Value
Temperature range	-40 to + 60° C
Spectral range	8 - 14 μm
Integration time range	1 - 80 μs
Size of the detector chip	640×480 pixels

Tab. 5.4: Parameters of the uncooled IR camera - Gobi640 GigE²³.

²¹<https://www.xenics.com/long-wave-infrared-imagers/gobi-640-series/> (2020-04-24)

²²https://www.ims.fraunhofer.de/en/Business_Units_and_Core_Compencies/IR-Imagers/Technologies/Microbolometers.html (2020-05-17)

²³<https://www.xenics.com/long-wave-infrared-imagers/gobi-640-series/> (2020-04-24)

Temperature sensor from Lake Shore Cryotronics

The product "Model 218 Temperature Monitor" has eight sensor inputs and supports Cryogenic Temperature Sensor with which it can measure temperatures from ~ 20 mK to 1,500 K²⁴. In this case, PT100 sensors are used.

5.2.2 Laboratory tests of source stability

Since the blackbody source is a core calibration element of the Warm Calibration Unit, the author has carefully characterized the temporal and spatial stability of this unit. Furthermore, one needs to test how the laboratory environment influences the stability of the source. The settling times to reach the required stability are also measured, as well as the temporal stability expected at different temperatures.

Air-conditioning dependence

This test analyses the influence of the laboratory environment, and in particular of the air-conditioning system, on the environmental temperature as well as on the flux measurement. The lab air-conditioning system is based on an active monitoring of the ambient temperature following a rectangular function aiming at maintaining this temperature as stable as possible within ± 0.5 °C. The air-conditioning cools down the environment to a nominal temperature. As soon as this value is reached, the air-conditioning stops. As a consequence, the environment slightly heats up, which triggers again a cooling cycle by the air-conditioning, following a saw-tooth behavior around the desired temperature.

In order to test the influence of the air-conditioning, two simultaneous measurements are conducted. The powermeter is placed in front of the blackbody cavity aperture, at a distance which is not essential since the goal is to measure a temporal stability. In parallel, the Testo Mini-Datalogger was positioned on the lab table to monitor the environmental temperature. Both the flux and the temperature were recorded simultaneously and this simple experiment was run over different week-ends, free of any human presence. A close view on a fraction of this temporal window is shown in Fig. 5.7, where it becomes visible that the spike-like pattern of the flux measured by the powermeter is correlated with the temperature correction induced by the air-conditioning system. The author does not need here for the purpose of this work to analyze quantitatively this behavior. What is important is to identify a possible bias in the measurement of the flux stability that results from small but regular variations of the laboratory environment. These variations do not probably impact the temperature of the ceramic in the blackbody source, but rather the thermal background in the lab that

²⁴<https://www.lakeshore.com/products/cryogenic-temperature-monitors/model-218/Pages/Overview.aspx> (2018-05-03)

is measured by the powermeter up to $25\ \mu\text{m}$. The only measure that can be taken in the case of a need for a highly stable environment over a short amount of time is to turn off the air-conditioning system and avoid the presence of a person in the room.

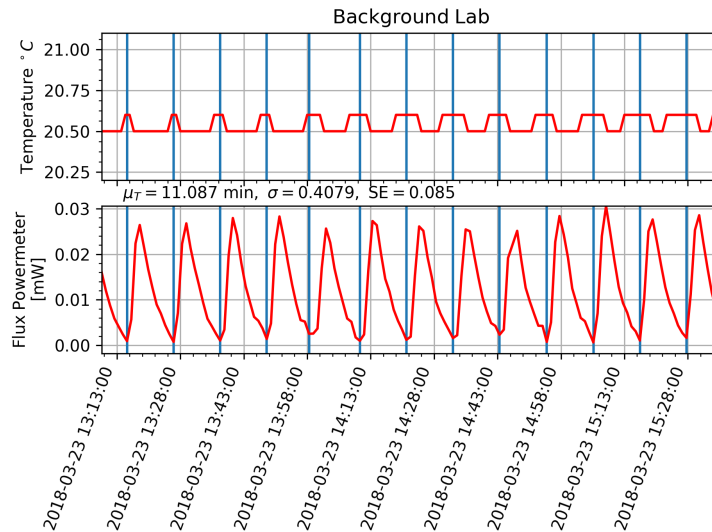


Fig. 5.7: Comparison of the measurements of the background flux with the background temperature.

Blackbody settling and cooling timescales

When turning on and operating the blackbody source, a procedure is required to indicate the characteristic time for the source to reach the nominal temperature desired by the operator, as well as the settling time after which the output power reaches a specific flux stability.

The powermeter described in Sect. 5.2.1 was connected to one of the output port of integrating sphere, itself coupled to the blackbody source (see Fig. 5.8). In this setup, the blackbody output power was recorded over several hours to take the first glimpse on its temporal stability.

First, the characteristic time needed for the blackbody to heat up is measured. The powermeter measured the incoming flux while the blackbody was turned off to start each measurement. After 30 min of background measurements, the blackbody was turned on and set successively to 50°C , 100°C , 200°C , 300°C , 400°C , 500°C , 600°C , 800°C , and 1000°C . From the results shown in Fig. 5.9, a warming up time from 35 min up to 67 min is measured before the flux stabilises. The criterion to assess sufficient flux stability is based on the visual inspection of the curve, when a horizontal plateau is reached for the flux. This qualitative criterion is sufficient to estimate the order of magnitude of source settling time. Similarly, one observes that the horizontal plateau is reached quicker for higher than lower temperatures. Generally, the stability timescale appears to be relatively long (~ 45 min on

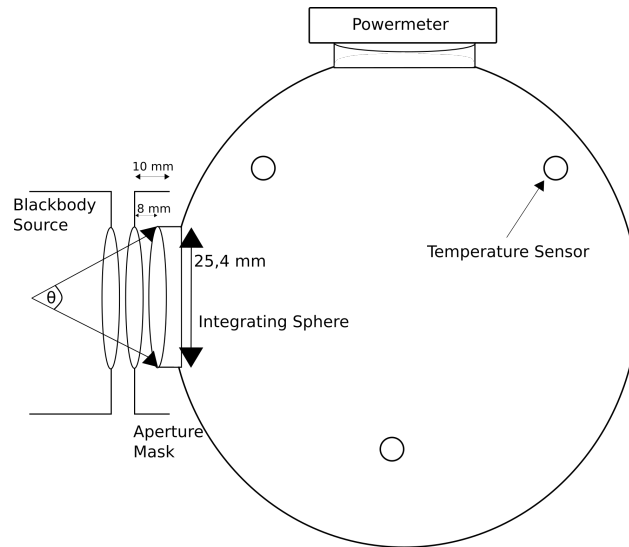


Fig. 5.8: Configuration of the setup for the stability measurement. The blackbody source is coupled to the integrating sphere and the flux is measured with the powermeter at the 25.4 mm diameter output port. The third output port is kept closed. The temperature sensors monitor the warm up of the integrating sphere itself. This figure is taken from Graf et al. (2020, p. 2).

average) which sets a constrain on the calibration plan of METIS.

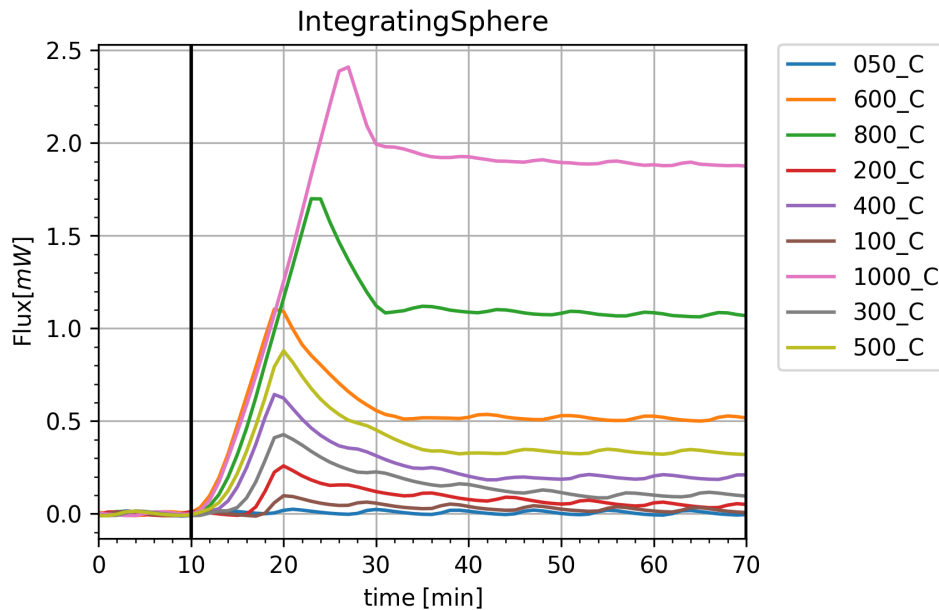


Fig. 5.9: The flux for different temperatures of the blackbody, measured by the powermeter, is plotted against time. The periodic oscillations visible in the plateau region originate from the air-conditioning influence. This figure is taken from Graf et al. (2020, p. 3).

Finally, a more detailed characterization of the properties of the blackbody source was conducted in order to better understand the timescales for cooling down the source using the

same setup of Fig. 5.8. The blackbody was initially set by its controller at 30° C and then raised to 350° C, 500° C, 750° C and finally to 1000° C. From the maximum value, the temperature was then reduced following the inverse sequence. Every set temperature was kept for one hour before changing it. The sequence of measurement is presented in Fig. 5.10. The temperature value entered with the controller (dashed line) is compared to the effective blackbody temperature that is read out from the controller (black line). As expected, a transition regime in which a characteristic peak of the physical temperature of the blackbody is observed before its final stabilization. The amplitude of this peak is considerably reduced towards the higher temperatures. On the contrary, during the process of decreasing the temperature, the transition 'reversed' peak is not as strong, but the cooling time scales appear to be longer than the warm-up timescales. Globally speaking, it is found that setting the temperature from one temperature to another should be about 45 min apart as the transition times for the lower temperatures take longer (Graf et al., 2020, p. 2).

These measurements are important in order to prepare the calibration time schedule precisely. The time in this schedule is limited, as the main part of the observing time should be observing and not calibrating. In addition, the measurements provided information, for example, about repeatability and stability of the blackbody temperature and generated flux intensity (Graf et al., 2020, p. 3).

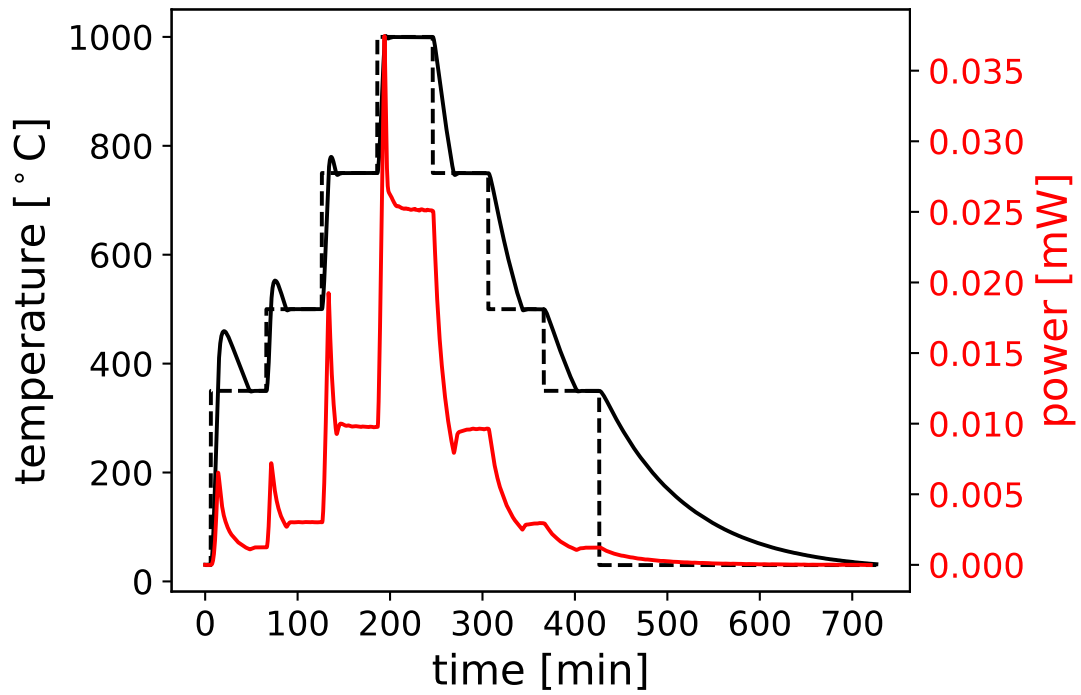


Fig. 5.10: Transition regime of the blackbody source in the warm-up and cool-down phases. The dashed curve indicate the different nominal temperatures set by the controller: 30°C, 350°C, 500°C, 750°C and 1000°C. The continuous line shows the effective changes in temperature as monitored through the read out temperature and for which a transition regime is observed. The red curve corresponds to the flux as measured with the powermeter.

Flux temporal stability

In a second step, the author measured the source stability over several hours for the different setting temperatures reported in Fig. 5.11 (Graf et al., 2020, p. 2). In this case the residual influence of the air-conditioning system of the laboratory is clearly visible and penalizing. In particular for low flux values, it is seen that the relative stability is worse than 10 % over a zoomed in time duration of about 70 min (see Table 5.5).

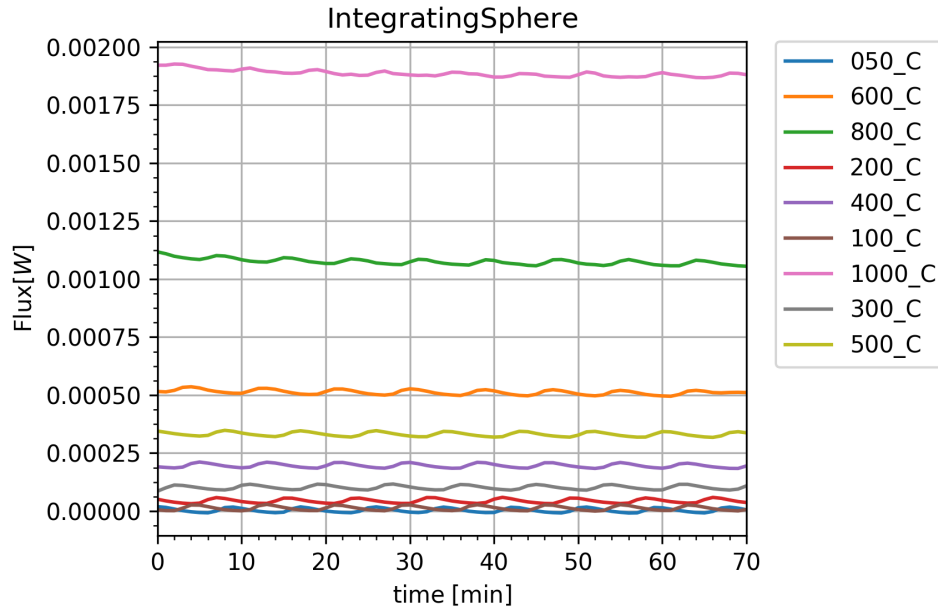


Fig. 5.11: Long-term stability of the blackbody where the periodic effect of the air-conditioning is visible.

Tab. 5.5: Mean and standard deviation of the flux temporal sequence reported in Fig. 5.11. The last column reports the flux relative stability over about one hour, which is in this case dominated by the influence of the air-conditioning in the lab.

Temperature [C°]	mean [W]	std [W]	relative stability [%]
50	4e-6	9e-6	225
100	1.3e-5	9e-6	69
200	4.4e-5	9e-6	20
300	1.02e-4	9e-6	8.8
400	1.96e-4	9e-6	4.6
500	3.31e-4	9e-6	2.7
600	5.06e-4	9e-6	1.8
800	1.071e-3	1.3e-5	1.2
1000	1.879e-3	1.4e-5	0.7

Before discussing the mitigation of the air-conditioning bias, the author exploits the results of Fig. 5.11 and Table 5.5 to allow a direct comparison between the (normalized) measured

flux and the expected theoretical flux for the nine different temperatures, as this is later done in Sect. 5.2.2. According to the specifications of the powermeter, the measured flux should be in principle integrated from 0.2 to $25\ \mu\text{m}$ for a given temperature of the blackbody. This comparison is shown in Fig. 5.12 (left) where the measured flux normalized to its maximum value (red filled circles) is compared to the theoretical blackbody emission in the aforementioned spectral range. While the exponential trend is observed, the theoretical and experimental values are not perfectly matching. It was then observed that when the lower cut-off wavelength was increased to $2.2\ \mu\text{m}$ instead of $0.2\ \mu\text{m}$ in the theoretical calculation, the match becomes almost excellent (see Fig. 5.12, right). This can easily be explained if one recalls the graph of Fig. 5.5: indeed, the gold reflectivity decreases very rapidly below ~ 1.5 to $2\ \mu\text{m}$, which results into an almost negligible flux contribution in the visible range. This shows that the conditions of testing of the WCU module are well understood.

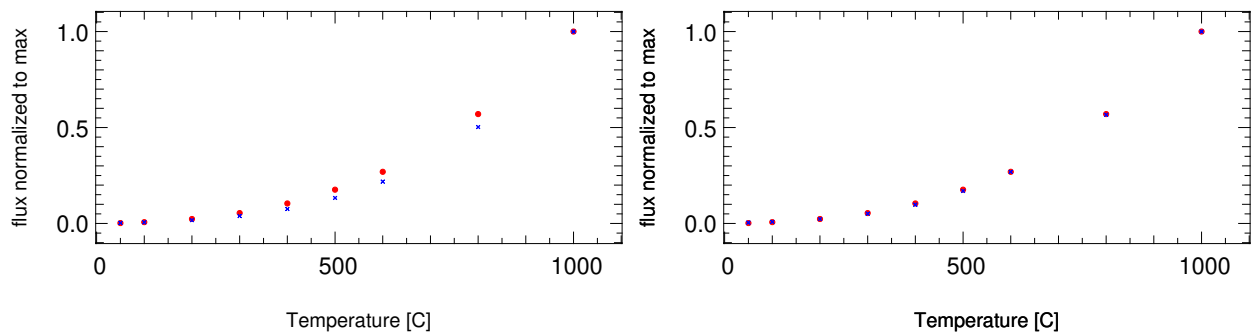


Fig. 5.12: Experimental (red filled dots) versus theoretical (blue crosses) normalized flux. On the left, the Planck's function is integrated from 0.2 to $25\ \mu\text{m}$ whereas on the right the lower cut-off wavelength is increased to $2.2\ \mu\text{m}$.

In order to further mitigate the stability bias due to the air-conditioning, the author simply reported the corresponding situation, namely with the A/C off. On the long-term this might not be a desirable solution, but it becomes critical for the goal of estimating the ultimate temporal stability of the source. Fig. 5.13 illustrates in a more direct way the comparison between the two situation for the case where the blackbody source temperature was set to 200°C . These plots illustrate both the settling time condition, which is confirmed to be in the range of $\sim 1\ \text{h}$, but more importantly the intrinsic stability of the source possibly. For $T = 200^\circ\text{C}$ in absence of A/C, the relative stability reaches, after flux stabilization, the value of $\sim 1\%$, which is a factor 20 better than in the case of the use of the A/C system. It is important to mention that in this experiment the author might ultimately be limited by the specification of the powermeter stability, and not by the stability of the blackbody source. Indeed, the blackbody source stability specified by the manufacturer is below 0.1% . However, the WCU team is interested here in an upper limit of the stability of the complete setup (blackbody source + integrating sphere + powermeter). For photometric calibration in

the mid-infrared range, a 1% stability of the calibration source will allow quite accurate estimates.

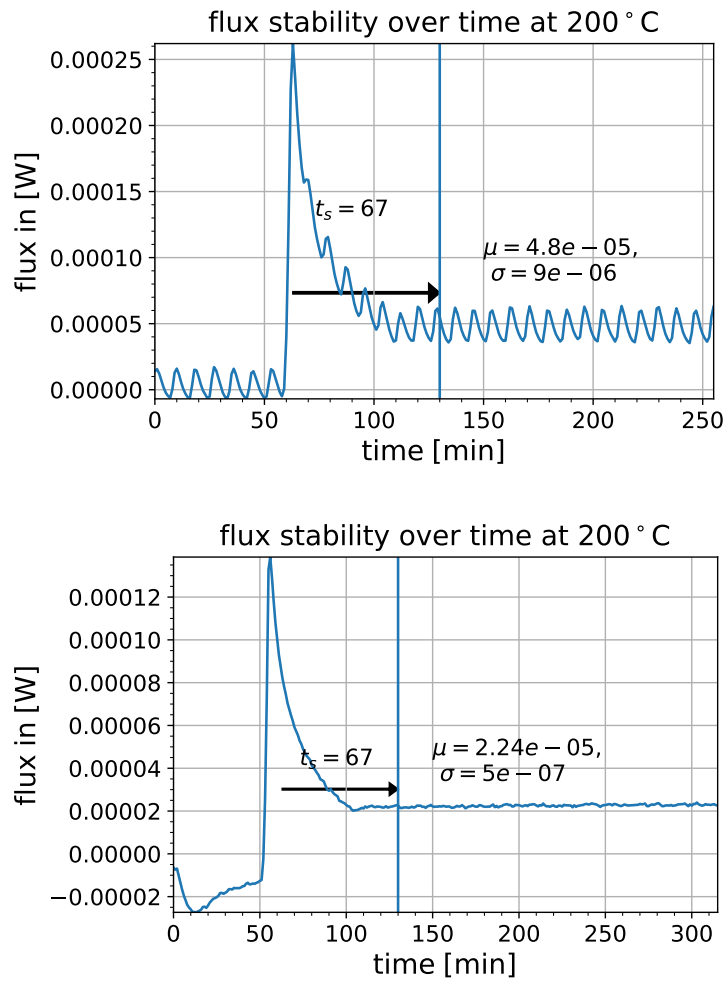


Fig. 5.13: Setup of the experiment is the same as in Fig. 5.18 but this time the measurements of the powermeter is displayed. (top) Measurements performed with air-conditioning. (bottom) Measurements performed without air-conditioning. One can see that the noise is also reduced. t_s is the settling time in minutes.

Comparison of flux experimental values with theoretical predictions

Here, a simple theoretical model of the flux output from the author's setup made of a blackbody source coupled to the integrating sphere is build and confronted to the measured experimental values. Once validated, this model can be later used to predict flux levels for different temperatures of the blackbody, which is relevant to estimate the achievable signal-to-noise ratio using the WCU calibration sources. The geometry used to perform the radiometric calculations is shown in Fig. 5.14 and Fig. 5.15.

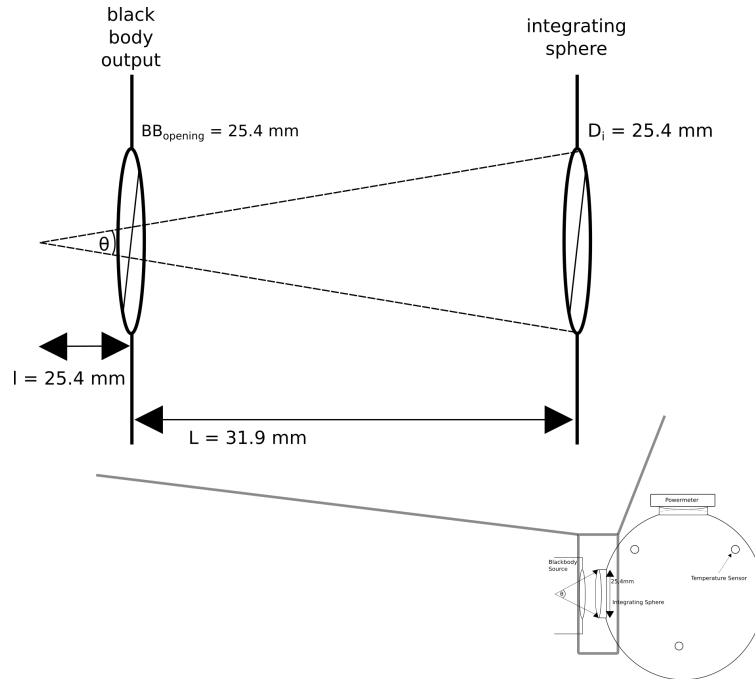


Fig. 5.14: Input geometry involving the blackbody source and the integrating sphere for the theoretical radiometric calculations. BB_{opening} is the diameter of the output aperture of blackbody source. D_i is the diameter of the input port of the integrating sphere. The emitting, lambertian, ceramic is located > 2.54 cm ahead from the blackbody output aperture. The relevant solid angle for the radiometric calculation is set by the input port of the integrating sphere.

Following Eq. 5.1 in the context of Fig. 5.14 the radiance at the integrating sphere output port can be estimated.

First, the flux Φ_i passing through the sphere input port is:

$$\Phi_i = \left(\pi \cdot \left(\frac{BB_{\text{opening}}}{2} \right)^2 \right) \cdot \left(\pi \cdot \left(\sin(\arctan(\frac{D_i/2}{L+l})) \right)^2 \right) \cdot \int_{\lambda_{\text{start}}}^{\lambda_{\text{stop}}} \frac{2hc^2}{\lambda^5} \cdot \frac{1}{(e^{\frac{hc}{\lambda k T_{BB}}} - 1)} d\lambda \quad (5.4)$$

with $BB_{\text{opening}} = D_i = 25.4$ mm. L and l are defined in Fig. 5.14. The quantities $\lambda_{\text{start}} = 0.2 \cdot 10^{-6}$ m and $\lambda_{\text{stop}} = 25 \cdot 10^{-6}$ m are the wavelength boundaries for the powermeter. Then, h is the

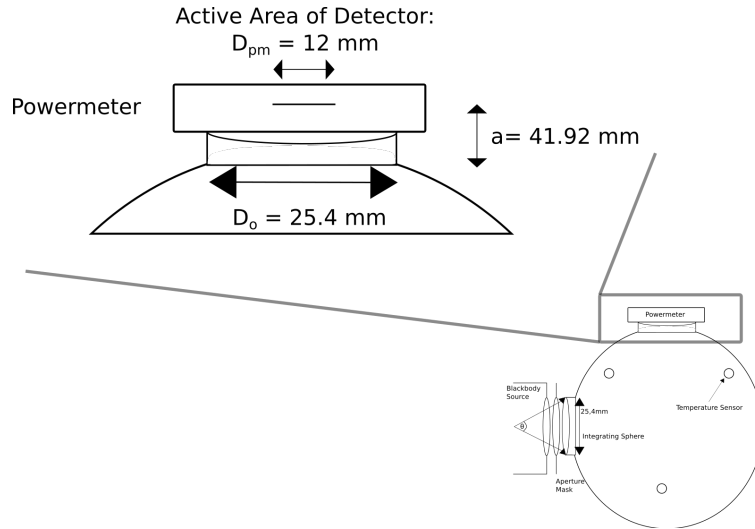


Fig. 5.15: Geometrical setup to determine the flux measured by the powermeter. To do so, it is important to know the path of the light between integrating sphere and powermeter. D_{pm} is the active area of the detector and D_o is the diameter of the opening of the integrating sphere.

Planck's constant, c the speed of light, k the Boltzmann's constant. The temperature of the source T_{BB} is varied between 320 K and 1300 K.

The sphere multiplier factor is

$$M = \frac{R}{1 - R \cdot \left(1 - \frac{A_i + A_o}{A_S}\right)} \quad (5.5)$$

where $A_S = \pi D_{\text{sphere}}^2$ is the internal surface of the integrating sphere with $D_{\text{sphere}} = 15.24$ cm and $A_{i/o} = \pi \left(\frac{D_{i/o}}{2}\right)^2$ is the area of the input, respectively output port of the sphere with $D_{i/o} = 2.54$ cm. R is the average gold reflectivity set to 0.95.

The radiance due to the self-emission of the sphere is further calculated following

$$L_{is} = 0.05 \int_{\lambda_{\text{start}}}^{\lambda_{\text{stop}}} \left(\frac{2hc^2}{\lambda^5} \cdot \frac{1}{\left(e^{\frac{hc}{\lambda k T_{is}}} - 1\right)} \right) d\lambda \quad (5.6)$$

where the factor 0.05 accounts for the low emissivity (i.e. high reflectivity) of the gold coated internal surface and T_{is} is the equilibrium temperature of the integrating sphere.

To compare it with the measurements done by the powermeter, the geometrical setup between the integrating sphere and the powermeter needs to be considered, which results in (see Fig. 5.15):

$$\Omega = \pi \cdot \left(\sin\left(\arctan\left(\frac{D_o/2}{a}\right)\right)\right)^2 \quad (5.7)$$

$$L_{\text{pm}} = 0.97L_S\Omega A_{\text{pm}} \quad (5.8)$$

with Ω being the solid angle, 0.97 is the “efficiency” of the powermeter detector (not 100 % of the radiation is absorbed), L_S is the flux exiting the integrating sphere and $A_{\text{pm}} = \pi(D_{\text{pm}}/2)^2$ is the active area of the powermeter detector.

The measured results are within the approximated range of the calculated fluxes (see Fig. 5.16).

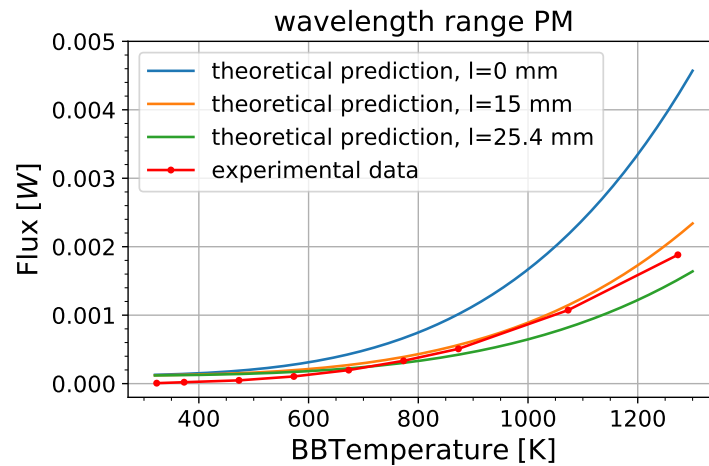


Fig. 5.16: Comparison of flux experimental values with theoretical predictions. The full spectral measurement range of the powermeter is considered from 0.2 to 25 μm , which implies that the self emission of the sphere is accounted for. The plot is very sensitive on the geometry (especially, the distance between BB and IS). As the cavity is far inside the blackbody, the light path is not straight, but is reflected inside the tube. Therefore, in this thesis three assumptions for the starting location for a straight path of the light ($l = 0, 15$ and 25.4 mm) are made. The blackbody temperature ranges from 300 K to 1300 K. For the self-emission of the sphere a fixed sphere temperature of $T_{\text{is}} \sim 25^\circ\text{C}$ is considered.

These calculations were made to ensure that the measured results are in agreement with the theory.

Thermal stability of the integrating sphere

The surface of integrating sphere is a potential source of undesired thermal background, which may add up to the contribution of the room temperature thermal emission. For this work, the author focuses on probing the expected temperature of the outer structure of the sphere to provide elements for the thermal assessment of the WCU through heat dissipation. Therefore, on top of the previous measurements with the powermeter, measurements with the PT100 sensors were performed to measure the temperature distribution on the sphere

and its influence and the environment. Six sensors were positioned on the surface of the sphere and distributed evenly, and two sensors were placed on the bench to appreciate possible heat dissipation via conduction in the metallic structures. Fig. 5.17 shows the results for two cases in which the blackbody source is set at 500°C and then 1000°C , with the air-conditioning system of the lab turned on. In all cases, the the distinguishable rise with the turning on of the blackbody is seen. To a smaller degree, the sensors positioned on the bench detect an increase in temperature due to heat conduction.

As expected, it is found that the increase in temperature of the surface of the integrating sphere depends on the blackbody set temperature. The sphere temperature does not exceed 22°C for a blackbody temperature set at 500°C , and $\sim 27^{\circ}\text{C}$ in the worst case for a blackbody temperature of 1000°C , respectively. The rather small increase in temperature of the bench suggests a relatively low efficient heat conduction process between the sphere and the bench, likely because of the small cross-section of the supporting post. This efficiency can be improved by inserting an optimized heat sink in the future.

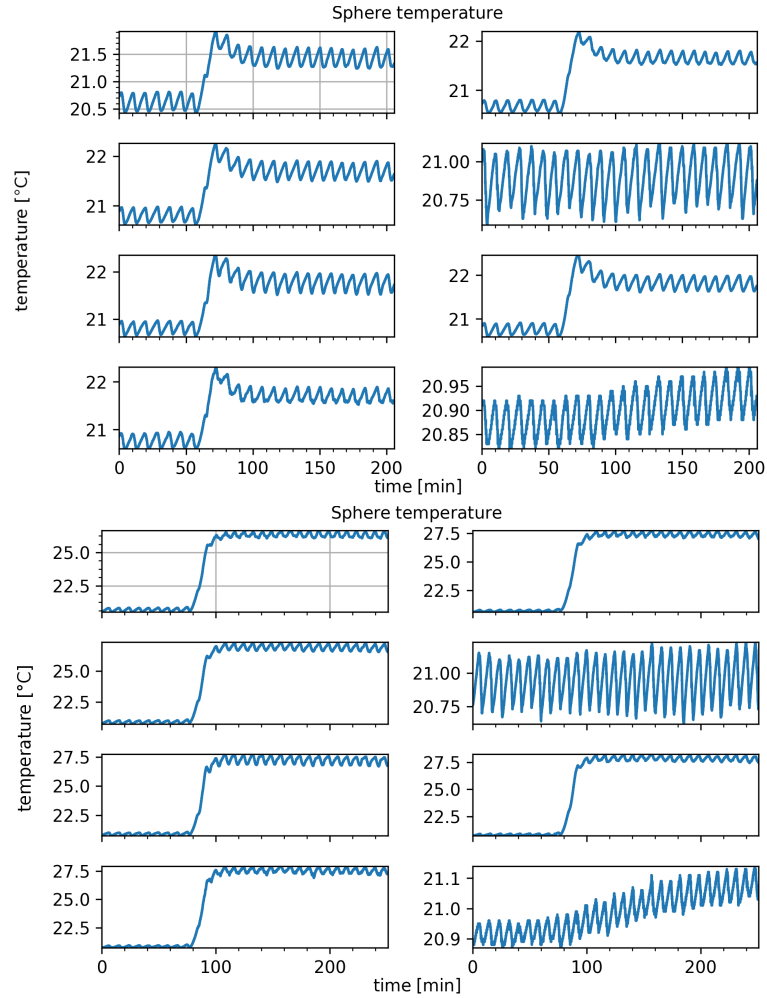


Fig. 5.17: Evolution of the temperature at the outer surface of the integrating sphere with the air-conditioning on. Six PT100 sensors were evenly distributed over the surface of the integrating sphere (plots 1-4 in the left column and the first plot on the top, as well as third plot in the right column), whereas two additional were positioned on the bench (second and last plots in the right column). The second plot in the right column measures the temperature on the bench roughly 1 m from the sphere and the last plot in the right column measures the temperature right underneath the integrating sphere. The eight plots on the top part correspond to the case where the temperature of the blackbody, to which the sphere is coupled, is set to 500° C. The eight plots on the bottom part correspond to a blackbody temperature of 1000° C.

To test how the measurements are effected by the laboratory environment without the air-conditioning, the previous measurements were repeated with this time a blackbody temperature set at 200° C, and with the air-conditioning turned on and off (see Fig. 5.18). First, as one expected the high-frequency variations due to the active control of the lab temperature clearly disappear when the air-conditioning is turned off.

With the air-conditioning turned on, only a small increase in temperature of $\lesssim 1^\circ\text{C}$ is observed for the sphere surface, which is in line with the sphere temperature being correlated with the set temperature for the blackbody. No clear temperature increase of the bench itself is being detected.

The results with the air-conditioning turned off are interesting. Apart from the disappearance of the high-frequency fluctuations, the author observes as expected an increase in the temperature deviation in comparison to the case where the air-conditioning is used. This temperature increase remains nonetheless reasonable, i.e. in the order of $\lesssim 1^\circ\text{C}$. However, it is observed that the temperature of the underlying bench increases in the same proportions. The argument on the heat conduction advanced previously can be seen under different light here: the absence of a temperature regulated by the air-conditioning allows the bench to behave as a heat sink, which in returns is observed in the form of an increased temperature change. The latter experiment is closer to the final operating condition of the WCU on the mountain, suggesting that efficient heat conduction could be the solution to mitigate the presence of unwanted localized hot spots in the WCU. Hence, the heat dissipation in the final WCU sub-system remains a critical point to be taken into account in the near future.

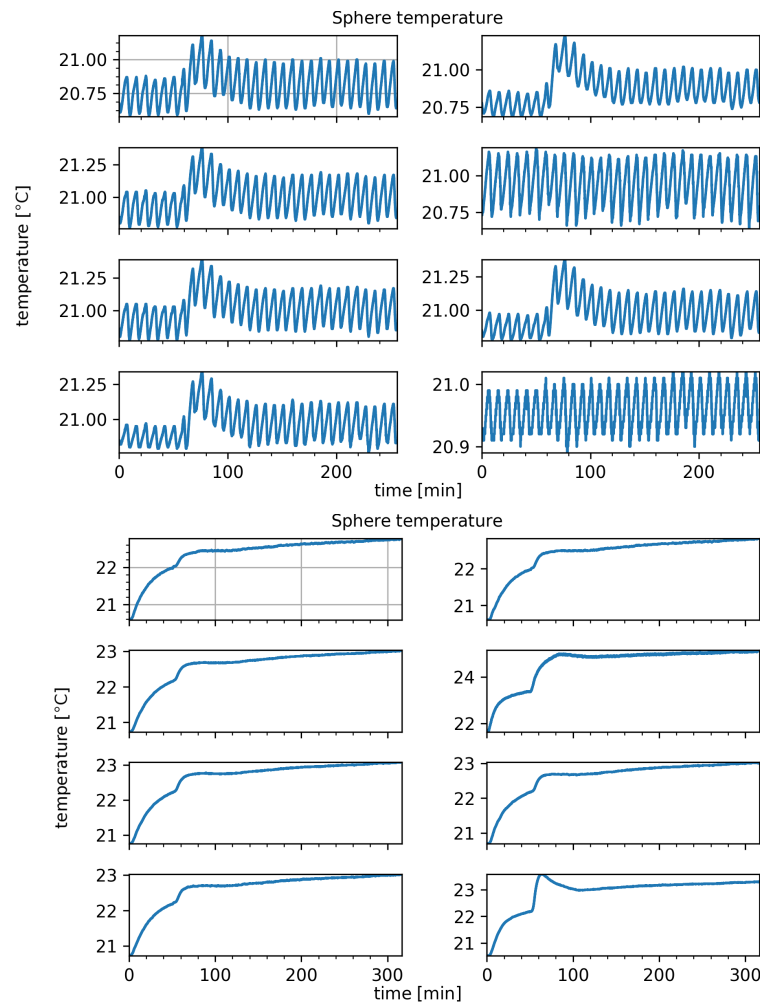


Fig. 5.18: Influence of the air-conditioning system of the laboratory on the heat dissipation from the integrating sphere. The setup for the top part is similar to Fig. 5.17. In the bottom part, the second plot in the right column measures the temperature of the airstream coming from the blackbody's fan. The last plot in the right column measures the temperature right next to the output of the blackbody on the manufacturer's aperture mask. In the top part, the air-conditioning is turned on. In the eight plots of the bottom part the air-conditioning was turned off.

5.2.3 Characterization of the spatial uniformity

In a second step, the output of the integrating sphere was measured with an uncooled thermal camera (N-Band: Gobi640 GigE) to test the spatial uniformity.

Spatial uniformity measurements

A spatially uniform output illumination from the integrating sphere of the WCU is key to allow the flat-field calibration of the detector. For this purpose, the focus is set on the integrating sphere and on the spatial uniformity of the output, which can be tested in the

laboratory. The camera was directed to image the 25.4 mm output port, while the blackbody is coupled to the input port of the integrating sphere (namely a 62.55 mm opening that has been reduced to 25.4 mm thanks to a gold cap provided by the manufacturer). Before characterizing the spatial flatness of the illumination at the output port of the sphere, it is necessary to characterize the flatness of the response of the Gobi640 camera itself. This is done by measuring a cold black surface cooled with liquid nitrogen (Graf et al., 2020, p. 3).

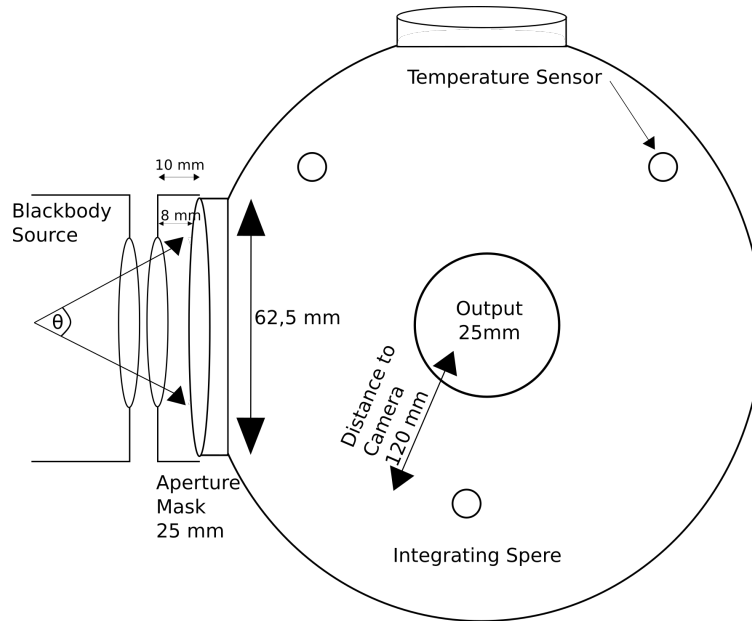


Fig. 5.19: Schematic view of the setup for the measurement of the spatial uniformity as seen from the camera. The camera is aligned with the 25.4 mm output port at a 120 mm distance. In this setup, the 62.55 mm input port faces the blackbody source with a gold coated mask in between that reduces the 62.55 mm port to a diameter of 25.4 mm. The second 25.4 mm output port on the top can be closed or used to attach the powermeter. This figure is taken from Graf et al. (2020, p. 3).

With the Gobi640 10- μm camera, a frame is taken every 2 μs with up to 15.000 frames that can be temporally co-added in order to reduce the noise associated to the thermal background.

In order to characterize the spatial uniformity camera's detector chip, the Gobi640 is directly imaging a highly spatially uniform cold load made out of a black metallic plate cooled in a liquid nitrogen bath. Once the LN_2 has completely evaporated, the camera objective is placed in direct contact with it and the frame recording process starts. This leads to a measurement of a camera "flat field", which helps to understand what is the limiting factor in later measuring the spatial uniformity of the illumination produced by the integrating sphere. Fig. 5.20 shows the final flat-field image of the Gobi640 camera obtained by av-

eraging 15.000 frames. The detector region that is not relevant for the later measurement using the integrating sphere is masked in blue. This leaves about 10000 pixels for which the histogram of the relative flux values is plotted in Fig. 5.20. It is observed that the standard deviation of the pixel values around the unity mean value is about 0.147%, which indicates that the uniformity across the area of interest does not deviate from pixel to pixel by more than 0.147% rms.

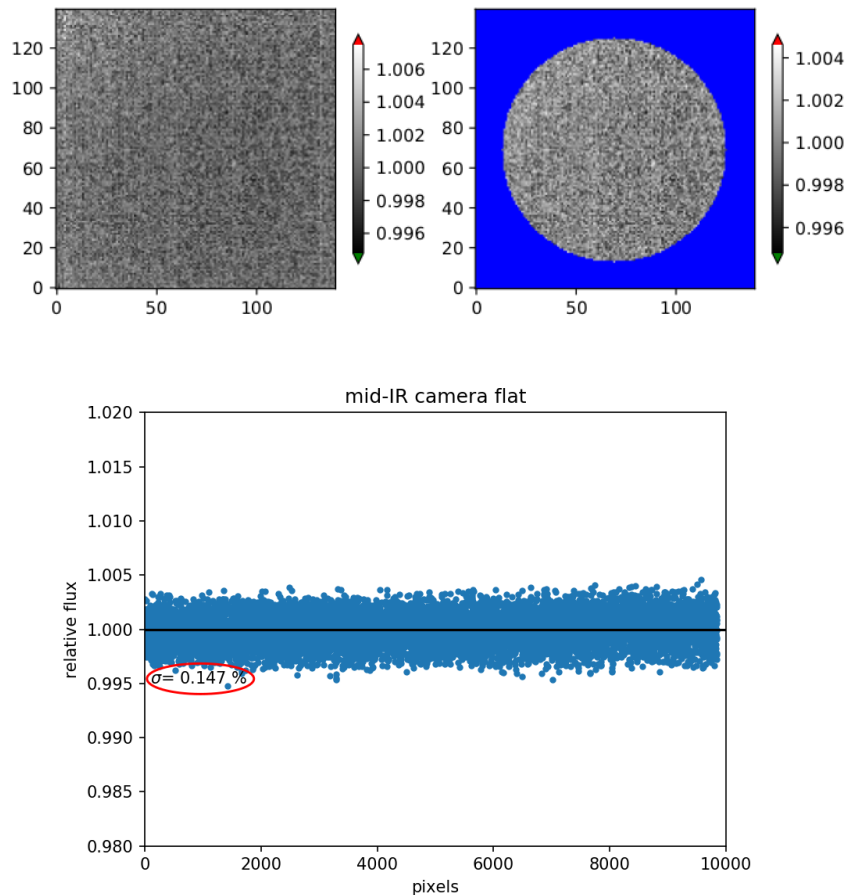


Fig. 5.20: Detector output while observing cold surface cooled with liquid nitrogen, where 15.000 frames are summed and then divided by that number. Top: two-dimensional output with no hot pixel found and corrected by the mean value. The top left figure shows the corrected output of the detector, while the right figure shows only the relevant area for the measurements of the sphere's output later. The blue area is not taken into account. The values inside the circle area were used to calculate the bottom picture. Bottom: In this plot, the relative flux against each pixel was plotted. This leads to a one-dimensional output plot of the sphere with the standard deviation (σ) calculated.

Before moving to the characterization of the flat-field produced by the sphere itself, it is interesting to analyse the uniformity of the camera flat-field as a function of the number of frames N that are co-added. Since the frame averaging increases the signal-to-noise ratio, it is expected that the spatial dispersion of the pixel values decreases with increasing N , up to

a point where the camera flat-field becomes dominated by the intrinsic non-uniformity of the camera itself (differences in pixel's gain, optical distortions etc...). This behavior is visible with the orange curve in Fig. 5.21 where a rapid increase of the field uniformity (i.e. a rapid decrease of the spatial dispersion in the pixel values) is observed when a larger number of frames is averaged. A plateau seems to be reached around $\sigma = 0.15\%$ although some further decrease cannot be completely excluded.

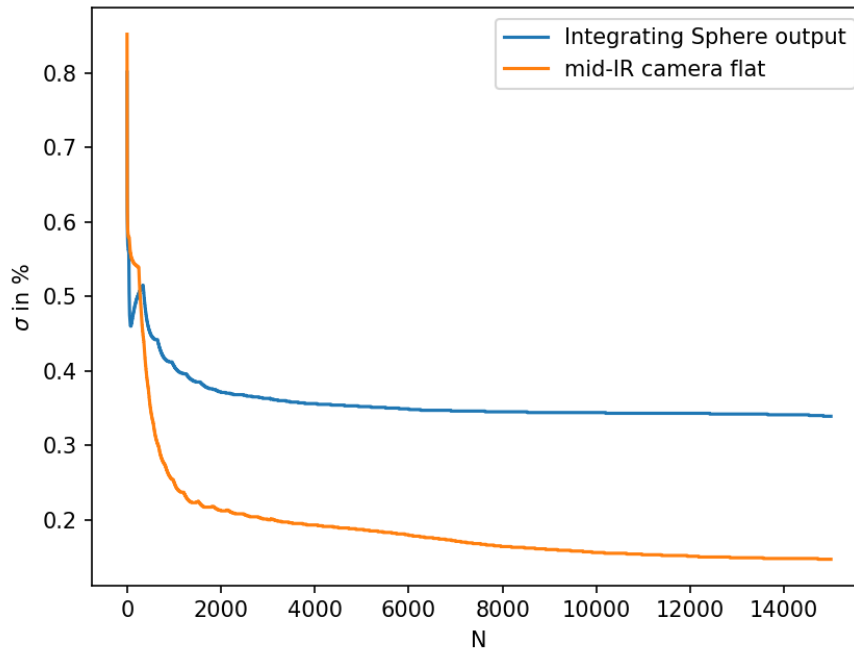


Fig. 5.21: Sigma (standard deviation of the flux) for a cold surface cooled with liquid nitrogen (orange line) and for the output of the sphere plotted (blue line) vs. the number of frames (N). This figure is taken from Graf et al. (2020, p. 5).

The author now turns to the characterization of the flat-field produced by the integrating sphere. Similarly, several images of the sphere output are recorded with the previously characterized Gobi camera and then temporally averaged.

From these images, the spatial uniformity is estimated by calculating the standard deviation of the pixel values distribution (see Fig. 5.22). In the case of the flat-field produced by the integrating sphere, the measured level of dispersion of the highest value of N is $\sigma = 0.386\%$. This value also reflects the impact of the camera flat-field since the two effects (sphere on one side, camera on the other side) are not disentangled. The comparison between the plots showing the relative flux as a function of the pixel number (Fig. 5.20 and Fig. 5.21), as well as the visual inspection of the integrating sphere's flat-field (Fig. 5.21), shows that a residual gradient. Despite this effect, it is shown that a spatial uniformity as high as 99.614% can be

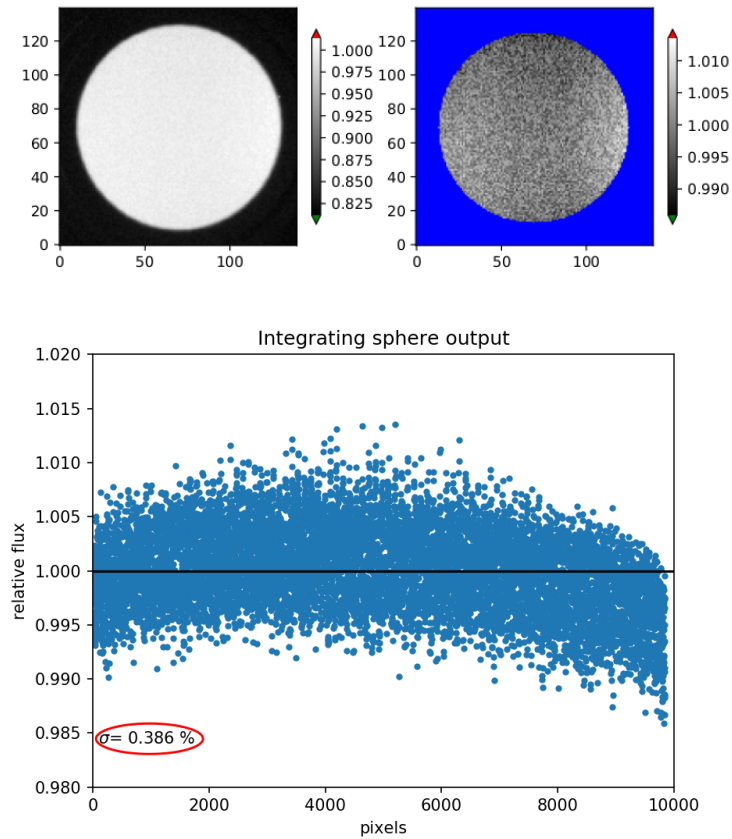


Fig. 5.22: Image of the output port of the integrating sphere obtained with the Gobi camera with the blackbody temperature set at 1000°C and averaged over 15.000 frames. The top left figure shows the integrating sphere's output with the sphere metallic body seen around (black area in the background). In the top right figure, the metallic housing has been masked (blue region) in order to account only for the values relevant for the uniformity measurement. Bottom: normalized flux against per pixel in the active area. This is comparable to an histogram plot for which the standard deviation can be estimated.

reached. It is important to remind that this number also includes the deviation to spatial uniformity of the camera.

In a comparable way to the case of the camera flat, Fig. 5.21 shows the influence of the frames co-addition on the level of uniformity. It is noticeable that the turnoff occurs around $N = 4000$ frames to reach a plateau not as deep as in the case of the camera flat, namely $\sigma = 0.38\%$. This clearly indicates that the flat-field obtained with the integrating sphere becomes dominated by static spatial structures, which is in adequacy with the goal of characterizing the ultimate level of achievable uniformity.

5.2.4 Aperture Mask experiment to measure the detector linearity

A functionality offered by the WCU of METIS is the assessment of the detector linearity, or in other words the proportionality between the number of photons incident on the detector and the number of electrons detected and measured by the read-out electronics. The detector linearity is an important aspect of astronomical cameras in order to measure a reliable photometry of stars or objects with different magnitude or brightness. Outside the so-called linearity range of the detector, the measured flux ratio between two astronomical objects does not reflect any longer the real flux ratio. Determining the range of linearity of an astronomical detector and how it may change over time is therefore an important calibration task. For METIS, the calibration of the detector linearity should be measured with an accuracy of less than 1%, which means that the flux ratio between two objects measured on the camera should correspond to the real flux ratio with an error of less than 1%. This is of course a challenging requirement, which demands a highly repeatable method. The simple idea to measure the detector linearity consists in illuminating the detector with a flat field that varies in intensity over time in regular, well characterized, steps. The instrumental concept to implement this idea is presented hereafter.

An obvious way to proceed in order to have a time-variable flux would be to change the temperature of the blackbody, which would result in different flux levels within a given spectral band. However, the author's measurements showed that after a modification of the blackbody temperature the settling time can be long before the flux level stabilizes again (see Fig. 5.10). Furthermore, with changing the temperature of the blackbody, the spectrum of the blackbody sources changes as well, which means that the detector linearity measurement may depend on the temperature of the source.

The WCU team, which includes the author, proposes to employ a wheel mask placed in between the blackbody source and the integrating sphere (see Fig. 5.23), having 20 different apertures with diameters ranging from 0.5 mm to 20 mm to efficiently crop the beam and control the amount of flux entering the integrating sphere, without modifying the spectrum of the source. One aperture of the wheel is actually a closed position with no hole drilled, which the author will refer to "blank". The blank area was included in order to estimate the thermal background contribution of the wheel mask itself. Each different aperture allows to change the incident flux in the sphere within minutes. The holes were drilled with an accuracy of 1 μ m and are listed in Table 6.1. The wheel consists of 5 mm thick aluminum, and each mask is made of 1 mm thick aluminum as it is shown in Fig. 5.24. The wheel and the integrating sphere are aligned with the blackbody's output, and the powermeter is connected to one of the output ports of the sphere (see Fig. 5.23).

In one single run, the flux passing through each of the twenty apertures is measured for 20 minutes per aperture. Five runs are acquired over several days. In order to identify

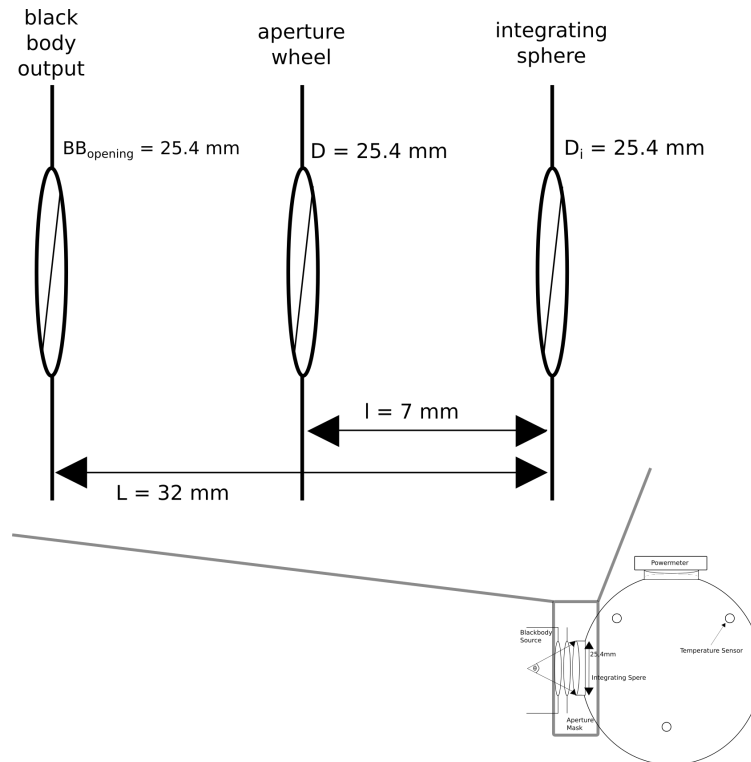


Fig. 5.23: Geometrical setup to test the aperture mask method. BB_{opening} is the output diameter for the blackbody, D is the diameter of the opening of the aperture wheel and D_i is the diameter of the opening of the integrating sphere.

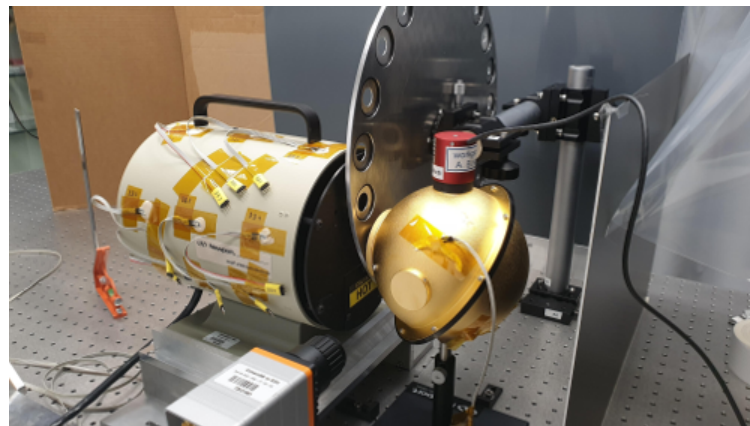


Fig. 5.24: Setup of with the aperture mask wheel. In the original setup, the mask wheel had to be turned manually. The apertures with the diameter of 0.5 mm and 1.53 mm are generally too small in radius to deliver a flux level distinguishable from noise. In the fifth run, the 25.4 mm diameter gold cap visible in the front of the picture and protecting the sphere from dust contamination is removed as the IR camera is collecting data simultaneously. This figure is taken from Graf et al. (2020, p. 6).

those apertures for which the signal-to-noise ratio is insufficient, the level of background flux emanating from the "blank" position before and after each measurement was estimated. As reported in Fig. 5.25, any measured flux level of the order of $\sim 0.1\text{-}0.2\text{ mW}$ or less can be

considered as being in the noise. This led to observe that the apertures with a diameter of 0.5 mm and 1.53 mm deliver flux levels that are generally indistinguishable from the thermal background (Graf et al., 2020, p. 4).

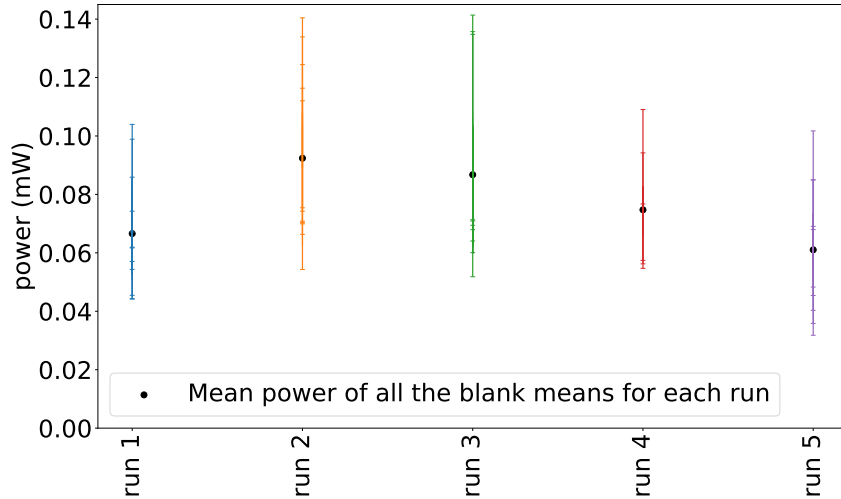


Fig. 5.25: Mean flux coming from all the blank aperture measurements measured with the powermeter. Those values indicate the background noise in the aperture wheel measurements. These values suggest that the smallest and second smallest apertures do not allow to reach sufficient signal-to-noise ratio.

Description of the measurement procedure

In the first place, the aperture wheel was rotated **manually** in order to position as accurately as possible each aperture in front of the opening of the blackbody source. As it was needed to understand the influence of the rotating order on to the flux measurement stability, the different apertures were positioned in front of the blackbody opening in a random order for the first three runs over five. For the following two runs the measurement was achieved from the smallest diameter to the largest one (Graf et al., 2020, p. 4). For each run, the standard deviation of the flux per aperture is measured and reported in Fig. 5.26. One can observe that the standard deviation of the measured flux per aperture is generally larger when the apertures are positioned in a random order (e.g., run #1, #2 and #3) than when they are positioned following the increasing order (e.g., run #4, #5). This can be explained as the metallic region around the corresponding aperture reaches more rapidly thermal equilibrium when moving from one aperture to the next nearby one (Graf et al., 2020, p. 4). This generally suggests that a sequential rotation of the wheel needs to be respected.

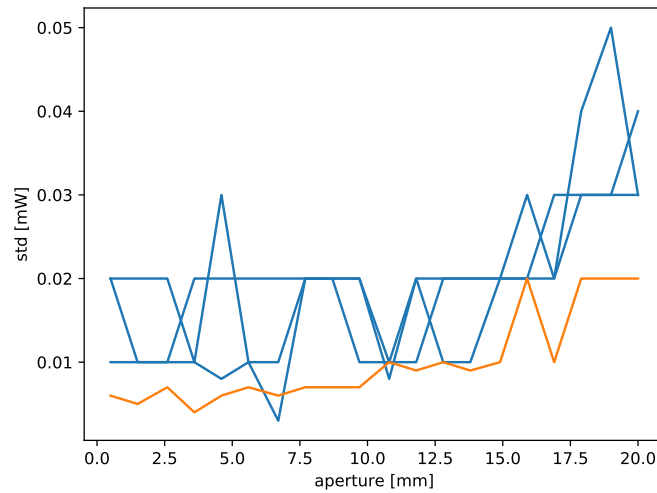


Fig. 5.26: Flux standard deviation per aperture for the different four manual runs. The fifth run is neglected as the air-conditioning is turned off and the IS sphere is opened to add the IR camera as a second detector. The blue curves corresponds to the first, second and third runs, the orange curve corresponds to the fourth run.

The author then used the values of the five different runs to build and inspect the corresponding linearity curve for the manual procedure. The average value per aperture with the associated standard deviation is displayed in Tab. 5.6. The results are reported in Fig. 5.27, where the output flux is measured as a function of the opening area.

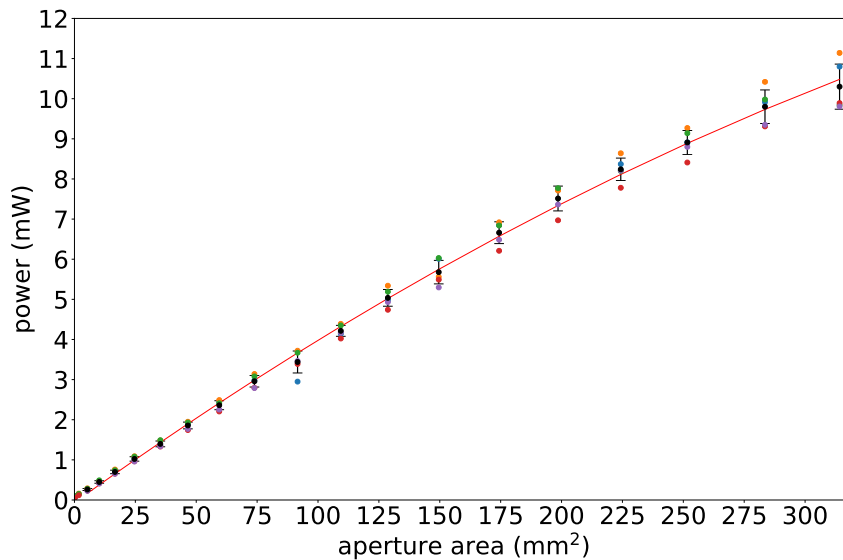


Fig. 5.27: Mean flux coming per aperture versus aperture area. For each aperture area, five measurements are acquired and plotted as colored dots, each color indicating the same measurement run. The black circles with error bars correspond to the average and standard deviation between the different runs. The red line is a second-degree polynomial regression. The fifth run is neglected as the air-conditioning is turned off and the IS sphere is opened to add the IR camera as a second detector.

Tab. 5.6: Flux average value per aperture with its standard deviation. The coefficient is the ratio between the standard deviation and the mean, in percent. One observes that handling the wheel manually leads to a stability not better than $\sim 5\%$, likely due to the difficulty of a repeatable alignment of each aperture with the blackbody opening.

areas [mm ²]	mean [mW]	std [mW]	coefficient [%]
0.2	0.082	0.019	23.35
1.83	0.145	0.016	11.0
5.12	0.261	0.024	9.19
10.06	0.449	0.031	6.99
16.66	0.699	0.043	6.22
24.91	1.023	0.055	5.39
34.81	1.398	0.072	5.14
46.37	1.857	0.084	4.53
59.59	2.362	0.112	4.73
74.46	2.958	0.143	4.84
90.98	3.439	0.273	7.96
109.16	4.215	0.136	3.24
128.99	5.037	0.209	4.14
150.48	5.678	0.293	5.15
173.62	6.661	0.272	4.08
198.42	7.513	0.309	4.12
224.87	8.24	0.280	3.39
252.98	8.91	0.298	3.35
282.74	9.8	0.418	4.27
314.15	10.3	0.562	5.46

It is noticeable that a linearity trend is observed for the first half of the curve, whereas a second-degree polynomial is required to fit the full data, pointing at a significant deviation from the expected linear behavior between the area of the apertures and the measured flux. This may result from a bias in the manual measurement, as one will see later. Furthermore, the quantification of the standard deviation of the five measurements per aperture, quoted as "coefficient" in Tab. 5.6, tests the repeatability of the method, which is a highly important parameter to guarantee the stability of the calibration of the detector linearity in the final instrument: one can observe a stability of $\sim 5\%$, which is not ideally suited to characterize the intrinsic linearity of a science grade detector. Therefore, a different approach is investigated through an automated method. Before presenting this approach, the influence of the environmental conditions as well as the impact of the detector being used are investigated.

Influence of the air-conditioning In the fifth and last run of this measurement serie, the air-conditioning in the optical lab was turned off. This allowed to check whether the

air-conditioning is influencing the outcome of the powermeter measurement (see Fig. 5.28). One can see that without the air-conditioning, the spikes coming from the air-conditioning are reduced but not fully gone. This is in agreement with the previous air-conditioning test performed for this thesis. This simple test reminds us that, during the AIV phase of METIS, the accurate control of the environmental conditions through appropriate control of the air flow is of major importance for the stability of the WCU thermal sources.

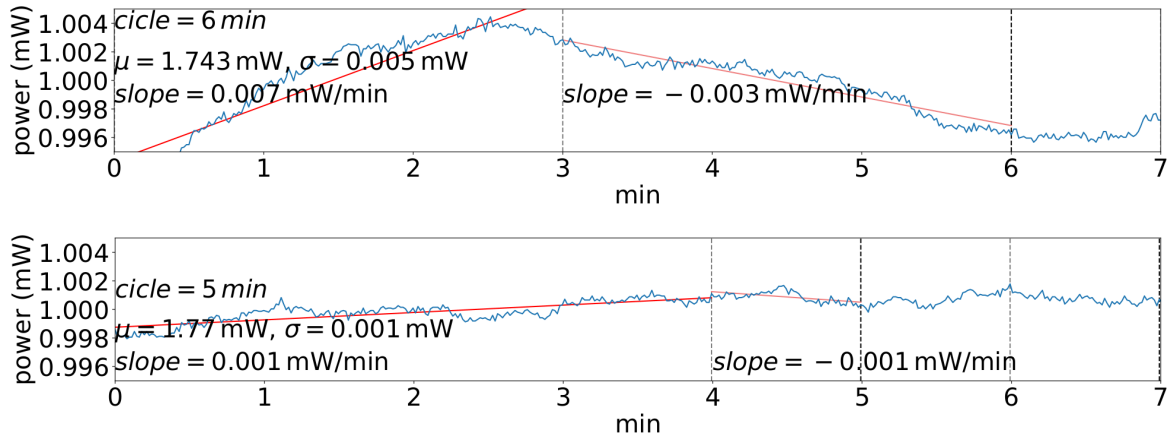


Fig. 5.28: Aperture mask measurements with the air-conditioning on and set at 18.9°C (top); With the air-conditioning turned off and the lab temperature around 22.5°C (bottom). The normalized flux is plotted against the time. As it takes one minute for the flux to stabilize, the first minute is not displayed in order to focus on the interesting part of the plot. For the first cycle (from first minimum to second minimum), the mean, the standard deviation and the slopes of the flux curve (displayed as the red lines) are calculated. The dashed vertical lines identify possible minima/maxima.

Automation of the measurement procedure

The downside of the manual intervention to rotate and position the wheel is the unavoidable influence of an external heat source – the operator’s hand – that may limit the repeatability of the measurement. In order to further improve the temporal stability of the experiment, the author attempted to automate the measurement, hence removing any human presence in the laboratory. For this, Moritz Prenzlöw from the institute electrical workshop introduced a stepper motor to remotely control the wheel via a python code. The author set up the mechanism in the experiment and performed a realignment of the system.

As in the previous tests, five consecutive runs were acquired with the wheel. The first three and the last two runs were executed at a different day, which allowed to take as much as possible into account the temporal variability of the environment, and therefore deliver a more robust comparison between the runs. As the 0.5 mm aperture was delivering flux at the background level, this measurement was removed. The last aperture, named here "fully open" position, has a diameter of 36.1 mm that is oversized with respect to the aperture of the blackbody source. The source was heated up with the wheel positioned in its fully open

position.

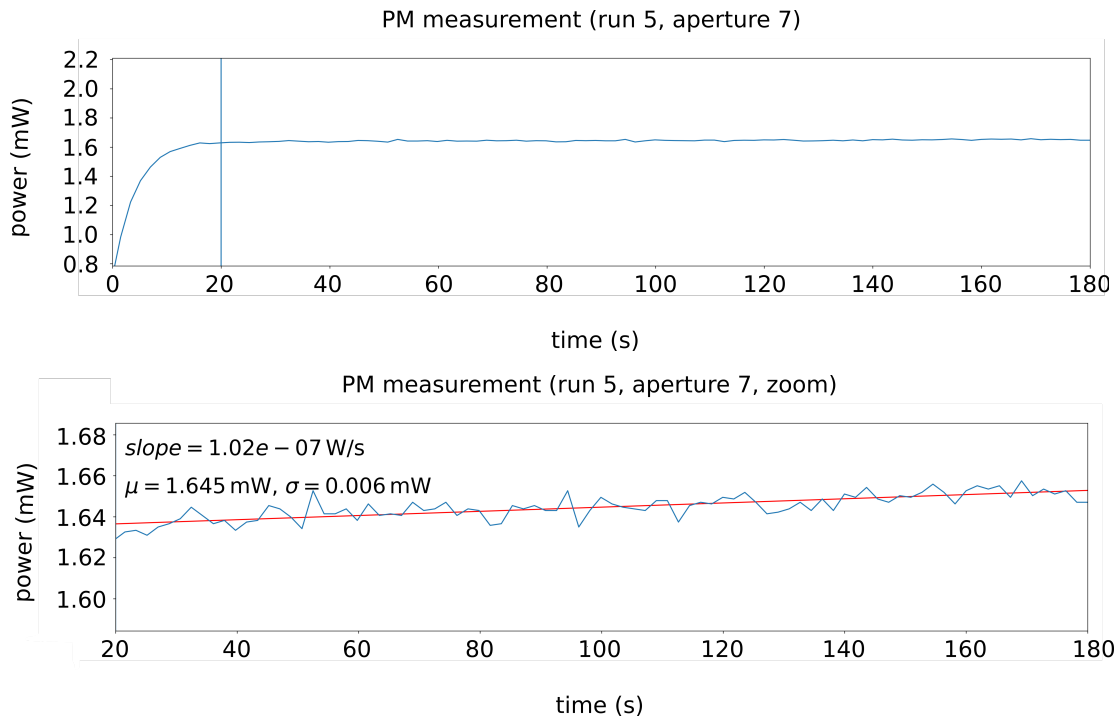


Fig. 5.29: Flux measurement obtained with the 7.68 mm aperture, with the air-conditioning system on, and setting the room temperature at 18.9° C (top). Zoom on the constant flux region after the first 20 s (bottom). The mean and the standard deviation as well the slope were calculated. The vertical line in the top figure indicates the beginning of the stable part. "PM" stands for "Power Meter".

After a warm-up of one hour to stabilize the source, the measurement was commenced by choosing the blank aperture as a starting point. Right after the wheel moved to the blank position, the measurement starts and lasts for a duration of 3 min per aperture before switching to the next aperture. For a given aperture, the flux recording rate is 1 Hz, giving about 180 measurement points per aperture. The full process is automated through a python code which the author wrote using existing scripts from the METIS team. As an example, the measurement of one aperture with the powermeter is shown in Fig. 5.29. In the figure, one can see that only 20s are necessary for the flux to stabilize, instead of the 60s necessary with the manual setup. When looking into more details, the author observes a slight drift of $\sim 0.1 \mu\text{W/s}$ of the measured power, or $\sim 0.9\%$ of the mean flux over the duration of the measurement. This is probably due to residual environmental or source instabilities (mainly due to the air-conditioning).

The main advantage of the automated method is that the wheel apertures are positioned with high repeatability (i.e. higher than with a manual adjustment) in front of the black-body aperture, which translates into a higher stability of the setup. The author analyzed the repeatability of the automated linearity measurement by monitoring the relative differences between the different runs. In Tab. 5.7 are reported for each aperture the mean and stan-

standard deviation of the measured power over the five runs. The relative error (fourth column) provides a robust indication on the repeatability of the process.

Tab. 5.7: Average flux value per aperture with its standard deviation with the automated approach. The coefficient is the ratio between the standard deviation and the mean, in percent. One can see that the coefficient, tracing the stability of the measurement, is significantly smaller than with the manual handling of the wheel.

areas [mm ²]	mean [mW]	std [mW]	coefficient [%]
0	0.16	0.068	42.4
1.83	0.18	0.036	19.73
5.12	0.27	0.023	8.49
10.06	0.43	0.014	3.18
16.66	0.65	0.013	1.96
24.91	0.93	0.007	0.77
34.81	1.28	0.006	0.46
46.37	1.65	0.009	0.53
59.59	2.14	0.013	0.61
74.46	2.68	0.016	0.60
90.98	3.23	0.019	0.60
109.16	3.85	0.021	0.54
128.99	4.52	0.025	0.55
150.48	5.23	0.032	0.61
173.62	5.99	0.038	0.64
198.42	6.8	0.038	0.56
224.87	7.59	0.048	0.63
252.98	8.38	0.048	0.58
282.74	9.3	0.061	0.65
314.15	10.24	0.068	0.66
506.70	13.73	0.081	0.59

Linearity and R^2 coefficient The visual inspection of the curve of Fig. 5.30 shows a clear linear relationship between the apertures and the measured power, except towards the high end of the curve for the largest aperture, as well as in the region of very small apertures (i.e. less than ~ 20 mm²) where the signal-to-noise ratio is lower. The calculation of the linear regression suggests a linear model given by

$$y = 0.249 + 3.23 \times 10^{-2} x \quad (5.9)$$

where x is aperture area in mm² and y the flux in mW. The quality of this fit is best made looking at the R^2 coefficient. The author derives the coefficient of determination R^2 that quantifies the quality of the fit between a serie of experimental points $[x_i, y_i]$ and the

parametrized model describing them. In the simple case of a linear fit like here, the coefficient of determination is the square of the more classical (Pearson) regression coefficient. R^2 is then given by

$$R^2 = 1 - \frac{\sum_1^n (y_{\text{exp},i} - y_{\text{mod},i})^2}{\sum_1^n (y_{\text{exp},i} - \bar{y})^2} \quad (5.10)$$

where $y_{\text{exp},i}$ is the experimental measurement number i , $y_{\text{mod},i}$ is the value predicted by the linear model for the input value and x_i , and \bar{y} the mean of the experimental points (see Tab. 5.7). When the full serie of 21 measurements is taken into account to estimate the goodness of the linearity fit, the value of $R^2 = 0.9829$ is retrieved, which suggests an adequacy with a linear model to better than 2%. However, this remains unsatisfactory for a calibration of the METIS detector linearity to better than 1%. As the first points relative to the small apertures correspond to a poor signal-to-noise ratio and the largest aperture appears to be a clear outlier to the linear fit, these measurement are removed to estimate the goodness of the fit. When considering the measurements from 5 to 20, a coefficient of determination $R^2 = 0.9989$, which indicates a much superior goodness of fit between the measured data and the linear model to better than 0.2%.

This clearly indicates that, despite the tiny fluctuations of the blackbody source and the intrinsic non-linearities of the powermeter, the method based on an automated aperture mask wheel is able to deliver a fairly good linear progression of the delivered flux levels, maintaining at the same time the temperature of the blackbody constant, and hence the spectral slope of the emission.

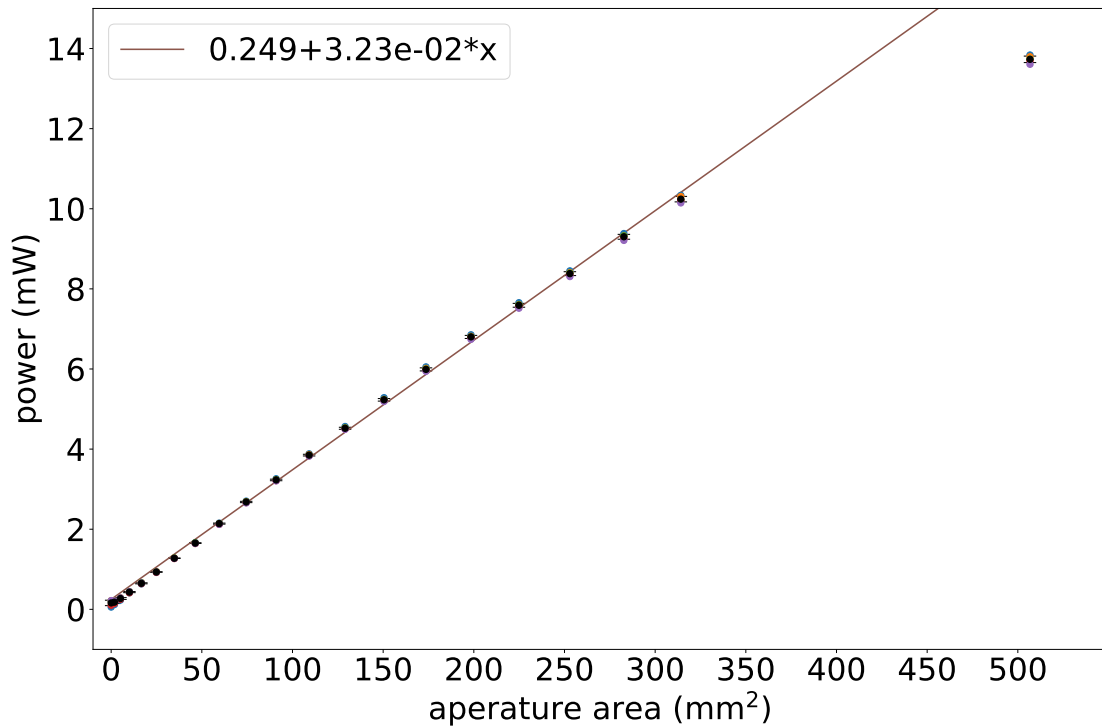


Fig. 5.30: The aperture mask test results where the mean flux measured by the powermeter is plotted against the aperture area. For each area, five measurements were conducted and plotted as a colored dot. The same color belongs to the same measurement run. The black dots are the average of each aperture opening area. The error analysis has been completed for the aperture mask tests. However, the error bars are presented here due to their low order value ($<1\%$ of value) they are almost not visible. The linear regression is fitted to match the apertures between 24.91 mm^2 and 314.15 mm^2 .

Repeatability Following the previous result, a more detailed analysis of the accuracy and stability of the linearity calibration can be obtained when looking at the repeatability of the linearity curve. This is measured through the coefficient reported in the last column of Tab. 5.7 which describes the relative dispersion of the flux measurement per aperture over the five different runs. It shows that, starting from the fifth aperture, the dispersion – and therefore the repeatability – lies between 0.5% and 0.7% . The automated approach, similar to what will be implemented in the WCU, is compliant with the original objective.

Detector dependency of the measurement As a confirmation test, the same test as above was conducted with the mid-IR camera as a detector instead of the powermeter. Five consecutive runs were acquired within a day. Positioned at 120 mm from the 25.4 mm output port of the sphere, one frame of $25 \mu\text{s}$ per aperture was acquired. The measured flux values (in counts) versus aperture size is reported in Tab. 5.8).

Tab. 5.8: Average flux value measured by the IR camera per aperture with its standard deviation with the automated approach. The coefficient is the ratio between the standard deviation and the mean, in percent. On can see that the coefficient, tracing the stability of the measurement, is significantly smaller than with the manual handling of the wheel.

areas [mm ²]	mean [pixel]	std [pixel]	coefficient [%]
0	5177	2607	50.36
1.83	4487	1906	42.48
5.12	4611	1342	29.10
10.06	4887	1170	23.94
16.66	5277	931	17.64
24.91	6443	990	15.37
34.81	8105	525	6.48
46.37	10288	848	8.25
59.59	12476	678	5.43
74.46	15919	723	4.54
90.98	19301	485	2.51
109.16	22505	919	4.08
128.99	25992	1219	4.69
150.48	30040	785	2.61
173.62	34651	806	2.33
198.42	39585	1080	2.73
224.87	45149	328	0.73
252.98	48798	1664	3.41
282.74	50841	725	1.43
314.15	51963	287	0.55
506.70	51477	220	0.43

Similarly to the measurements conducted with the powermeter, the linearity and the repeatability of the method are analyzed. The inspection of the curve shows a linear relationship between the apertures and the measured power when neglecting several of the smallest and largest apertures (Fig. 5.31). The calculation of the linear regression in the range from 24.91 to 282.74 mm² gives for the linear model:

$$y = 1557 + 190x \quad (5.11)$$

Therefore, similarly to the powermeter measurements those apertures were removed for the estimation of the goodness of the fit. When considering the measurements from 5 to 18,

a coefficient of determination $R^2 = 0.9993$ can be reached (see Tab. 5.8). This indicates a goodness of the fit between the measured data and the linear model to be better than 0.1% which means the automated aperture mask wheel can deliver independent of the detector fairly good linear progression.

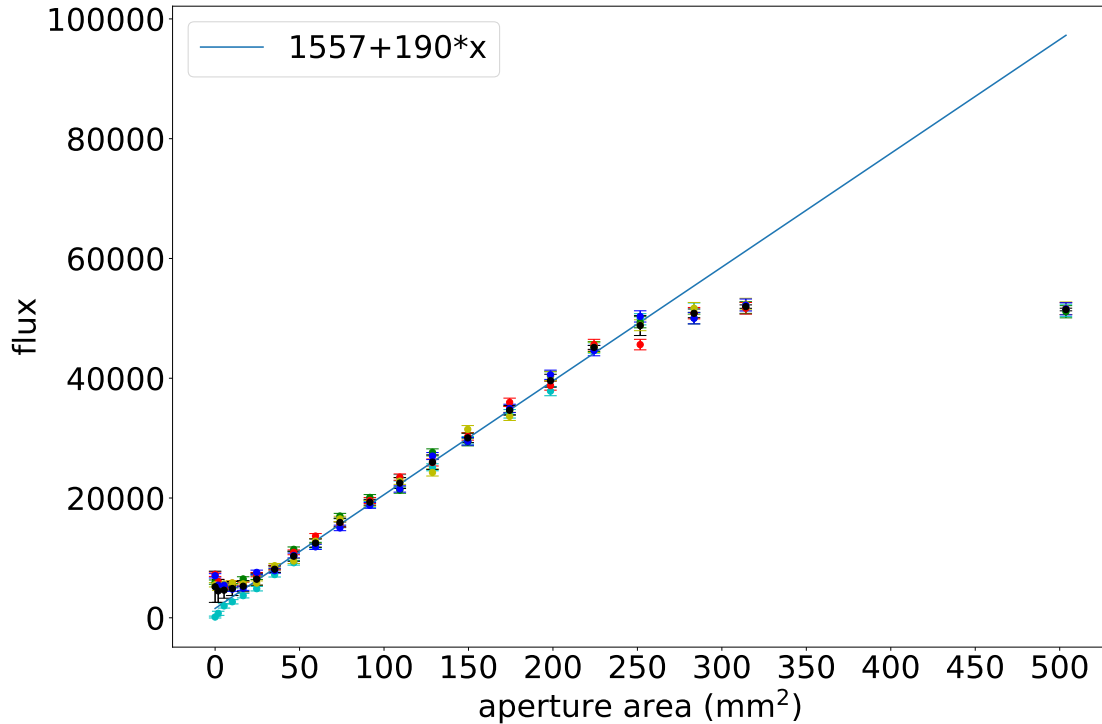


Fig. 5.31: Aperture mask test results with the mean flux measured with the mid-IR Gobi camera. For each area, five measurements were conducted and plotted as a colored dot. The same color belongs to the same measurement run. The black dots are the average of each aperture opening area. The linear regression accounts only for the aperture values ranging from 24.91 mm² and 282.74 mm². Beyond these boundaries, linearity is not possibly observed.

The more interesting comparison with the measurement of Tab. 5.7 is on the repeatability, which can be assessed with the last column of Tab. 5.8. Using the IR camera as the detector, the dispersion lies between 0.43% and 15.37% starting from the fifth aperture. Therefore, the measurement appears less repeatable than with the powermeter detector. This may be due to the short integration time of 25 μ s imposed with the mid-IR camera, as opposed to the 3 min time span in the case of the powermeter, with the consequent degradation in the signal-to-noise ratio.

One last remark needs to be made regarding the temporal stability of the source itself. The controller of the blackbody source allows to monitor accurately the temperature of the ceramic producing the infrared radiation, showing a stability of $\pm 0.1^\circ\text{C}$ over a one-hour duration (Fig. 5.32). Integrating the Planck's radiation law and assuming an emissivity of

one, this translates into an uncertainty of about $\pm 0.02\%$ on the radiance of the blackbody source at $T = 1000^\circ\text{C}$ over the mid-infrared range. This suggests that the limiting factor for the stability and repeatability of the linearity measurement resides primarily in the accuracy of the powermeter itself rather than on the intrinsic variability of the blackbody source.

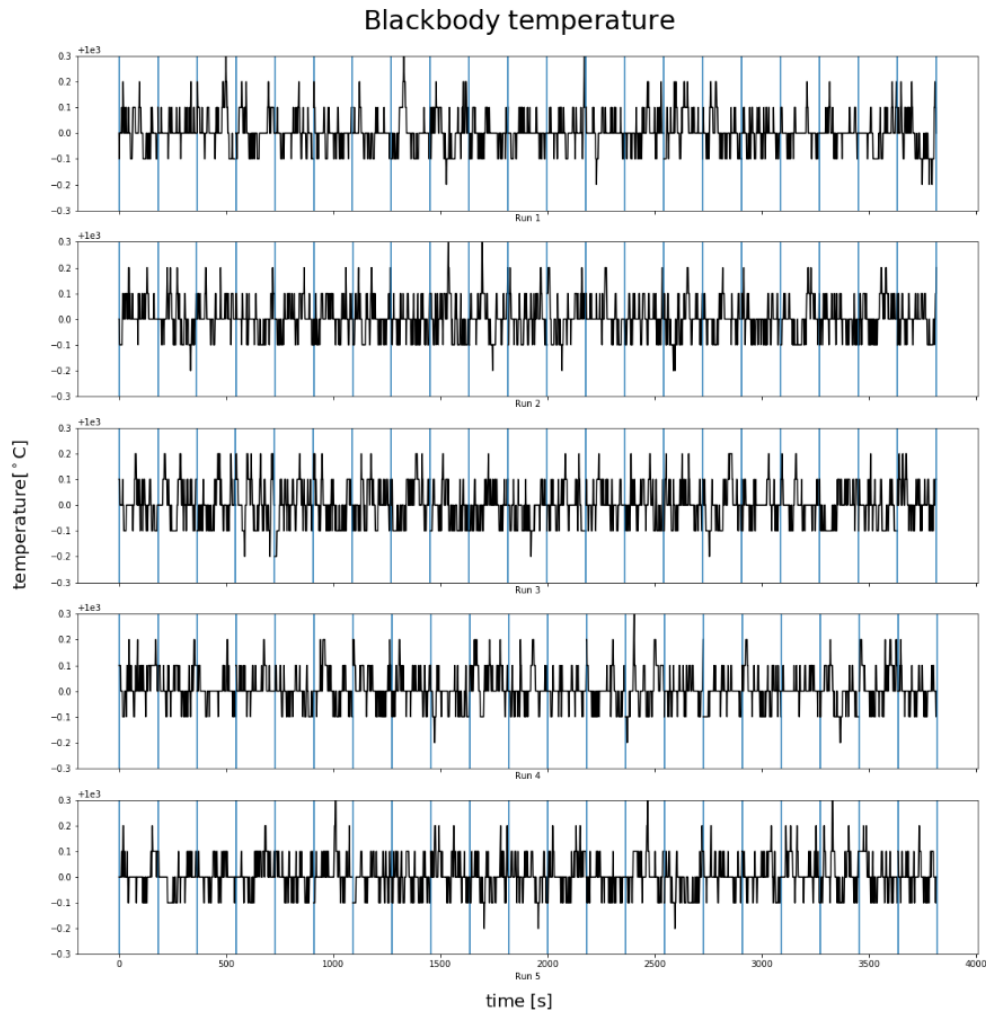


Fig. 5.32: Temperature of the blackbody ceramic over one hour for each of the five run. The graphs report the temperature excess (positive values) or deficit (negative values) with respect to the set temperature of 1000°C . The temperature remains highly stable with an error of $\pm 0.1^\circ\text{C}$.

5.2.5 Pinhole tests

Pinhole masks need to be developed and inserted in front of the output port of the sphere in order to generate point sources for the calibration of the imaging performances of METIS. In the current laboratory setup, these pinhole masks are connected to the 90° one-inch output port.

Material tests

The material choice to fabricate the pinhole masks is critical for generating a point source well contrasted against its the surrounding material acting as a background source. For example, if PVC is used as a material, it heats up rapidly so that the contrast between the pinhole and the surrounding material decreases significantly. Different materials with different thermal conductivity were tested for this purpose (see Tab. 5.9). Another parameter influencing the results is the coating/structure of the surface of the pinhole mask. Towards the inside of the integrating sphere, the radiation impinging on the mask should be reflected back in order to minimize the heat generated into the mask's substrate. On the other hand, if the mask surface oriented outwards the sphere is a high reflectivity and polished surface, this would impacts negatively the measurement as it would reflect the background infrared radiation from the laboratory towards the detector. Hence, the mask surface oriented outwards should be possibly be a matt surface. Note that this is true because the imaging system in the author's lab experiment is not telecentric.

Pinholes made from steel, brass, and aluminum were produced to test the materials and surface structure. To test the materials, the same setup shown in Fig. 5.19 is used. The pinhole mask is adjusted at the output port of the integrating sphere and the mid-infrared IR camera Gobi640 is used as the imager.

When using the pinholes made of brass and steel, i.e. the two materials with lowest thermal conductivity, it was very difficult to distinguish the pinhole from the surrounding mask material due to the low brightness contrast (see Fig. 5.33). Thus, those two materials were no longer tested and were discarded from the possible solutions to be adopted for the pinhole masks. Copper and silver could not be tested. The aluminum pinhole was tested further, as well as the idea of gold coating a pinhole entirely to possibly reach a higher thermal conductivity (see Fig. 5.34).

The gold-coated pinhole was manufactured using first an aluminum substrate that was sand-blasted first on both sides in order to increase the surface roughness. The substrate was then coated with gold deposited on the both sides. In this way, the aspect of the gold-coated pin-

Material	Thermal Conductivity [W/(mK)]
steel	46
brass	121
aluminium	237
gold (pure)	318
copper	401
silver	429

Tab. 5.9: Thermal conductivity of different materials at 20° C (Tipler & Mosca, 2009, p. 782; Davis & et. al., 2001, p. 64).

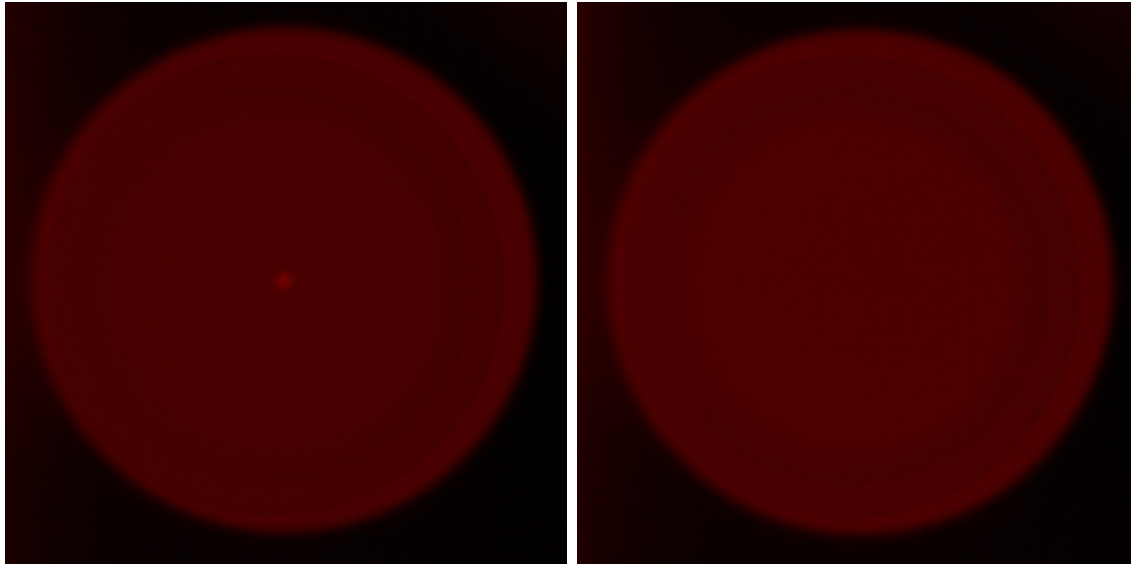


Fig. 5.33: Imaging of the back-reflected pinhole in the case of a brass pinhole mask (left) and a steel pinhole mask (right) as measured with IR camera. One observes the low resulting contrast between the central pinhole and the surrounding metal of the mask.

hole mask is similar to internal and external surfaces of the integrating sphere (see Fig. 5.35), which maximizes the uniformity of the radiation field. For the case where the pinhole mask is made only of aluminum, i.e. with no coating, a spray paint was applied on the surface to produce a matt effect. Note that the matt property of the surface was sought because of the configuration of the author's measuring setup. In the case of the final WCU, the optical design is telecentric. This means that if a high-reflectivity and low-roughness mask is positioned at the focal plane, the METIS detector will be pointing at a mirror-like surface: this means that the detector will actually "see" inside the cryostat, which will significantly reduce the thermal background captured by the detector.

This qualitative experiment shows the importance of properly selecting the material of the pinhole mask in order to obtain a contrasted point-like source.

Analyzing the images obtained with the aluminum pinhole mask, the author measures that

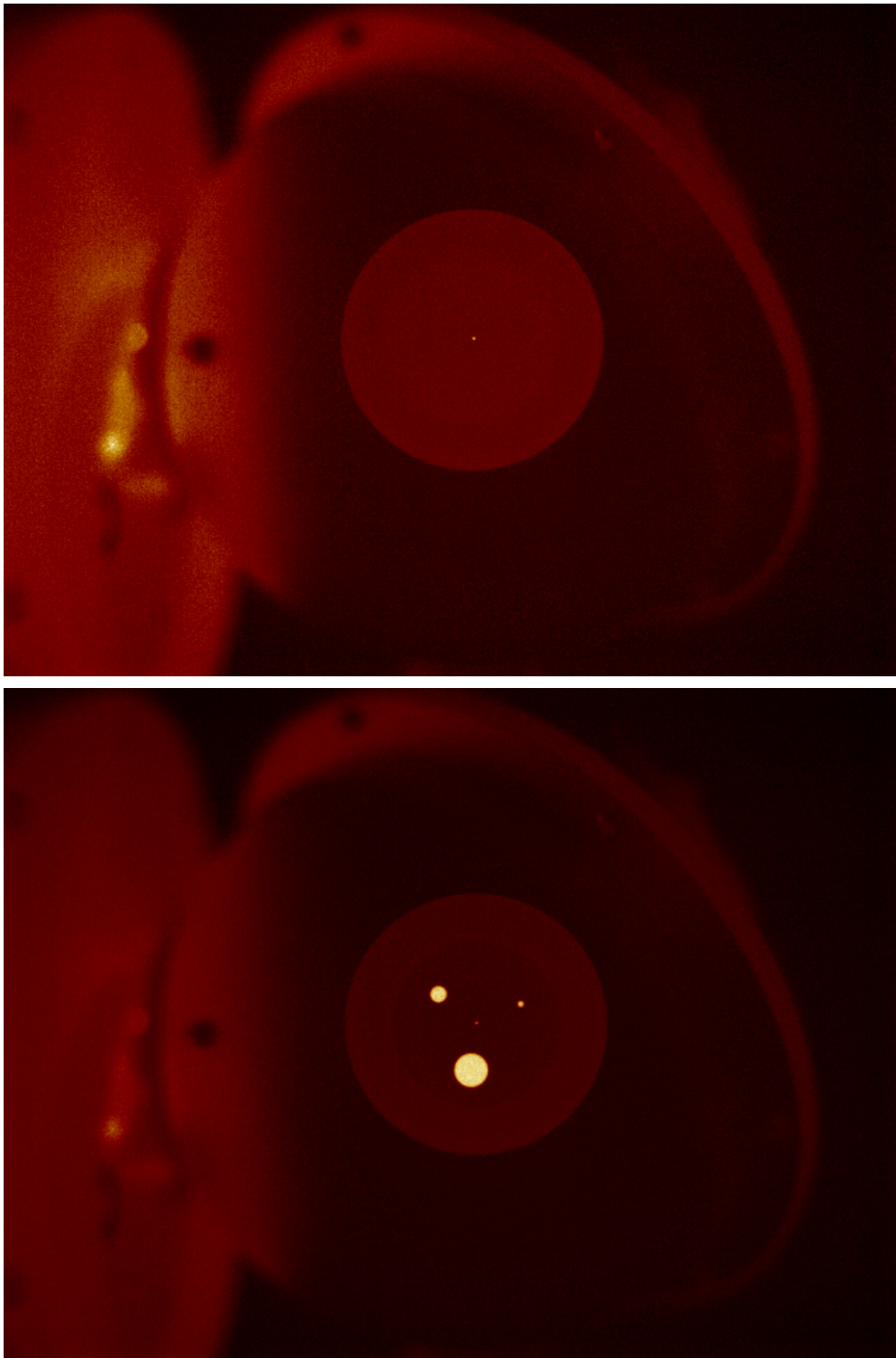


Fig. 5.34: Pinhole mask made of aluminium (top) and later coated with gold (bottom) as measured with IR camera.

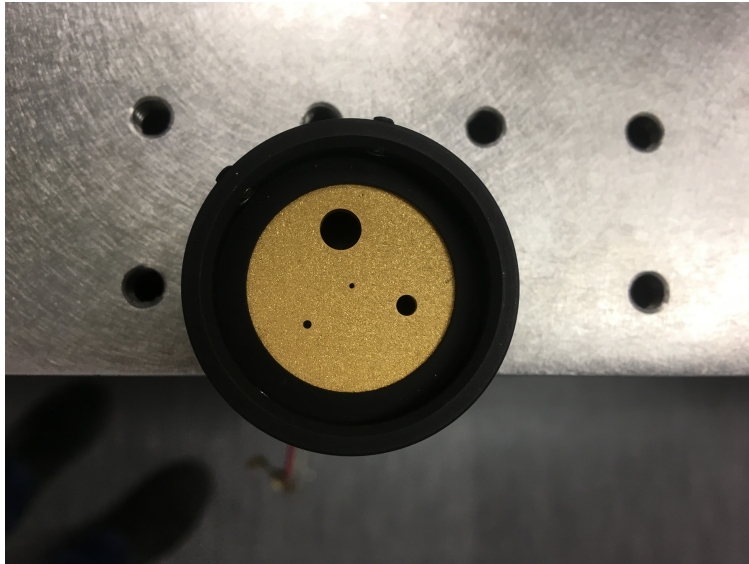


Fig. 5.35: Pinhole mask with different sizes for openings.

the intensity of the pixels in the pinhole region is 9.22% higher than the pixel intensity in the area surrounding the pinhole. This level of contrast is significant, as this can be visually seen in Fig. 5.34. For the case of gold-coated pinhole mask, the contrast measured is 10.68%. This data suggests that the gold-coated pinhole mask leads to a higher intensity contrast. It should be noted that the reported contrast correspond to the case of a direct image, as opposed to a "background-subtracted" image. The latter case would correspond to a situation where the image in Fig. 5.34 with the blackbody source turned off would be subtracted to the same image with the blackbody source turned on. This is typically referred as "chopping" in astronomy. The resulting subtracted image would allow to compare the pinhole flux directly to the background noise. However, the presented result already allows to appreciate the level of reachable contrast.

A similar measurement was later executed but this time with a PT100 temperature sensor attached to the surface of the pinhole (see Fig. 5.36). The goal is to measure, in the same experimental conditions for the blackbody source, the temperature of the pinhole mask surface.

The results of those measurements are presented in Fig. 5.37. First, they indicate that a comparable temperature higher than 25°C is reached. Despite the higher thermal conductivity of (pure) gold compared to aluminum, a slightly lower temperature is measured for the latter. This small difference might be explained by the fact that the gold is applied here just as a coating, meaning the author is not in presence of a pure gold pinhole mask. But most probably the difference comes from the different geometries between the gold-coated and the

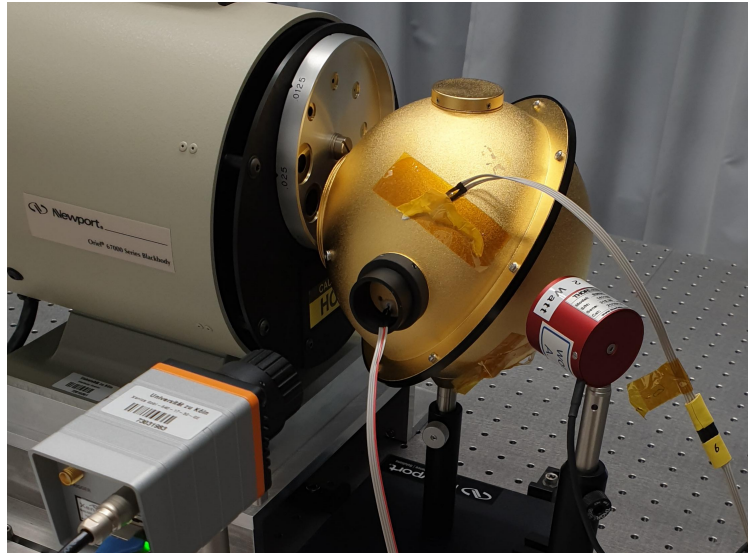


Fig. 5.36: Setup with a temperature sensor PT100 connected to the pinhole mask.

aluminum pinhole masks. The former has three clear apertures whereas the second has only one (see Fig. 5.34). Hence, the radiating surface for the gold-coated pinhole mask is not as large as in the case of the aluminum mask, leading to the small increase in temperature observed.

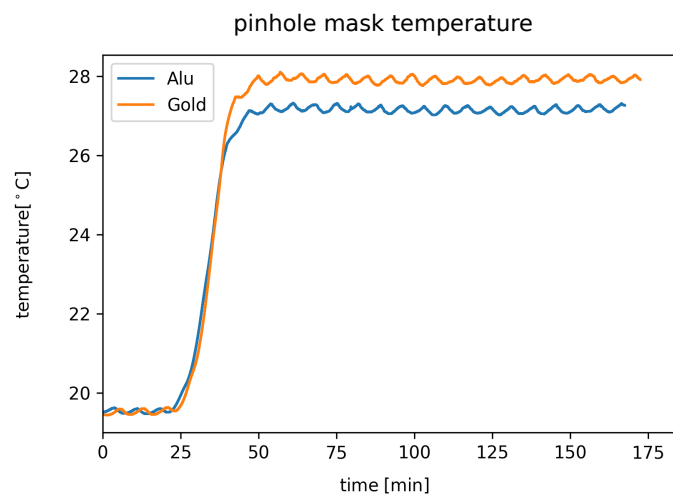


Fig. 5.37: Comparison of aluminium and gold-coated pinhole.

6 Discussion

First, the results discovered in this thesis are discussed then they are concluded. To keep the same order as in the thesis, the first part of each section is about FARGO3D, and the second part is about the contribution to METIS.

6.1 Discussion

In this section the findings of this thesis are discussed.

6.1.1 Kepler 38

In this Ph.D. thesis, numerical experiments on the Kepler 38 test case were conducted. For the setup, the author visited the expert of circumbinary exoplanets, Professor Dr. Nader Haghighipour. In this early phase, the initial conditions and boundary parameters were studied and tested. Those tests were compared with previous studies of Kley & Haghighipour (2014) and improved with the newest knowledge from Thun et al. (2017) and Thun & Kley (2018). Moreover, the results were discussed with the developer of the FARGO3D code, Dr. Frédéric Massét. This was required to ensure a proper setup of the simulation parameter to have results accepted by the scientific community and which could then be analyzed. The advantage of the three-dimensional simulation is, of course, to provide a more detailed picture of the system and in particular of possible non-plane symmetric effects.

One initial goal was to understand the migration of Kepler 38 in a 3D disk perturbed by the tidal effects of the central binary and to compare the results with previous studies. After performing extensive tests of the binary setup, the results showed that an inclination of the planet's orbit with respect to the computation mid-plane could be triggered, despite the full initial coplanarity of the system at $T = 0 T_{\text{bin}}$. This can be considered as a new result since most of the hydrodynamic simulations investigating the feedback of the binary's tidal effect were conducted through two-dimensional codes, or using three-dimensional codes only in the case of primordially misaligned systems (Pierens & Nelson, 2018). To understand the cause of the induced misalignment in the Kepler 38 system, different numerical experiments were

performed. First, a single star setup was implemented to serve as a reference to be compared to. Then, several tests involving the presence of the central binary star with different orbital parameters were conducted. The knowledge gained through those numerical experiments inspired additional investigation involving the varying of the disk's parameters (e.g. the disk's mass). The results clearly indicate that the measured inclination, despite its small value, is not resulting from numerical noise and that the overall behavior of the planet appears in agreement with previous studies.

The results for the Kepler 38 simulations with an embedded planet were validated through comparisons to former studies done in this field.

Planet Parameter

The planet ($0.34 M_{\text{Jup}}$) is inserted at 0.98 AU in a locally isothermal disk with an aspect ratio ($H/r = 0.05$) and viscosity parameter ($\alpha = 0.01$). It was found that the migration of the planet stops, for a binary system with $e_{\text{bin}} = 0.1$, just outside of the cavity and remained in orbit with $a_p = 0.51$ (using the Stockholm condition) and $a_p = 0.54$ (without using the Stockholm condition). The stopping location is close to the stability radius 0.40 AU and comparable to the reported separation of 0.46 AU of the planet with respect to the central binary (Orosz et al., 2012, p. 13). This agrees with previous studies by Kley & Haghighipour (2014) and Thun & Kley (2018). Moreover, the independent findings on the stopping location of the planet as a function of the disk mass and starting location reported by Thun & Kley (2018, p. A47) could be confirmed.

Thun et al. (2017, p. 15) indicated that the disk's inner boundary needs to be of the same order as the binary separation. Accordingly, the inner boundary (i.e., the radius of the computational hole) in this work is chosen to be smaller than the value used by Kley & Haghighipour (2014). Furthermore, the influence of the location of the inner boundary on the size of the cavity could be confirmed. The simulation of the same setup but with different inner boundary locations (1.0/1.3 CU or 0.1469 AU/0.1910 AU) showed a slightly larger cavity with an increasing inner boundary condition. As stated before, the influence is minimal. However, according to Thun et al. (2017, p. 15), this correlation of the inner boundary's location and the size of the cavity only holds as long the boundary location is in the same order as the binary separation and the 3:1 Lindblad resonance remains in the computational domain.

The binary's eccentricity is another factor influencing the inner cavity's size and thus the planet's stopping location. With larger binary eccentricities, the inner cavity grows in size. This is in agreement with the theory of stable orbits around binary stars (Holman & Wiegert, 1999, p. 626). According to this reference, the larger the stellar eccentricity, the larger the stability radius. In the simulations without the Stockholm condition, i.e. with $0.021 M_{\odot}$

disk mass and for the binary eccentricity of 0.1, the periastron of the inner cavity is about 0.54 AU away from the center of mass and the stability radius is roughly 0.40 AU. Using a binary eccentricity of 0.5, the periastron of the inner cavity is moved to roughly 0.75 AU from the center of mass, with the stability radius being about 0.58 AU.

The influence of the mass ratio of the binary on the inner cavity is found to be negligibly small. This is in agreement with the equation for the stability radius by Holman & Wiegert (1999, p. 626). A change in the mass ratio has only a minor influence on the location of the smallest stable orbit.

The disk mass is not influencing the inner cavity's radius. However, the disk mass influences the migration speed. For heavier disks, a faster migration is seen, whereas, in disks with a lower mass, the migration speed is reduced. This follows the analytical Eq. 4.10 by Tanaka et al. (2002, p. 1271) where they treat the three-dimensional evolution of the disk. Similar results are obtained when comparing the results of our numerical experiments with the analytically computed values.

The eccentricity of the planet's orbit increases as it migrates closer to the central binary. As it reaches its final position, the oscillations in the planet's eccentricity becomes regular. Depending on the simulation, the eccentricity varies between ~ 0.06 and 0.25 (using the Stockholm condition and for an initial disk mass $0.007 M_{\odot}$) and between ~ 0.075 and 0.21 (without the Stockholm condition and an initial disk mass $0.01 M_{\odot}$). For the latter case, and considering the mass of $0.34 M_{\text{jup}}$ adopted in this thesis, the author observes a rapid increase of the planet eccentricity that converges towards $e_p \sim 0.15$, hence at an intermediate value between $e_p \sim 0.03$ and $e_p \sim 0.2$ as reported by Thun & Kley (2018) for $M_p = 0.38 M_{\text{jup}}$ and $M_p = 0.3 M_{\text{jup}}$, respectively. The turning point occurs around $t = 3000 T_{\text{bin}}$, which corresponds roughly to the point in time when the migration speed strongly decreases. Moreover, the type I migration with no gap opening is observed. This is in agreement with the gap opening criterion by Crida et al. (2006, p. 17).

Planet parameters relevant for the 3D simulation case

The planetary system Kepler 38 has not been simulated with 3D hydrodynamical simulations until this thesis. The detection of the movement of the planet in the z direction was obtained in this thesis. In the Kepler 38 setup using implementing the Stockholm condition and a disk mass of $0.007 M_{\odot}$, the planet's inclination oscillates between 0.05° and $\sim 0.4^{\circ}$, which is well in agreement with the observed upper limit of $\sim 0.2^{\circ}$ for the inclination (Orosz et al., 2012, p. 13). The temporal evolution of the planet's inclination indicates that "spike" values as high as 0.4° are detected, although for most of the time covered by the simulation

($T = 5500 T_{\text{bin}}$), the inclination value is lower than 0.2° .

In the simulation without the Stockholm condition and with a highly massive disk of $0.1 M_\odot$ the inclination oscillates around 0.05° but with higher "spikes" in the initial phases of the simulation for which the disk mass has not yet significantly decreased. For lower disk masses, the inclination decreases. This indicates a relationship between the mass of the disk and the inclination.

The author could show a correlation between the disk mass and the amplitude of the inclination, if all other parameters are kept the same. Therefore, it is important to remember that in the setup with the Stockholm condition the $0.007 M_\odot$ disk mass raises by a factor of 10 within the first $1000 T_{\text{bin}}$. For the setup without the Stockholm condition the $0.1 M_\odot$ disk mass is roughly decreasing by 13 % over $1000 T_{\text{bin}}$. This very different disk behavior is influencing the amplitude of the inclination.

Pierens & Nelson (2018, p. 2555) studied in the Kepler 413 planetary system the impact of a primordial misalignment of the circumbinary disk relative to the binary orbit onto the final orbital properties of a migrating planet embedded in the disk and initially co-aligned with it. The authors show that whether the planetary orbit realigns with the central binary stars or remains co-aligned with the disk depends on the disk's mass. Disks around 1 or 2 MMSN lead to either damping of the planet's orbit towards the binary orbit for the first case, or an inclined planet's orbit smaller than the inclination of the disk in the latter case.

The tidal forces of the binary influence the structure of the gas distribution, leading to spatial asymmetries with respect to the mid-plane. Such asymmetries remain undetectable, within the numerical noise, in the single star setup. In the case with the Stockholm condition being implemented and with a consequently (unphysical) rising disk mass, one can see in the density distribution of the xz vertical plane that asymmetries are building up over time. Even so, the simulation started completely co-planar. A similar effect can be seen in the setup without the Stockholm condition being implemented. However, the vertical asymmetries are observed at the beginning of the simulation when the disk mass is still high, while they visually diminish as the disk mass decreases. The decrease in the intensity of the vertical asymmetries in the gas distribution and the decrease of inclination correlate. The author can analyze the cause of these asymmetries by calculating the different forces acting on the planet at the beginning of the simulation. One sees already within the first $10 T_{\text{bin}}$ that the total force on the planet has a vertical z component.

As the gravitational force due to the central binary takes over only beyond this point in time, one can see turbulence building up in the gas density as suggested by Kurbatov et al. (2014, 2017), with the α viscosity being responsible for this turbulence (Shakura & Sunyaev, 1973, p. 343).

This α parameter combines two important mechanisms for the angular momentum trans-

port, i.e., the magnetic field and the turbulence. Thus, it allows computing the appearance of the disk without needing a detailed account of the mechanisms of the angular momentum transfer (Shakura & Sunyaev, 1973, p. 343). The hydrodynamic force resulting from this α viscosity is the origin of the vertical movement in the z direction, but it is impossible to determine the exact source as the α viscosity accounts for two effects, indistinguishably. However, turbulence is seen in the vertical distribution of the gas density, and the α viscosity also reflects the turbulence. Therefore, it is likely that hydrodynamic forces connected to the turbulence in the disk are at the origin of the primordial change in the mutual inclination of the planetary orbit.

The relationship between the inclination and the α viscosity shows that an increasing magnitude of the z component of the hydrodynamical force is seen with a decreasing viscosity parameter. The author concludes that a higher viscosity creates more friction, and thus the inclination introduced by the binary is damped. Reversely, a lower value of the α viscosity parameter would induce a higher mutual inclination of the planet's orbit.

In disks with an identical value of the α viscosity, the inclination of the planet's orbit increases with the disk mass if all the other simulation parameters are kept the same. Therefore, this correlation holds when comparing the results from simulations with the Stockholm condition or without the Stockholm condition separately. Thus, one cannot compare the simulation results with the Stockholm condition with the simulation results without the Stockholm condition. Hence, the hydrodynamical force increases with the disk's mass, assuming a fixed value of the α viscosity. This proportionality relationship between the inclination of the planet's orbit and the disk mass is also shown in this thesis through various simulation experiments. The author could confirm that $M_{\text{disk}} \propto i_{1/2}$ in simulations with raising and falling disk masses. As a consequence, the planet's orbit is affected by a larger inclination with a heavier disk. Other authors also showed the influence of the disk mass onto the planet's evolution. For example, Pierens & Nelson (2018, p. 2558) found that with higher disk masses (>2 MMSN), the disk gravity starts to change the evolution of the planet. Lubow & Martin (2016, p. 13) found in s-type systems that towards higher disk masses, the misalignment becomes more significant because of the secular resonance.

The α viscosity alone is not the origin of the vertical displacement of the planet, as in the single case with the same setup as in the binary case, this movement is insignificant. It only becomes significant in the binary case, with the tidal forces generating increased turbulence. By comparing both cases, a significant difference in the vertical gas density distribution in the disk is shown, as well as in the magnitude of the different force components.

The author could also visualize the turbulence with the z velocity in the disk, which is neglectable small in the single star system and significantly large in the binary system. Moreover, the turbulence is first in the inner region, and later in the simulation, it is throughout the disk.

The simulations suggest that the tidal effects resulting from the binary nature, significantly influencing the circumbinary disk environment. This was also suggested by Kurbatov et al. (2017), who found that already small-scale perturbations in the inner disk create turbulence in the entire disk. Stronger asymmetries in the vertical gas density distribution were observed in the binary case compared to the single star case. This implies that this effect results from enhanced turbulence due to the binary nature of the central star. In return, this impacts the magnitude of the hydrodynamic force acting on the planet in the early phases of the simulation. This thesis concludes that the enhancement of turbulence leads to the observed vertical displacement of the planet. It is unlike that the disk is solely responsible for the misalignment of the planet, as the numerical experiment shows a misalignment of 0.05° for the more realistic case without the Stockholm condition and the Kepler 38 system has a misalignment of $\leq 0.2^\circ$.

Even with different boundary conditions and the newly released code, the author could confirm those results.

The limitations of the simulations are mainly due to the assumptions made. For instance, the planet is not accreting, the disk size is only presenting the inner region of the CB disk (due to computational limitations), the (vertical) resolution of the grid is limited (one could get finer details on the small spatial scales, but at the cost of a significantly higher computational cost), and the effect of a potential magnetic field is not included. As opposed to the case of the more massive Herbig stars in which the stellar magnetic field has a minimal influence, T Tauri stars similar to Kepler 38 in its early evolution stage exhibit stronger, detectable, magnetic fields which may also influence the question studied in this thesis.

In future studies, the behavior of an already inclined planet or an inclined disk could be studied to analyze if this initial inclination gets amplified. Another interesting study could be to consider a larger circumstellar disk in order to simulate a larger mass reservoir in the outer regions of the disk. Moreover, one could study a larger sample of different binary systems and the influence of the binary separation on the vertical displacement of the planet. The accretion from material onto the planet, and thus a changing planet mass, would improve the model to a more realistic one. One could also test the setup of Kepler 38 with different hydrodynamical codes to further reinforce the conclusions, and account for the effects of the

stellar magnetic field.

FARGO3D is developed to study the temporal evolution of a disk or accreting systems. Thus, another element of future work could be implementing the connection to the radiative transfer code RADMC3D. It calculates how the flux is radiated throughout the disk. Making an hypothesis on the gas-dust coupling factor, the time-dependent maps of the gas density distribution can be used to generate synthetic observables from existing or future instruments such as METIS on the ELT. Nonetheless, it is unclear yet if such small effects could be assessed observationally with the current instrumentation. This would justify the development of a corresponding feasibility study.

6.1.2 METIS

The future METIS instrument will play a vital role in observing the above's findings. The sub-systems Warm Calibration Unit (WCU) is located outside of the cryogenic part of METIS and delivers calibration during on-sky operations ensuring long-term measurement repeatability, which is crucial for precise measurements. Since the blackbody source combined with the integrating sphere is a core calibration element of the WCU, the author has carefully characterized the temporal stability and spatial uniformity of this unit.

Therefore, the settling times to reach the required stability were measured. The warming up time of the blackbody was found to be dependent on the final temperatures. Higher temperatures are reached quicker than lower temperatures. Nevertheless, 35 min up to 67 min are needed to get a stable output.

The temporal stability expected at different temperatures is clearly influenced by the A/C which influences particularly low flux values. The relative stability is worse than 10% over a time duration of about 70 min.

Thus, the author tested how the laboratory environment influences the stability of the source. The relative stability measured by the powermeter coming from the blackbody at $T = 200^\circ\text{C}$ has a value of $\sim 1\%$ with the absence of the A/C and is by a factor of 20 better than with the A/C. It is important to mention that in this experiment, the author might ultimately be limited by the specification of the powermeter stability, not by the blackbody source's stability. Indeed, the blackbody source stability specified by the manufacturer is below 0.1%. However, the WCU team is interested here in an upper limit of the stability of the complete setup (blackbody source + integrating sphere + powermeter). For photometric calibrations of the WCU this will allow quite accurate estimates.

The surface of integrating sphere is a potential source of undesired thermal background,

which may add up to the contribution of the room temperature thermal emission. For this work, the author measured the temperature of the outer structure of the sphere to provide elements for the thermal assessment of the WCU through heat dissipation. As expected, it is found that the increase in temperature of the surface of the integrating sphere depends on the blackbody set temperature. The sphere temperature does not exceed 22°C for a blackbody temperature set at 500°C , and $\sim 27^{\circ}\text{C}$ in the worst case for a blackbody temperature of 1000°C , respectively. The rather small increase in temperature of the bench suggests a relatively low efficient heat conduction process between the sphere and the bench, likely because of the small cross-section of the supporting post. This efficiency can be improved by inserting an optimized heat sink in the future.

The results at 200°C with a turned off A/C are interesting. Apart from the disappearance of the high-frequency fluctuations, the author observes an increase in the temperature deviation compared to the case where the A/C is used. This temperature increase remains nonetheless reasonable, i.e., in the order of $\leq 1^{\circ}\text{C}$. However, it is observed that the temperature of the underlying bench increases in the same proportions. The argument on the heat conduction advanced previously can be seen under different light here: the absence of a temperature regulated by the A/C allows the bench to behave as a heat sink, which in returns is observed in the form of an increased temperature change. The latter experiment is closer to the final operating condition of the WCU on the mountain, suggesting that efficient heat conduction could be the solution to mitigate the presence of unwanted localized hot spots in the WCU. Hence, the heat dissipation in the final WCU sub-system remains a critical point to be taken into account in the near future.

The output of the integrating sphere was measured with an uncooled thermal camera to test the spatial uniformity. A spatially uniform output illumination from the integrating sphere of the WCU is key to allow the flat-field calibration of the detector. The spatial uniformity is 99.614% for 15.000 frames. Much less frames can be taken to reach a sufficient accuracy. 4.000 frames with the IR camera already generate a measurement accuracy of $>99.5\%$.

A functionality offered by the WCU of METIS is the assessment of the detector linearity. For METIS, the calibration of the detector linearity should be measured with an accuracy of less than 1%, which means that the flux ratio between two objects measured on the camera should correspond to the real flux ratio with an error of less than 1%. An obvious way to proceed in order to have a time-variable flux would be to change the temperature of the blackbody, which would result in different flux levels within a given spectral band. However, the author's measurements showed that after a modification of the blackbody temperature the settling time can be long before the flux level stabilizes again. Furthermore, with changing the temperature of the blackbody, the spectrum of the blackbody sources changes as

well, which means that the detector linearity measurement may depend on the source's temperature. The author found that this mask (in the current layout) can reduce the calibrating time for each aperture to 20 min in the manual setup and 3 min in the automated setup. For the manual setup, there is significant deviation from the expected linear behavior between the area of the apertures and the measured flux. This results from a bias in the manual measurement. Furthermore, the repeatability of the method, which is a highly important parameter to guarantee the stability of the calibration of the detector linearity in the final instrument: one can observe a stability of $\sim 5\%$, which is not ideally suited to characterize the intrinsic linearity of a science grade detector. Therefore, a different approach is investigated through an automated method.

Considering the automated mask and measuring the output flux of each aperture with the powermeter shows the linear relationship between the apertures and the measured power. Using only the apertures between 24.91 mm (aperture 5) and 314.15 mm (aperture 20), one gets a fit better than 0.2%. This is better than the requirement of the METIS detector ($< 1\%$). Using only apertures starting from aperture five is due to the high signal-to-noise ratio. This influences the repeatability as well. Therefore, only masks with a repeatability between 0.5 and 0.7% are used. This clearly indicates that, despite the tiny fluctuations of the blackbody source and the intrinsic non-linearities of the powermeter, the method based on an automated aperture mask wheel is able to deliver a fairly good linear progression of the delivered flux levels, maintaining at the same time the temperature of the blackbody constant, and hence the spectral slope of the emission.

Adding the uncooled IR camera as a second detector and only considering the measurements between 24.91 mm (aperture 5) to 282.74 mm (aperture 18) a coefficient of determination $R^2 = 0.9993$ can be reached. This indicates a goodness of the fit between the measured data and the linear model to be better than 0.1%, which means the automated aperture mask wheel can deliver fairly good linear progression independent of the detector.

The pinholes need to be developed and inserted in front of the output port of the sphere in order to generate point sources for the calibration of the imaging performances of METIS. The key to successfully developing those pinholes is finding the suitable material/coating for the pinhole. As different materials heat up differently, it adds noise to the measurements. Thus, a material with a surface is needed that does not heat up quickly, does not reflect heat from the detector itself or surrounding (important for laboratory setup, not final WCU design as the latter is telecentric), and transports heat away quickly. Thus in this work, different materials were tested; aluminum and gold-coated pinholes were the ones that had promising results. In the detector's IR spectrum, the gold-coated pinhole had the higher ratio (10.68%) between the pixel intensity from the pinhole region compared with the pixel

intensity of the pixel in the area surrounding the pinhole.

A similar measurement was later executed but this time with a PT100 temperature sensor attached to the surface of the pinhole. They indicate that a comparable temperature higher than 25°C is reached. Despite the higher thermal conductivity of (pure) gold compared to aluminum, a slightly lower temperature is measured for the latter. This small difference might be explained by the fact that the gold is applied here just as a coating. But most probably, the difference comes from the different geometries between the gold-coated and the aluminum pinhole masks. The radiating surface for the gold-coated pinhole mask is not as large as in the case of the aluminum mask, leading to the small increase in temperature observed. For future work, the gold-coated surface pinholes with the final design geometry for the WCU should be tested.

Theory and observation are equally necessary and need to be further developed. In the future, the planet's parameters mentioned above can be better determined in observations through new telescopes or instruments with better resolution and sensitivity.

6.2 Conclusion

In contrast to previous works, this thesis showed the orbital evolution of a circumbinary Saturn-Mass planet in a scenario of primordial co-alignment of the system (binary orbit, planet orbit, disk mid-plane). The author tested the hypothesis of whether turbulence could generate hydrodynamical forces onto an existing, migrating planet. This triggers an initial inclination of the planet's orbit, which was investigated with the FARGO3D three-dimensional hydrodynamical (HD) code in this thesis.

As such inclination effects were expected to be small, the system Kepler 38 was adopted as a test case, in which the circumbinary planet is tilted by less than 0.2° . Then, it was investigated how the disk properties (in particular its mass and viscosity) combined with the dynamical interaction with the central binary result in inhomogeneities in the vertical disk's structure directly influencing the inclination of the planetary orbit.

Below, the most important results are summarized.

- **The author could confirm the influence of the inner cavity on the stopping location of the planet:** The planet's migration stopped just outside the cavity and remained in orbit with $a_p = 0.51$ (using the Stockholm condition) and $a_p = 0.54$ (without using the Stockholm condition). The stopping location is close to the stability radius 0.40 AU and comparable to the reported separation of 0.46 AU .

The stopping location of the planet is independent of the function of the disk mass

and the starting location of the planet.

The author could confirm the influence of the location of the inner boundary on the size of the cavity. The simulation showed a slightly larger cavity with an increasing inner boundary condition. As stated before, the influence is minimal.

The binary's eccentricity influences the inner cavity's size, i.e., larger binary eccentricities lead to larger inner cavity size. In the simulations with a binary eccentricity of 0.1, the periastron of the inner cavity is about 0.54 AU away from the center of mass, and the stability radius is roughly 0.40 AU. Using a binary eccentricity of 0.5, the periastron of the inner cavity is moved to roughly 0.75 AU from the center of mass, with the stability radius being about 0.58 AU.

The influence of the mass ratio of the binary on the inner cavity is found to be negligibly small. A change in the mass ratio has only a minor influence on the location of the smallest stable orbit.

The disk mass does not influence the inner cavity's radius, but the disk mass influences the migration speed. For heavier disks, a faster migration is seen, whereas the migration speed is reduced in disks with a lower mass.

- **The author showed the correlation between the disk mass and the amplitude of the inclination:** Therefore, experiments with rising (with Stockholm) and decreasing disk mass (without Stockholm) were performed. The higher the disk mass, the higher the asymmetries (with the same Stockholm condition).
- **The author demonstrated the tidal forces of the binary influence the structure of the gas distribution:** Those forces lead to spatial asymmetries with respect to the mid-plane. In the single star setup, such asymmetries remain undetectable within the numerical noise. In the xz vertical plane density distribution asymmetries are building up over time. Even so, the simulation started completely co-planar. A later decrease in the intensity of the vertical asymmetries in the gas distribution and the inclination decrease correlates. The hydrodynamic force resulting from this α viscosity originates from the vertical movement in the z direction. Later, the gravitational force due to the central binary takes over.
- **The author displays the inclination of the planet's orbit increases with the disk mass (with all other parameters kept the same):** Hence, the hydrodynamical force increases with the disk's mass.
- **The author proves the α viscosity alone is not the origin of the vertical displacement of the planet:** This vertical displacement is insignificant in the single case with the same setup as the binary case. It only becomes significant in the binary

case, with the tidal forces generating increased turbulence. By comparing both cases, a significant difference in the vertical gas density distribution in the disk is shown, as well as in the magnitude of the different force components.

The visualized turbulence with the z velocity in the disk is neglectable small in the single star system and significantly large in the binary system. This underlines the findings of the significant role of the binary in this thesis. Moreover, the turbulence is first in the inner region, and later in the simulation, it is throughout the disk.

Nevertheless, it is unlike that the disk and binary star is solely responsible for the misalignment of the planet, as the numerical experiment shows a misalignment of 0.05° for the more realistic case without the Stockholm condition and the Kepler 38 system has a misalignment of $\leq 0.2^\circ$.

From the observations point of view, the questions addressed numerically are not simple to investigate. However, indirect effects on the planetary environment – namely the disk – could be investigated through observations. The type of disks relevant to this thesis’s simulations can be observed in the near- and mid-infrared. However, the current observational facilities lack enough angular resolution.

This thesis produced the prototyping measurements to verify the flux properties coming from the integrating sphere. This helps to provide the calibration of the integrating sphere output. Furthermore, the calibration accuracy was determined, and the contribution to developing the aperture mask and the pinholes were detailed. Thus this thesis provides an estimate of the mask that should be used within the WCU. This work contributed to developing METIS and will bring forward the understanding of the evolution of exoplanets in binary systems.

In the following, the most important METIS results are displayed:

- The warming up time of the blackbody is dependent on the final temperatures. Higher temperatures are reached quicker than lower temperatures. The experiments show the blackbody needs from 35 min up to 67 min to get a stable output.
- The temporal stability is clearly influenced by the A/C, which influences particularly low flux values, where the relative stability is worse than 10 % over a time duration of about 70 min.

The relative stability at $T = 200^\circ \text{C}$ has a value of $\sim 1\%$ with the absence of the A/C and is by a factor of 20 better than with the A/C.

- The increase in temperature of the surface of the integrating sphere depends on the blackbody set temperature. The sphere temperature does not exceed 22°C for a black-

body temperature set at 500°C , and $\sim 27^{\circ}\text{C}$ in the worst case for a blackbody temperature of 1000°C .

- To reach the spatial uniformity of $>99.5\%$, one should take at least 4.000 frames to minimize the noise.
- It is recommended to use the automated aperture wheel mask to control the flux level without changing the flux spectrum. The linear relationship between the apertures and the measured power was shown using only the apertures between 24.91 mm (aperture 5) and 314.15 mm (aperture 20). There the repeatability is between 0.5 and 0.7% and the fit is better than 0.2% (requirement of the METIS detector $< 1\%$).
- The uncooled IR camera is a second detector, where only the measurements between 24.91 mm (aperture 5) to 282.74 mm (aperture 18) are considered. Then a coefficient of determination $R^2 = 0.9993$ can be reached. The goodness of the fit between the measured data and the linear model is better than 0.1%, which means the automated aperture mask wheel can deliver fairly good linear progression independent of the detector.
- The coating/material of the pinhole also significantly influences the outcome of the results. Testing two pinholes with the most promising results, aluminum, and gold-coated aluminum, they reach a comparable temperature higher than 25°C . Depending on the material, the temperature and the flux vary.

All results of the numerical experiments and laboratory experiments are stored on hard drives for 10 years with Prof. Dr. Lucas Labadie.

Appendix

Convergence tests of the grid

Eight different grid resolutions were simulated for 20 binary revolutions (1.08 Kepler 38 years $\hat{=}$ 0.003 Earth years) to test the convergence of the grid, which is roughly one orbit of the planet. The setup is simulated with the Stockholm criteria turned on. N_x is varied between the values 256, 512, and 1024, N_y between 512 and 1024, and N_z between 39, 64, 80, 128, and 256. The value N_z is influencing the computational time significantly (see Fig. 6.1). In all the simulations, the results fluctuate around the same values. Moreover, the size of the grid chosen does not influence the movement in the xy-plane of the planet (see Fig. 6.2). That is why the setup with the shortest calculation time ($256 \times 512 \times 39$) was chosen.

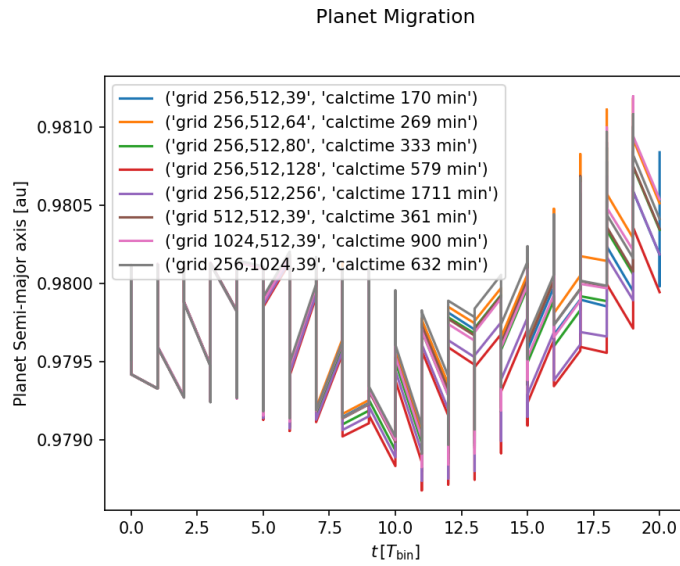


Fig. 6.1: Results of simulations with different grid resolutions with the planet's semi-major axis plotted against the time in binary evolution. Every color corresponds to one grid resolution that is displayed with the computational time needed for that simulation. One can see that with the same N_x , N_y but with the largest N_z (256) and smallest N_z (39), one gets the same results in the last two calculation steps.

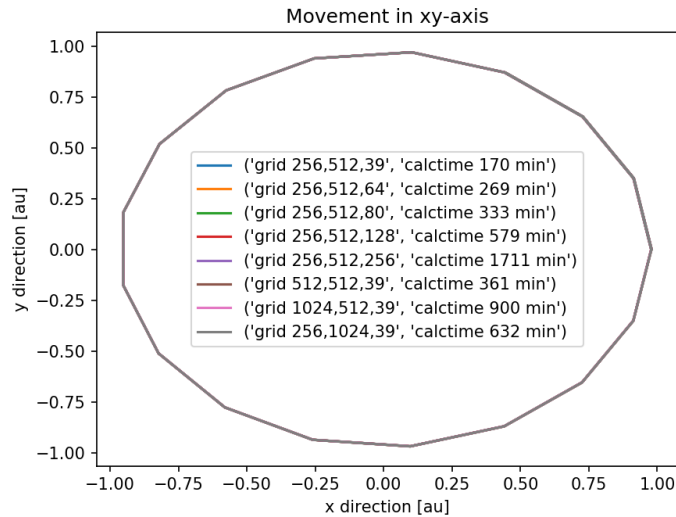


Fig. 6.2: Results of simulations with different grid resolutions. The planets y-position is plotted against the x-position. One can see in all the simulations the result is basically the same. No significant difference.

Migration of the planet with sigmaslope -0.5

The migration of the planet is much quicker with the lower sigmaslope, the eccentricity higher, as well as the inclination (see Fig. 6.3). Thus this parameter influences the outcome of the simulation as the diskmass is much higher when Σ_{ref} is kept constant.

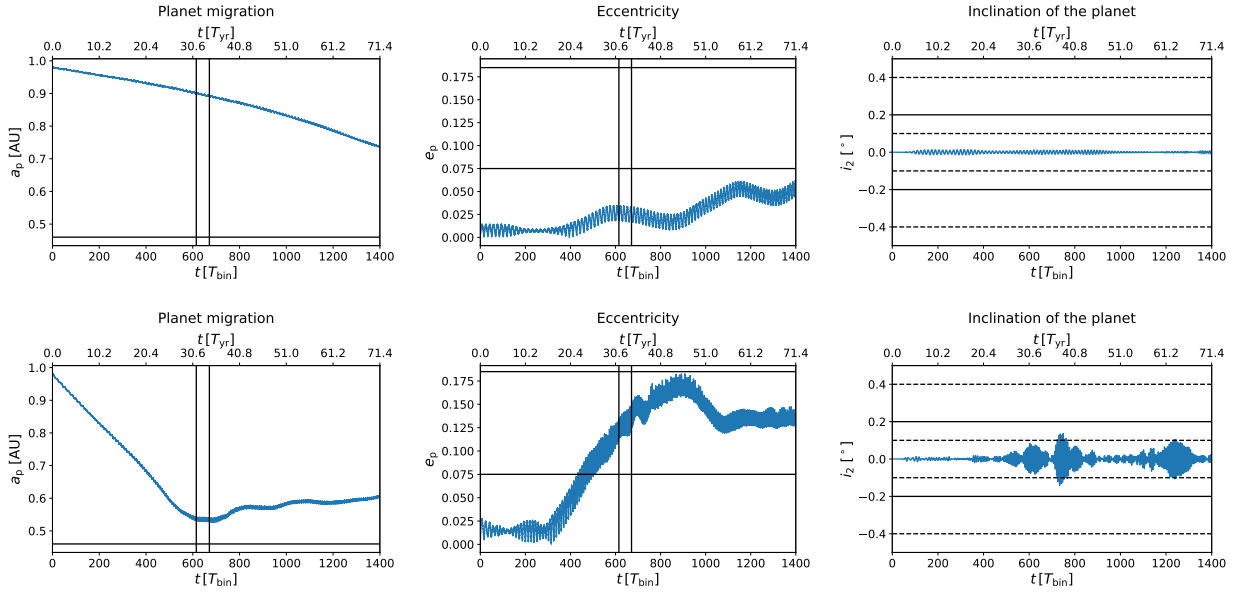


Fig. 6.3: The planets' evolution of the semi-major axis of the binary setup without the Stockholm condition, with $\Sigma = 2.514 \times 10^{-4}$ and power-law for Σ being -1.5 resulting in a disk mass $0.01 M_{\odot}$ (top) and with $\Sigma = 2.514 \times 10^{-4}$ and power-law for Σ being -0.5 resulting in a disk mass $\sim 0.07 M_{\odot}$ (bottom). The left figure shows the evolution over 1400 binary revolutions (on the top axis, the transformation to Earth years is shown). The horizontal line is the observed planet's location (0.46 AU). The migration in the setup with Stockholm condition happened mostly between 615 and 671 binary revolutions (solid vertical lines). In the top simulation the migration process takes much longer and in the bottom simulation with $p = -0.5$ the migration process it happens in the first $500 T_{\text{bin}}$ as the mass is higher. The middle figure shows the evolution of the planet's eccentricity, and the right figure shows the inclination. In the latest figures, the black lines are the same as in the with Stockholm setup. This helps with the comparison.

Disk with no planet in the single setup with default star

The simulation in Fig. 6.4 was done with a starting disk mass $0.007 M_{\odot}$ and with the Stockholm condition turned on. It is a single setup with default star simulation but without a planet.

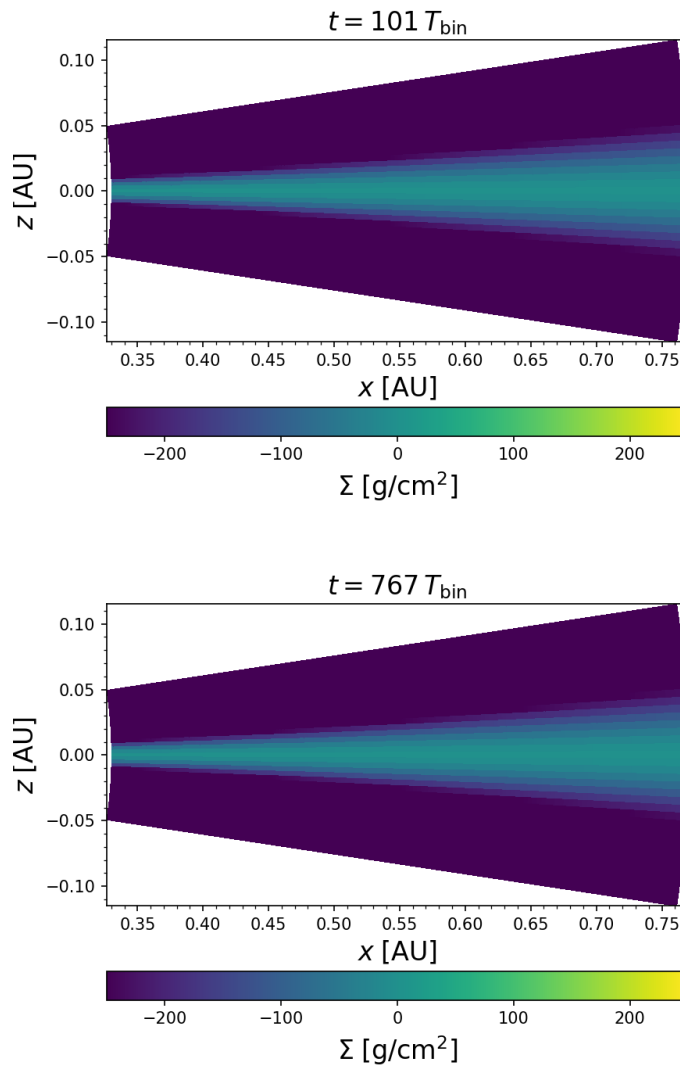


Fig. 6.4: The results of the simulation without a planet are shown. One can see that the single setup is symmetric over time and not disturbed in any way. This is expected by a single default star in the center of mass with no planet inserted.

Inclination of the planet towards the mid-plane in single star system with Stockholm condition

The inclination towards the mid-plane in the single star case with the Stockholm condition is shown in Fig. 6.5. One can see the inclination stays zero.

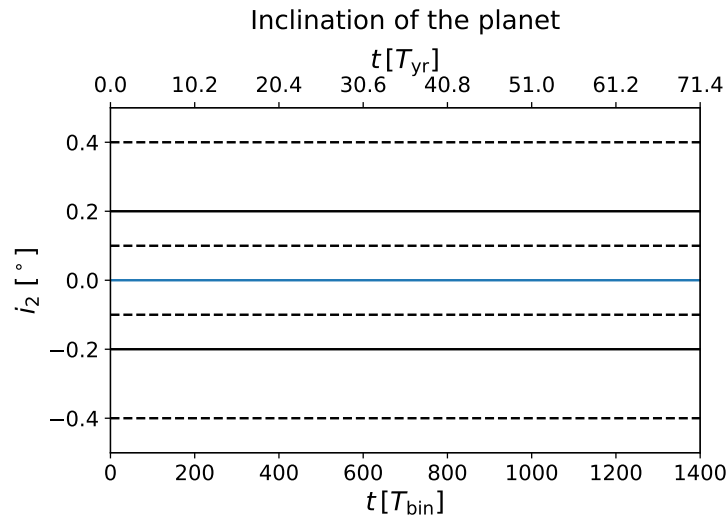


Fig. 6.5: The plot shows the inclination of the planet with respect to the mid-plane in the z direction.

Different location of the outer boundary

According to Thun et al. (2017, p. 8) the optimal outer boundary is set to $40 a_{\text{bin}}$ which would be in our case roughly 6 AU. Because of the long computational times, the outer boundary is reduced. Test simulations showed that this reduction does not influence the output (see Fig. 6.6). Thus the outer boundary of $a_{\text{bin}} = 2.1$ AU is taken, which is close to Kley & Haghighipour (2014, p. 3) and a good trade-off between computational time and size. This simulation was done with a starting disk mass $0.007 M_{\odot}$ and the Stockholm condition turned on.

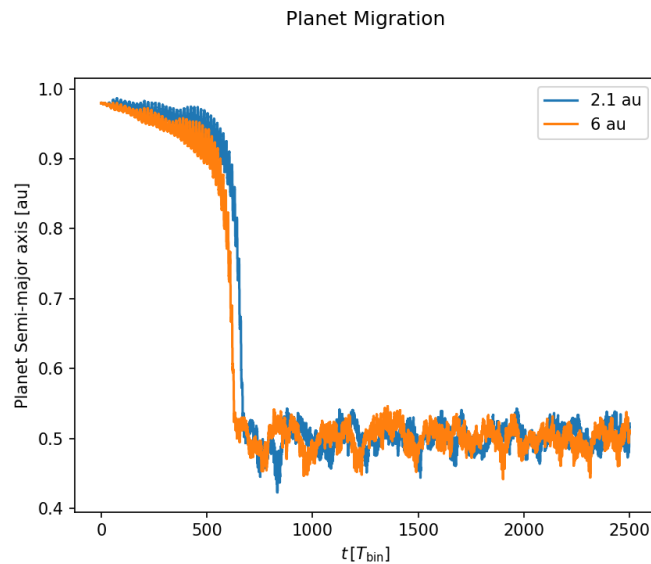


Fig. 6.6: The results of simulations with different outer boundaries are shown, where the planet’s semi-major axis is plotted against the time in binary revolutions with an outer boundary of 2.1 AU and 6 AU. The figure shows a bit of difference because of the different outer boundary locations.

FARGO3D Inputfiles

Input file for the setup without the Stockholm condition.

p3disof_test.par file:

Setup p3disof_test

Disk parameters

AspectRatio	0.05	Thickness over Radius in the disc
Sigma0	2.51390456e-4	1.25695228e-3 2.51390456e-3
Alpha	1.0e-2	
SigmaSlope	1.5	Slope of surface
FlaringIndex	0.0	

Planet parameters

PlanetConfig	planets/SuperEarth_test.cfg	
ThicknessSmoothing	0.6	Smoothing parameters in disk thickness
Eccentricity	0.0	
ExcludeHill	No	
INCLINATION	0.0	

Numerical method parameters

Disk	YES
OmegaFrame	0.0
Frame	F
IndirectTerm	Yes
Spacing	log

Mesh parameters

Nx	256	Azimuthal number of zones
Ny	512	Radial number of zones
Nz	39	Number of zones in colatitude
Ymin	1.3	Inner boundary radius
Ymax	14.28	Outer boundary radius
Zmin	1.42079632679489661922	
Zmax	1.72079632679489661922	
Xmin	-3.141592653589793	
Xmax	3.14159265358979	

Output control parameters

Ntot	200000	Total number of time steps 10000
Ninterm	10	Time steps between outputs
DT	6.28318530717959e-1	Time step length. 2PI = 1 orbit
OutputDir	/projects/...	

Field	gasdens
PlotLine	field[-1, :, :]
RHOFLOR	1.0e-13

p3disof_test.opt file:

MONITOR_2D = MASS | MOM_X

```
#Dimension(s) of Simulation. Here 3D (Phi,r,theta)
FARGO_OPT += -DX
FARGO_OPT += -DY
FARGO_OPT += -DZ

#Coordinate System.
FARGO_OPT += -DSPHERICAL

#Equation of State
FARGO_OPT += -DISOTHERMAL

FARGO_OPT += -DNODEFAULTSTAR
FARGO_OPT += -DSTOCKHOLM
FARGO_OPT += -DALPHA VISCOSITY
FARGO_OPT += -DPOTENTIAL

#Cuda blocks
ifeq (${GPU}, 1)
FARGO_OPT += -DBLOCK_X=16
FARGO_OPT += -DBLOCK_Y=8
FARGO_OPT += -DBLOCK_Z=4
endif
```

Planetary file SuperEarth_test.cfg:

# Planet Name	Distance	Mass	Accretion	Feels Disk	Feels Others
Kepler38A	6.28	0.8	0.0	NO	YES
Kepler38B	0.1	0.2	0.0	NO	YES
Kepler38c	6.6667	0.00025	0.0	YES	YES

Boundary Conditions:

Density:

```
Ymin: SYMMETRIC
Ymax: SYMMETRIC
Zmin: KEPLERIAN3DSPHDENSCOL
Zmax: KEPLERIAN3DSPHDENSCOL
```

Vx:

Ymin: KEPLERIAN3DSPHVAZIMRAD
Ymax: KEPLERIAN3DSPHVAZIMRAD
Zmin: KEPLERIAN3DSPHVAZIMCOL
Zmax: KEPLERIAN3DSPHVAZIMCOL

Vy:

Ymin: OUTFLOW
Ymax: ANTISYMMETRIC
Zmin: SYMMETRIC
Zmax: SYMMETRIC

Vz:

Ymin: SYMMETRIC
Ymax: SYMMETRIC
Zmin: ANTISYMMETRIC
Zmax: ANTISYMMETRIC

Aperture Mask

Manuel Setup

Tab. 6.1: Sizes of the apertures for manual setup

diameters [mm]	areas [mm ²]
blank	0
0.50	0.2
1.526	1.83
2.553	5.12
3.579	10.06
4.605	16.66
5.632	24.91
6.658	34.81
7.684	46.37
8.711	59.59
9.737	74.46
10.763	90.98
11.79	109.16
12.816	128.99
13.842	150.48
14.868	173.62
15.905	198.42
16.921	224.87
17.947	252.98
18.974	282.74
20.00	314.15

Automated Setup

Tab. 6.2: Sizes of the apertures for automatic setup

diameters [mm]	areas [mm ²]
blank	0
1.526	1.83
2.553	5.12
3.579	10.06
4.605	16.66
5.632	24.91
6.658	34.81
7.684	46.37
8.711	59.59
9.737	74.46
10.763	90.98
11.79	109.16
12.816	128.99
13.842	150.48
14.868	173.62
15.905	198.42
16.921	224.87
17.947	252.98
18.974	282.74
20.00	314.15
25.40 (36.1)	506.71

Bibliography

- Agertz O., et al., 2007, *Monthly Notices of the Royal Astronomical Society*, 380, 963
- Akeson R. L., Jensen E. L. N., Carpenter J., Ricci L., Laos S., Nogueira N. F., Suen-Lewis E. M., 2019, *The Astrophysical Journal*, 872, 158
- Aly H., Dehnen W., Nixon C., King A., 2015, *Monthly Notices of the Royal Astronomical Society*, 449, 65
- Andrews L. C., 1997, *Special Functions of Mathematics for Engineers*, Second Edition. SPIE Press
- Armitage P. J., 2007, Technical Report 1969, Lecture notes on the formation and early evolution of planetary systems
- Armitage P. J., 2009a, Giant planet formation. Cambridge University Press, p. 185–217
- Armitage P. J., 2009b, Protoplanetary disk structure. Cambridge University Press, p. 34–64
- Armitage P. J., 2009c, Protoplanetary disk evolution. Cambridge University Press, p. 65–108
- Artymowicz P., Lubow S. H., 1994, *Astrophysical Journal*, 421, 651
- Augereau J.-C., Duchêne G., Hönig S., Kraus S., Paladini C., Kraus S., Monnier J. D., 2015, Planet Formation Imager (PFI)
- Baccichet N., 2017, Technical report, WCU fluxes and design trade-off
- Baccichet N., et al., 2018, in Evans C. J., Simard L., Takami H., eds, Vol. 10702, *Ground-based and Airborne Instrumentation for Astronomy VII*. SPIE, pp 2829 – 2839
- Baruteau C., et al., 2013, *Protostars Planets VI*, 1312, 24
- Bate M. R., 2012, *Monthly Notices of the Royal Astronomical Society*, 419, 3115
- Bate M. R., Lodato G., Pringle J. E., 2010, *Monthly Notices of the Royal Astronomical Society*, 401, 1505

- Batygin K., 2012, *Nature*, 491, 418
- Beckwith S. V. W., 1990, *The Astronomical Journal*, 99, 924
- Beckwith S. V., Sargent A. I., 1996, *Nature*, 383, 139
- Belloche A., 2013, *EAS Publications Series*, 62, 25
- Benítez-Llambay P., Masset F., 2015a, *FARGO3D*, fargo.in2p3.fr/
- Benítez-Llambay P., Masset F., 2015b, *FARGO3D User Guide Release 1.2*, <http://fargo.in2p3.fr/manuals/FARGO3DUserGuide.pdf>
- Benítez-Llambay P., Masset F., 2016, *The Astrophysical Journal Supplement Series*, 223
- Benítez-Llambay P., Masset F. S., 2019, *FARGO3D 2.0 documentation*, <https://fargo3d.bitbucket.io/>
- Benítez-Llambay P., Ramos X. S., Beaugé C., Masset F. S., 2016, *The Astronomical Journal*, 826, 9
- Birnstiel T., Dullemond C. P., Brauer F., 2010, *Astronomy and Astrophysics*, 513, 1
- Bitsch B., Kley W., 2011, *Astronomy and Astrophysics*, 530, 1
- Bouvier J., Tessier E., Cabrit S., 1992, *Astronomy and Astrophysics*, 261, 451
- Brandl B. R., et al., 2016, in Evans C. J., Simard L., Takami H., eds, Vol. 9908, *Ground-based and Airborne Instrumentation for Astronomy VI*. SPIE, pp 633 – 647
- Brandl B. R., et al., 2018, in Evans C. J., Simard L., Takami H., eds, Vol. 10702, *Ground-based and Airborne Instrumentation for Astronomy VII*. SPIE, pp 582 – 596
- Campbell B., Walker G. A. H., Yang S., 1988, *Astrophysical Journal*, 331, 902
- Chametla R. O., Sánchez-Salcedo F. J., Masset F. S., Hidalgo-Gómez A. M., 2017, *Monthly Notices of the Royal Astronomical Society*, 468, 4610
- Chatterjee S., Ford E. B., Matsumura S., Rasio F. A., 2008, *The Astrophysical Journal*, 686, 580
- Chen C., Franchini A., Lubow S. H., Martin R. G., 2019, *Monthly Notices of the Royal Astronomical Society*, 490, 5634
- Chen C., Lubow S. H., Martin R. G., 2020, *Monthly Notices of the Royal Astronomical Society*, 494, 4645

- Chorin A. J., Marsden Jerrold E. 1993, *The Equations of Motion*, 4 edn
- Cieza L. A., et al., 2009, *The Astrophysical Journal*, 696, L84
- Cresswell P., Dirksen G., Kley W., Nelson R. P., 2007, *Astronomy and Astrophysics*, 473, 329
- Crida A., Morbidelli A., Masset F., 2006, *Icarus*, 181, 587
- Crida A., Morbidelli A., Masset F., 2007, *Astronomy and Astrophysics*, 461, 1173
- Czekala I., Chiang E., Andrews S. M., Jensen E. L. N., Torres G., Wilner D. J., Stassun K. G., Macintosh B., 2019, *The Astrophysical Journal*, 883, 22
- Davis J., et. al. 2001, *Copper and Copper Alloys*. ASM specialty handbook, ASM International
- De Val-Borro M., et al., 2006, *Monthly Notices of the Royal Astronomical Society*, 370, 529
- Dellar P. J., 2001, *Physical Review E - Statistical Physics, Plasmas, Fluids, and Related Interdisciplinary Topics*, 64, 11
- Doolin S., Blundell K. M., 2011, *Monthly Notices of the Royal Astronomical Society*, 418, 2656
- Doyle L. R., et al., 2011, *Science*, 333, 1602
- Duchêne G., 2010, *The Astrophysical Journal Letters*, 709, 114
- Dullemond C. P., 2013, in *Les Houches*. <http://www.ita.uni-heidelberg.de/~dullemond/lectures/leshouches2013.pdf>
- Dullemond C. P., Dominik C., 2004, *Astronomy and Astrophysics*, 417, 159
- Dullemond C. P., Juhasz A., Pohl A., Sereshti F., Shetty R., Peters T., Commercon B., Flock M., 2012, *RADMC-3D: A multi-purpose radiative transfer tool* (ascl:1202.015)
- Duquennoy A., Mayor M., 1991, *Astronomy and Astrophysics* (ISSN 0004-6361), 248, 485
- Eupen F., et al., 2021, *Astronomy and Astrophysics*, 648
- Fabrycky D., Tremaine S., 2007, *The Astrophysical Journal*, 669, 1298
- Farago F., Laskar J., 2010, *Monthly Notices of the Royal Astronomical Society*, 401, 1189
- Foucart F., Lai D., 2014, *Monthly Notices of the Royal Astronomical Society*, 445, 1731

- Franchini A., Martin R. G., Lubow S. H., 2020, *Monthly Notices of the Royal Astronomical Society*, 491, 5351
- Garufi A., et al., 2017, *Astronomy and Astrophysics*, 603, A21
- Graf S., Rutowska M., Wiest M., Rost S., Straubmeier C., Labadie L., 2020, in Evans C. J., Bryant J. J., Motohara K., eds, Vol. 11447, *Ground-based and Airborne Instrumentation for Astronomy VIII*. SPIE, pp 577 – 585
- Günther R., Kley W., 2002, *Astronomy and Astrophysics*, 387, 550
- Haghighipour N., 2008, *Exoplanets*, pp 223–257
- Haghighipour N., Dvorak R., Pilat-Lohinger E., 2010, *Planetary Dynamics and Habitable Planet Formation in Binary Star Systems*. Springer Netherlands, Dordrecht, pp 285–327
- Hanssen L., Snail K., 2006, *Integrating Spheres for Mid- and Near-Infrared Reflection Spectroscopy*. p. 19
- Hatzes A. P., Cochran W. D., Endl M., McArthur B., Paulson D. B., Walker G. A. H., Campbell B., Yang S., 2003, *The Astrophysical Journal*, 599, 1383
- Holman M. J., Wiegert P. A., 1999, *The Astronomical Journal*
- Johnson M., 2017, Kepler and K2 mission overview, https://www.nasa.gov/mission_pages/kepler/overview/index.html
- Kimmig, C. N. Dullemond, C. P. Kley, W. 2020, *Astronomy and Astrophysics*, 633, 9
- Kirk B., et al., 2016, *The Astronomical Journal*, 151, 68
- Klahr H., Pfeil T., Schreiber A., 2018, *Handbook of Exoplanets*, pp 2251–2286
- Kley W., 2013. Vorlesungsskript. <https://www.tat.physik.uni-tuebingen.de/~kley/lehre/theoast/script/skript.pdf>
- Kley W., Haghighipour N., 2014, *Astronomy and Astrophysics*, 564, A72
- Kley W., Haghighipour N., 2015, *Astronomy and Astrophysics*, 581, A20
- Kley W., Nelson R. P., 2010, *Early Evolution of Planets in Binaries: Planet–Disk Interaction*. Springer Netherlands, Dordrecht, pp 135–165
- Kley W., Nelson R. P., 2012, *Annual Reviews of Astronomy and Astrophysics*, p. 43
- Kloster D. L., Flock M., 2019, *Monthly Notices of the Royal Astronomical Society*, 487, 5372

- Koch D. G., et al., 2010, *Astrophysical Journal Letters*, 713
- Kostov V. B., et al., 2014, *Astrophysical Journal*, 784
- Kurbatov E. P., Bisikalo D. V., Kaygorodov P. V., 2014, *Physics-Uspekhi*, 57, 787
- Kurbatov E. P., Sytov A. Y., Bisikalo D. V., 2017, *Astronomy Reports*, 61, 1031
- Lada C. J., 1987, *Symposium - International Astronomical Union*, 115, 1
- Lai D., Foucart F., 2012, *Proceedings of the International Astronomical Union*, 8, 146
- Lubow S. H., Martin R. G., 2016, *The Astrophysical Journal*, 817, 30
- Martin R. G., Lubow S. H., 2017, *The Astrophysical Journal*, 835, L28
- Martín E. L., Magazzù A., Delfosse X., Mathieu R. D., 2005, *Astronomy & Astrophysics*, 429, 939
- Martin R. G., Lubow S. H., Nixon C., Armitage P. J., 2016, *Monthly Notices of the Royal Astronomical Society*, 458, 4345
- Marzari F., Thebault P., 2019, *Galaxies*, 7, 1
- Masset F. S., 2002, *Astronomy and Astrophysics*, 387, 605
- Masset F. S., Benítez-Llambay P., 2016, *The Astrophysical Journal*, 817, 19
- Masset F. S., Morbidelli A., Crida A., Ferreira J., 2006, *The Astrophysical Journal*, 642, 478
- Mathieu R., Stassun K., Basri G., Jensen E., JohnsKrull C., Valenti J., Hartmann L., 1997, *Astronomical Journal*, 113, 1841
- McNally C. P., Nelson R. P., Paardekooper S. J., Benítez-Llambay P., 2019, *Monthly Notices of the Royal Astronomical Society*, 484, 728
- Monnier J. D., et al., 2019, *The Astrophysical Journal*, 872, 122
- Müller T. W. A., Kley W., Meru F., 2012, *Astronomy and Astrophysics*, 541
- NASA, NASA Exoplanet Archive, <https://exoplanetarchive.ipac.caltech.edu/overview/Kepler-38>
- Nelson R. P., Gressel O., 2010, *Monthly Notices of the Royal Astronomical Society*, 409, 639
- Nixon C. J., 2012, *Monthly Notices of the Royal Astronomical Society*, 423, 2597

- Orosz J. A., et al., 2012, *The Astrophysical Journal*, 758, 1
- Panić O., et al., 2021, *Monthly Notices of the Royal Astronomical Society*, 501, 4317
- Picogna, G. Marzari, F. 2015, *Astronomy and Astrophysics*, 583, A133
- Pierens A., Nelson R. P., 2007, *Astronomy and Astrophysics*, 472, 993
- Pierens A., Nelson R. P., 2018, *Monthly Notices of the Royal Astronomical Society*, 477, 2547
- Pierens, A. Nelson, R. P. 2008, *Astronomy and Astrophysics*, 483, 633
- Pierens, A. Nelson, R. P. 2013, *Astronomy and Astrophysics*, 556, A134
- Pierens A., McNally C. P., Nelson R. P., 2020, *Monthly Notices of the Royal Astronomical Society*, 496, 2849
- Pilat-Lohinger E., Eggl S., Bazso A., 2019, *Habitability of Known Planets in Binary Star Systems*. World Scientific Publishing Company, pp 115–141
- Prato L., Weinberger A. J., 2010, *Disks Around Young Binary Stars*. Springer Netherlands, Dordrecht, p. 332
- Price D. J., Monaghan J. J., 2004, *Monthly Notices of the Royal Astronomical Society*, 348, 139
- Pringle J. E., 1991, *Monthly Notices of the Royal Astronomical Society*, 248, 754
- Queloz D., et al., 2000, *Astronomy and Astrophysics*, 354, 99
- Quintana E. V., Lissauer J. J., 2006, *Icarus*, 185, 1
- Raghavan D., et al., 2010, *The Astrophysical Journal Supplement Series*, 190, 1
- Rosotti G. P., 2014, *Proto-planetary disc evolution and dispersal*
- Rutowska M., et al., 2020, in Evans C. J., Bryant J. J., Motohara K., eds, Vol. 11447, *Ground-based and Airborne Instrumentation for Astronomy VIII*. SPIE, pp 586 – 596
- Schwarz R., 2021, *Catalogue of exoplanets*, <https://www.univie.ac.at/adg/schwarz/multiple.html>
- Schwarz R., Funk B., Zechner R., Bazsó Á., 2016, *Monthly Notices of the Royal Astronomical Society*, 460, 3598

- Shakura N. I., Sunyaev R. A., 1973, *Astronomy and Astrophysics*, 500, 33
- Shore S. N., 1992, *An Introduction to Astrophysical Hydrodynamics*. Academic Press
- Shu F. H., 1992, *The Physics of Astrophysics: Gas dynamics*. University Science Books
- Silsbee K., Rafikov R. R., 2015, *Astrophysical Journal*, 808
- Smallwood J. L., Lubow S. H., Franchini A., Martin R. G., 2019, *Monthly Notices of the Royal Astronomical Society*, 486, 2919
- Stone J. M., Norman M. L., 1992, *The Astrophysical Journal Supplement Series*, 80, 753
- Taha A. S., et al., 2018, *Astronomy and Astrophysics*, 612, 1
- Tanaka H., Ward W. R., 2004, *The Astrophysical Journal*, 602, 388
- Tanaka H., Takeuchi T., Ward W. R., 2002, *The Astrophysical Journal*, 565, 1257
- Thun D., Kley W., 2018, *Astronomy and Astrophysics*, 616, 19
- Thun D., Kley W., Picogna G., 2017, *Astronomy and Astrophysics*, 604, A102
- Tipler P. A., Mosca G., 2009, *Physik: für Wissenschaftler und Ingenieure*. Spektrum Akademischer Verlag, <https://books.google.de/books?id=60HtPgAACAAJ>
- Touma J. R., Tremaine S., Kazandjian M. V., 2009, *Monthly Notices of the Royal Astronomical Society*, 394, 1085
- Tricco T. S., 2019, *Monthly Notices of the Royal Astronomical Society*, 488, 5210
- UCLA, Observing Mercury, <http://www.physics.ucla.edu/%7Ehuffman/merc.html>
- Walker G. A. H., Bohlender D. A., Walker A. R., Irwin A. W., Yang S. L. S., Larson A., 1992, *Astrophysical Journal Letters*, 396, L91
- Weidenschilling S. J., 1977, *Astrophys Space Sci*, 51, 153
- Welsh W. F., Orosz J. A., 2018, in Belmonte A. J., Deeg H. J., eds, , *Handbook of Exoplanets*. Springer, Cham, pp 1–21, doi:10.1007/978-3-319-30648-3
- Welsh W. F., et al., 2012, *Nature*, 481, 475
- Welsh W. F., Orosz J. A., Carter J. A., Fabrycky D. C., Team K., 2013, *Recent Kepler Results On Circumbinary Planets*. p. 8, <https://arxiv.org/pdf/1308.6328.pdf>

Winn J. N., Fabrycky D. C., 2015, *Annu. Rev. Astron. Astrophys.*, 53, 409

Wu Y., Lithwick Y., 2011, *Astrophysical Journal*, 735

Ziegler U., 1998, *Computer Physics Communications*, 109, 111

List of Figures

2.1	classification of YSOs	8
2.2	surface density of 2D disk: spiral arms	12
2.3	circumbinary 2D disk	13
2.4	largest critical semi-major axis vs. the binary separation	15
2.5	mean free path	17
2.6	s-type configuration with a misaligned disk/planet	24
3.1	structure and float chart for FARGO3D	33
3.2	sketch of aspect ratio h	34
3.3	surface density of different disk sizes and masses	41
3.4	density transformation CU to CGS units	47
3.5	velocity transformation CU to CGS units	47
3.6	sketch of linearly spaced grid cells after the transformation	48
3.7	volume density distribution of the z plane	49
3.8	disk with Cartesian Grid vs. polar grid of the z plane	50
3.9	subtracted volume density distribution of the z plane	50
4.1	sketch of binary setup to visualize the two different inclination angles	52
4.2	velocity within the disk of single star setup	53
4.3	disk mass evolution of single default setup (with/without Stockholm, with planet, $M_{\text{disk}} = 0.01 M_{\odot}$)	53
4.4	planet parameter evolution for single default setup (with/without Stockholm, with planet, $M_{\text{disk}} = 0.01 M_{\odot}$)	54
4.5	mutual inclination of disk and normal vector in single default setup (without Stockholm, with planet, $M_{\text{disk}} = 0.01 M_{\odot}$)	56
4.6	mutual inclination of planet and normal vector in single default setup (without Stockholm, with planet, $M_{\text{disk}} = 0.01 M_{\odot}$)	56
4.7	stellar parameter evolution of the single star setup (no default case, without Stockholm, with planet, $M_{\text{disk}} = 0.01 M_{\odot}$ and $0.1 M_{\odot}$)	59

4.8	surface density in the mid-plane for single star setup (no default case, without Stockholm, with planet, $M_{\text{disk}} = 0.01 M_{\odot}$ and $0.1 M_{\odot}$)	60
4.9	planet parameter evolution of the single star setup (no default case, without Stockholm, with planet, $M_{\text{disk}} = 0.01 M_{\odot}$ and $0.1 M_{\odot}$)	61
4.10	mutual inclination of planet and normal vector in single star setup (no default case, without Stockholm, with planet, $M_{\text{disk}} = 0.1 M_{\odot}$)	63
4.11	disk mass evolution of single star setup (no default case, without Stockholm, with planet, $M_{\text{disk}} = 0.01 M_{\odot}$)	63
4.12	planet parameter evolution of binary system without disk interaction (with Stockholm, $M_{\text{disk}} = 0.007 M_{\odot}$)	65
4.13	subtraction two-dimensional surface density plot of the xz plane (with Stockholm, without planet, $M_{\text{disk}} = 0.007 M_{\odot}$)	65
4.14	mutual inclination of disk and normal vector in binary setup (with Stockholm, without planet, $M_{\text{disk}} = 0.007 M_{\odot}$)	66
4.15	evolution of mutual inclination of disk and normal vector in binary setup (with Stockholm, without planet, $M_{\text{disk}} = 0.007 M_{\odot}$)	67
4.16	disk mass evolution of binary setup (with Stockholm, without planet, $M_{\text{disk}} = 0.007 M_{\odot}$)	68
4.17	two-dimensional plots of the surface density of the mid-plane in the binary setup (with Stockholm, with planet, $M_{\text{disk}} = 0.007 M_{\odot}$)	69
4.18	two-dimensional xy plane plots of the surface density in the binary setup (with Stockholm, with planet, $M_{\text{disk}} = 0.007 M_{\odot}$)	70
4.19	disk mass evolution with/without planet of binary setup (with Stockholm, $M_{\text{disk}} = 0.007 M_{\odot}$)	71
4.20	azimuthally-averaged plot of the surface density for the binary setup (with Stockholm, with planet, $M_{\text{disk}} = 0.007 M_{\odot}$)	72
4.21	planet parameter evolution for different disk densities for the binary setup (with Stockholm, with planet, $M_{\text{disk}} = 0.007 M_{\odot}$)	72
4.22	inclination of the planet with respect to the mid-plane (with Stockholm, with planet, $M_{\text{disk}} = 0.007 M_{\odot}$)	74
4.23	two-dimensional xz plane plots of the surface density in the binary setup (with Stockholm, with planet, $M_{\text{disk}} = 0.007 M_{\odot}$)	74
4.24	subtracted two-dimensional xz plane plots of the surface density in the binary setup with (with Stockholm, with planet, $M_{\text{disk}} = 0.007 M_{\odot}$)	75
4.25	disk mass evolution of binary/single star setup (with Stockholm, with planet, $M_{\text{disk}} = 0.007 M_{\odot}$)	77

4.26 force in z direction on the planet in the binary system (with Stockholm, with planet, $M_{\text{disk}} = 0.007 M_{\odot}$)	77
4.27 F_z evolution in the single and binary case (with Stockholm condition, $M_{\text{disk}} = 0.007 M_{\odot}$)	78
4.28 mutual inclination of disk and normal vector in binary setup (with Stockholm, with planet, $M_{\text{disk}} = 0.007 M_{\odot}$)	79
4.29 mutual inclination of planet and normal vector in binary setup (with Stockholm, with planet, $M_{\text{disk}} = 0.007 M_{\odot}$)	80
4.30 noise of simulation for binary setup (with Stockholm, with planet, $M_{\text{disk}} = 0.007 M_{\odot}$)	81
4.31 planet parameter evolution: semi-major axis of the binary setup (with Stockholm, with planet, $M_{\text{disk}} = 0.007 M_{\odot}$)	81
4.32 planet migration with different starting locations for the binary setup (with Stockholm, with planet, $M_{\text{disk}} = 0.007 M_{\odot}$)	83
4.33 planet parameter evolution: eccentricity of the binary setup with the Stockholm condition (with Stockholm, with planet, $M_{\text{disk}} = 0.007 M_{\odot}$)	83
4.34 disk mass evolution of the binary setup (without the Stockholm condition, with planet, $M_{\text{disk}} = 0.01 M_{\odot}$)	84
4.35 subtracted two-dimensional xz plane plots of the surface density in the binary setup (without Stockholm condition, no planet, $M_{\text{disk}} = 0.01 M_{\odot}$)	85
4.36 planet parameter of the binary setup with a different inner boundary location (without the Stockholm condition, $M_{\text{disk}} = 0.021 M_{\odot}$ and $M_{\text{disk}} = 0.01 M_{\odot}$)	86
4.37 disk mass evolution of the binary setup with a different inner boundary location (without the Stockholm condition, with planet, $M_{\text{disk}} = 0.01 M_{\odot}$)	86
4.38 azimuthally-averaged plot of the surface density of the binary setup with a different inner boundary location (without the Stockholm condition, with planet, $M_{\text{disk}} = 0.01 M_{\odot}$)	87
4.39 azimuthally-averaged plot of the surface density of the binary setup with a different viscosity (without the Stockholm condition, with planet, $M_{\text{disk}} = 0.01 M_{\odot}$)	88
4.40 planet parameter of the binary setup with a different viscosity (without the Stockholm condition, with planet, $M_{\text{disk}} = 0.01 M_{\odot}$)	88
4.41 $F_{\text{hd},z}$ of the binary setup with a different viscosity and different disk mass (without the Stockholm condition, with planet, $M_{\text{disk}} = 0.01 M_{\odot}$ and $M_{\text{disk}} = 0.1 M_{\odot}$)	89
4.42 noise of simulation for binary setup (without the Stockholm condition, with planet, $M_{\text{disk}} = 0.01 M_{\odot}$)	89

4.43	two-dimensional xy plane plots of the surface density of the mid-plane in the binary setup (without the Stockholm condition, with planet, $M_{\text{disk}} = 0.01 M_{\odot}$)	91
4.44	two-dimensional xy plane plots of the surface density in the binary setup (without the Stockholm condition, with planet, $M_{\text{disk}} = 0.01 M_{\odot}$)	92
4.45	azimuthally-averaged plot of the surface density for the binary setup (without the Stockholm condition, with planet, $M_{\text{disk}} = 0.01 M_{\odot}$)	94
4.46	planet parameter: semi-major axis of the binary setup (without the Stockholm condition, $M_{\text{disk}} = 0.01 M_{\odot}$)	94
4.47	planet parameter of the binary setup with different disk masses (without the Stockholm condition)	96
4.48	two-dimensional xy plane plots of the surface density in the mid-plane in the binary setup for different binary eccentricities (without Stockholm condition, with planet, $M_{\text{disk}} = 0.021 M_{\odot}$)	97
4.49	planet parameter for the binary setup with different binary eccentricities (without the Stockholm condition, $M_{\text{disk}} = 0.021 M_{\odot}$ disk)	97
4.50	planet parameter for the binary setup with $e_b = 0.5$ (without the Stockholm condition, $M_{\text{disk}} = 0.021 M_{\odot}$)	98
4.51	planet parameter for the binary setup with different binary mass ratios (without the Stockholm condition, $M_{\text{disk}} = 0.021 M_{\odot}$ disk)	99
4.52	planets' parameter evolution in the binary setup (without the Stockholm condition, $M_{\text{disk}} = 0.01 M_{\odot}$ and $M_{\text{disk}} = 0.1 M_{\odot}$)	101
4.53	mutual inclination of planet and normal vector in binary setup (without Stockholm condition, $M_{\text{disk}} = 0.01 M_{\odot}$ and $M_{\text{disk}} = 0.1 M_{\odot}$)	101
4.54	mutual inclination of planet/disk and normal vector in binary setup (without Stockholm condition, $M_{\text{disk}} = 0.01 M_{\odot}$)	102
4.55	subtracted two-dimensional xz plane plots of the surface density in the binary setup (without Stockholm condition, $M_{\text{disk}} = 0.01 M_{\odot}$ and $M_{\text{disk}} = 0.1 M_{\odot}$)	103
4.56	two-dimensional xz plane plots of the surface density in the binary setup (without Stockholm condition, with planet, $M_{\text{disk}} = 0.01 M_{\odot}$)	104
4.57	subtracted two-dimensional xz plane plots of the surface density in the binary setup (without Stockholm condition, with planet, $M_{\text{disk}} = 0.01 M_{\odot}$)	105
4.58	subtracted two-dimensional xz plane plots of the surface density in the binary setup (without Stockholm condition, $M_{\text{disk}} = 0.1 M_{\odot}$)	106
4.59	subtracted two-dimensional xz plane plots of the surface density in the single star setup (without Stockholm condition, $M_{\text{disk}} = 0.01 M_{\odot}$)	107
4.60	subtracted two-dimensional xz plane plot at $768 T_{\text{bin}}$ of the surface density in the binary setup (without Stockholm condition, $M_{\text{disk}} = 0.1 M_{\odot}$)	108

4.61 ratio $\rho_\phi(r) = \Sigma_{\text{up}}/\Sigma_{\text{low}}$ in the single and binary setup (without Stockholm condition, $M_{\text{disk}} = 0.01 M_\odot$)	109
4.62 F_z evolution in the single and binary case (without Stockholm condition, $M_{\text{disk}} = 0.01 M_\odot$)	109
4.63 F_z on the planet in the binary system (without the Stockholm condition, $M_{\text{disk}} = 0.01 M_\odot$ and $M_{\text{disk}} = 0.1 M_\odot$)	110
4.64 normalized disk mass evolution of the binary setup (without the Stockholm condition, $M_{\text{disk}} = 0.01 M_\odot$ and $M_{\text{disk}} = 0.1 M_\odot$)	111
4.65 disk mass evolution of the binary setup with ANTISYMMETRIC vs. OUTFLOW boundary condition (without the Stockholm condition, $M_{\text{disk}} = 0.01 M_\odot$)	113
4.66 mutual inclination of the planet's angular momentum vector and normal vector in binary setup with ANTISYMMETRIC vs. OUTFLOW boundary condition (without Stockholm condition, $M_{\text{disk}} = 0.01 M_\odot$)	114
4.67 F_z evolution in the binary setup with ANTISYMMETRIC vs. OUTFLOW boundary condition (without Stockholm condition, $M_{\text{disk}} = 0.01 M_\odot$)	114
4.68 mutual inclination of the planet's angular momentum vector and normal vector in the new/old binary setup (without Stockholm condition, $M_{\text{disk}} = 0.01 M_\odot$)	115
4.69 hydrodynamical force in the new/old binary setup (without Stockholm condition, $M_{\text{disk}} = 0.01 M_\odot$)	115
4.70 combined velocity in z direction in the new binary/single star setup (without Stockholm condition, $M_{\text{disk}} = 0.01 M_\odot$)	116
4.71 combined velocity in z direction in the new evolved binary setup (without Stockholm condition, $M_{\text{disk}} = 0.01 M_\odot$)	116
5.1 schematic view of the METIS instrument	121
5.2 functionalities of the WCU	122
5.3 schematic of the WCU	123
5.4 CAD model of the Integrating Sphere	126
5.5 reflectivity of gold	127
5.6 multiplication-factor M dependence on ρ and f	128
5.7 comparison to flux/temperature	130
5.8 setup 1 (BB, Wheel, IS and PM)	131
5.9 warm-up timescale of the blackbody source	131
5.10 transition times of the blackbody, when it is warmed up and cooled down . .	133
5.11 stability phase of the blackbody source	134
5.12 experimental versus theoretical normalized flux	135
5.13 temperature of the integrating sphere, with/without AC	136

5.14	geometrical setup to determine the radiometric flux	137
5.15	geometrical setup to determine the flux (IS,PM)	138
5.16	comparison to calculation	139
5.17	stability phase of the blackbody	141
5.18	temperature of the integrating sphere, with/without AC	143
5.19	setup 2 (BB, Wheel, IS, Camera)	144
5.20	detector output while observing cold surface cooled with liquid nitrogen	145
5.21	sigma (standard deviation of the flux) for a cold surface	146
5.22	noise reduced integrating sphere output at 1000° C	147
5.23	geometrical setup for the aperture mask experiment	149
5.24	setup of the mask measurement	149
5.25	mean flux coming from the blank aperture measured by the powermeter (manual mask)	150
5.26	standard deviation of the mean values for the different apertures (manual mask)	151
5.27	mean flux coming from the aperture mask measured by the powermeter (manual mask)	151
5.28	aperture mask measurements with and without air-conditioning (manual mask)	153
5.29	results of the 7.68 mm aperture mask measurements with air-conditioning (automated mask)	154
5.30	mean flux measured by the powermeter plotted against aperture area (automated mask)	157
5.31	mean flux measured by the IR camera plotted against aperture area (automated mask)	159
5.32	temperature of the blackbody over time for each run (automated mask)	160
5.33	pinhole tests gold/alu	162
5.34	pinhole tests gold/alu	163
5.35	gold-coated pinhole	164
5.36	pinhole tests temperature gold	165
5.37	comparison of Aluminium and gold-coated pinhole	165
6.1	different grid resolutions: planet's semi-major axis (with Stockholm, with planet, $M_{\text{disk}} = 0.007 M_{\odot}$)	180
6.2	different grid resolutions: xy-plane (with Stockholm, with planet, $M_{\text{disk}} = 0.007 M_{\odot}$)	180
6.3	planets' evolution with power-law $p = -1.5$ and $p = -0.5$ (binary star system, without Stockholm, with planet, $M_{\text{disk}} = 0.01 M_{\odot}$ and $M_{\text{disk}} = 0.07 M_{\odot}$)	181
6.4	single setup (with Stockholm, without planet, $M_{\text{disk}} = 0.007 M_{\odot}$)	182

6.5	inclination of the planet with respect to the mid-plane (single star system, with Stockholm, with planet, $M_{\text{disk}} = 0.007 M_{\odot}$)	183
6.6	different outer boundaries (binary star system, with Stockholm, with planet, $M_{\text{disk}} = 0.007 M_{\odot}$)	184

List of Tables

2.1	binary separations with disk types	10
3.1	binary and planet parameters of Kepler 38 from observations	32
3.2	correspondence between X, Y, Z and the spherical coordinate system	35
3.3	analytic surface densities of different disk sizes and masses	40
3.4	disk mass calculated with the different methods	43
4.1	force in CGS units on planet at different T_{bin} of single default setup (without Stockholm, $M_{\text{disk}} = 0.01 M_{\odot}$ and $0.01 M_{\odot}$)	58
4.2	mutual inclination in degree of the normal vector and the disk's angular momentum vector at different T_{bin} of single star setup (without Stockholm, $M_{\text{disk}} = 0.01 M_{\odot}$ and $0.01 M_{\odot}$)	62
4.3	mutual inclination in degree of the normal vector and the planet's angular momentum vector at different T_{bin} of single star setup (without Stockholm, $M_{\text{disk}} = 0.01 M_{\odot}$ and $0.01 M_{\odot}$)	62
4.4	force in CGS units in on planet at different T_{bin} of single star setup (without Stockholm, $M_{\text{disk}} = 0.01 M_{\odot}$ and $0.01 M_{\odot}$)	62
4.5	mutual inclination in degree between the normal vector and the angular momentum of the disk at different T_{bin} in the binary setup (with Stockholm, without planet, $M_{\text{disk}} = 0.007 M_{\odot}$)	66
4.6	mutual inclination in degree between the normal vector and the angular momentum of the disk in binary setup/single star setup (with Stockholm, with planet, $M_{\text{disk}} = 0.007 M_{\odot}$)	78
4.7	mutual inclination in degree between the normal vector (binary angular momentum) and the angular momentum of the planet at different T_{bin} (with Stockholm, with planet, $M_{\text{disk}} = 0.007 M_{\odot}$)	80
4.8	computed migration time	95
4.9	stability limits for p-type planets semi-major axis for different binary eccentricities	97

4.10	stability limits for p-type planets semi-major axis for different binary mass ratios and $e_b = 0.1$	98
4.11	mutual inclination in degree between the normal vector and the disk's angular momentum vector at different T_{bin} in the binary/single star setup for different star eccentricities (without Stockholm condition, $M_{\text{disk}} = 0.01 M_{\odot}$ and $0.1 M_{\odot}$)	100
4.12	mutual inclination in degree between the normal vector and the angular momentum vector of the planet at different T_{bin} for different disk masses and star eccentricities	102
4.13	force in CGS units in z direction on planet at different T_{bin} for different star eccentricities (without Stockholm condition, $M_{\text{disk}} = 0.01 M_{\odot}$ and $0.1 M_{\odot}$)	112
5.1	parameters of the blackbody source	124
5.2	parameters of the powermeter	125
5.3	parameters of the Testo 174-2010 Mini-Datalogger	125
5.4	parameters of the uncooled IR camera - Gobi640 GigE	128
5.5	mean and standard deviation of the flux temporal sequence	134
5.6	flux average value per aperture with its standard deviation	152
5.7	average flux value per aperture with its standard deviation with the automated approach	155
5.8	average flux value measured by the IR camera per aperture with its standard deviation with the automated approach	158
5.9	thermal conductivity of different materials at 20°C	162
6.1	sizes of the apertures for manual setup	188
6.2	sizes of the apertures for automatic setup	189

Eidesstattliche Erklärung

Hiermit versichere ich an Eides statt, dass ich die vorliegende Dissertation selbstständig und ohne die Benutzung anderer als der angegebenen Hilfsmittel und Literatur angefertigt habe. Alle Stellen, die wörtlich oder sinngemäß aus veröffentlichten und nicht veröffentlichten Werken dem Wortlaut oder dem Sinn nach entnommen wurden, sind als solche kenntlich gemacht. Ich versichere an Eides statt, dass diese Dissertation noch keiner anderen Fakultät oder Universität zur Prüfung vorgelegen hat; dass sie - abgesehen von unten angegebenen Teilpublikationen und eingebundenen Artikeln und Manuskripten - noch nicht veröffentlicht worden ist sowie, dass ich eine Veröffentlichung der Dissertation vor Abschluss der Promotion nicht ohne Genehmigung des Promotionsausschusses vornehmen werde. Die Bestimmungen dieser Ordnung sind mir bekannt. Darüber hinaus erkläre ich hiermit, dass ich die Ordnung zur Sicherung guter wissenschaftlicher Praxis und zum Umgang mit wissenschaftlichem Fehlverhalten der Universität zu Köln gelesen und sie bei der Durchführung der Dissertation zugrundeliegenden Arbeiten und der schriftlich verfassten Dissertation beachtet habe und verpflichte mich hiermit, die dort genannten Vorgaben bei allen wissenschaftlichen Tätigkeiten zu beachten und umzusetzen. Ich versichere, dass die eingereichte elektronische Fassung der eingereichten Druckfassung vollständig entspricht.

Teilpublikationen:

Graf S., Rutowska M., Wiest M., Rost S., Straubmeier C., Labadie L., 2020, in Evans C. J., Bryant J. J., Motohara K., eds, Vol. 11447, Ground-based and Airborne Instrumentation for Astronomy VIII. SPIE, pp 577 – 585

Weitere Publikationen:

Monika Rutowska, Tarun Sharma, Michael Wiest, Sabine Graf, Christian Straubmeier, Stefan Rost, Lucas Labadie, Andreas Eckart, Leonard Burtscher, Tibor Agócs, Dirk Lesman, Remko Stuik, Adrian Glauser, Bernhard Brandl, Felix Bettonvil, 2020, Proc. SPIE 11447, Ground-based and Airborne Instrumentation for Astronomy VIII., pp. 2T-1 - 2T-11

Hürth, 07.06.2022